Corrugated Webs and Lateral Restraints in Plate Girders for Bridges

by

J. Cafolla, Ing.(Dist.)

(neè Vendráková)

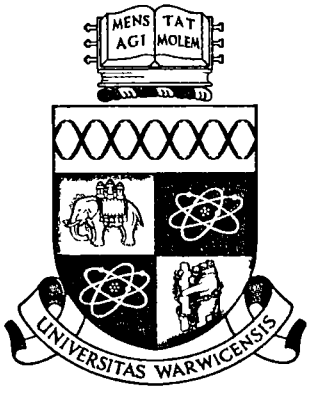

Department of Engineering

University of Warwick

Coventry CV4 7AL

The United Kingdom

A thesis submitted to the University of Warwick for the degree of

DOCTOR OF PHILOSOPHY

December, 1995

TO MY PARENTS

AND

TO MY HUSBAND

Contents

List of Tables

List of Figures

Acknowledgement

I am deeply grateful to my supervisor, Professor R.P. Johnson. His guidance, advice and encouragement has helped me a great deal in completing this research work.

I would like to thank the Steel Construction Institute for their financial support from the Market Development Fund. I also wish to thank Rowecord Engineering, Newport, and Cleveland Structural Engineering, Darlington, for their kind help with fabrication of the test specimens.

My thanks also goes to Cass Hayward and Partners, consulting engineers for providing me with the drawings and calculations of an existing plate girder highway bridge.

I express my gratitude to Professor D.A. Nethercot, Nottingham University, and to Dr. J. Tubman, Scott Wilson Kirkpatrick, for their advice during the work on lateral restraints.

My appreciation also goes to Mr. C. Banks and his team for their skilful work in preparing and assisting with the experiments.

Finally, I would like to say thank you to my parents and my husband whose care, support and love are extremely important for me.

Declaration

I hereby declare that all the investigations presented in this thesis are my own except where specific reference has been made to the work of others. No part of this thesis has been submitted to any other university or institution for credit or award.

Abstract

In the thesis two problems have been studied: the first one is the use of corrugated webs in plate girders for composite bridges; the second one is the study of lateral restraints in composite bridges.

In structural design corrugated webs are frequently used in beams for buildings in Sweden. They have also been used in four bridges in France and two in Japan. The shear stresses of corrugated panels were the main subject of previous studies. This thesis deals with local flange buckling of beams with corrugated webs. Computer analyses give a ratio of areas for use in design of the compressed flange. The validity of this ratio is confirmed by experimental work undertaken on five specimens (two of them loaded by bending only; three loaded by a combination of bending and shear). The interaction between the local buckling of the flange and web buckling is examined. A formula for calculating the effective shear modulus is given. The possible methods of fabrication of a cambered beam with a corrugated web are shown here and the problems which could arise are discussed. There is also a comparison between the design of an existing bridge and a new design where a plane web in a plate girder is replaced by a corrugated web.

The second part of the thesis contains computational investigations of the lateral restraints in composite plate girder bridges. This method of investigation is more appropriate than laboratory testing, due to the difficulty of fabricating steelwork to maximum permitted imperfections. Numerical elastic finite element analyses with geometric non-linear facilities are used on a relevant part of the structure (a compressed flange) that has the maximum allowed geometric imperfections. The F-forces in elastic lateral restraints modelled by spring elements are then determined. This study concentrates particularly on design forces for bracings at the supports of simply-supported and continuous composite UB and plate girder bridges.

Notation

Notation for Part I

a	length of a panel of a corrugated web; a parameter which defined a parabola shaped curve
b	width of a flat panel of a corrugated web (see Fig. 2.1)
b_{f}	width of a flange of a beam with equal flanges
b_{fc}	width of a flange in compression
b_{ft}	width of a flange in tension
$b_{\mathrm{f,concr}}$	width of a concrete slab of a composite beam
b_{h}	$= b/2$
b_0	$= 2b + 2d$
c	flange outstand; camber of a beam
c_{btm}, c_{top}	measured distances (see Fig. 7.1)
c_{span}	camber of a girder within a span of a bridge
c_{L}, c_{A}, c_{S}	large, average and small outstands of a flange attached to a corrugated web
d	width of a sloping panel of a corrugated web in plan (see Fig. 2.1)
d_{h}	$= d/2$
d_1, d_2	measured lengths of diagonal LVDTs (see Fig. 7.1)
$d_{1\gamma}$, $d_{2\gamma}$	shortened and extended diagonals, respectively, after shear load was applied
e	allowed deviation in a pair of fold lines
f_{y}	yield stress

h	depth of a beam (see Fig. 2.1)
h_{eff}	depth of an imaginary beam without any web between the flanges with the thicknesses defined by $t_{\text{fc,I}}$ and $t_{\text{ft,I}}$
h_{w}	width of a web
k	buckling coefficient (see eq. 1.3 or 1.23)
k_{f}	reducing factor for local buckling (see eq. 1.5)
k_{u}	buckling coefficient dependent on the boundary conditions
l	length of a beam; mean value of l_1 and l_2 defined in eq. 8.12
l_{compr}	measured length of LVDT attached to the compressed flange (see Fig. 7.1)
l_{d1}, l_{d2}	the average values of the measured diagonals from both sides of a specimen
l_{end}	length of the end parts of an existing bridge girder
$l_{\text{endplates}}$	measured length between two end plates (see Fig. 7.1)
l_{gauge}	mean value of l_{compr} and l_{tens} for specimens CW1 and CW2; length of specimens CW4 and CW5
l_{mid}	length of the middle part of the existing bridge girder
l_{n}	shorter edge of a specimen from side view
l_{p}	longer edge of a specimen from side view
l_{s}	distance of the applied shear force F_{s} from a cross-section where the moment M_1 is calculated
l_{tb}	measured length between top and bottom horizontally placed LVDTs (see Fig. 7.1)
l_{tens}	measured length of LVDTs attached to the tension flange (see Fig. 7.1)

l_1, l_2	distances of the points where forces F_l and F_w were applied, respectively, from the outside surface of the compression flange of specimens (see Fig. 8.3)
n	number of nodes
$\mathbf{n}$	vector perpendicular to the shell mid–surface of a parabolic shell element
n_y	yield membrane load (uniformly distributed load along the shorter edges of compressed flange)
n_t	uniformly distributed load along the shorter edges of a tension flange
n_I	nearest integer value given by eq. 1.16
q	uniformly distributed load
s	$= 2b + 2d \sec \alpha$; length along an unfolded corrugated plate
t_{concr}	thickness of a concrete slab of a composite beam
t_f	thickness of a flange of a beam with equal flanges
t_{fc}, t_{ft}	thicknesses of flanges in compression or tension, respectively
$t_{f,A}$, $t_{f,I}$	effective thicknesses of flanges of an imaginary beam, without any web between the flanges, developed from tension or pure bending, respectively, by finite element analyses
$t_{fc,A}$, $t_{fc,I}$	effective thicknesses of compression flange of an imaginary beam, without any web between the flanges, developed from tension or pure bending, respectively, based on the equation developed by finite element analyses (see eqs. 8.6 and 8.7)

$t_{\mathrm{ft,A}}$, $t_{\mathrm{ft,I}}$	effective thicknesses of tension flange of an imaginary beam, without any web between the flanges, developed from tension or pure bending, respectively, based on the equation developed by finite element analyses (see eqs. 8.6 and 8.7)
t_{top}, t_{btm}	measured distances of top and bottom ends of tension LVDTs from the outside surface of the flange (see Fig. 7.1)
t_{w}	thickness of a web
w	error in a pair of folds of a corrugated plate when folded with a deviation (eq. 3.11)
w_{t}	total error for one wave of a corrugation (eq. 3.12)
x, y, z	axes of the right–handed coordinate system with z–axis as the longitudinal one
y_{corr}	y–coordinate of a corner point on a longitudinal edge of a corrugated panel (Tables 3.2 and 3.3)
y_{e}	distance of the midpoint of an element from the neutral axis
y_{flat}	y–coordinate of a corner point on a longitudinal edge of a flat panel (Tables 3.2 and 3.3)
y_{p}	y–coordinate of a point on a smooth parabola in Table 3.5
y_{FE}	y–coordinate of a corner point on a longitudinal edge of a corrugated panel bent to create a camber obtained from finite element analysis (Table 3.5)
y_{T}	distance of the bottom surface of a flange of a composite girder from the neutral axis (see Fig. 4.1)
y_{1}	distance of the outside surface of compression flange from the neutral axis

z_{corr}	z–coordinate of a corner point on a longitudinal edge of a corrugated panel (Tables 3.2 and 3.3)
z_{flat}	z–coordinate of a corner point on a longitudinal edge of a flat panel (Tables 3.2 and 3.3)
z_{i}	z–coordinate of a node i
$\{d\}$	eigenvector defined by finite element software
A	cross–sectional area
A_{eff}	effective cross sectional area of a beam with a corrugated web calculated from the results of finite element analyses of a model loaded by tension only
A_{fc}, A_{ft}	cross–sectional areas of the compression or tension flanges, respectively
A_{ratio}	a ratio of the flange areas cut by a corrugated web (see eq. 5.5 and Fig. 5.13)
B	$= M_{\text{b}}h$; bimoment in a beam with a corrugated web
C_{pr}	predicted compression force in a test specimen
D	stiffness of a plate
D_{y}, D_{z}, D_1, D_2	bending stiffnesses of a corrugated plate
D_{zy}	twisting stiffness of a corrugated plate
E	Young's modulus
E_{com}, E_{ten}, E_{web}	Young's modulus of compression, tension flanges and a web, respectively
$E_{\text{e,b}}$; $E_{\text{e,t}}$	effective Young's modulus of a corrugated plate when loaded by pure bending and uniform tension, respectively
F	total compression force applied to a specimen in tests
F_{l}	bending load applied in a test

F_n	tension force applied to a corrugated panel to create a camber (see Fig. 3.6)
F_s	shear load applied in a test
F_t	pulling forces applied to the top corners of a corrugated plate to create a camber (see Fig. 3.6)
F_w	self–weight of the upper part of the test rig
F_z	force applied to a corrugated web in z–direction
$F_{z,e}$, $M_{x,e}$	internal element forces
F_M	couple of forces applied at the corners of a corrugated panel to create a camber (see Fig. 3.6)
G	elastic shear modulus
G_{eff}	effective shear modulus of a corrugated web
G_{est}	estimated value of an elastic shear modulus
I_{eff}	second moment of area of a beam with a corrugated web calculated from the results of finite element analyses of a model loaded by pure bending only
I_x, I_y, I_z	second moments of area of a corrugated plate cross–sections
$I_{x,w}$, $I_{x,o}$	second moment of areas of a beam with a corrugated web including and excluding the web, respectively
$I_{y,f}$	second moment of area of a flange
I_1	second moment of area of a specimen
$I_{1,eff}$, $z_{1,eff}$	second moment of area and the distance of the outside surface of compression flange from the neutral axis for an imaginary beam without any web between the flanges with the thicknesses defined by $t_{fc,I}$ and $t_{ft,I}$

I_2, M_2, y_2	second moment of area, bending moment and distance of the outside surface of compression flange from the neutral axis, respectively, for an imaginary BEAM 2 explained in Section 8.1.1.4
K_u	shear buckling coefficient defined by eq. 1.28
L	length of a span
M	bending moment
M_b	bending moment of a flange attached to a corrugated web created by a shear force in the web
$M_{b,max}$	maximum in–plane bending moment of a flange attached to a corrugated web
$M_{b,FEA}$	in–plane bending moment of a flange created by shear in a corrugated web obtained from finite element analysis
$M_{b,1}$, $M_{b,2}$, $M_{b,3}$	in–plane bending moments of the flange along a corrugated web
M_{fix}	bending moment at fixed end
M_{int}	bending moment above an internal support
M_x, M_y, M_z	bending moments of a plate around x, y and z–axes, respectively
M_{yz}, M_{zy}	twisting moments per unit length of a plate
M_1	total bending moment applied to a specimen in tests
N_{cr}	elastic critical buckling load of a strut
N_y	compressive load when the yield stress is reached in a strut
R	radius of a curvature
R_b	reaction forces in fixed bottom corners of a corrugated plate when creating a camber (see Fig. 3.6)
R_i	reaction force at a node i

T	shear force per unit length along the longitudinal edges of a corrugated web
T_{fix}	shear force at fixed end
T_{int}	shear force above an internal support
T_{pr}	predicted tension force in a test specimen
U_{e}	external energy
U_{i}	total internal strain energy
U_{AB}, U_{BC}	internal strain energies defined in Appendix C
V	shear force in a web
V_{cr}	critical buckling shear force of a plate
V_{d}	factored design vertical shear force at a support or at a splice taken from the original design of a plate girder bridge
V_{zy}	shear force of a plate
W	section modulus of a beam
W_{f}	section modulus of a flange
W_{btm}, W_{top}	section modulus of bottom and top surface of steel flanges in a composite bridge girder, respectively
$[K_{\text{e}}]$	linear stiffness matrix defined by finite element software
$[K_{\text{ssref}}]$	reference stress stiffness matrix defined by finite element software
$\{R_{\text{ref}}\}$	reference load defined by finite element software
α	angle between flat and sloping panels of a corrugated web
β	parameter which characterises the boundary conditions of a plate edges
β_{j}	an angle shown in Fig. 5.13
γ	shear strain

γ_1, γ_2	shear strains (see Fig. 2.10)
δ	longitudinal shear deformation of a specimen or a model
$\delta_{top} - \delta_{btm}$	difference of top and bottom horizontal deformations measured along the loading beams
ϵ_i	measured strains in the rectangular rosettes where the axes of the three gauges are spaced at 45° intervals
ε	strain; rotational stiffness parameter for Fig. 1.3
ε_c	mean strain of a compressed flange
ε_f	mean value of a strain of a compressed flange
ε_{max}	maximum strain on the longitudinal edge of a corrugated plate when creating a camber
ε_t	mean strain of a tension flange
ε_{theory}	theoretical mean strain of compression flange according to linear elastic theory
ζ_1, ζ_2	coefficients given by eq. 1.20 and 1.21
θ_{btm}	measured rotation of the bottom end plate of specimens CW4 and CW5
θ_i	inelastic rotation
θ_t	total rotation
θ_{top}	measured rotation of the top end plate of specimens CW4 and CW5
θ_y, θ_z	curvatures per unit length of an element of a corrugated plate
θ_{zy}	twist per unit length of an element of a corrugated plate
ι	$= b/(2t_w)$
κ	$= d/(2t_w)$
κ_c	multiplier dependent on ζ_1 and ζ_2 in eq. 1.19

λ_b	$= N_{cr}/N_y$; critical load factor multiplier on the reference load referred to a critical buckling load coefficient
λ_w	slenderness of a flat part of a corrugated web
$\bar{\lambda}$	slenderness of a flange outstand
$\bar{\lambda}_p$	plate slenderness
$\bar{\lambda}_L$, $\bar{\lambda}_A$, $\bar{\lambda}_S$	slendernesses of large, average and small outstands of flanges
ν	Poisson's ratio
ϖ	smallest positive real root of eq. 1.17 or eq. 1.24
ρ	radius of curvature of the neutral plane in bending
σ	direct stress
σ_b	additional bimoment stress in a flange attached to a corrugated web
σ_{cr}	elastic critical buckling stress
$\sigma_{cr,L}$, $\sigma_{cr,A}$, $\sigma_{cr,S}$	critical stresses computed from eq. 8.16 for large, average and small outstands, respectively
$\sigma_{d,L}$, $\sigma_{d,A}$, $\sigma_{d,S}$	design values of compression stresses based on EC3 methods for large, average and small outstands, respectively
σ_{fix}	direct stress at fixed end
σ_{int}	direct stress above an internal support
σ_{max}	maximum compressive stress in a specimen calculated on the outside surface of the flange using measured geometrical values; maximum stress on the longitudinal edge of a corrugated plate or a flange
σ_{princ}	the principal stresses in a web
σ_z	direct longitudinal stress
τ	shear stress

τ_f	post buckling failure in shear
$\tau_{cr,gl}$	critical global buckling of a corrugated web
$\tau_{cr,loc}$	ideal local buckling of a flat part of a corrugated web
τ_m	interaction between global and local buckling modes
τ_y	shear yield limit
$\tau_{U.L.S.}$	shear stress at ultimate limit state
ϕ	curvature
ϕ_e	elastic curvature
ϕ_i	inelastic curvature
ϕ_{mean}	mean curvature
φ	angular allowed deviation in pair of fold lines
χ	reduction factor for strut buckling from EC3 for class 4 cross–section
ω	angle between a diagonal and shorter edge of a specimen from side view before loading the specimen by shear
Δ_{bend}	deformation defined by eq. 8.37
Δ_{shear}, Δ_z	deformations defined by eq. 8.38
Δy	$= y_{flat} - y_{corr}$; or $= y_{FE} - y_p$
Δz	extension of the top longitudinal edge of a corrugated panel when creating a camber by *in–plane* bending
Ω	angle between the edges of a specimen from side view after loading the specimen by shear

Notation for Part II

a_i	known amplitudes of initial shape given by eq. 13.1
$\bar{a}_i$	unknown amplitudes of deformed shape given by eq. 13.2

a_{max}	maximum initial imperfection of a beam of overall length L_G
a_o	maximum initial imperfection of a beam given by BS 5400: Part 6 for the length of the beam L_u
b_f	width of a rectangular cross–section
d_1, d_2	depth of a U–framed bridge girder as defined by BS 5400: Part 3 and shown in Fig. 10.1
f_c, f_u	restraining forces per unit length acting at the tips of continuous restraint provided by a deck, as defined by BS 5400: Part 3, Clause 9.12.3
f_y	yield stress
k	$= N/EI$
k_i	spring constant defined by Winter (see eq. 12.2)
k_n	$= 2K_b/(n-1)$; stiffness of the multiple springs where $n > 3$
l	length of a strut used as a model for validation of the software
l_e	effective length of beams subjected to lateral torsional buckling as defined by BS 5400: Part 3, Clause 9.6
$\bar{l}$	length in plan of the model used for validation of the software
l"	deformed length of the model used for validation of the software
n	number of equal lengths of the beam with overall length $3L_u$
q	uniformly distributed axial force per unit length
t_f	thickness of a rectangular cross–section
w	deformation of the model used for validation of the software in the direction of applied force W

x, y, z	axes of the right–handed coordinate system with x–axis as the longitudinal one and $I_y < I_z$ where cross-section is of a rectangular shape
A	cross sectional area
A_{fc}	area of compression flange
C_4	factor dependent on a moment gradient defined by EC3
D	diameter of the cross–section of the model used for validation of the software
E	Young's modulus
F_c, F_u	restraining forces acting at the tips of intermediate discrete U–frames as defined by BS 5400: Part 3, Clause 9.12.2
F_u	$= K_b \delta_b$
$F_{u,max}$	maximum of the forces F_u for multiple intermediate bracings
$F_{u,N1}$, $F_{u,N26}$, ...	lateral forces at node 1, node 26, ...
F_R	restraint forces at supports given by BS 5400: Part 3, Clause 9.12.4
I	second moment of area of a cross–section
I_y	$= t_f^3 b_f / 12$
I_z	$= b_f^3 t_f / 12$
K	stiffness of a spring element used as an elastic intermediate support
K_b	stiffness of a spring element used for modelling an elastic bracing
K_{b1}, K_{b2}	$= K_b$ for two intermediate elastic bracings ($n = 3$)
K_s	spring stiffness in the model used for validation of the software

K_1, K_2	stiffnesses of the elastic supports at the ends of a beam
L_{cr}	critical buckling length taken as the distance between two braced points
L_u	length of a beam between neighbouring restraints
L_G	overall length of a beam
M	bending moment in a loaded strut
M_{cr}	elastic critical bending moment
N	axial force
N_a, N_b	axial forces in the model used for validation of the software without and with a spring at an end, respectively
N_{cr}	Euler's elastic critical buckling force
N_l, N_h	lower and higher boundary of an axial force of the interval equal to the applied load increment within which the axial force at first yield (N_y) was reached
N_{pl}	plastic axial force used as a failure load defined by $f_y A_{fc}$
N_y	axial force at first yield
N_{y1}	axial force at left support when first yield occured anywhere along the main member when the main member was loaded by non–uniform axial force
N_{y2}	axial force at right support when first yield occured anywhere along the main member when the main member was loaded by non–uniform axial force
N_R	design resisting force used for comparison of the results with the code; it is defined in EC3 as χN_{pl}
P	constant compression force
R_{s1}, R_{s2}	lateral reaction forces at left and right supports, respectively

W	loading force of the model used for validation of the software
β	slenderness of a strut defined by Fig. 10 of BS 5400
γ_M	safety factor (= 1.5)
δ_b	deformation of a beam in the horizontal xy plane at the braced point
$\delta_{b,max}$	maximum deformation in one of the springs where more than one elastic bracing is modelled
δ_{b1}, δ_{b2}	deformations of the springs along the axis No. 1 and 2 in Fig. 12.3, respectively, at first yield for multiple elastic bracings
$\delta_{b1,l}$, $\delta_{b1,h}$	deformations of the springs corresponding with N_l and N_h along the axes No. 1 in Fig. 12.3
$\delta_{b2,l}$, $\delta_{b2,h}$	deformations of the springs corresponding with N_l and N_h along the axes No. 2 in Fig. 12.3
$\delta_{x,N1}$, $\delta_{x,N26}$, ...	longitudinal deformation of node 1, node 26, ...
$\delta_{y,N1}$, $\delta_{y,N26}$, ...	lateral deformation of node 1, node 26, ...
δ_B	deformation of the middle point of a compressed strut
$\bar{\lambda}$	slenderness of a strut
σ_{fc}	maximum compressive stress in the flange
σ_l, σ_h	stresses corresponding with N_l and N_h
σ_y	maximum stress reached at a cross–section along a beam which was taken as first yield in the beam
χ	function of the slenderness defined by curve c in EC3
ΔW	load increment applied to the model used for validation of the software

Subscripts A, B, C etc. added to some of the above variables refer to the initial shapes A, B, C etc.

Part I

Plate girders with trapezoidally corrugated webs

Chapter 1

Corrugated webs and panels – previous studies

1.1 Introduction and literature review

Corrugated sheets and panels are common structural elements which have been used in building constructions for many years. As one of the oldest types of formed steel products, they are frequently used in various shapes as roofing and siding material. They are also used for the internal spar webs of high–speed aircraft. Corrugated plates found their applicability in off–shore structures. Recently, they have become popular as webs of beams and girders, mainly in Europe and Japan.

Their main advantage is as a possible way of achieving adequate out–of–plane stiffness without alternative usage of stiffeners or thicker plates.

Much research has been done on the in–plane shear strength of corrugated plates, which is one of the most important loading conditions. In the 1960's the elastic buckling behaviour of light–gauge, corrugated metal shear diaphragms was studied by Easley and McFarland [10, 11]. They developed an approximate method of calculating the global critical shear buckling stress of a corrugated plate based on orthotropic plate theory. A review of their approximation is given in Section 1.2. They performed the experimental study described in [10, 11] which was designed to check the accuracy of the equations. Their theoretical predictions of shear buckling

behaviour agreed reasonably well with the behaviour observed in the experiments.

An investigation in the area of corrugated steel sheeting aimed mainly to survey the relevant factors and to indicate how the shear flexibility and strength may be predicted. In his study Bryan [4, 5] gives formulae for calculating the shear effects in corrugating sheeting in elastic and plastic design provided that the flexibility in shear and ultimate shear load of the sheeting can be calculated. However, these structural elements are combined with purlins and fasteners and they are loaded by bending out–of–plane which creates different boundary conditions from the ones studied here.

In the last few decades, interest in using corrugated plates has been focussed on the possibility of using them as a part of beams and girders in buildings and bridge structures. Economical design of beams and girders normally requires thin webs. The conventional use of stiffeners introduces some disadvantages. Fabrication cost can be reduced by eliminating the manual welding required for the stiffeners in conventional beams with plane webs. With the developments in welding technology, the welding of a corrugated web to flanges can be automatized nowadays. Another disadvantage of using stiffeners is in welding of transverse stiffeners which reduces the fatigue strength. Korashy and Varga [29] tested conventionally stiffened beams and beams stiffened by corrugations under cyclic loads. The beams with a corrugated web showed about 50 % higher fatigue strength than the conventionally stiffened beams, in which the stiffeners were welded to the tension flange. The increase in fatigue strength for beams stiffened by corrugations was about 25 % in comparison with conventionally stiffened beams where the stiffeners were cut off short of the tension flange.

The same conclusion is given in [12]. Harrison made fatigue tests of two plate girders, in which he used corrugated webs instead of conventional transverse stiffeners. However, he states that the beams with a corrugated web are not as good in fatigue as unstiffened girders made with automatic welding. On the other hand, his information is limited by the results only from these two tests.

The aim of Libove's research [15, 33, 34, 35] was to find the influence of four different kinds of discrete attachments between the edges of a corrugated web and

framing members under pure shear. The results based on elastic analysis showed that the stiffness of discretely attached corrugated plates was greatly dependent on the details of the attachment. A wide variety of geometries, which have been presented for trapezoidally corrugated plates, showed how the stiffness varied with the shape of cross–section. However, Libove's studies are mostly applicable to aircraft design.

The most comprehensive theoretical and experimental investigation was done at Chalmers University of Technology in Sweden [3, 30, 31, 32]. Several series of tests on trapezoidally corrugated webs and panels under axial and shear loading were performed. The test specimens were constructed with corrugated panels with thickness which varied between 1 and 2.6 mm, and slenderness ratio which varied between 2000 and 230. Two different shear buckling modes were investigated here. Local buckling of a flat part between the corrugations was concluded to be the governing one for shear failure if the critical buckling stress is below or in the area of the shear yield stress of the material. The tests showed that this was valid for shear buckling for girder depths up to the region where global buckling with the buckles developing along the whole panel web became critical. Equations for calculating the global buckling, developed on the assumption of an orthotropic plate with properties defined by the cross–section of one wave length of the corrugation shape, were used in the form of common formulae given by Easley and McFarland [10, 11]. The formula for interactive buckling was developed and it was verified by the experimental results. It was found that the post–critical strength for panels loaded in pure shear was about 50–60 % of the maximum load. Although the tension field was observed in the far post–buckling range only after very large deformations, it was concluded that it was not possible to consider it in design. Research involving the axial compression in a parallel direction with the corrugations was performed as a part of this Swedish project [31]. The combined axial compression and shear investigation led to the conclusion, that the best interaction curve was a circular one. This type of axial compression is, however, not considered in present research.

Luo and Edlund [38, 39] performed computer analyses of Leiva's test specimens using the finite strip method. The results from finite strip analysis showed good agreement with the full–scale tests, especially in the case when the panel is subjected

to pure shear loading.

The investigations in Sweden led to wide usage of beams with corrugated webs in building construction. Since the mid 1970's, beams with corrugated webs have dominated the Swedish market for small and medium span steel roofs with girders of constant or linearly varied depth [62]. They are widely used, especially in the regions close to manufacturing factories.

The French government has recently supported research on using corrugated panels in bridge structures. Some design studies [6, 7] were done which led to the contracts for Campenon Bernard's projects. Four bridges have been constructed: the three span Pont de Cognac with a trapezoidal box with concrete flanges and corrugated steel webs (1986); Maupre viaduct with overall length about 325 m and triangular box girder deck consisting of a concrete–filled steel tube with two 'pleated' 8 mm steel webs and a prestressed concrete slab (1987); Asterix plate girder bridge with overall length about 75 m. The construction of the fourth bridge in Southern France, Pont de la Corniche, was finished recently. It is a box girder bridge with curved soffit. The bridges were built without any major technical difficulties and they have been successful in practice.

Using corrugated plates in bridge superstructures has several advantages and disadvantages. They were summarised by Prof. R.P. Johnson in March 1993, as shown in appendix A.

The analysis of a newly constructed composite PC box girder in Japan is given in [54]. It is a 31 m long single–span bridge with two boxes with webs made of corrugated plates. Exterior cables are used for prestressing the concrete. In general the paper shows a great potential in using corrugated plates for short and medium span bridges. Some difficulties were pointed out concerning the warping stresses due to torsion, which seems to play an important role in design of PC box girders.

In summary, the above mentioned research done on corrugated plates was mainly oriented to finding the shear stiffness and critical shear buckling stress of the plate. There is no evidence of any kind of investigation to find the actual bending stiffness of a corrugated web in an I–section, since it is considered to be negligibly low. Design of a compression flange attached to a corrugated web appears not to take account

of possible local buckling of large outstands. The designed bridges were verified for their safety of design, but no general rules or suggestions were given for design of other bridges in different conditions. Some comparison between a redesigned bridge girder with a corrugated web and an existing one with a plane web could be useful, to explore the economic advantages of using the corrugated web.

Some other papers deal with investigations of beams with corrugated webs. Mostly they are specific to a problem not in the interest of the author, as for example references [36, 37]. They deal with the influence of the openings in a corrugated web on its shear capacity. Bridge girders do not need openings and it is more likely that they will be avoided in bridge design.

Research on beams with corrugated webs was performed on Slovak Technical University of Bratislava in the 1970's [48, 49]. The beams with corrugated webs were replaced in design by equivalent beams with plane webs, which had their thickness calculated from rather complicated formulae. Therefore no further use of this research has been considered here.

The following three sections in this chapter summarise the main development and use of the formulae for calculating the critical shear buckling stresses of a corrugated panel as they were developed in the above mentioned references. A proposition for a verification procedure as suggested by Raoul [43] is given.

1.2 Shear buckling

1.2.1 General

There are various limits for the stresses, and different influences may interact so that failure may be premature. It is presumed that the shear stress is evenly distributed over the total depth of the web, Fig. 1.1, $\tau = V/t_w h_w$.

In general a corrugated web can buckle in two different modes, local and global. The limiting stresses are the yield limit τ_y, ideal local buckling $\tau_{cr,loc}$ of a flat part of a corrugation, post–buckling failure τ_f, global buckling $\tau_{cr,gl}$, and interaction between local and global buckling modes τ_m.

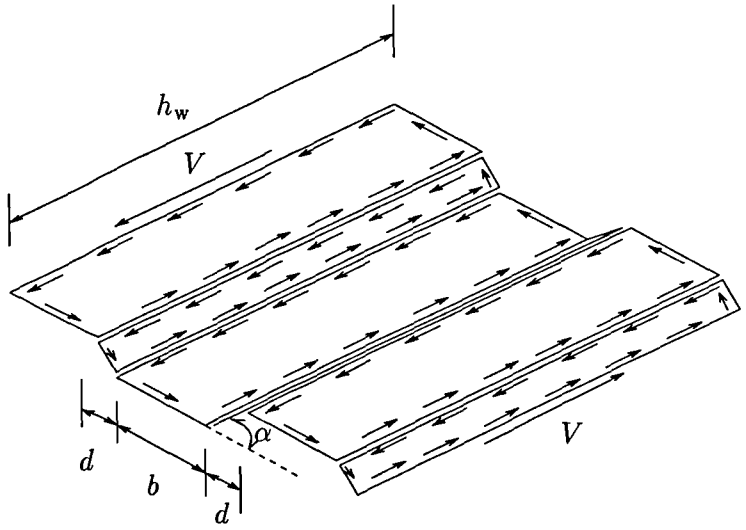

Figure 1.1: Trapezoidally corrugated plate under shear force.

1.2.2 Yield limit for pure shear

Theoretically the stress must be less than the yield limit τ_y

$$\tau \leq \tau_y = \frac{f_y}{\sqrt{3}} \approx 0.6 f_y \tag{1.1}$$

1.2.3 Local buckling mode

Local buckling may occur when a flat plate between corrugations has a large breadth to thickness ratio. The formula for this mode can be taken from classical analysis [3, 31] as

$$\tau_{cr,loc} = k \frac{\pi^2 E}{12(1-\nu^2)} \left(\frac{t_w}{b}\right)^2 \tag{1.2}$$

where E is Young's modulus of elasticity, ν is Poisson's ratio, and k is a buckling coefficient. Assuming that the flat plate has hinged and laterally restrained edges at the corrugation folds the buckling coefficient k is

$$k = 5.34 + 4 \left(\frac{b}{h_w}\right)^2 \tag{1.3}$$

For ideal buckling, with hinged edges and negligible b/h_w ratio in eq. 1.3, the

critical value for local buckling can be written

$$\frac{\tau_{cr,loc}}{f_y} = \frac{4.83}{\lambda_w^2} \tag{1.4}$$

where $\lambda_w^2 = (b/t_w)^2 f_y/E$.

Following the assumptions made in France [43], the local buckling of a plane panel should be reduced by a factor due to the fact that the elementary panels are not exactly hinged – small movements perpendicular to the web are possible. The critical value of shear stress for local buckling mode is then

$$\tau_{cr,loc} = k_f \frac{5.34\pi^2 E}{12(1-\nu^2)} \left(\frac{t_w}{b}\right)^2 \tag{1.5}$$

where k_f is the reducing factor determined by some French studies (Campenon Bernard) as $k_f = 0.88$.

1.2.4 Post–buckling failure

A correction of the critical local stress should be made to take into account the geometrical defects and the residual stresses. Bergfelt and Leiva [3] give the formula for the *post–buckling failure* stress as

$$\tau_f = \sqrt{\tau_{cr,loc}\tau_y} = \sqrt{\tau_{cr,loc} 0.6 f_y} \tag{1.6}$$

where $\tau_{cr,loc} < \tau_y$.

Raoul [43] gives the correction for this stress according to Eurocode 3: Part 1.1 [55]:

$$\tau_f = 0.9\sqrt{\tau_{cr,loc}\tau_y} \leq \tau_y \tag{1.7}$$

1.2.5 Global buckling

The following theoretical analyses in the literature are based on the assumption that a corrugated diaphragm can be analysed as a thin, orthotropic plate, of uniform thickness with material constants equal to the gross material constants of one

repeating cross–section of the corrugated panels in the diaphragm.

The bending moments per unit length, M_y and M_z[1], which act on $b_0 \times b_0$ element from a diaphragm, as shown in Fig. 1.2, are related to the curvatures θ_y and θ_z of

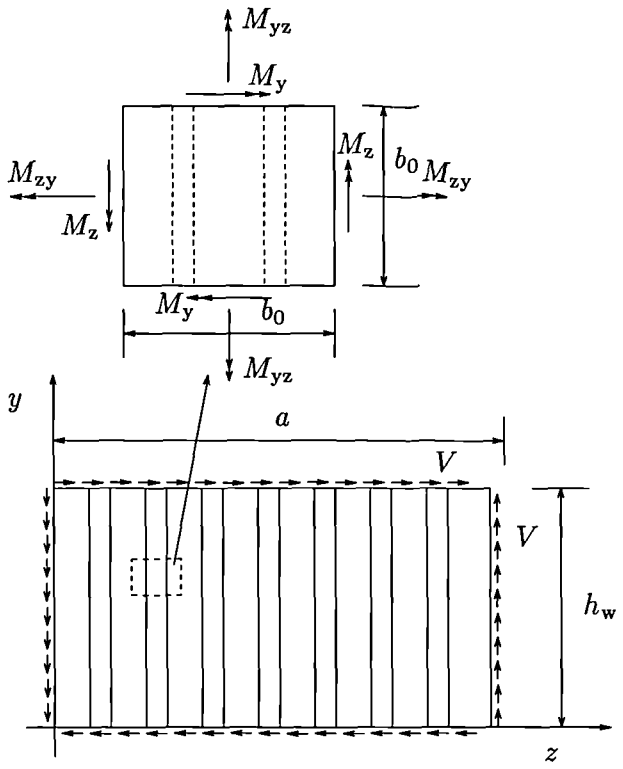

Figure 1.2: Coordinate system and element isolated.

the element; the twisting moments per unit length, M_{zy} and M_{yz} are related to the local twist per unit length θ_{zy} of the element. The relations are

$$M_z = D_z\theta_z + D_1\theta_y \tag{1.8}$$

$$M_y = D_2\theta_z + D_y\theta_y \tag{1.9}$$

$$M_{zy} = D_{zy}\theta_{zy} \tag{1.10}$$

where for corrugated sheets of any cross–section, the constants in eqs. 1.8 and 1.9

[1]The right–handed coordinate system with z axis as the longitudinal one was used in Part I of the present thesis.

are

$$D_z = \frac{b_0}{s}\frac{Et_w^3}{12} \tag{1.11}$$

$$D_y = \frac{EI_y}{b_0} \tag{1.12}$$

$$D_1 = D_2 = 0 \tag{1.13}$$

where $s = 2b + 2d\sec\alpha$ is an arc length of one repeating corrugation shape; I_y is the second moment of area of one repeating cross–section of the corrugation about its neutral axis:

$$I_y = 2bt_w\left(\frac{d\tan\alpha}{2}\right)^2 + 2t_w\frac{d^3(\tan\alpha)^2}{12\cos\alpha} \tag{1.14}$$

The geometry of the web is defined by $b_0 = 2b + 2d$, b, d, t_w, h_w, α according to Fig. 1.1 and 1.2. The missing expression $(1 - \nu^2)$ in eq. 1.11 was shown to be of no importance [11] and for simplicity it was omitted.

The condition $D_1 = D_2 = 0$ (eq. 1.13) is an approximation that is valid only when $D_y \gg D_z$; and D_{zy} is the same order of magnitude as D_z. This is usually true for all types of corrugated sheets. A reasonable limiting condition for its applicability should be $D_y > 50D_z$ [11]. In the other of Easley's paper [10] the limiting condition is more strict, given as $D_y > 200D_z$. The first condition was considered in the thesis.

Easley and McFarland [11] analysed a corrugated web according to both small and large deflection theories. They developed the critical buckling shear force per unit length of the form

$$V_{cr} = D_y\pi^2\left(\frac{a}{2\varpi n_I^2 h_w^4} + \frac{3\varpi}{h_w^2} + \frac{\varpi^3 n_I^2}{2a^2}\right) + D_z\pi^2\frac{n_I^2}{2\varpi a^2} + D_{zy}\pi^2\left(\frac{1}{2\varpi h_w^2} + \frac{\varpi n_I^2}{2a^2}\right) \tag{1.15}$$

for which a and h_w are the plate dimensions (Fig. 1.2); D_z, D_y, and D_{zy} are the bending and twisting stiffnesses per unit length of the plate. n_I is the nearest integer value given by

$$n_I = \frac{a}{h_w}\left(\frac{D_y}{\varpi^4 D_y + \varpi^2 D_{zy} + D_z}\right)^{1/4} \tag{1.16}$$

and ϖ is the smallest positive real root of

$$8D_y^2\varpi^8 + \frac{27}{4}D_yD_{zy}\varpi^6 + \left(11D_zD_y - \frac{11}{4}D_{zy}^2\right)\varpi^4 + \left(\frac{D_{zy}^3}{4D_y} - 3D_zD_{zy}\right)\varpi^2 + \left(\frac{D_{zy}^2D_z}{4D_y} - D_z^2\right) = 0 \quad (1.17)$$

Eqs. 1.15, 1.16 and 1.17 were derived using the Ritz energy method. The conditions for validity of eq. 1.13 can allow the critical shear buckling force to be simplified to the form

$$V_{cr} = 36\frac{D_z^{1/4}D_y^{3/4}}{h_w^2} \quad (1.18)$$

Bergman and Reissner's formulae (given in reference [10]) are determined also from analysis of plates having different flexural rigidities in two perpendicular directions. Their formula is

$$V_{cr} = 4\kappa_c\frac{D_z^{1/4}D_y^{3/4}}{h_w^2} \quad (1.19)$$

in which κ_c is a multiplier dependent upon

$$\zeta_1 = 2\frac{(D_zD_y)^{1/2}}{D_{zy}} \quad (1.20)$$

and

$$\zeta_2 = \frac{h_w}{a}\left(\frac{D_z}{D_y}\right)^{1/2} \quad (1.21)$$

If D_y is much larger than D_z, and D_{zy} and a/h_w are small enough that ζ_2 is less than about 0.4, the value of κ_c is approximately 9.0 $\Rightarrow 4\kappa_c = 36$ which agrees with eq. 1.18.

Hlaváček [13] developed the buckling load formula on the basis of buckling behaviour in shear of flat sheets reinforced by separate equally spaced stiffeners symmetrically attached to both faces of the sheet, but intended that his results should be applicable to corrugated metal diaphragms as well. His formula is

$$V_{cr} = k\frac{D_z}{h_w^2} \quad (1.22)$$

where

$$k = \pi^2 \left(\frac{4 D_z \varpi}{D_y} + 4\varpi + \frac{2}{\varpi} + \frac{1}{2\varpi^3} \right) \tag{1.23}$$

in which ϖ is the smallest real root of

$$\frac{D_y}{D_z} = \frac{3}{8\varpi^4} + \frac{1}{8\varpi^2} - 1 \tag{1.24}$$

He simplified it to

$$\varpi = \left(\frac{3 D_z}{8 D_y} \right)^{1/4} \tag{1.25}$$

then

$$k = 41 \left(\frac{D_y}{D_z} \right)^{3/4} \tag{1.26}$$

which finally gives

$$V_{cr} = 41 \frac{D_z^{1/4} D_y^{3/4}}{h_w^2} \tag{1.27}$$

Peterson and Card [42] developed the buckling load through the value of a shear buckling coefficient

$$K_u = \frac{V_{zy} h_w^2}{4 (D_z D_y^3)^{1/4}} \tag{1.28}$$

where K_u is plotted as a function of parameter $(a/h_w)(D_y/D_z)^{1/4}$ for different values of a rotational stiffness parameter ε. Then according to Fig. 1.3

a) for a web fixed at two edges, where $\varepsilon = \infty$, $K_{u,min} = 15.1$ and

$$V_{zy} = 60.4 \frac{D_z^{1/4} D_y^{3/4}}{h_w^2} \tag{1.29}$$

b) for simply supported edges, where $\varepsilon = 0$, $K_{u,min} = 8.1$ and

$$V_{zy} = 32.4 \frac{D_z^{1/4} D_y^{3/4}}{h_w^2} \tag{1.30}$$

The eqs. 1.29 and 1.30 give the values 60.4 and 32.4 between which the value of critical buckling load lies and which depends on assumptions concerning edge conditions.

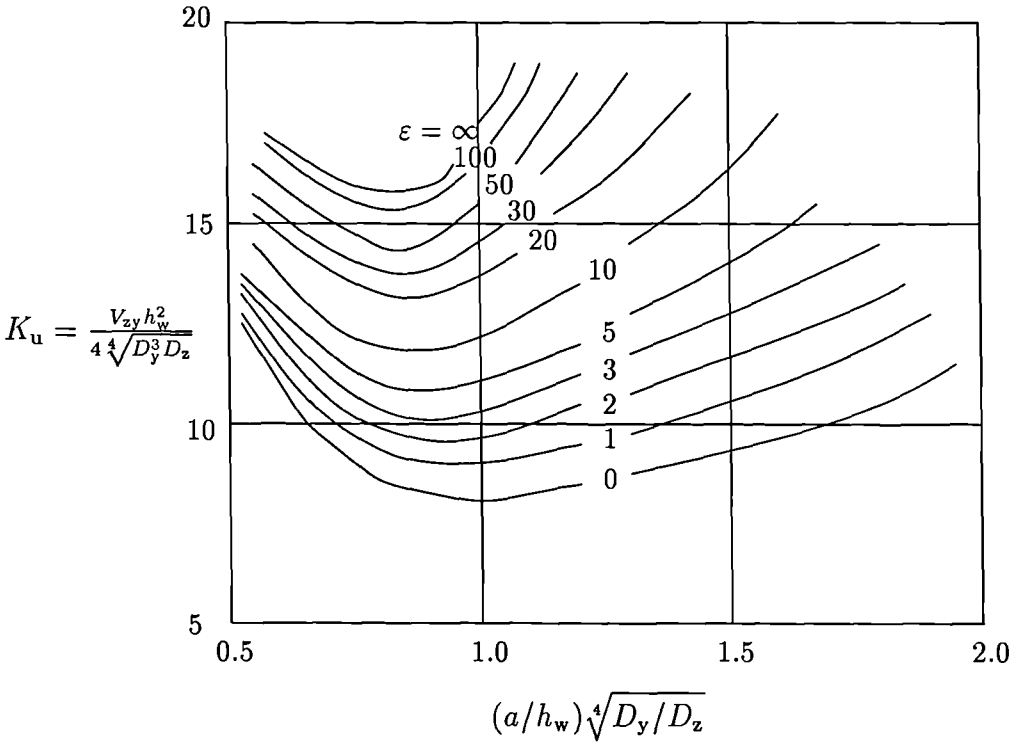

Figure 1.3: Shear buckling coefficient for a corrugated plate.

Bergfelt and Leiva [3] use the formula eq. 1.18 in more general form

$$V_{cr} = k_u \frac{D_z^{1/4} D_y^{3/4}}{h_w^2} \tag{1.31}$$

where D_z, D_y are defined by eqs. 1.11 and 1.12 and k_u depends on edge conditions, where the boundary for the value k_u are the same as in eqs. 1.29 and 1.30. So thus $V_{cr} = V_{zy}$ from eq. 1.29 for fixed edges which will in practice correspond to a web welded to flanges.

Leiva uses the formula

$$V_{cr} = 36\beta \frac{D_z^{1/4} D_y^{3/4}}{h_w^2} \tag{1.32}$$

in his paper [31] where he studies panels with unevenly corrugated webs, and with webs with corrugated ribs and wider flat parts. The parameter $\beta = 1.0$ for simply supported corrugated diaphragms, and $\beta = 1.9$ for diaphragms with clamped edges. He supposes the web panel to be simply supported at the stiffening edge plates, so $\beta = 1.0$.

Raoul [43] gives V_{cr} in the form of eq. 1.31. According to him $k_u = 32.4$ is rather conservative since the web is fixed in the upper slab. He suggests that more studies are needed, to choose between 32.4 and 60.4.

In the present work the form of eq. 1.30 was used in calculations, since the value of $k_u = 32.4$ is the most conservative one.

1.2.6 Proposal for a verification procedure

The following conservative formulae have been proposed [43] to be used for verification

$$\tau_{U.L.S.} \begin{cases} \leq & \frac{2}{3}\tau_m \\ \leq & \frac{1}{2}\tau_{cr,gl} \\ \leq & \tau_y \\ \leq & \tau_{cr,loc} \\ \leq & \tau_f \end{cases} \tag{1.33}$$

Factors 2/3 and 1/2 are purely indicative.

In formulae 1.33 τ_m is given by Bergfelt, Leiva, and Edlund [3, 32] who proposed an interaction formula, based on a series of tests, in the form

$$\frac{1}{\tau_m} = \frac{1}{\tau_{cr,loc}} + \frac{1}{\tau_{cr,gl}} \tag{1.34}$$

Global critical shear stress, $\tau_{cr,gl}$, is calculated from V_{cr}/t_w given in eq. 1.30; local critical shear stress, $\tau_{cr,loc}$, is defined by eq. 1.2; and post–buckling failure τ_f is given in eq. 1.6, where $\tau_y = 0.6 f_y$.

Chapter 2

Stresses in a corrugated web

2.1 Introduction

In thin walled beams the distribution of shear stresses along the depth of the beam shows that the shear stresses in flanges in comparison with those in the web are in many cases negligible. The vertical shear force in the beam is therefore resisted mainly by the web. This chapter shows the relation between the geometry of a corrugated web and its shear stresses. The bending stiffness of a beam with a corrugated web is compared with the bending stiffness of a conventional I–section beam. Finite element analyses are used for this purpose. The effective shear modulus of beams with corrugated webs is found. Shear force in the beams has bimoment effects on the beam flanges since the flat panels of the corrugated web are attached eccentrically to the flanges. These effects and the calculations of the additional stresses in the flange tips are shown.

2.2 Influence of the web geometry on shear stresses

The design of a corrugated web has to be verified for shear stresses as given in Section 1.2.6. Knowledge of the relationship between the geometrical dimensions and shear stresses can make the choice of the dimensions easier for initial design.

Section 1.2 describes the two possible modes of shear buckling. The limiting

stresses are given, as they were developed by various investigators. The two main limiting stresses, which can influence a possible premature failure of a structure, are ideal local buckling, $\tau_{cr,loc}$, of a flat part of a corrugation, and global buckling, $\tau_{cr,gl}$.

The first one, $\tau_{cr,loc}$, is defined by eq. 1.5. For simplicity, k_f is assumed to be equal to 1. The geometry of a beam with a corrugated web is shown in Fig. 2.1. The shear stress for global buckling of the web is $\tau_{cr,gl} = V_{zy}/t_w$, where V_{zy} is given

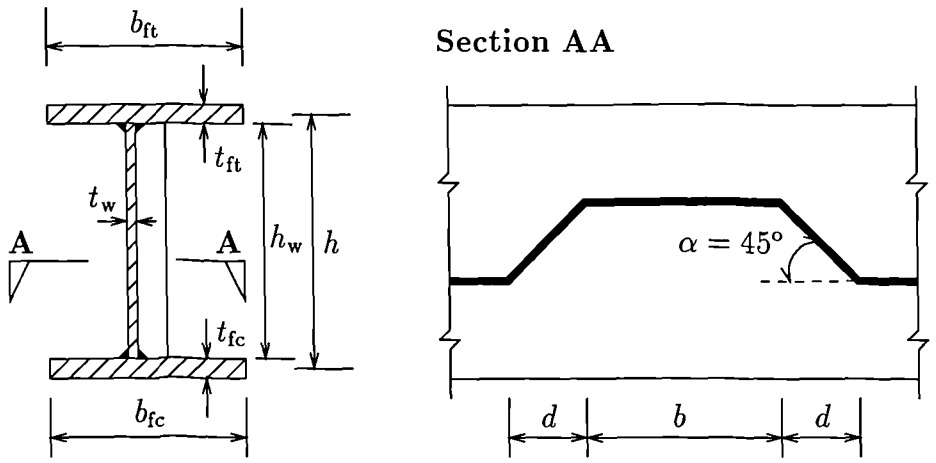

Figure 2.1: Geometry of a beam with a corrugated web.

by eq. 1.30. D_z, D_y and I_y are defined by 1.11, 1.12 and 1.14, respectively. The interaction formula is given by eq. 1.34.

From eqs. 1.5, 1.30, 1.34 and simplifying for $\alpha = 45°$, the final relationship between the geometry of a corrugated web and shear stresses is

$$\left(\frac{h_w}{t_w}\right)^2 = \left[2.7\left(\frac{E}{\tau_y}\right)\left(\frac{\tau_y}{\tau_m}\right) - 0.307\left(1-\nu^2\right)\left(\frac{b}{t_w}\right)^2\right]\sqrt[4]{(\mathrm{FR})} \tag{2.1}$$

where

$$(\mathrm{FR}) = \frac{27(b/t_w)^3(d/t_w)^6 + 38.18(b/t_w)^2(d/t_w)^7 + 18(b/t_w)(d/t_w)^8 + 2.83(d/t_w)^9}{(b/t_w)^3 + 3.41(b/t_w)^2(d/t_w) + 3.83(b/t_w)(d/t_w)^2 + 1.41(d/t_w)^3} \tag{2.2}$$

and τ_y is defined by eq. 1.1.

For steel with Young modulus $E = 210$ kN/mm^2, Poisson ratio $\nu = 0.3$ and yield

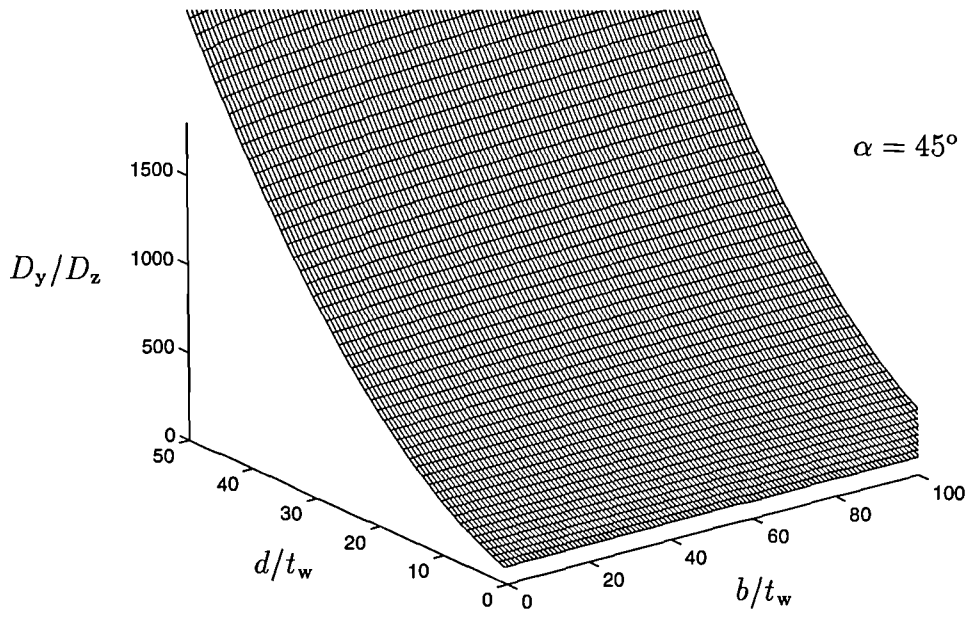

Figure 2.2: Plate stiffness of a corrugated web.

stress $f_y = 300$ N/mm^2 eq. 2.1 becomes

$$\left(\frac{h_w}{t_w}\right)^2 = \left[3273\left(\frac{\tau_y}{\tau_m}\right) - 0.28\left(\frac{b}{t_w}\right)^2\right]\sqrt[4]{(FR)} \tag{2.3}$$

Let us assume only local buckling of a flat part of a corrugated web (i.e. $b > d\sec\alpha$). From eq. 1.5, where $k_f = 1$, $E = 210$ kN/mm^2, $\nu = 0.3$ and $f_y = 300$ N/mm^2

$$\frac{\tau_{cr,loc}}{\tau_y} = 5852\left(\frac{t_w}{b}\right)^2 \tag{2.4}$$

From eq. 2.4, $b/t_w < 100$ for $\tau_{cr,loc}/\tau_y > 0.5$, which is a practical upper limit for ratio b/t_w.

A reasonable limiting condition for the ratio D_y/D_z is that $D_y/D_z > 50$ [11]. Substituting eqs. 1.11 and 1.12 into this ratio leads to the following relationship:

$$\frac{D_y}{D_z} = \frac{3(b/t_w)^2(d/t_w)^2 + 5.66(b/t_w)(d/t_w)^3 + 2(d/t_w)^4}{[(b/t_w) + (d/t_w)]^2} \tag{2.5}$$

Fig. 2.2 is plotted for eq. 2.5. It shows that the ratio D_y/D_z does not depend much

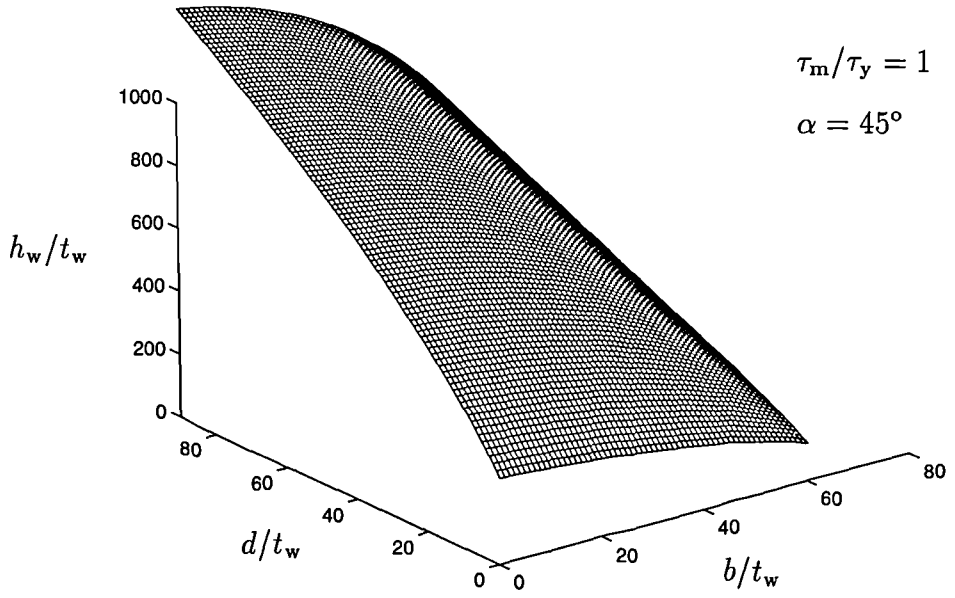

Figure 2.3: The main geometrical characteristics of a corrugated web.

on the ratio b/t_w for given value d/t_w. But it strongly depends on the ratio d/t_w for given value of b/t_w. For minimum value of $D_y/D_z = 50$ and any value of b/t_w (say 40) the ratio $d/t_w = 4.1$. This suggests the choice of the lower boundary for the ratio d/t_w as 5, when $\alpha = 45°$.

Having set the boundary for the ratios b/t_w and d/t_w a 3D diagram can be plotted from eq. 2.3 as shown in Fig. 2.3 for $\tau_m/\tau_y = 1$.

These diagrams can suggest suitable ratios h_w/t_w, b/t_w and d/t_w for an economical design of corrugated webs. For given vertical shear, τ_m, which in practice would be probably $3\tau_y$ to $4\tau_y$, given h_w and fixed t_w, values of b, d and α can be chosen to minimise the volume per unit area. Another method of optimisation is to put $d \sec \alpha = b$ to minimise the amount of plate bending needed, or to optimise on α.

The above mentioned ideas are based on the referenced work which itself suggests that more investigation should be performed on the shear capacity of corrugated webs. The subject of the present thesis is mainly the behaviour of the flange attached to a corrugated web. Therefore design rules for corrugated webs are not further discussed.

2.3 Bending stiffness

2.3.1 A beam with a plane web

2.3.1.1 Stresses and deformations in pure bending

Pure bending will create the angle $\mathrm{d}\varphi$ between the planes of two cross–sections distance $\mathrm{d}z$ apart (Fig. 2.4). The radius of curvature of the neutral plane is ρ. From

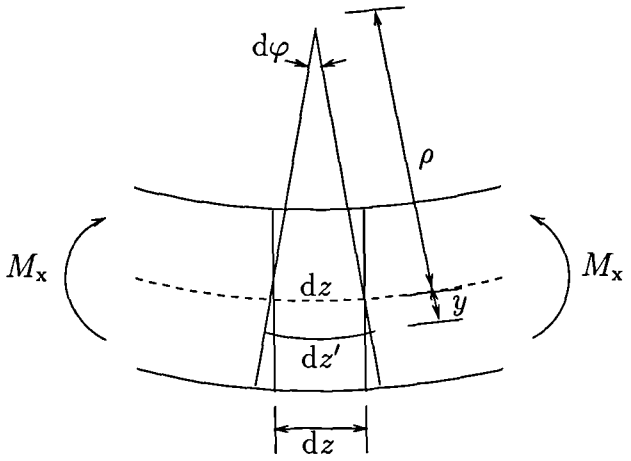

Figure 2.4: Simple bending of a beam.

the geometry of Fig. 2.4 it can be written

$$\mathrm{d}z = \rho \mathrm{d}\varphi \tag{2.6}$$

$$\mathrm{d}z' = (\rho + y)\mathrm{d}\varphi \tag{2.7}$$

$$\Delta \mathrm{d}z = \mathrm{d}z' - \mathrm{d}z = \rho \mathrm{d}\varphi - \rho \mathrm{d}\varphi + y \mathrm{d}\varphi = y \mathrm{d}\varphi \tag{2.8}$$

Then for strain

$$\epsilon_z = \frac{\Delta \mathrm{d}z}{\mathrm{d}z} = \frac{y \mathrm{d}\varphi}{\rho \mathrm{d}\varphi} = \frac{y}{\rho} \tag{2.9}$$

According to linear elastic theory (Hooke's law) and the equilibrium of the forces

and bending moments in element dz:

$$EI_{\mathrm{x}} = M_{\mathrm{x}} \frac{Ey}{\sigma_{\mathrm{z}}} \tag{2.10}$$

2.3.1.2 Direct Calculation of I_{x}

For a beam with simple I–cross–section the second moment of area is calculated

- a cross–section with a web

$$I_{\mathrm{x,w}} = \frac{1}{12} t_{\mathrm{w}} h_{\mathrm{w}}^3 + \frac{2}{12} b_{\mathrm{f}} t_{\mathrm{f}}^3 + \frac{1}{2} b_{\mathrm{f}} t_{\mathrm{f}} (h_{\mathrm{w}} + t_{\mathrm{f}})^2 \tag{2.11}$$

- a cross-section without a web

$$I_{\mathrm{x,o}} = \frac{2}{12} b_{\mathrm{f}} t_{\mathrm{f}}^3 + \frac{1}{2} b_{\mathrm{f}} t_{\mathrm{f}} (h_{\mathrm{w}} + t_{\mathrm{f}})^2 \tag{2.12}$$

2.3.2 A beam with a corrugated web

There is no simple way to determine the linear–elastic bending stiffness directly because the shape of cross–section is changing longitudinally. However, there is a possibility to define it with the help of finite element analyses which were used in this case.

2.3.2.1 Creating models

The I–DEAS software, version 6 [60] was used for these first–order finite element analyses. Thin–shell linear quadrilateral elements were used for mesh generation. Each element had four nodes. Three translational degrees of freedom and three rotational degrees of freedom were assigned to each node. Translations were in the direction of the nodal displacement coordinate system of axes which for the present analyses were defined in the same way as the global coordinate system. It was right–handed with the z–axis as the longitudinal one. Rotations were about the nodal displacement coordinate system axes.

In the present analyses the loading of the structure was performed by applying

the displacements of nodes on the shorter edges of the flange as shown in Fig. 2.5, while keeping the x– and z–displacements of the top longitudinal edge of the web unchanged. This edge represented the neutral axis of the beam cross-section.

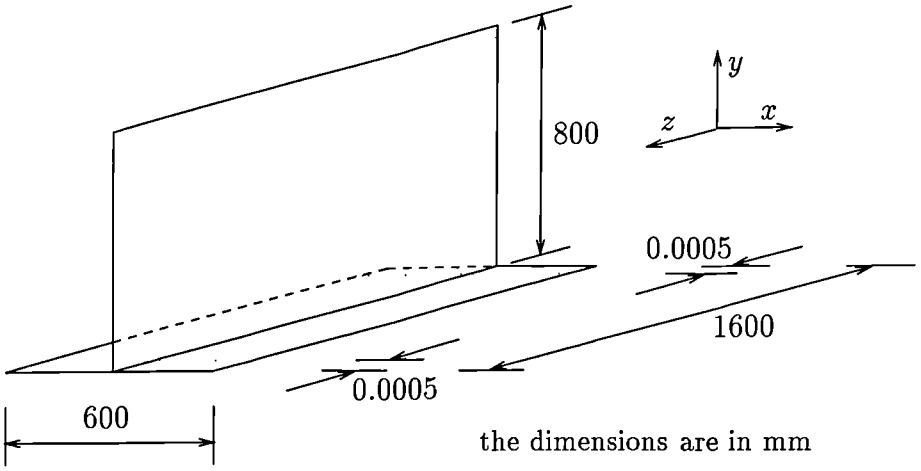

Figure 2.5: Dimensions of models.

The geometry of each model (with a plane or a corrugated web) is shown in Fig. 2.5. Half of the beam depth was modelled with corrugations as shown in Fig. 2.6. Angle α was varied. For the first set of analyses $h/2 = 800$ mm, which

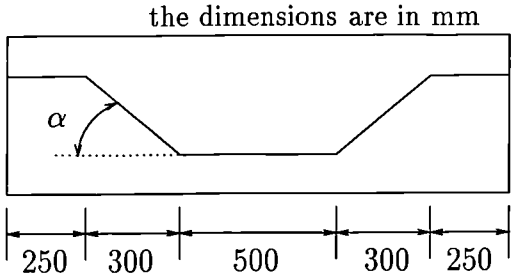

Figure 2.6: Dimensions of corrugations.

gives the slenderness of the web $h_w/t_w = 195$. For the second set $h/2 = 400$ mm with $h_w/t_w = 95$. The thickness of the web $t_w = 8$ mm; the flange $t_f = 40$ mm. The Young's modulus $E = 210$ kN/mm^2 and the Poisson ratio $\nu = 0.29$.

For a constant overall length, l, of a model, the ratio $d \tan \alpha$ was varied from 0 to 0.5. The numbers of elements in each model are given in Table 2.1.

	Set 1 — $h_w/t_w = 195$		**Set 2** — $h_w/t_w = 95$	
$d \tan \alpha / b_f$	number of elements	in flange/ in web	number of elements	in flange/ in web
0	224	96/128	160	96/64
0.083	258	102/156	178	102/76
0.167	236	100/136	168	100/68
0.25	290	108/182	214	108/106
0.333	284	104/180		
0.417	250	114/136		
0.5	273	117/156		

Table 2.1: Numbers of elements in the models.

2.3.2.2 Analysing the results

After creating a model and running the program the shell stress resultants (Fig. 2.7) and stresses as an output data were obtained, from which the bending moment

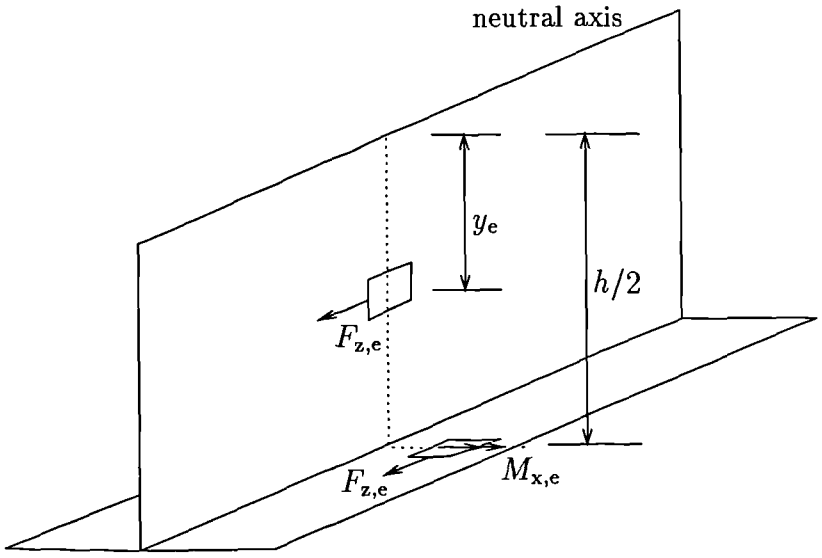

Figure 2.7: Shell stress resultants.

M_x and compression stress σ_z (eq. 2.10) on the bottom surface of the flange were calculated in following way

$$M_x = \left(\sum M_{x,e} + \sum F_{z,e} y_e\right) \times 2 \tag{2.13}$$

$$\sigma_z = \frac{\sum \sigma_{z,e}}{n} \tag{2.14}$$

where $M_{x,e}$, $F_{z,e}$ are shell stress resultants of each element which occured in the analysed cross–section (Fig. 2.7); y_e is the distance of the element from the neutral axis; $\sigma_{z,e}$ is the compression stress in the flange element; n is the number of elements in the flange in the cross–section used in analysis. The eq. 2.10 is used to determine EI_x, where $y = (h_w + t_f)/2$. Results are given in Table 2.2 and plotted in Fig. 2.8.

	Set 1 — $h_w/t_w = 195$		**Set 2** — $h_w/t_w = 95$	
$d \tan \alpha / b_f$	$EI_x/10^{15}$	$EI_x/EI_{x,w}$	$EI_x/10^{15}$	$EI_x/EI_{x,w}$
	Nmm^2		Nmm^2	
eq. 2.11	6.984	1.000	1.676	1.000
eq. 2.12	6.453	0.924	1.614	0.963
0.000	6.972	0.998	1.683	1.004
0.083	6.525	0.934	1.638	0.977
0.167	6.462	0.925	1.628	0.971
0.250	6.430	0.921	1.623	0.968
0.333	6.424	0.920		0.969
0.417	6.430	0.921		0.967
0.500	6.441	0.922		0.968

Table 2.2: Bending stiffness of a beam with a corrugated web.

The bending stiffness of a beam with a corrugated web falls quickly, approximately to the value of the bending stiffness of a beam having no web at all. For the slender beams ($h_w/t_w = 195$) the value of the bending stiffness is reduced with a steeper slope of the curve than for the shallower beams ($h_w/t_w = 95$). For the ratios $d \tan \alpha / b_f < 0.1$ either d or α would be so small that the condition for $D_y \gg D_z$ would not be satisfied. For practical purposes the calculation of bending stiffness of the beam with a corrugated web, where the cross–section area of the web is not taken to the consideration, is on the safe side and is sufficiently accurate.

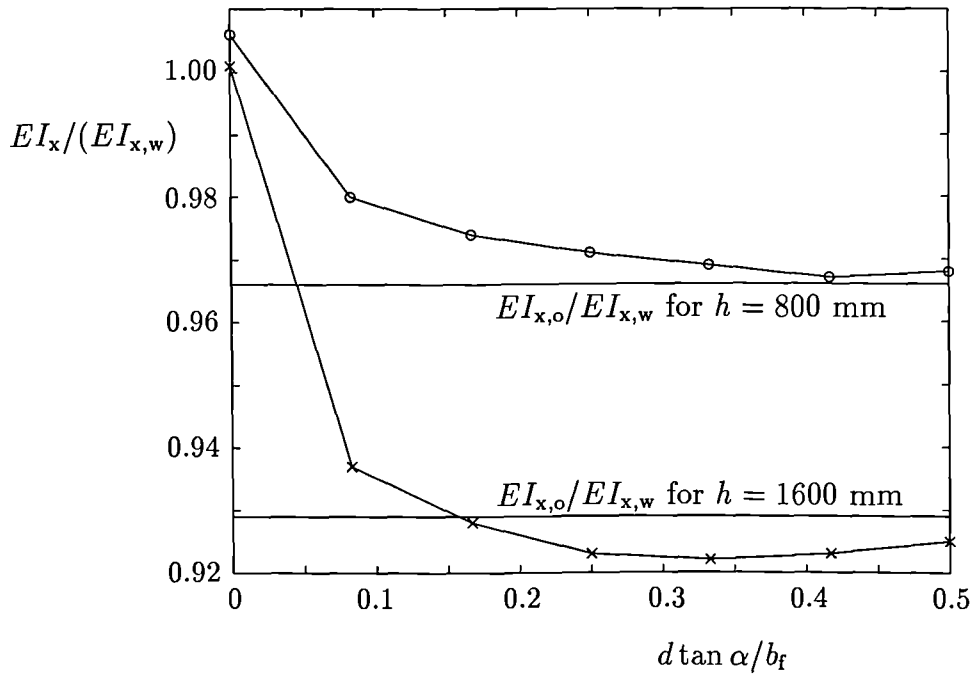

Figure 2.8: Bending stiffness of a beam with a corrugated web.

2.4 Shear stiffness

2.4.1 Analytical analysis

The assumptions made before any calculation are the following: elastic behaviour of the sheeting; no buckling considered; uniform shear force per unit length of plate, on a section cut by a horizontal plane; indentations in the plate do not reduce local in–plane stiffness of the plate; shear stress along the corrugated shape remains constant.

The shear force applied to length b_0 is $\tau b_0 t_w$ where b_0 and τ are shown in Fig. 2.9. The mean horizontal stress along AE (see Fig. 2.10) is τ, and is equal to the complementary shear stress along AF.

Fig. 2.10 (a) can be redrawn to Fig. 2.10 (b) where it can be clearly seen that for the plate ABGF the strain is

$$\gamma_2 = \frac{\tau}{G} \tag{2.15}$$

where G is shear modulus of steel.

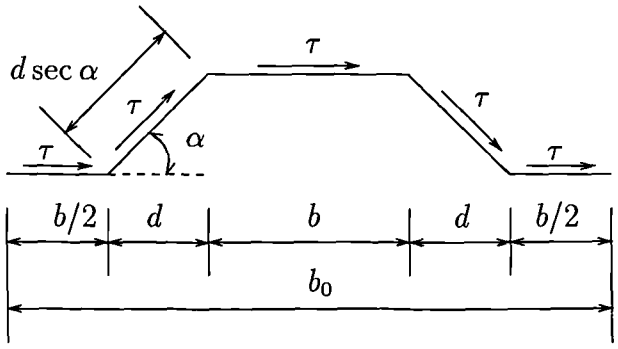

Figure 2.9: Cross–section of one corrugation.

If the "sloping parts" (shown as *slop.* in Fig. 2.10) were in the same plane as the flat parts, point D would be located at point C. The length BD is equal to $d \sec \alpha$, so is the length BC. From the geometry the distance between lines b and c is $\gamma_2 d \sec \alpha$, where the assumption of small γ_2 allows $\sin \gamma_2 \approx \tan \gamma_2 \approx \gamma_2$. Because of the folding of the plate, point C moves to the point D, which creates the additional shear strain γ_1. From Fig. 2.10 (a) the distances between the horizontal lines a & b and d & e are equal with a value $\gamma_2 b/2$. The sum of two shear strains is then (the angle created by the lines a and AE)

$$\gamma_1 + \gamma_2 = \frac{\gamma_2 (b + d \sec \alpha)}{b_0/2} \tag{2.16}$$

For the whole corrugated plate AEIF the shear strain is

$$\gamma_1 + \gamma_2 = \frac{\tau}{G_{\text{eff}}} \tag{2.17}$$

where G_{eff} is the effective shear modulus of a corrugated sheeting.

Substituting eqs. 2.15 and 2.17 into eq. 2.16, the effective shear modulus of a corrugated sheeting can be calculated from

$$\frac{G_{\text{eff}}}{G} = \frac{\gamma_2}{\gamma_1 + \gamma_2} = \frac{b_0}{2(b + d \sec \alpha)} \tag{2.18}$$

The eq. 2.18 shows that the ratio of shear modulus of the corrugated sheeting to shear modulus of flat plate is the same as the ratio of the length of the sheeting to its unfolded length.

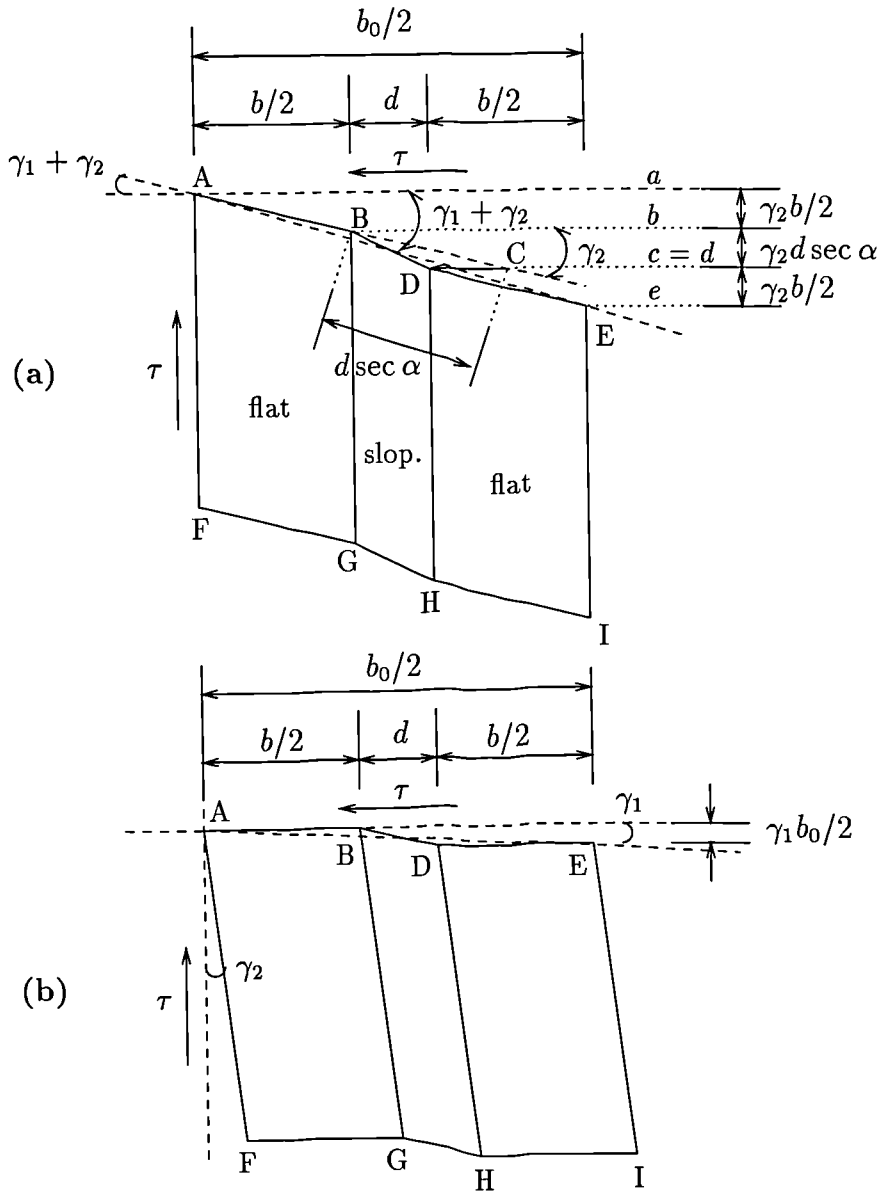

Figure 2.10: Elevation of half of one corrugation.

2.4.2 Finite element analysis

2.4.2.1 Creating a model

The I-DEAS software, version 6 [60] was used for linear elastic analyses to find the effective shear modulus of a corrugated panel. A model with fixed geometry, as shown in Fig. 2.11, was created. The only variable was the angle of the sloping

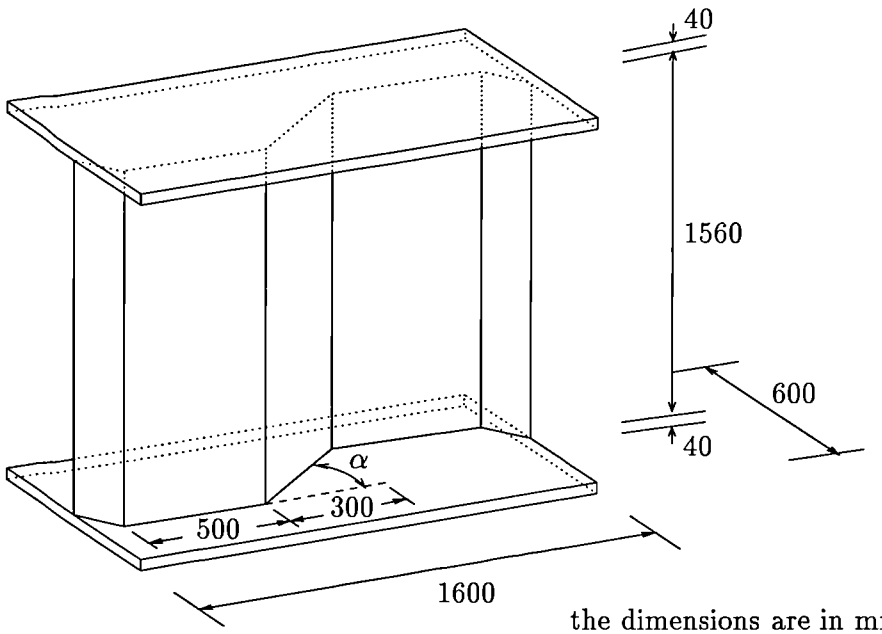

Figure 2.11: The geometry of the model for finite element analyses.

parts of a corrugation, α. It was changed from 0° to 45°. Thickness of the web was $t_w = 8$ mm. Thin-shell linear quadrilateral elements were used with the same material and element properties as in Section 2.3.2. The numbers of elements for each model are listed in Table 2.3.

The boundary conditions are shown in Figs. 2.12 to 2.14. The y-direction restraints (Fig. 2.12) were placed in each node along the edges BD and EG. The z-direction restraint in point A and the x-direction restraints in points B, D and F prevented rigid body movement of the model.

Each model was initially loaded just by constant longitudinal edge pressure (Fig. 2.13) placed on the edges EF and GH on the top and bottom flanges to create

Model	$d \tan \alpha$	α	number of elements	in flange/ in web
1	0	0.00	448	96/256
2	50	9.46	548	108/332
3	100	18.44	514	113/288
4	150	26.57	540	126/288
5	200	33.69	536	124/288
6	250	39.81	540	126/288
7	300	45.00	624	141/342

Table 2.3: Numbers of elements in each model.

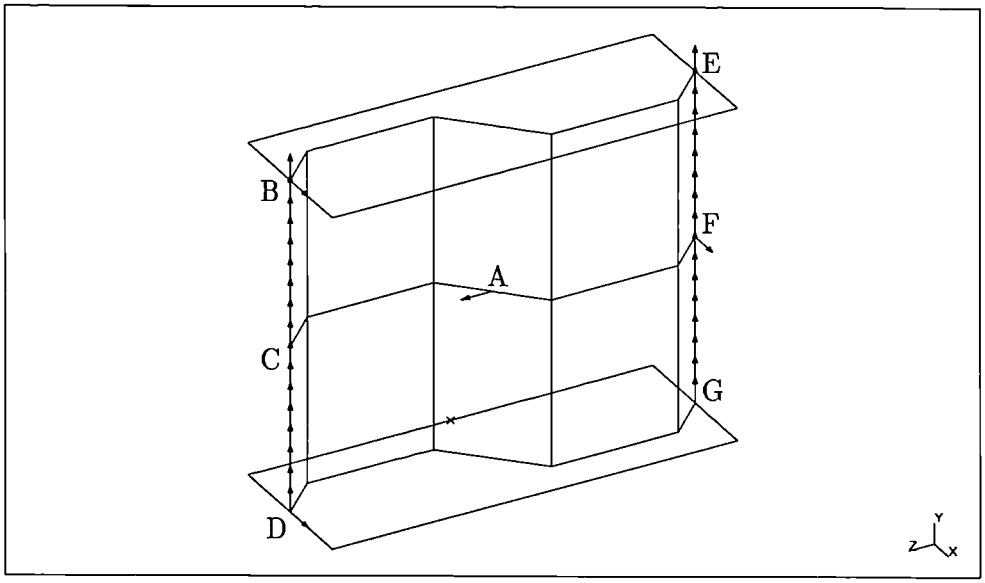

Figure 2.12: Restraint set for finite element analysis.

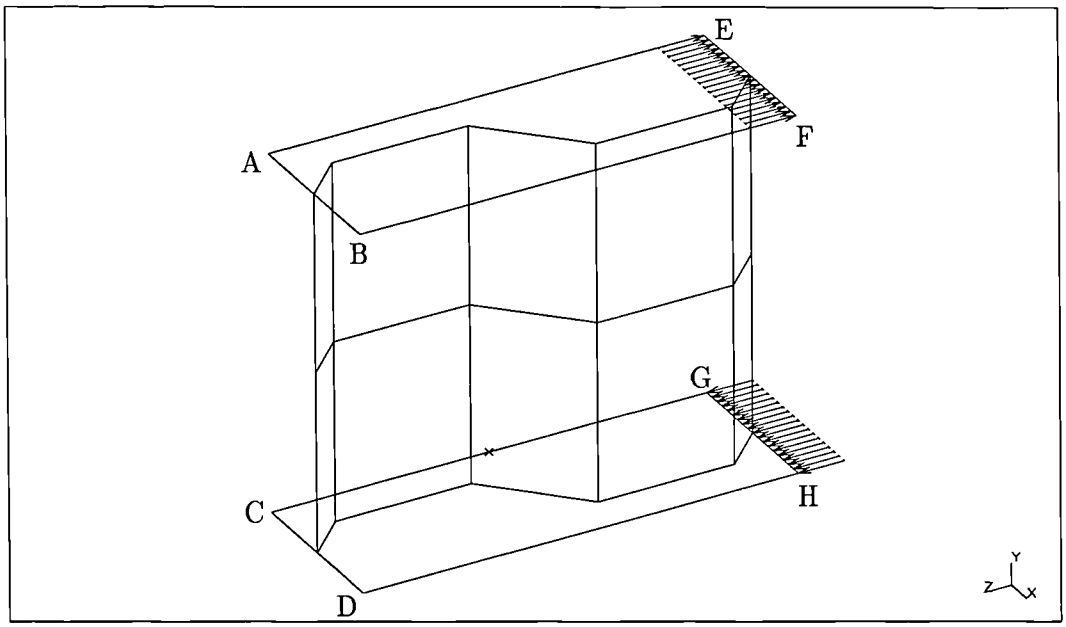

Figure 2.13: Shear loading.

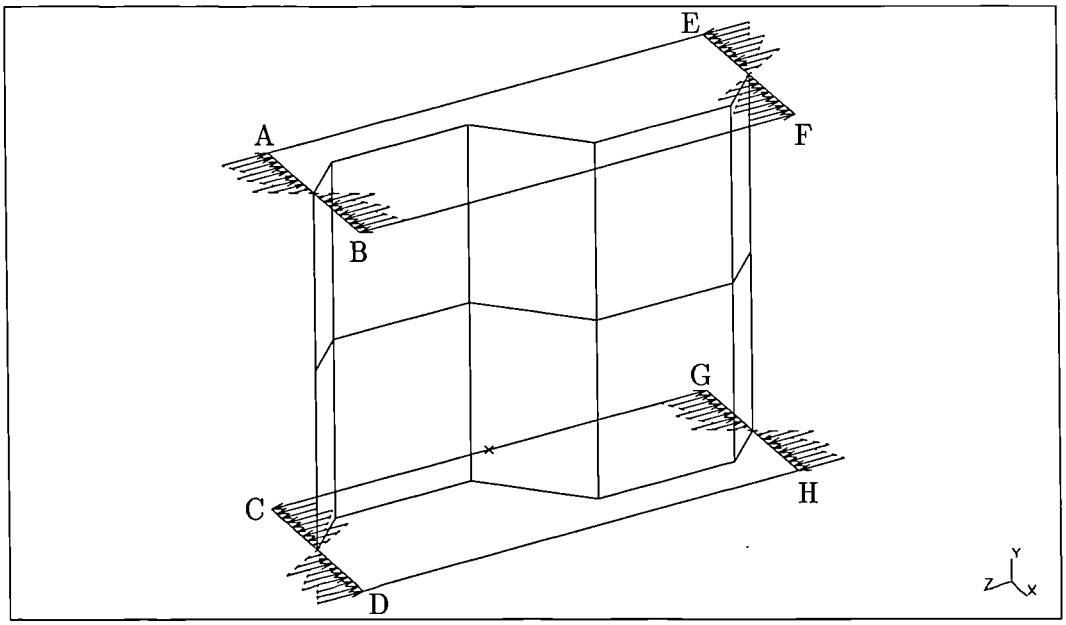

Figure 2.14: Bimoment loading.

loading of the model in pure shear. During the analyses, bimoment effects in the flanges were observed. These effects are described and explained in Section 2.5. This led to the additional loading of the flange edges (Fig. 2.14) which did not influence the shear analyses of the web. The additional loading was a pure bending in the plane of a flange created by linearly distributed edge pressure. The result of this additional loading was that the two shorter edges of the flange remained parallel as it was expected due to continuity of the flanges since the shorter edges were one corrugation apart.

2.4.2.2 Analysing the results

From the restraint set (Fig. 2.12) the shear stress in the web was calculated by

$$\tau = \frac{\sum_{i=1}^{n} R_{\mathrm{i}}}{t_{\mathrm{w}} h_{\mathrm{w}}} \tag{2.19}$$

where n was the number of nodes on one free edge of the web, R_{i} was the vertical reaction in each node of the edge.

Shear strain was obtained from the longitudinal deformations of the web (see Fig. 2.15)

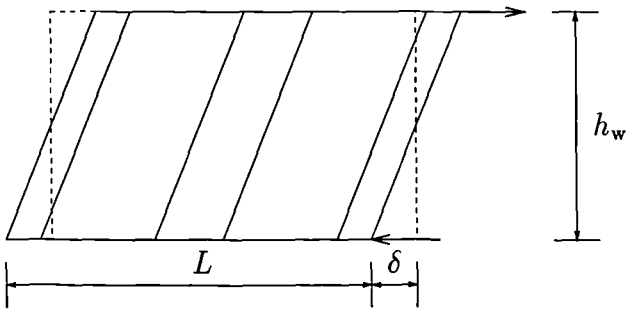

Figure 2.15: Shear deformation of the web.

$$\gamma = \frac{2\delta}{h_{\mathrm{w}}} \tag{2.20}$$

The effective shear modulus of the corrugated web was

$$G_{\text{eff}} = \frac{\tau}{\gamma} \tag{2.21}$$

where τ is taken from eq. 2.19, and γ is from eq. 2.20.

The results are summarised in Table 2.4 and plotted in Fig. 2.16.

Model	$h_w/(d \tan \alpha)$	finite elements G_{eff}/G	eq. 2.18 G_{eff}/G
1		1.000	1.000
2	32.0	0.993	0.995
3	16.0	0.977	0.980
4	10.6	0.951	0.958
5	8.0	0.919	0.929
6	6.4	0.882	0.898
7	5.3	0.844	0.866

Table 2.4: The effective shear modulus of a corrugated web.

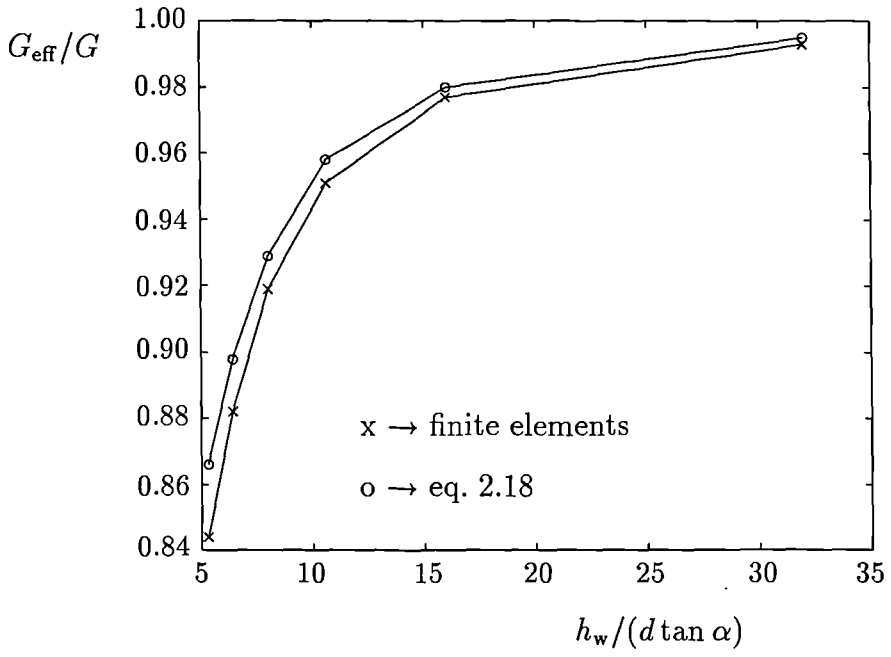

Figure 2.16: Effective shear modulus of a corrugated web.

The results obtained by both analytical solution (eq. 2.18) and linear finite el-

ement analysis are in very good agreement. Thus the effective shear modulus of a corrugated web is in the same ratio to the shear modulus of the material as the ratio of the length of the sheeting to its unfolded length.

2.5 Bimoment effects

Analyses of beams with corrugated webs for shear stresses have shown the appearance of a bimoment in the top and bottom flanges. This section describes the reasons for these effects and gives an approximate method for determining the bimoment.

2.5.1 Finite element analysis

The analyses were performed simultaneously with the analyses of shear stresses in a corrugated web. The models were therefore the same as described in Section 2.4. The loading of the structure shown in Fig. 2.13 creates shear force along the edges of the web (Fig. 2.17). The flat parts of the corrugated web are eccentrically attached

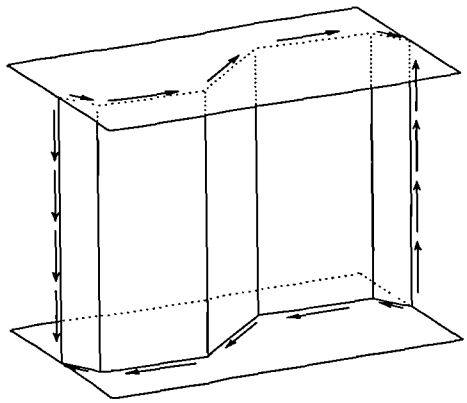

Figure 2.17: Shear force in the web.

to the flanges. The force coming from the shear in the web therefore causes in–plane bending of each flange. The top and bottom edges of the web have shear forces in opposite directions which cause moments in the top and bottom flanges of opposite sign, known as a bimoment.

Loading a model by pure shear only, as shown in Fig. 2.13, results in the deformations shown in Fig. 2.18. Both flanges are bent in their planes in opposite

directions (dashed lines indicates a model in its undeformed shape). Fig. 2.19 shows a deformed flange by in–plane bending (compare with the top flange of Fig. 2.18).

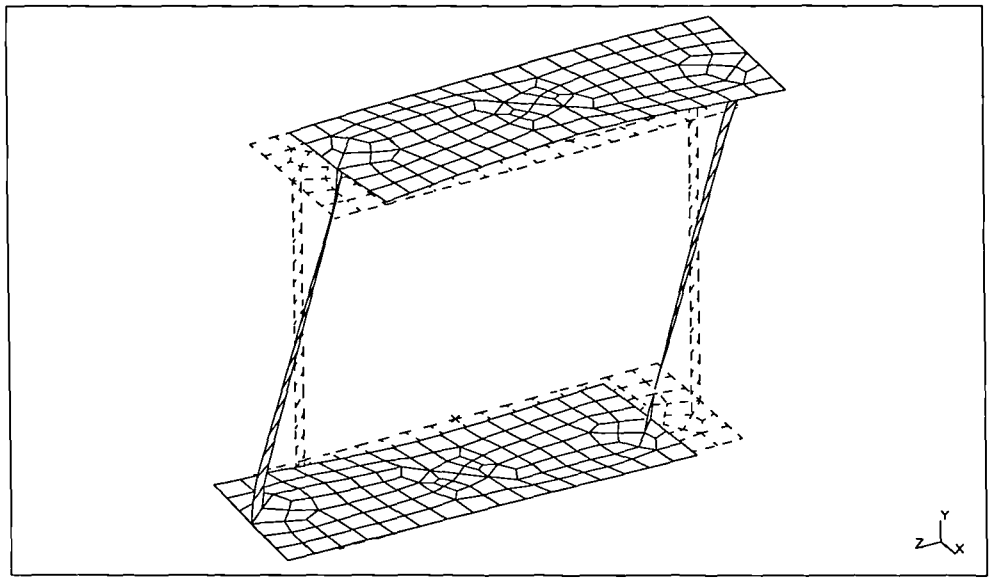

Figure 2.18: Deformations of the flanges from shear in the web.

The bending moment is then determined from the deformation following the simple elastic bending theory

$$M_{\mathrm{b,FEA}} = EI_{\mathrm{y,f}}\frac{\mathrm{d}^2 z}{\mathrm{d}x^2} \tag{2.22}$$

where E is modulus of elasticity; $I_{\mathrm{y,f}}$ is the second moment of area of the flange cross–section. The bending moment $M_{\mathrm{b,FEA}}$ is varying along the flange as shown in Fig. 2.20. Its value is the same in the cross–sections, which are one corrugation apart. The angle ϕ (see Fig. 2.19) created by two such cross–sections, when applying $M_{\mathrm{b,FEA}}$, can be found from deformations of the model, thus the radius $\rho = 1600/\phi$ can be calculated (1600 is the length of the model). The angle ϕ is small thus the assumption $1/\rho = \mathrm{d}^2 z/\mathrm{d}x^2$ is made.

In a real beam this in–plane bending of the flange is prevented by continuity of the beam. Therefore opposite bending moments have to be applied to both flanges so that their shorter edges, which are one corrugation apart, remain parallel. In finite element analysis this was performed by loading the shorter flange edges

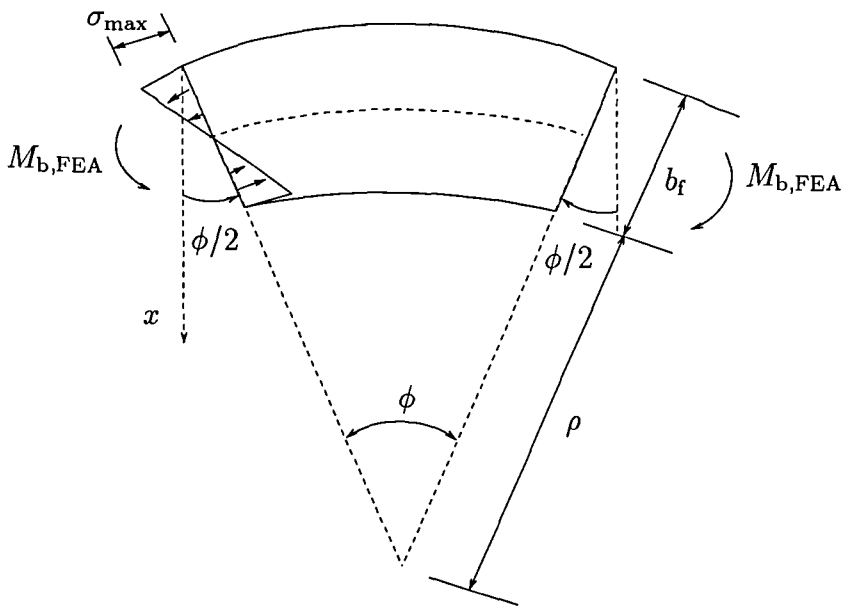

Figure 2.19: In–plane bending of a flange.

i	σ_i	$M_{b,i}$	i	σ_i	$M_{b,i}$	i	σ_i	$M_{b,i}$
	mN/mm^2	kNmm		mN/mm^2	kNmm		mN/mm^2	kNmm
1	14.6	35.04	7	-11.4	-27.32	13	-3.1	-7.44
2	11.7	28.02	8	-12.6	-30.34	14	1.9	4.56
3	7.6	18.38	9	-14.1	-33.74	15	6.9	16.68
4	2.6	6.23	10	-12.9	-30.85	16	11.8	28.2
5	-2.4	-5.78	11	-11.4	-27.36	17	14.6	34.99
6	-7.1	-16.93	12	-7.8	-18.6			

Table 2.5: Stresses and moments in a flange taken from finite element analysis.

by linearly distributed edge pressure, as shown in Fig. 2.14 (the load shown in the figure is linearly distributed in spite of the way how the software sketched it). The value for the distributed load was defined from the bending stress in a flange, $\sigma_{max} = M_{b,FEA}/W_f$; where W_f was the section modulus of the flange cross–section.

The final loading for the shear analysis was a combination of the shear and bimoment loadings, as shown in Figs. 2.13 and 2.14.

The output from the finite element analyses gave the change of bending moment along a flange, listed in Table 2.5 for one of the models, where $\alpha = 45°$. The corresponding cross–sections, marked as i in Table 2.5, are shown in Fig. 2.20. The variation of the bending moment is then plotted. There is a linear relationship

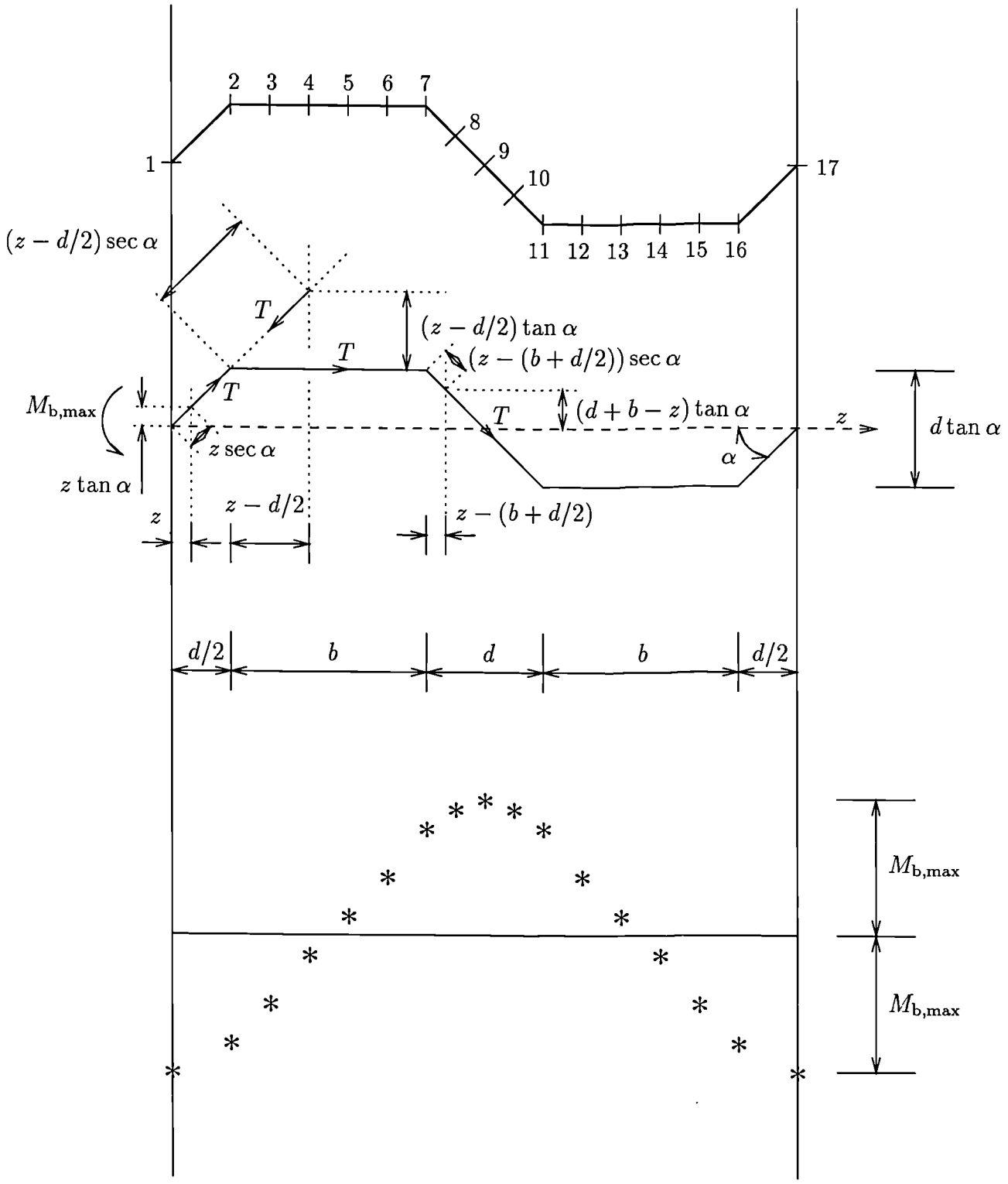

Figure 2.20: Variation of bimoment along the beam.

between bending moment and a bimoment: $B = M_b h$ where B is the bimoment; M_b the in-plane bending moment in two flanges acting in opposite directions in a cross-section of a beam; h is the distance between the mid-planes of the flanges. Thus the diagram in Fig. 2.20 represents also the variation of the bimoment along the beam with a corrugated web, for h = const.

The maximum bending moments, $M_{b,max}$ for various angles α, obtained from finite element analyses, are given in Table 2.6.

		finite elements	eq. 2.27	
model	α	$M_{b,max}$	$M_{b,max}$	difference
		kNmm	kNmm	%
1	0.00	0.00	0.00	
2	9.46	5.74	6.09	5.7
3	18.44	12.07	12.19	0.9
4	26.57	18.06	18.28	1.2
5	33.69	24.14	24.37	0.9
6	39.81	30.24	30.47	0.7
7	45.00	36.19	36.56	1.0

Table 2.6: In-plane bending moment in the flange.

2.5.2 Analytical solution

For one repeating corrugation the forces in an attached flange are assumed to be as shown in Fig. 2.20. $M_{b,max}$ is the maximum in-plane bending moment; T is the shear force per unit length along the web. For each cross-section of the flange the moment equilibrium is (see Fig. 2.20):

1. In the interval $0 \leq z \leq d/2$

$$M_{b,1} = M_{b,max} - T\cos\alpha \times z\sec\alpha \times \frac{z\tan\alpha}{2} - T\sin\alpha \times z\sec\alpha \times \frac{z}{2}$$

from which

$$M_{b,1} = M_{b,max} - Tz^2\tan\alpha \tag{2.23}$$

2. In the interval $d/2 \leq z \leq d/2 + b$

$$\begin{aligned} M_{\mathrm{b},2} &= M_{\mathrm{b},1} \\ &+ T\cos\alpha \times [z - (d/2)] \sec\alpha \times \left[(d/2)\tan\alpha + \frac{(z - d/2)\tan\alpha}{2}\right] \\ &+ T\sin\alpha \times [z - (d/2)] \sec\alpha \times \frac{z - d/2}{2} \\ &- T\,[z - (d/2)] \times (d/2)\tan\alpha \end{aligned}$$

where $M_{\mathrm{b},1}$ is not a constant. It is the function of z given by eq. 2.23, corrected by the second and the third lines of the above expression, from which

$$M_{\mathrm{b},2} = M_{\mathrm{b},1} - T\tan\alpha\,[z - (d/2)]^2 \tag{2.24}$$

3. In the interval $d/2 + b \leq z \leq b + d$

$$\begin{aligned} M_{\mathrm{b},3} &= M_{\mathrm{b},2} \\ &+ T \times [z - (b + d/2)] \times (d/2)\tan\alpha \\ &- T\cos\alpha \times [z - (b + d/2)] \sec\alpha \times \left\{(d/2)\tan\alpha - \frac{[z - (b + d/2)]\tan\alpha}{2}\right\} \\ &+ T\sin\alpha \times [z - (b + d/2)] \sec\alpha \times \frac{z - (b + d/2)}{2} \end{aligned}$$

where again $M_{\mathrm{b},2}$ is a function of z given by eq. 2.24 and corrected in the above expression which then gives

$$M_{\mathrm{b},3} = M_{\mathrm{b},2} + T\tan\alpha\,[z - (b + d/2)]^2 \tag{2.25}$$

Eqs. 2.23, 2.24, or 2.25 are then used, depending on the place where the moment is calculated.

According to the diagram in Fig. 2.20 the moment $M_{\mathrm{b}} = 0$ when $z = (d + b)/2$, and $M_{\mathrm{b}} = -M_{\mathrm{b,max}}$ when $z = d + b$. From these conditions for

a) $z = (d + b)/2$ from eq. 2.24

$$M_{\mathrm{b,max}} = T(d/4)(2b + d)\tan\alpha \tag{2.26}$$

b) $z = d + b$ from eq. 2.25

$$M_{\mathrm{b,max}} = T(d/4)(2b + d)\tan\alpha \tag{2.27}$$

Eqs. 2.26 and 2.27 are in agreement so it could be considered as a formula for determining the maximum in–plane moment in a flange arising from shear in web. The values of $M_{\mathrm{b,max}}$ calculated from eq. 2.26 (or 2.27) for various angles α are given in Table 2.6. They are in very good agreement with the ones obtained from finite element analyses. Flange elements around the web corners in model 2 had to have one very small angle to match $\alpha \approx 10°$. This might create numerical approximations in creating the stiffness matrix, leading to the discrepancy of 5.7 %. All the other models differ from the analytical solution only by about 1 %.

The values of the moments calculated from eq. 2.26 are generally larger, so they are on the safe side of design if eq. 2.26 is going to be considered.

2.5.3 Bimoments in bridge structures

The worst situation in the design of a beam with a corrugated web can arise when shear force acts together with bending moment in the same cross–section. In that case the additional direct stresses in flanges arisen from the bimoment will increase the total longitudinal stress in the flange. This is the case for a continuous beam above an internal support or a fixed–ended beam, as shown in Fig. 2.21.

The bending moment above the internal support in Fig. 2.21 (a) is given by

$$M_{\mathrm{int}} = \frac{qL^2}{8} \tag{2.28}$$

and the shear force in the same cross–section by

$$T_{\text{int}} = \frac{5qL}{8} \tag{2.29}$$

where q is a uniformly distributed load; L is a span. The ratio $M_{\text{int}}/T_{\text{int}}$ for $T = T_{\text{int}}/h$, where T is the shear force per unit length, gives

$$M_{\text{int}} = \frac{TLh}{5} \tag{2.30}$$

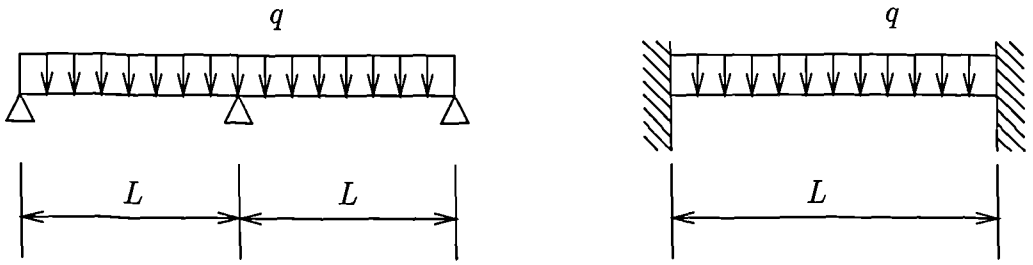

Figure 2.21: Continuous and fixed–ended beams.

From eqs. 2.27 and 2.30

$$\frac{M_{\text{b,max}}}{M_{\text{int}}} = \frac{5d(2b+d)\tan\alpha}{4Lh} \tag{2.31}$$

The direct stress σ_{b} created by moment $M_{\text{b,max}}$ in a flange is $\sigma_{\text{b}} = M_{\text{b,max}}/W_{\text{f}}$ where $W_{\text{f}} = b_{\text{f}}^2 t_{\text{f}}/6$ is the section modulus of a flange. Thus

$$\sigma_{\text{b}} = \frac{6M_{\text{b,max}}}{b_{\text{f}}^2 t_{\text{f}}} \tag{2.32}$$

The direct stress σ_{int} created by moment M_{int} in the bottom flange above the internal support is $\sigma_{\text{int}} = M_{\text{int}}/W$ where $W = 2I/h = b_{\text{f}} t_{\text{f}} h$ (for simplicity considering only two identical flanges without a web and with their centre–planes at spacing h). Thus

$$\sigma_{\text{int}} = \frac{M_{\text{int}}}{b_{\text{f}} t_{\text{f}} h} \tag{2.33}$$

Substituting eq. 2.31 into eqs. 2.32 and 2.33 results in

$$\frac{\sigma_b}{\sigma_{int}} = \frac{15d\tan\alpha}{2b_f L}(2b+d) \tag{2.34}$$

The same method was used to find the equation for a fixed ended beam as shown in Fig. 2.21 (b). The bending moment and shear force at a fixed end are

$$M_{fix} = \frac{qL^2}{12} \tag{2.35}$$

$$T_{fix} = \frac{qL}{2} \tag{2.36}$$

Thus the final equation for the stresses is

$$\frac{\sigma_b}{\sigma_{fix}} = \frac{9d\tan\alpha}{b_f L}(2b+d) \tag{2.37}$$

Table 2.7 gives the values of ratios h/d which represents the ratio of the depth of

h/d	continuous beam			fixed–ended beam		
	$100\sigma_b/\sigma_{int}$			$100\sigma_b/\sigma_{fix}$		
	$\alpha = 30°$	$\alpha = 45°$	$\alpha = 60°$	$\alpha = 30°$	$\alpha = 45°$	$\alpha = 60°$
10	4.69	8.13	14.07	5.63	9.75	16.89
15	3.13	5.42	9.26	3.75	6.50	11.26
20	2.35	4.06	7.04	2.81	4.88	8.44
25	1.87	3.25	5.63	2.25	3.90	6.75
30	1.56	2.71	4.69	1.88	3.25	5.63
35	1.34	2.32	4.02	1.61	2.79	4.82
40	1.17	2.03	3.52	1.41	2.44	4.22

Table 2.7: Bimoment stresses.

the beam to d. Using eqs. 2.34 and 2.37 gives the values of σ_b/σ_{int} and σ_b/σ_{fix} where σ_b is the maximum bimoment stress in the flange; σ_{int} is the maximum bending stress above an internal support in the continuous beam; σ_{fix} is the maximum bending stress at the fixed end. The geometry of the corrugated web is as in Fig. 2.11 where $b = 500$ mm; $d = 300$ mm and $L = 20h$. Thus the diagrams in Figs. 2.22 and 2.23 represent the maximum bimoment stresses in the flange versus the geometry of the

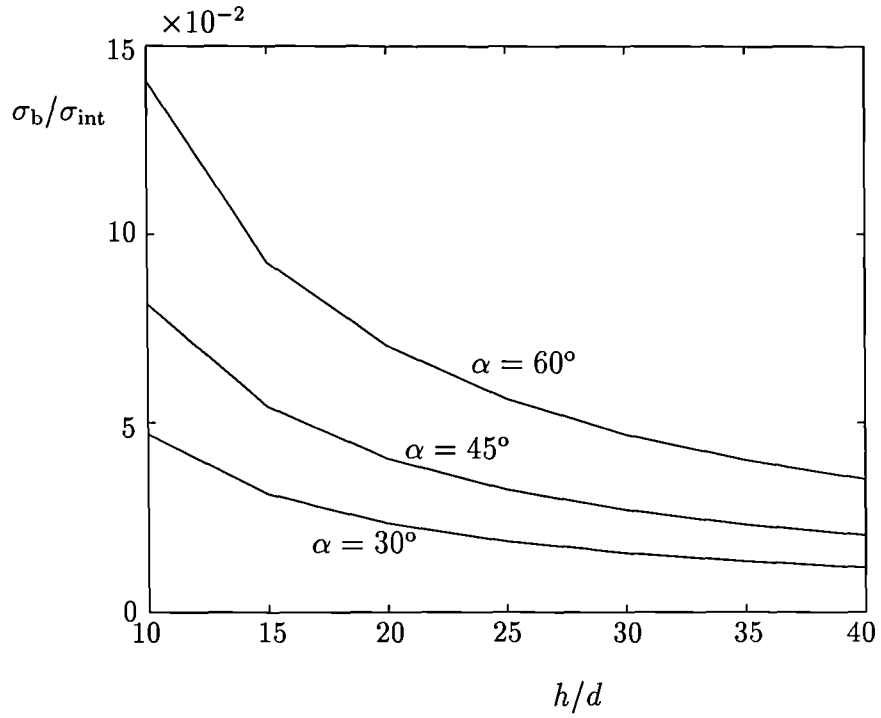

Figure 2.22: Continuous beam.

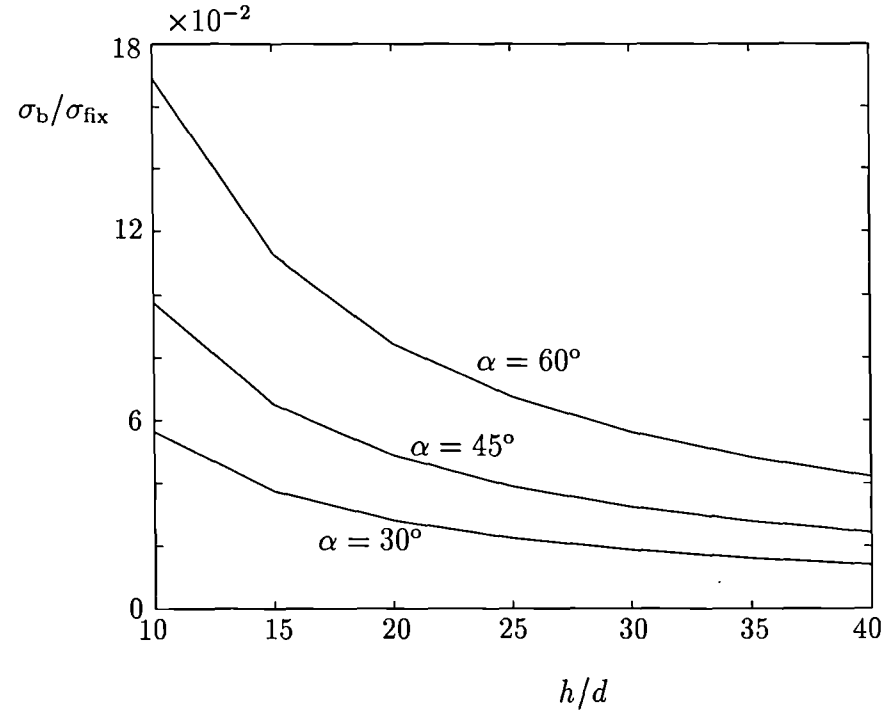

Figure 2.23: Fixed–ended beam.

corrugated web.

The additional stress σ_b decreases with increase of the ratio h/d. With a suitable choice of geometrical dimensions this additional stress can be limited to less than 10 % of the direct stress coming from hogging bending moment above the internal support or at the fixed end.

2.6 Summary on stresses in beams with corrugated webs

Linear elastic investigations of a beam with a corrugated web developed in this chapter showed the following:

1. The relationship between geometrical properties of a corrugated web and shear stresses is defined by eq. 2.3. This relationship suggests suitable ratios h_w/t_w, b/t_w and d/t_w for an economical design of corrugated webs. In practice, a vertical shear stress, depth of a beam and thickness of a web are usually given before designing the geometrical shape of a corrugated web. Thus the optimum values of b, d and α can be found from the above mentioned relationship. However, this *optimalization* ratio is based on the referenced work which itself suggests that more investigation should be performed on the shear capacity of corrugated webs, and does not give design rules for corrugated webs.

2. For practical purposes the calculation of the bending stiffness of a beam with a corrugated web, where the cross-section area of the web is not taken into consideration, is on the safe side and is sufficiently accurate.

3. The effective shear modulus of a corrugated web is in the same ratio to the shear modulus of the material as the ratio of the length of the sheeting to its unfolded length.

4. Shear forces in a corrugated web cause the appearance of a bimoment in the beam. This bimoment is formed by in-plane bending moments of opposite direction in the flanges. A formula to calculate the maximum in-plane bending

moments is given (eq. 2.26). The additional stresses in flange tips depend on the type of bridge structure and the geometry of the corrugated web. Two types of structure are shown to demonstrate that with a suitable and careful choice of geometrical dimensions this additional stress can be limited to less than 10 % of the direct stress coming from hogging bending moment above an internal support or at a fixed end.

Chapter 3

Fabrication of cambered or non–uniform plate girders with corrugated webs

3.1 Introduction

The dead weight of a bridge beam causes initial bending of the beam without having any additional loading on it. To avoid the unnecessary additional displacement, bridge girders are curved in workshops in the opposite way they will deform under dead load later.

Cambering beams with a flat web is usually performed by cutting the longitudinal edges of the web in the required curve and then welding it together with two bent flanges.

In the case of a corrugated web it is not so simple because cutting the designed curve perpendicular to the middle plane of a corrugated plate would required a very precise device. The plate is not cut in a single line, but it needs to be cut in three dimensions.

There are two main ways of avoiding direct cutting of the corrugated plate. The first is to cut the flat plate before its forming; the second is to camber the beam by bending it in its plane. Both of these methods are described below.

3.2 Cutting the flat plate before its forming

Beams are cambered mainly to improve their appearance. The amount depends on the supporting conditions of the bridge and its length. For simply supported beams the camber is typically equal to $L/300$, where L is the total length of the bridge beam between supports.

Considering 15 m as a maximum length of flat plate which could be made and the possible creation of a simply supported beam with three web plates (Fig. 3.1), the actual total length of the bridge could be obtained for the required shape of corrugated web. A camber is usually formed in the shape of parabola. Therefore

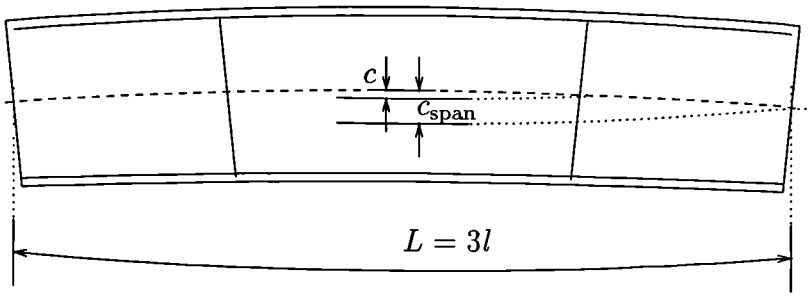

Figure 3.1: The whole cambered bridge girder.

the middle plate has to be bent more than the two side plates.

The middle curved shape of a corrugated web is a part of the curve defined for a whole bridge beam (curve 1 in Fig. 3.2). Assume curve 2 is a parabola, which represents a shape of cambered flat plate. The length of this plate is equal to the

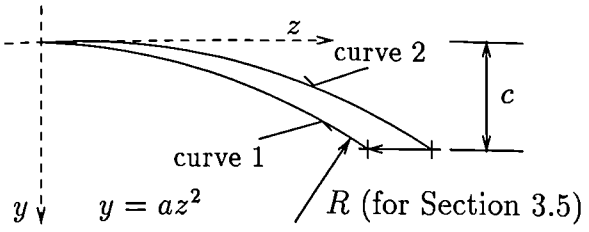

Figure 3.2: Parabola shaped curved for creating a camber.

unfolded length of the corrugated plate. What are the errors between a parabolic curve 1 and the edge of the corrugated web? Are these discrepancies small enough to be bridged by the web–to–flange welds? The folding of a pre–cambered flat plate has to be done perpendicular to its initial straight longitudinal edge. Any diversion from this direction will increase the gaps between web and flange (see Section 3.4).

The y and z–coordinates listed in Tables 3.2 and 3.3 represents the coordinates of each corner point of the corrugated line for pre–cambered flat (curve 2) and corrugated plates (curve 1), respectively. The z–coordinates for curve 1 are determined by projection of the points of the corrugated shape into z axis while the z–coordinates for curve 2 are given by the actual length of corrugated shape. The difference between the y–coordinates gives the error between the parabolic curve 1 and the edge of the corrugated web. The appearance of negative values means that the points of corrugated web edge would have been above the curve 1. Therefore the web has to be moved down by the maximum negative value, which increases the gaps with positive values.

There were two models analysed by the method described above. Their geometry is listed in Table 3.1. In the table, *unfolded length* is the length of the flat plate before

		model 1	model 2
b	mm	400	500
d	mm	150	300
α	°	45	45
$2b + 2d \sec \alpha$	mm	1224.26	1848.53
unfolded length	mm	15000	15000
folded length	mm	13508.8	13012
number of waves		12	15
remainder	mm	354.4	356
camber of middle plate	mm	15.01	14.46

Table 3.1: Geometry of two models.

its forming into a corrugated plate; *folded length* is the longitudinal projection of corrugated plate; *number of waves* is the number of whole wavelengths, $2b+2d \sec \alpha$, which fit into the plate; *remainder* represents the lengths of the plate at its ends

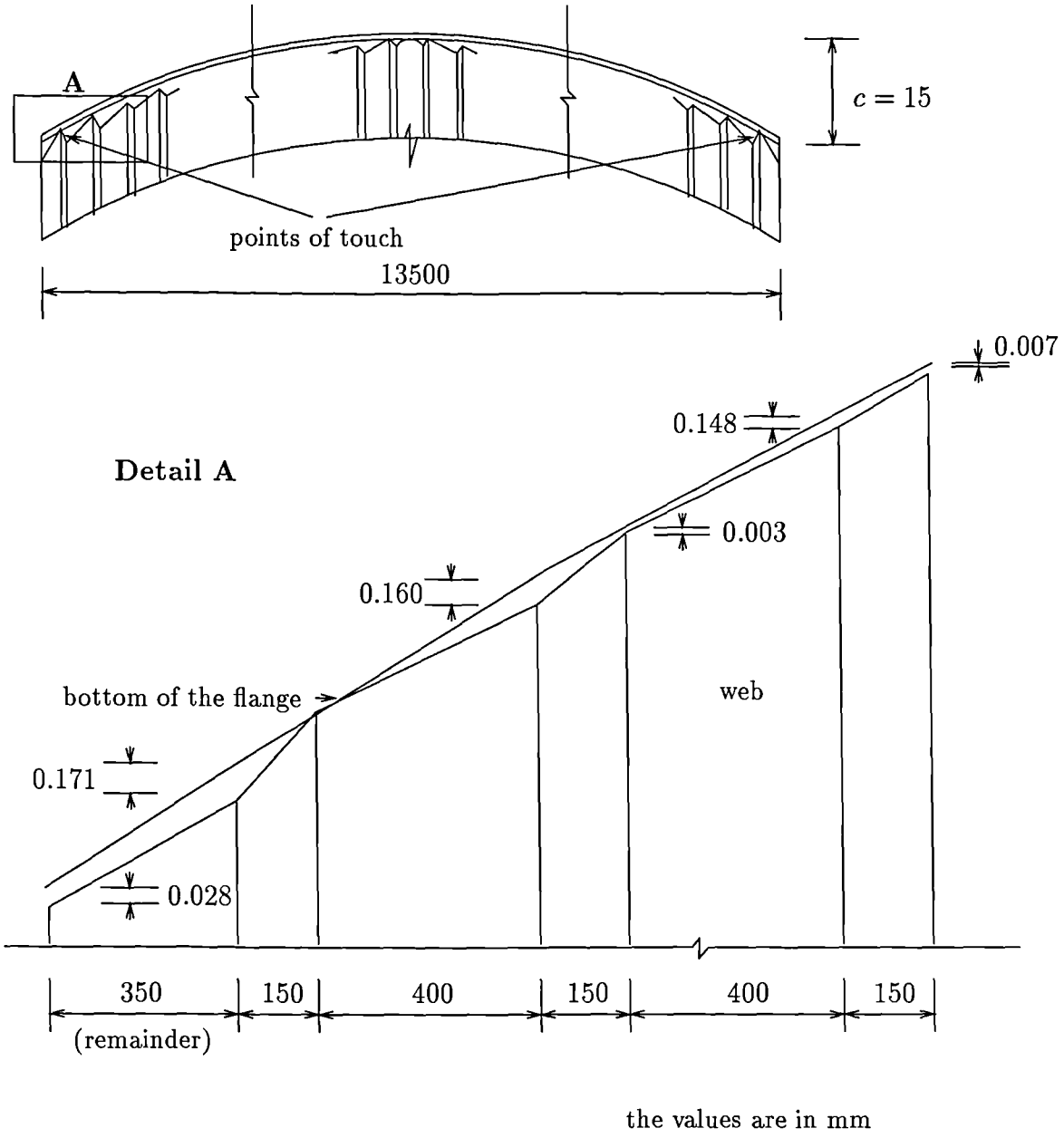

Figure 3.3: Sketch of a cambered corrugated beam when the curve is cut before forming.

flat plate curve 2 of Fig. 3.2 $a = 2.67 \times 10^{-7}$		corrugated plate curve 1 of Fig. 3.2 $a = 3.3 \times 10^{-7}$		differences	
z_{flat}	y_{flat}	z_{corr}	y_{corr}	$\Delta y = y_{\text{flat}} - y_{\text{corr}}$	final gap
mm	mm	mm	mm	mm	mm
0.00	0.000	0	0.000	0.000	0.058
200.00	0.011	200	0.013	-0.003	0.055
412.13	0.045	350	0.040	0.005	0.063
812.13	0.176	750	0.186	-0.010	0.048
1024.26	0.280	900	0.267	0.013	0.071
1424.26	0.541	1300	0.558	-0.015	0.043
1636.40	0.715	1450	0.694	0.021	0.079
2036.40	1.107	1850	1.129	-0.022	0.036
2248.53	1.349	2000	1.320	0.029	0.087
2648.53	1.872	2400	1.900	-0.028	0.030
2860.66	2.184	2550	2.145	0.039	0.097
3260.66	2.837	2950	2.871	-0.034	0.024
3472.79	3.218	3100	3.170	0.048	0.106
3872.79	4.002	3500	4.041	-0.039	0.019
4084.94	4.453	3650	4.395	0.058	0.116
4484.92	5.367	4050	5.411	-0.044	0.014
4697.06	5.887	4200	5.815	0.068	0.126
5097.06	6.933	4600	6.980	-0.047	0.011
5309.19	7.522	4750	7.443	0.079	0.137
5709.19	8.698	5150	8.749	-0.051	0.007
5921.32	9.356	5300	9.266	0.090	0.148
6321.32	10.663	5700	10.718	-0.055	0.003
6533.45	11.391	5850	11.289	0.102	0.160
6933.45	12.828	6250	12.889	-0.058	0.000
7145.58	13.625	6400	13.512	0.113	**0.171**
7500.00	15.010	6754	15.040	-0.030	0.028

Table 3.2: Determining the gaps for model 1.

less than a whole wavelength (see also Fig. 3.3); and *camber of middle plate* is shown in Fig. 3.1 as *c*.

Fig. 3.3 shows part of the web–flange interface for model 1. Model 2 was chosen later to enable comparison with the second method of creating the camber by bending an already corrugated plate.

flat plate curve 2 of Fig. 3.2 $a = 2.57 \times 10^{-7}$		corrugated plate curve 1 of Fig. 3.2 $a = 3.42 \times 10^{-7}$		differences	
z_{flat}	y_{flat}	z_{corr}	y_{corr}	$\Delta y = y_{\text{flat}} - y_{\text{corr}}$	final gap
mm	mm	mm	mm	mm	mm
0.00	0.000	0	0.000	0.000	0.091
250.00	0.016	250	0.021	-0.005	0.086
674.26	0.117	550	0.103	0.014	0.105
1174.26	0.354	1050	0.377	-0.023	0.068
1598.53	0.657	1350	0.623	0.034	0.125
2098.53	1.132	1850	1.169	-0.037	0.054
2522.79	1.136	2150	1.579	0.057	0.148
3022.79	2.347	2650	2.399	-0.050	0.041
3447.06	3.055	2950	2.972	0.083	0.174
3947.06	4.005	3450	4.065	-0.060	0.031
4371.32	4.912	3750	4.803	0.109	0.200
4871.32	6.100	4250	6.169	-0.069	0.022
5295.58	7.209	4550	7.071	0.138	0.229
5795.58	8.635	5050	8.711	-0.076	0.015
6216.85	9.935	5350	9.776	0.156	0.247
6716.85	11.598	5850	11.689	-0.091	0.000
7141.11	13.109	6150	12.919	0.190	**0.281**
7500.00	14.460	6506	14.460	0.000	0.090

Table 3.3: Determining the gaps for model 2.

The values listed in Tables 3.2 and 3.3 were calculated from the equation for a parabola, $y = az^2$. The symmetry of the parabola is used thus only one half of it is listed here. Values in the column *final gap* are calculated as $\Delta y - \Delta y_{\text{max,negative}}$. Thus for example, the maximum negative value of Δy in Table 3.2 is -0.058. So the values in the column *final gap* are $\Delta y - (-0.058)$.

As can be seen from Tables 3.2 and 3.3 (see also Fig. 3.3), the maximum gap

between the web and flange will arise close to the ends of the plate. For the model 1 it is 0.171 mm and for the model 2 it is 0.281 mm. Gaps of this size should not cause difficulties in welding the flanges to the web.

3.3 Creating a camber by bending a corrugated plate

3.3.1 Finite element analysis

The other way of producing a camber of a corrugated plate is by bending the plate in its plane. That means that the corrugations are formed before the plate is bent for the required camber.

For this method of cambering, finite element analysis was used. The objective was to find the tensile force, which is needed to bend the corrugated plate into the desired shape. This force is acting at the top corners of the plate, while the bottom ones are restrained. The force was determined from applying the deformations at the edges of the plate as shown in Figs. 3.4 and 3.5 (c).

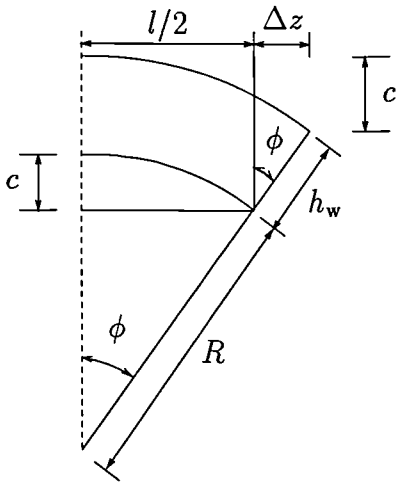

Figure 3.4: Applied deformation to a corrugated plate.

The maximum deformation in longitudinal direction Δz is

$$\Delta z = h_w \sin\phi \tag{3.1}$$

From Fig. 3.4

$$\sin\phi = \frac{l/2}{R} \tag{3.2}$$

$$R = \frac{(l/2)^2 + c^2}{2c} \tag{3.3}$$

$$\sin\phi = \frac{lc}{(l/2)^2 + c^2} \tag{3.4}$$

Substituting eq. 3.4 into eq. 3.1 the required longitudinal deformation of one edge during bending the web is

$$\Delta z = \frac{lch_w}{(l/2)^2 + c^2} \tag{3.5}$$

The geometry of the corrugated plate and the camber were the same as for model 2 in Section 3.2. The whole web depth 1600 mm (without flanges) was modelled using the I-DEAS software version 6. Linear elastic theory was applied using parabolical quadrilateral shell elements (more detailed explanation of the type of the elements used here can be found in Section 5.1.2 or in on-line manual of the Master Series version of the software). The total number of elements was 384 and the total number of nodes was 1293. The boundary conditions are shown in Fig. 3.5. The model was loaded by forced displacements such that the conditions for pure tension, pure bending and combination of tension and bending were created. To avoid global lateral movement of the web, restraints in the direction perpendicular to the longitudinal plane of the web were provided.

For model 2: $l = 13012$ mm, $c = 15$ mm, and $h_w = 1600$ mm. Δz was calculated from eq. 3.5 which was calculated for combination of tension and bending. The same value was used for loading by pure tension or pure bending only: $\Delta z = 7.38$ mm. (All three analyses were performed separately. Thus the sum of the results from the pure tension and pure bending analyses will not give the results of the combination of tension and bending analysis, since Δz was the same for all three of them. The sum of the results of the first two analyses should give double the results from the

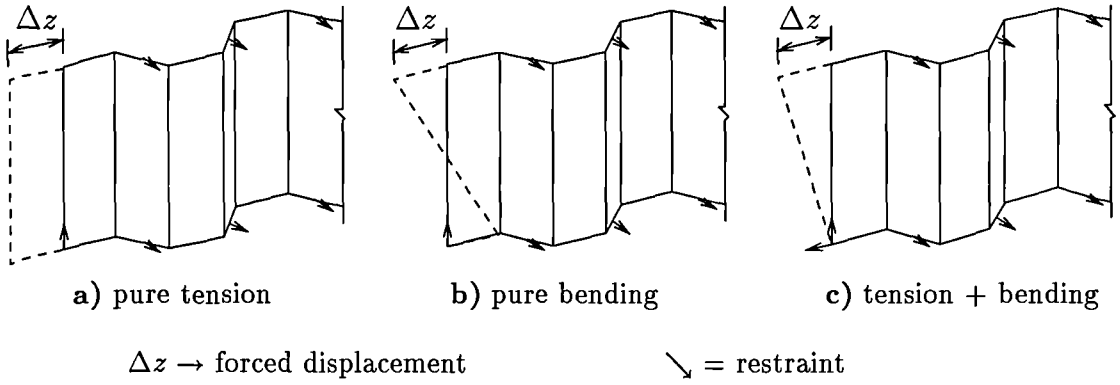

Figure 3.5: Restraint sets of the model in finite element analysis.

third analysis. This was proved to be true — see Table 3.4.)

The reaction forces at each node of the shorter edge of the plate were obtained. Thus the overall tension force, F_n, and the bending moment, M, were calculated from the reaction forces, R_i. This tension force and bending moment were then transferred to a single tension force (Fig. 3.6), $F_t = F_n/2 + F_M$, acting in the top corners of the plate (point A), while holding the bottom corners fixed (point B), where the reaction is $R_b = F_n/2 - F_M$.

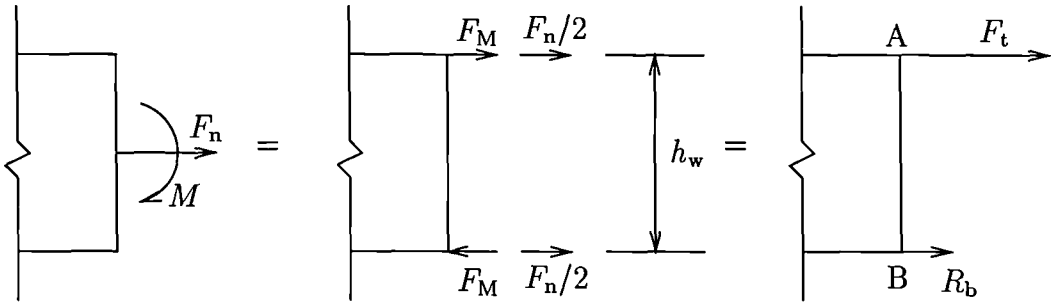

Figure 3.6: Transferring a tension force and a bending moment to two forces.

Table 3.4 lists the reaction forces at each node of the shorter edge of the plate and the position of a node in relation to the longitudinal centre–line of the model. The tension force and the bending moment are calculated as given in the table.

The required camber can be created also by loading the corrugated plate by pure

bending. In this case the middle points of the shorter edges of the plate have to be fixed and the plate corners have to be loaded by equal forces F_M (the top corners by tension forces; the bottom corners by compression forces). For the given geometry and required $c = 15$ mm the forces F_M are equal to 125 N.

	tension	bending	tens.+ bend.
z_i	R_i		
mm	N		
800.0	65.67	54.64	60.18
666.7	169.01	161.92	165.51
533.3	44.03	42.35	43.17
400.0	60.43	55.80	57.80
266.7	23.36	6.83	15.39
133.3	58.02	12.07	35.02
0	27.28	0.01	13.65
-133.3	57.93	-12.01	23.00
-266.7	23.99	-7.01	8.32
-400.0	59.69	-55.82	2.13
-533.3	44.18	-42.15	0.80
-666.7	169.11	-161.92	3.77
-800.0	65.66	-54.70	5.43
$F_n = \sum R_i$ (N)	868.36	0.01	434.17
$M = \sum(R_i z_i)$ (kNmm)	0.001	400	200
$F_M = M/h_w$ (N)	0.001	250	125

Table 3.4: Reaction forces from finite element analysis.

To create the camber of the corrugated plate ($c = 15$ mm) by the way mentioned above (fixing the bottom corners of the plate and pulling the top corners apart) the required *pulling* force acting at the top corners of the plate is then $F_t = 342$ N, while the reaction at the bottom corners is $R_b = 92$ N for the combination of tension and bending loading.

3.3.2 Analytical solution

The finite element analysis gave an approximate value of the force needed to create the cambered corrugated plate. In design practice there is often no similar software available. Therefore it is useful to have an analytical approach. The results obtained from both analytical and numerical solutions can be compared.

Appendix C shows the calculation of the *effective* elastic modulus, $E_{e,t}$, $E_{e,b}$, of the corrugated plate under uniform tension and pure bending, respectively. For the given model 2, used in finite element analysis (see Table 3.1), the variables κ and ι have the following values:

$$\kappa = d_h/t_w = d/(2t_w) = 300/(2 \times 8) = 18.75$$

$$\iota = b_h/t_w = b/(2t_w) = 500/(2 \times 8) = 31.25.$$

Thus using eqs. C.9 and C.29 two values of the effective Young's modulus for tension and bending are

- for uniform tension: $E_{e,t}/E = 2.96 \times 10^{-4}$
- for pure bending: $E_{e,b}/E = 2.38 \times 10^{-4}$

To calculate the forces needed to pull the top corners apart, while fixing the bottom corners of a corrugated plate to create the required camber, the following method is suggested:

1. Calculate the effective values of $E_{e,t}$ and $E_{e,b}$ from eqs. C.9 and C.29.
2. Use the following equations to calculate the force F_n and moment M

$$F_n = h_w t_w \varepsilon_{max} E \left(\frac{E_{e,t}}{E}\right) \tag{3.6}$$

$$M = \frac{h_w^2 t_w \varepsilon_{max} E}{6} \left(\frac{E_{e,b}}{E}\right) \tag{3.7}$$

in which ε_{max} is determined from $\Delta z/2$ when using eq. 3.5.

3. Calculate the pulling forces $F_t = F_n/2 + F_M$ (as shown in Fig. 3.6) where $F_M = M/h_w$. The reaction forces at the fixed corners are $R_b = F_n/2 - F_M$.

For model 2 the combination of tension and bending shown in Fig. 3.5 is the sum of uniform tension with longitudinal strain $\varepsilon_{max} = (7.38/6505)/2 = 5.67 \times 10^{-4}$ and pure bending with the maximum strains in the corners $\varepsilon_{max} = \pm 5.67 \times 10^{-4}$. The forces are

$$F_n = 1600 \times 8 \times 5.67 \times 10^{-4} \times 2.1 \times 10^5 \left(2.96 \times 10^{-4}\right) = 451 \text{ N}$$

$$M = \frac{1600^2 \times 8 \times 5.67 \times 10^{-4} \times 2.1 \times 10^5}{6} \left(2.38 \times 10^{-4}\right) = 240 \text{ kNmm}$$

which gives $F_M = 97000/1600 = 61$ N. Thus the pulling force is $F_t = 451/2 + 61 = 287$ N and reaction is $R_b = 451/2 - 61 = 165$ N

The differences between the forces F_t and R_b obtained from the finite element analyses (Section 3.3.1) and from the analytical solution are about 16 % and 44 %, respectively. The reason for this is explained below.

The finite element analysis in Section 3.3.1 was performed on the model as shown in Fig. 3.5. This means that the forced deformations were applied on the shorter ends of the plate for a given geometry. By doing so, the corrugated plate was loaded eccentrically, which created reaction forces also in lateral restraints that were placed in the middle of all the sloping parts of the plate. Therefore further finite element analyses were performed, in which the forced deformations were applied as shown in Fig. 3.7 and all the lateral restraints were removed. The effective Young's modulus, for pure tension and pure bending, respectively, was calculated from eqs. 3.6 and 3.7. For the given model, where $h_w = 1600$ mm, $t_w = 8$ mm, $\varepsilon_{max} = 7.38/6000 = 1.23 \times 10^{-3}$, $E = 210$ kN/mm^{-2}, the finite element analysis gave the following results: $F_n = 1064$ N and $M = 450$ kNmm. F_n and M were calculated as shown in Table 3.4. Using eqs. 3.6 and 3.7 the effective Young's modulus is $E_{e,t}/E = 3.22 \times 10^{-4}$ for pure tension and $E_{e,t}/E = 5.1 \times 10^{-4}$ for pure bending. Comparing these two values to the values obtained from eqs. C.9 and C.29 gives differences of 8 % for pure tension and 53 % for pure bending. This rather

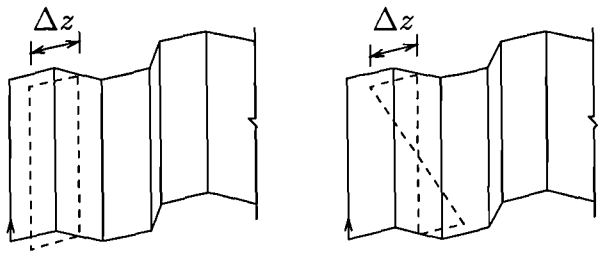

Figure 3.7: Restraint sets of the model in finite element analysis.

large difference between the finite element analysis and the analytical solution for pure bending causes the discrepancies when comparing F_t and R_b obtained from these two different methods of calculation. The reason for this difference was not traced. Shell elements were designed to model thin smooth surfaces under membrane stresses – mostly tension stresses. The finite element model of a corrugated plate had sharp edges between sloping and flat panels of the plate. It appears that the shell elements used for the bending analysis were not the best choice and it is the most likely explanation for the above mentioned discrepancies. Three more models (with different geometry) were analysed. They all varied by up to 60 % from the analytical solutions.

A careful check of the analytical solution given in Appendix C makes the author confident in saying that the analytical solution is correct. The main aim of this work was to find approximate values for the pulling forces needed to pull the top corners of a corrugated plate apart while fixing the bottom corners thereby creating the required camber. These forces then indicate what type of tension jack is needed. Since both solutions give the effective Young's modulus to the same order of magnitude, the forces can be considered as a reasonable estimate.

3.3.3 Discrepancies in corner points of a corrugated panel

Displacements in the y–direction are listed in Table 3.5. They were obtained from finite element analysis as described in Section 3.3.1. The *smooth parabola* was calculated such that the end points of both models had the same y–coordinates. The

parabola shape was chosen to create the same required shape of a camber as in Section 3.2. Bending a plane by pulling its top corners apart while the bottom corners are fixed will create a circular shape of camber. In the given scale the difference between the chosen parabola and a circle is negligible. The maximum gap obtained by finite element analysis would appear in the middle of the plate and its value is 0.178 mm. This is about 36 % less than the maximum gap created when the edge of the flat plate is cut to a curve before the corrugations are formed (compare with Table 3.3).

	points of smooth parabola $a = 3.544 \times 10^{-7}$	displacements from finite elements	differences	
z	y_{p}	y_{FE}	$\Delta y = y_{\mathrm{FE}} - y_{\mathrm{p}}$	final gap
mm	mm	mm	mm	mm
0	0.0	0.0	0.0	0.045
250	0.022	0.015	0.128	0.173
550	0.107	0.24	0.133	**0.178**
1050	0.391	0.51	0.119	0.164
1350	0.646	0.77	0.124	0.169
1850	1.213	1.32	0.107	0.152
2150	1.638	1.74	0.102	0.147
2650	2.489	2.58	0.091	0.136
2950	3.084	3.17	0.086	0.131
3450	4.218	4.28	0.062	0.107
3750	4.983	5.036	0.053	0.098
4250	6.401	6.431	0.030	0.075
4550	7.336	7.353	0.017	0.062
5050	9.037	9.028	-0.009	0.036
5350	10.143	10.118	-0.025	0.020
5850	12.128	12.084	-0.044	0.001
6150	13.403	13.358	-0.045	0.0
6506	15	15	0.0	0.045

Table 3.5: Determining the gaps for model 2 from finite element analysis.

3.4 Allowed tolerance in a pair of fold lines

All the calculations done above were based on the assumption that the folds of the web are made without any deviation from the vertical direction. That means all foldings are exactly parallel and perpendicular either to the line connecting two points at the top of the edges in case of creating the camber before folding, or to the longitudinal edge of the corrugated web in case of creating the camber by bending of the folded plate.

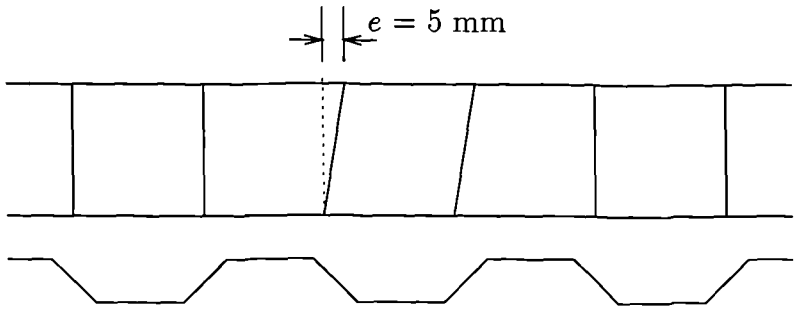

Figure 3.8: Allowed tolerance in pair of fold lines.

Analysing the first case where foldings are made after creating the camber, there is the possibility that a pair of fold lines is made with some deviation (see Fig. 3.8).

Fig. 3.9 shows the projection of folding the plate with deviation φ into the plane of the paper. From the simple geometry of this picture:

$$CB' = d \sec \alpha \tag{3.8}$$

$$CE = \frac{d}{\cos \alpha} \cos \alpha = d \tag{3.9}$$

$$EB = d(\sec \alpha - 1) \tag{3.10}$$

$$w = EF = EB \sin \varphi = d \sin \varphi (\sec \alpha - 1) \tag{3.11}$$

Total error for one wave is:

$$w_t = 2 \times w \tag{3.12}$$

For model 2 where $h_w = 1600$ mm, $b = 500$ mm, $d = 300$ mm, $t_w = 8$ mm,

$\alpha = 45°$ and maximum allowed deviation is $e = 5$ mm, the error from eq. 3.12 is $w_t = 2 \times 300 \times 0.414 \times (5/1600) = 0.776$ mm.

However, this error is cumulative for the extra folds.

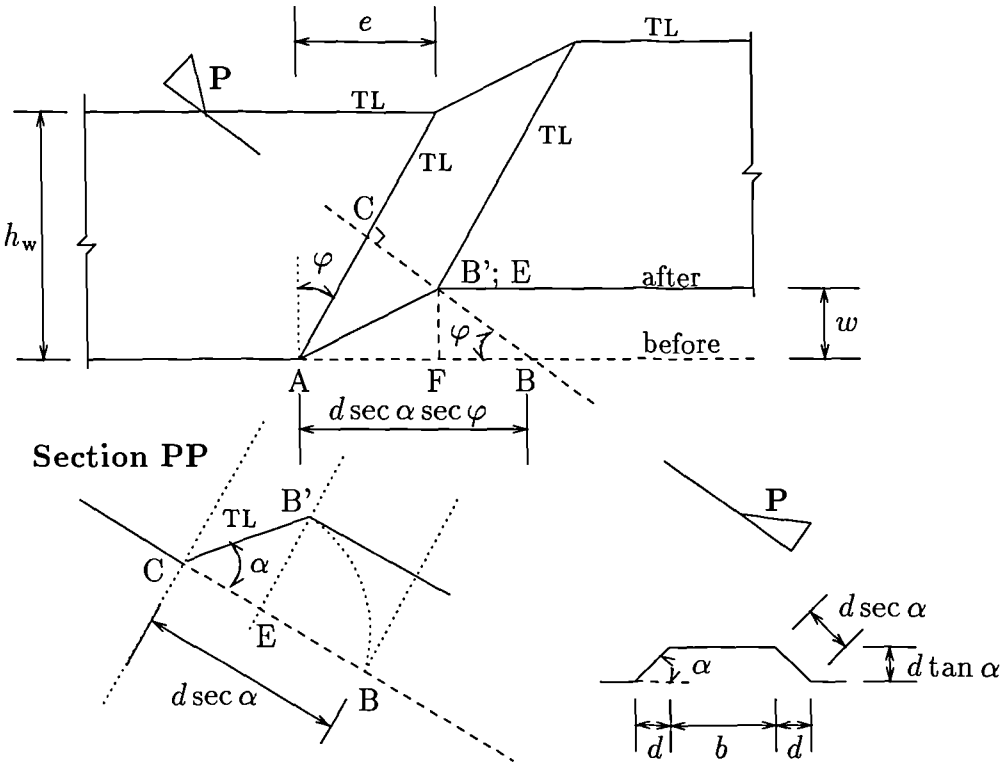

Figure 3.9: Deviation of the folds.

3.5 Girder with curved soffit

A similar problem could arise in case of the girder shown in Fig. 3.10. The method

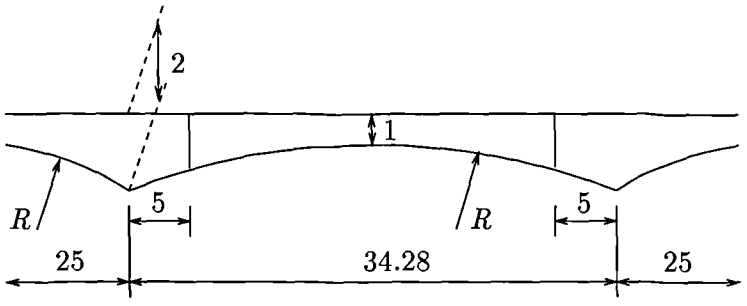

dimensions are in metres

Figure 3.10: Girder with curved soffit.

of determining the gaps is the same as it was in Section 3.2. First there is the assumption that the gaps that arise from cambering this type of beam are negligible, so that the calculation is done just for creating the curved bottom edge. This curve is assumed to be in the shape of circle. Both the radii for the flat plane and the corrugated plane can be defined by $R = (y^2 + z^2)/2y$ from which

$$y = R - \sqrt{R^2 - z^2} \tag{3.13}$$

Table 3.6 lists the first and the last pair of folded lines for the 12.14 m long corrugated plate (half of the middle part of the girder is (34.28 - 2×5)/2 = 12.14 in Fig 3.10). The table shows that the maximum negative and positive values of error are in the last fold. Summarising their absolute values the total error which could be obtained is 5.386 mm. The initial assumption was to neglect the cambering of the beam. Now if the error coming from cambering (Section 3.2 – Table 3.4), which is about 0.3 mm, is added, the total gap between the web and flange becomes about 5.7 mm.

geometry of corrugated plate		
b	mm	500
d	mm	300
α	°	45
$2b + 2d \sec \alpha$	mm	1848.53
unfolded length	mm	14000
folded length	mm	12136
number of waves		14
remainder	mm	386

corrugated plate $R = 1.473 \times 10^5$		flat plate $R = 1.96 \times 10^5$		difference
z_{corr}	y_{corr}	z_{flat}	y_{flat}	$\Delta y = y_{\text{flat}} - y_{\text{corr}}$
mm	mm	mm	mm	mm
first pair of folded lines in the middle of the plate				
0	0.000	0.00	0.000	0.000
250	0.212	250.26	0.159	-0.053
550	1.027	671.26	1.150	0.123
1050	3.742	1174.26	3.518	-0.224
1350	6.186	1598.52	6.520	0.334
last pair of folded lines				
10650	385.454	12265.38	384.212	-1.242
10950	407.506	12689.64	411.280	3.774
11450	445.628	13189.64	444.367	**-1.261**
11750	469.324	13613.90	473.449	**4.125**
12136	500.719	14000.00	500.719	0.000

Table 3.6: Girder with curved soffit.

3.6 Summary on fabrication of corrugated webs

Fabrication for two types of plate girders were considered in this chapter: cambering a girder with uniform depth; cutting a web of a girder with curved soffit. Mathematical methods and linear elastic final element analyses were used to conclude the following:

1. There are two ways of fabricating a cambered beam of uniform depth with a corrugated web. The first is cutting the flat plate before it is corrugated. The second is creating a camber by bending an already corrugated plate in a plane parallel to the flat panels of the plate. The second method involves forces less than 0.5 kN to pull the top corners of the plate apart while fixing the bottom corners so the required camber is formed.

2. By forming a corrugated plate into a cambered shape by either of the methods mentioned above, the top or bottom surfaces of the corrugated plate will not be in one curved plane, which creates gaps when attaching the web to the flanges. It was found that these gaps are sufficiently small not to cause difficulties in welding the flanges to the web.

3. It is shown that the error that arises from the maximum likely deviation of a pair of folds is within the allowed range and should not cause difficulties in welding the flanges to the web. The formula to calculate this error is given by eq. 3.11. However, this error is cumulative for the extra folds.

4. If a bridge girder has a curved soffit, and the first method of conclusion 1 is used, the possible discrepancies in the longitudinal edges between web and flanges are shown to be too large for joining the web and flanges by welding. Corrugated plates are therefore not recommended for use in bridge girders with a curved soffit, unless a better method of fabrication can be devised, than cutting the bottom longitudinal edge of the web plate to a circular arc before corrugating it. This apply to long plates. The bridge in Southern France built recently (Pont de la Corniche), has a curved soffit. It was erected in 3 m long segments, thus there was no problem to weld the web to the bottom flange.

Chapter 4

Re-design of Avon Bridge

4.1 Introduction

The saving on a volume of steel seems to be one of the advantages of using a corrugated plate instead of plane one in bridge plate girders. The corrugated webs do not need transverse stiffeners and their thicknesses can be reduced to 6 to 8 mm.

The present chapter contains a re-design of a typical plate girder. The dimensions were taken from drawings and calculations of a plate girder highway bridge which were provided by Cass Hayward and Partners, consulting engineers.

Only one of the girders of the real bridge was considered here. It was a simply-supported girder of span 37 m, with vertically stiffened webs 15 mm thick at midspan, and 20 mm thick near supports. Weathering steel was used, thus a corrosion allowance of 2 mm on each face was made in the original design. Steel of Grade 50 was used.

4.2 The original design

Fig. 4.1 shows a typical cross–section of the girder. The original geometrical dimensions are listed in Table 4.1 (without 2 mm of corrosion allowance).

The yield stress of the steel is 355 N/mm^2, which gives shear yield stress τ_y = 205 N/mm^2. The factored design vertical shear force at the support is V_d = 2387 kN.

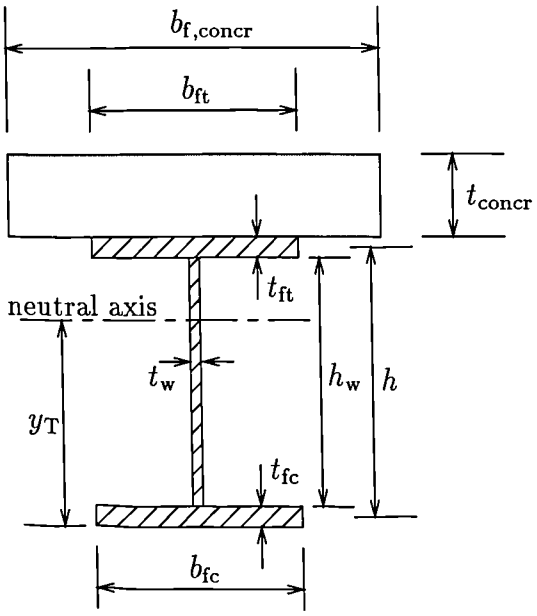

Figure 4.1: A typical cross–section of a composite plate girder.

		at the ends	at midspan
$b_{f,concr} \times t_{concr}$	mm	3275 × 250	3275 × 250
$b_{ft} \times t_{ft}$	mm	596 × 28	596 × 38
$t_w \times h_w$	mm	16 × 1726	11 × 1706
$b_{fc} \times t_{fc}$	mm	596 × 46	596 × 56

Table 4.1: The original geometrical dimensions.

The internal factored design vertical shear force (at a splice) is $V_d = 719$ kN and the design maximum bending moment is $M = 14183$ kNm. Factored bending moments are listed in Tables 4.2 or 4.3. The lengths of the end parts of the girder are $l_{end} = 10.865$ m, and that of the middle part is $l_{mid} = 16$ m.

4.3 The new design

4.3.1 Web

The end parts of the girder where $l_{end} = 10.865$ m

The geometrical dimensions of the web are as follows (see Fig. 2.1 for notation): $h_w = 1726$ mm; $t_w = 8$ mm; $b = 450$ mm; $d = 240$ mm; $\alpha = 45°$.

The verification has to satisfy the conditions given in expressions 1.33. The ultimate limit state is:

$$\tau_{U.L.S.} = \frac{V_d}{t_w h_w} = \frac{2387000}{8 \times 1726} = 173 \text{ N/mm}^2$$

The critical local buckling (eq. 1.5 for $k_f = 0.88$):

$$\tau_{cr,loc} = \frac{0.88 \times 5.34 \times \pi^2 \times 2.1 \times 10^5}{12 \times (1 - 0.3^2)} \left(\frac{8}{450}\right)^2 = 282 \text{ N/mm}^2$$

The critical global buckling (eqs. 1.11, 1.12 and 1.31 for $k_u = 32.4$):

$$b_0 = 2 \times 450 + 2 \times 240 = 1380 \text{ mm}$$

$$s = 2 \times 450 + 2 \times 240 \times \sqrt{2} = 1579 \text{ mm}$$

$$I_y = 2 \times 450 \times 8 \times \left(\frac{240}{2}\right)^2 + \frac{2 \times \sqrt{2} \times 240^3 \times 8}{12} = 1.3 \times 10^8 \text{ mm}^4$$

$$D_z = \frac{1380 \times 2.1 \times 10^5 \times 8^3}{12 \times 1579} = 7.8 \times 10^6 \text{ Nmm}$$

$$D_y = \frac{2.1 \times 10^5 \times 1.3 \times 10^8}{1380} = 2 \times 10^{10} \text{ Nmm}$$

$$\tau_{cr,gl} = \frac{32.4 \times \sqrt[4]{7.8 \times 10^6 \times (2 \times 10^{10})^3}}{1726^2 \times 8} = 3821 \text{ N/mm}^2$$

$$\frac{1}{2}\tau_{cr,gl} = 3821/2 = 1910 \text{ N/mm}^2$$

Interaction of critical local and critical global buckling (eq. 1.34):

$$\tau_m = \frac{1}{1/282 + 1/3821} = 263 \text{ N/mm}^2$$

$$\frac{2}{3}\tau_m = 2 \times 263/3 = 175 \text{ N/mm}^2$$

Post–buckling failure (eq. 1.6)

$$\tau_f = \sqrt{282 \times 205} = 240 \text{ N/mm}^2$$

The conditions in 1.33 are:

$$\tau_{U.L.S.} = 173 \text{ N/mm}^2 \begin{cases} \leq 175 \text{ N/mm}^2 \\ \leq 1910 \text{ N/mm}^2 \\ \leq 205 \text{ N/mm}^2 \\ \leq 282 \text{ N/mm}^2 \\ \leq 240 \text{ N/mm}^2 \end{cases}$$

Thus all five conditions are satisfied.

The middle part of the girder where $l_{mid} = 16$ m

The geometrical dimensions of the web are: $h_w = 1706$ mm; $t_w = 6$ mm; $b = 480$ mm; $d = 240$ mm; $\alpha = 45°$.

The ultimate limit state is:

$$\tau_{U.L.S.} = \frac{V_d}{t_w h_w} = \frac{719000}{6 \times 1706} = 70 \text{ N/mm}^2$$

The critical local buckling (eq. 1.5 for $k_f = 0.88$):

$$\tau_{cr,loc} = \frac{0.88 \times 5.34 \times \pi^2 \times 2.1 \times 10^5}{12 \times (1 - 0.3^2)} \left(\frac{6}{480}\right)^2 = 139 \text{ N/mm}^2$$

The critical global buckling (eqs. 1.11, 1.12 and 1.31 for $k_u = 32.4$):

$$b_0 = 2 \times 480 + 2 \times 240 = 1440 \text{ mm}$$

$$s = 2 \times 480 + 2 \times 240 \times \sqrt{2} = 1639 \text{ mm}$$

$$I_y = 2 \times 480 \times 6 \times \left(\frac{240}{2}\right)^2 + \frac{2 \times \sqrt{2} \times 240^3 \times 6}{12} = 10^8 \text{ mm}^4$$

$$D_z = \frac{1440 \times 2.1 \times 10^5 \times 6^3}{12 \times 1639} = 3.3 \times 10^6 \text{ Nmm}$$

$$D_y = \frac{2.1 \times 10^5 \times 10^8}{1440} = 1.46 \times 10^{10} \text{ Nmm}$$

$$\tau_{cr,gl} = \frac{32.4 \times \sqrt[4]{3.3 \times 10^6 \times (1.46 \times 10^{10})^3}}{1706^2 \times 6} = 3321 \text{ N/mm}^2$$

$$\frac{1}{2}\tau_{cr,gl} = 3321/2 = 1661 \text{ N/mm}^2$$

Interaction of critical local and critical global buckling (eq. 1.34):

$$\tau_m = \frac{1}{1/139 + 1/3321} = 133 \text{ N/mm}^2$$

$$\frac{2}{3}\tau_m = 2 \times 263/3 = 89 \text{ N/mm}^2$$

Post-buckling failure (eq. 1.6)

$$\tau_f = \sqrt{139 \times 205} = 169 \text{ N/mm}^2$$

The conditions in 1.33 are:

$$\tau_{U.L.S.} = 70 \text{ N/mm}^2 \begin{cases} \leq & 89 \text{ N/mm}^2 \\ \leq & 1661 \text{ N/mm}^2 \\ \leq & 205 \text{ N/mm}^2 \\ \leq & 139 \text{ N/mm}^2 \\ \leq & 169 \text{ N/mm}^2 \end{cases}$$

Thus all five conditions are satisfied again.

4.3.2 Flanges

The maximum bending moment for a simply supported beam is in the middle of the beam. Therefore only the middle part of the girder is considered here. The corrugated web is considered to resist no bending stresses, thus the web is excluded from the following calculations. Table 4.2 summarises the geometrical properties and stresses of the section. Notation is as in Fig. 4.1.

$b_{ft} = 596$ mm	$b_{fc} = 596$ mm
$t_{ft} = 38$ mm	$t_{fc} = 56$ mm
$b_{f,concr} = 3275$ mm	$t_{f,concr} = 250$ mm
$h_w = 1706$ mm	

	Section		
	steel	composite	
		$n = 6.6$	$n = 13.2$
y_T (mm)	737	1555	1361
$10^{-6} I_x$ (mm^4)	41500	96600	83400
$10^{-6} W_{top}$ (mm^3)	39	395	190
$10^{-6} W_{btm}$ (mm^3)	56	62	61

		Stresses	
loading	factored BM	top surf.	btm surf.
	kNm	N/mm^2	N/mm^2
dead steel	1363	34.95	24.21
dead concr.	3948	101.23	70.12
deck surfacing	1691	8.9	27.59
HA + HB/HC	11063	28.01	178.44
shrinkage		33.6	4.8
total		206.69	305.16
permissible		205	299
action	not OK		

Table 4.2: The original design of the flanges.

Using the same flange dimensions as in the original design would not be accepted as shown in Table 4.2. There is need to increase the cross–section area of the flanges. Table 4.3 gives the new design of the flanges.

It is assumed that the end parts of the girder will have the same increase in cross–sectional area of the flanges. The overall depth of the girders remains the same

which means that by increasing the flange thicknesses the value of h_w decreases by 6 mm (see Tables 4.2 and 4.3). This will slightly decrease the slenderness of the web

$b_{ft} = 600$ mm	$b_{fc} = 600$ mm
$t_{ft} = 40$ mm	$t_{fc} = 60$ mm
$b_{f,concr} = 3275$ mm	$t_{f,concr} = 250$ mm
$h_w = 1700$ mm	

	Section		
	steel	composite	
		$n = 6.6$	$n = 13.2$
y_T (mm)	730	1535	1337
$10^{-6} I_x$ (mm^4)	44100	103000	88000
$10^{-6} W_{top}$ (mm^3)	41	390	190
$10^{-6} W_{btm}$ (mm^3)	60	67	66

		Stresses	
loading	factored BM	top surf.	btm surf.
	kNm	N/mm^2	N/mm^2
dead steel	1363	33.08	22.57
dead concr.	3948	95.83	65.36
deck surfacing	1691	8.9	25.62
HA + HB/HC	11063	28.37	164.87
shrinkage		33.6	4.8
total		199.78	283.22
permissible		205	299
action	OK		

Table 4.3: The new design of the flanges.

panels. Thus the global critical shear stress will increase only by about 1 %. This is considered to be negligible and no further verifications for shear stresses were done.

Table 4.4 summarises the calculations of the volume of both girders — the original and new design. (Bearing stiffeners and bracings are omitted in both designs.)

Comparing the volumes of the webs for original and new designs gives the difference as 44 %. But there is an increase by 16 % in the volume of the flanges of the new design. This reduces the final difference between the volumes to only 9.5 %.

The original design of the web plates was conservative. The thicknesses of 15 mm and 20 mm (corroded to 11 mm and 16 mm) were used because they corresponded

		END PART	MIDDLE PART
Original design — web			
$h_w \times t_w$	mm × mm	1726 × 16	1706 × 11
length	mm	10865	16000
volume	m^3	2 × 0.300	0.300
TOTAL VOLUME OF WEB (m^3)			0.900
Original design — stiffeners			
cross–section	mm × mm	148 × 16	148 × 16
depth	mm	(1800 - 30 - 50 - 22)	(1800 - 40 - 60 - 22)
number		3	4
volume	m^3	2 × 0.012	0.016
TOTAL VOLUME OF STIFFENERS (m^3)			0.040
Original design — flanges			
$b_{ft} \times t_{ft}$	mm × mm	596 × 28	596 × 38
$b_{fc} \times t_{fc}$	mm × mm	596 × 46	596 × 56
length	mm	10865	16000
volume	m^3	2 × 0.479	0.896
TOTAL VOLUME OF FLANGES (m^3)			1.855
Total volume (m^3)			**2.795**
New design — web			
$h_w \times t_w$	mm × mm	1720 × 8	1700 × 6
$b_0/2$	mm	690	720
$s/2$	mm	789.41	819.41
number of $b_0/2$		15	22
unfolded length	mm	12356	18187
volume	mm^3	2 × 0.170	0.186
TOTAL VOLUME OF WEB (m^3)			0.526
New design — flanges			
$b_{ft} \times t_{ft}$	mm × mm	600 × 30	600 × 40
$b_{fc} \times t_{fc}$	mm × mm	600 × 50	600 × 60
length	mm	10865	16000
volume	mm^3	2 × 0.522	0.960
TOTAL VOLUME OF FLANGES (m^3)			2.003
Total volume (m^3)			**2.529**

Table 4.4: Volume of the original and new design for the girder MB5.

with thicknesses being used on another (larger) bridge in the same contract and it was cost–effective to rationalise on thickness in WR steel. Rough calculations were done later and they showed that a web of 13 mm (9 mm corroded) could have been used instead of the one with 20 mm thickness. The volume of the original web design (using 9 mm plate for end and middle parts of the girder) would be only 0.583 m^3 (not 0.9 m^3 as in Table 4.4). Thus the saving on the volume of the web would be only 16 % and there would be no overall savings at all.

4.4 Summary on re–design of Avon Bridge

A typical plate girder of a simply supported bridge was considered in this chapter. In this type of bridges bending stresses are governing factors in a design. Corrugated webs make no contribution to caring the bending stresses at all thus the flange volume has to be increased, as it was done in the shown example. Therefore no overall saving on the volume of steel used was found for this plate girder. However, the theoretical saving on volume of steel used for the web itself, when comparing plane and corrugated webs, can be about 16 %. For composite box–girder bridges the situation would be different as the new web would increase distortional stiffness, which would lead to other savings, and the increase in area of flanges would probably be less. Box–girder bridges were not considered in the present work.

Chapter 5

Finite element analysis of local buckling of compressed flange

5.1 Some facts about the software

5.1.1 General

The same software I–DEAS was used for analytical local buckling analysis of a compressed flange of a beam with a corrugated web as for analytical investigation of bending and shear of the beam in Chapter 2.

A different type of element was used for buckling analysis. The *linear* quadrilateral thin shell elements used in shear and bending analyses were not satisfactory for elastic critical buckling analysis. The analysis of a simple strut by I–DEAS software gave unsatisfactory results for the elastic critical buckling load using *linear* shell elements, in contrary with simple strut theory developed by Timoshenko [46]. The difference between Timoshenko's theoretical solution and the one given by I–DEAS using *linear* shell elements was about 80 %. The solution by I–DEAS itself was influenced very strongly by mesh generation.

These discrepancies were avoided by using *parabolic* quadrilateral thin shell elements. The validation of their usage is described in the following sections.

5.1.2 Parabolic quadrilateral thin shell elements

As Fig. 5.1 shows, a parabolic quadrilateral thin shell element has eight nodes.

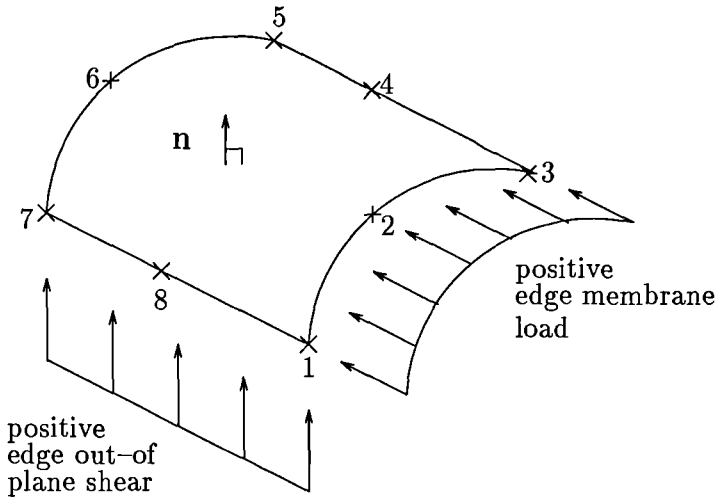

Figure 5.1: Parabolic quadrilateral shell element.

Three translational degrees of freedom and three rotational degrees of freedom are assigned to each node. The vector **n** is perpendicular to the shell mid–surface and is directed consistent with a right–hand–rule system of nodal connectivity. The top surface of the element lies on the positive side of **n**.

Translations are in the direction of the nodal displacement coordinate system of axes which for the present analysis was defined in the same way as the global coordinate system. Rotations are about the nodal displacement coordinate system axes.

In the present analysis edge membrane load and edge out–of–plane shear were used. They are defined as in Fig. 5.1.

The material for the elements was chosen to be isotropic with basic characteristics: $E = 210$ kN/mm^2; $\nu = 0.3$; and $f_y = 300$ N/mm^2. Constant thickness of an element was defined.

According to the manual [60], the element is designed to provide approximate solutions using Mindlin [41] shell theory. A parabolic distribution of transverse shear stress is included. For flat shells of constant thickness (plates) a Heterosis

formulation [14] is employed in conjunction with proprietary shape functions. The membrane and bending patch tests are satisfied.

5.1.3 Linear buckling analysis

The buckling analysis solution is based on principle of virtual displacements which states that: *If an elastic body is in equilibrium and experiences an admissible virtual displacement then the total internal virtual work is equal to the external virtual work* (taken from I–DEAS Smart View of Master Series).

The basis for the analysis is explained in Ref. [60] as follows:

"If the idea of elements with internal interpolating functions is introduced, the usual finite element matrix equations are created, where the internal virtual work or strain energy due to the virtual displacement becomes the element stiffness times the nodal displacements and the external virtual work due to the applied forces is the vector of applied forces. The small strain assumption is used in obtaining the stiffness matrix.

"Linear buckling analysis begins by applying a reference load $\{R_{\text{ref}}\}$ and performing a standard linear statics analysis to obtain stresses. A reference stress stiffness matrix $[K_{\text{ssref}}]$ is then formed. The stresses and hence the stress stiffness are linear functions of the reference load.

"A condition of neutral stability is reached when the reference loads are such that displacements may occur without any additional application of loads. In effect the body has zero additional strain energy for certain deformed shapes of arbitrary magnitude. This can be mathematically expressed as the following eigenvalue problem

$$([K_{\text{l}}] + \lambda_{\text{b}}[K_{\text{ssref}}])\,\{d\} = \{0\} \tag{5.1}$$

where $[K_{\text{l}}]$ is the linear stiffness; λ_{b} is the critical load factor multiplier on the reference load (eigenvalue) and $\{d\}$ is the displacement shape requiring no additional loads (eigenvector). The eigenvalue problem is solved in the Model Solution package using the standard simultaneous vector iteration algorithm used in normal mode dynamics.

"Linear buckling analysis assumes that the equilibrium configuration just prior to buckling is the same as the initial geometry (small displacement assumption)."

5.1.4 Validation of the software

5.1.4.1 Simple strut theory

To prove the correctness of using the software for buckling analysis the simple strut theory was chosen for comparison with the results obtained from I-DEAS solution.

A plate with cross-section 8 mm × 200 mm and length 675 mm was designed. It was simply supported and loaded by the edge membrane load on both the shorter edges (Fig. 5.2).

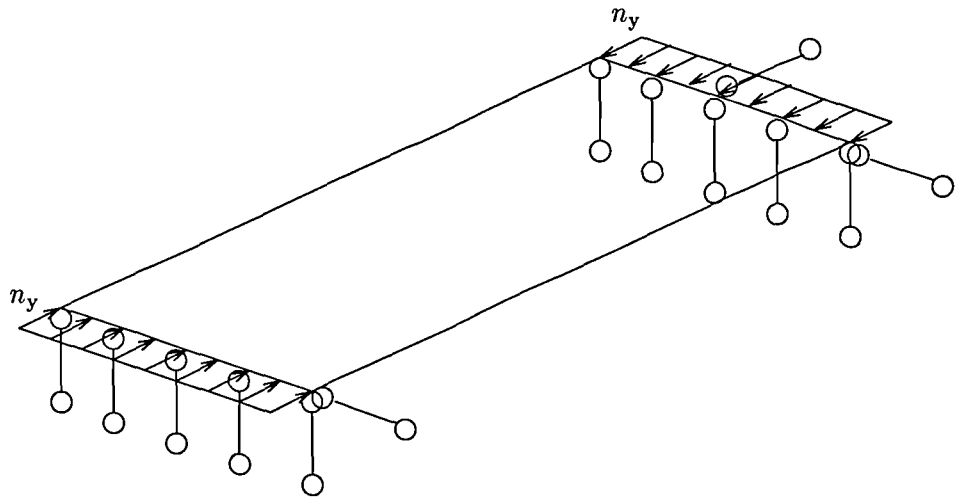

Figure 5.2: Boundary conditions for simple strut.

The load was chosen as the *yield* membrane load defined by

$$n_y = \frac{f_y A}{b_f} \tag{5.2}$$

where $f_y = 300$ N/mm^2; $A = (8{\times}200)$ mm^2; and $b_f = 200$ mm. So $n_y = 2400$ N/mm.

The number of elements varied from 85 to 340 (see Table 5.1) to show the convergence to the theoretical value.

Model	Num. of elements	Num. of nodes	λ_b
STRUT-1	85	300	0.081519
STRUT 2	114	393	0.081515
STRUT-3	161	544	0.081511
STRUT-4	216	719	0.081507
STRUT 5	340	1109	0.081502

Table 5.1: Basic characteristics of the models used for finite element analysis for comparison with strut theory.

The output of the buckling solution gives the critical load factor multiplier on the applied load λ_b. The presented models were loaded by the yield load, so the critical load factor itself gave the relative critical buckling load scaled on the y–axis of Fig. 5.3.

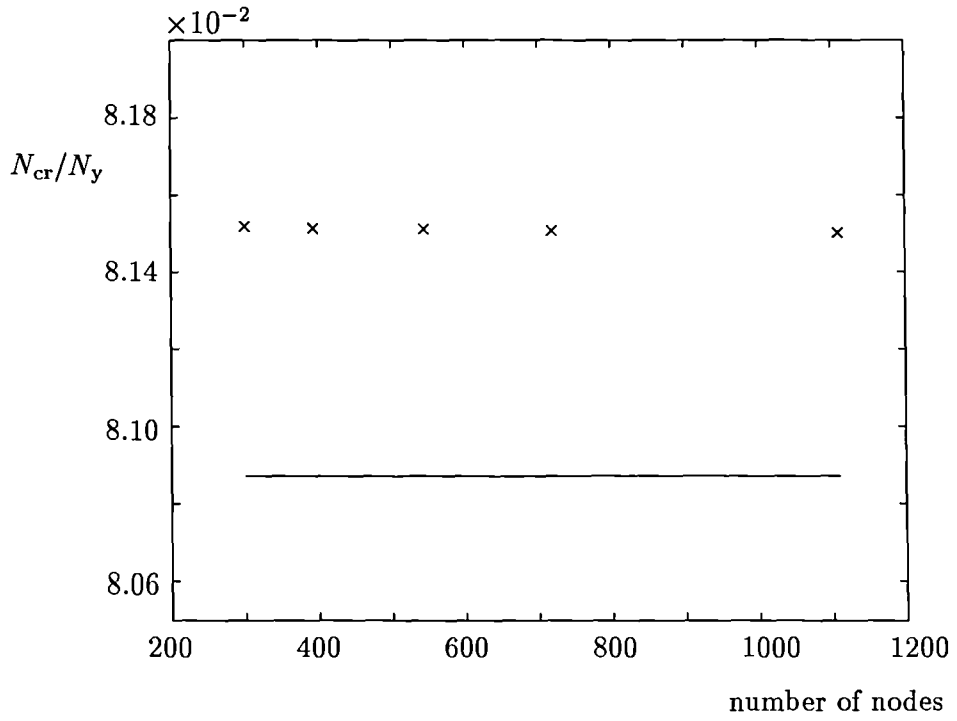

Figure 5.3: Elastic critical buckling force.

Timoshenko's elastic theory gives the elastic critical buckling load for a strut

$$N_{cr} = \frac{\pi^2 EI}{l^2} \tag{5.3}$$

where for the given example $E = 210$ kN/mm^2; $I = 8533$ mm^4; and $l = 675$ mm; so the critical force is $N_{cr} = 38.82$ kN. In relation to yield force $N_y = f_y A = 300 \times 8 \times 200 = 480$ kN, N_{cr} gives the relative elastic critical stress as $\lambda = 0.08087$. This is shown as the horizontal line in Fig. 5.3.

Fig. 5.3 shows good agreement of the finite element solution with the theory, with the difference only 0.7 % and the results from finite element analysis on the safe side of the theoretical value.

5.1.4.2 Plate simply supported on three sides and free on one longitudinal side

Another check on the finite element analysis was performed using plate buckling. The model chosen is shown in Fig. 5.4. The geometry and the loading of the plate

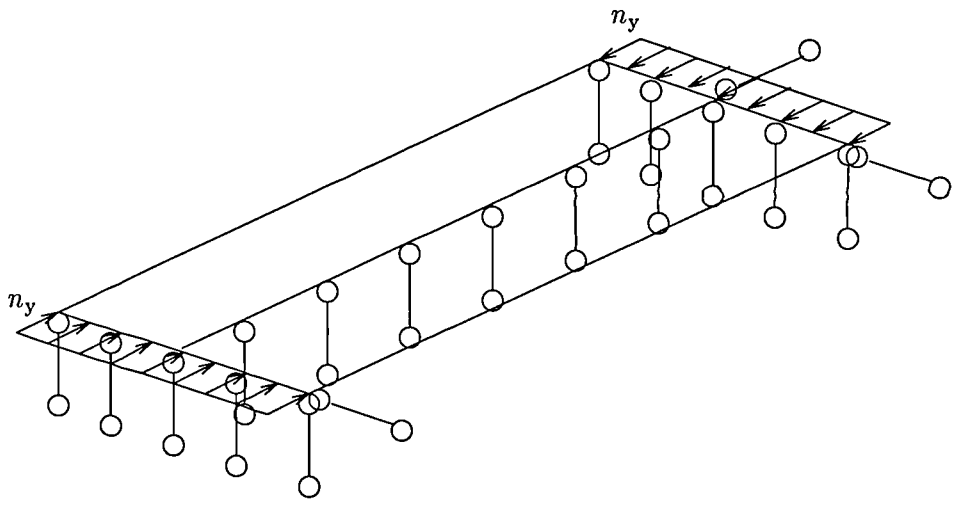

Figure 5.4: Boundary conditions for plate simply supported on three edges and free on one longitudinal edge.

was the same as in Section 5.1.4.1. The difference was in boundary conditions. The longitudinal centreline of the plate was supported in the direction perpendicular to the plate. The number of elements varied from 114 to 630 (see Table 5.2). Johnston's [28] elastic theory gives the elastic critical buckling stress for a plate

Model	Num. of elements	Num. of nodes	λ_b
PLATE–1	114	393	1.76715
PLATE–2	138	473	1.76501
PLATE–3	216	719	1.75923
PLATE–4	340	1109	1.75255
PLATE–5	630	2009	1.7447

Table 5.2: Models used in finite element analyses.

simply supported on three sides and free on one longitudinal side as:

$$\sigma_{cr} = 0.425 \frac{\pi^2 E}{12(1-\nu^2)} \left(\frac{t_f}{c}\right)^2 \tag{5.4}$$

where t_f and c are the thickness and outstand of a flange, respectively. For the given

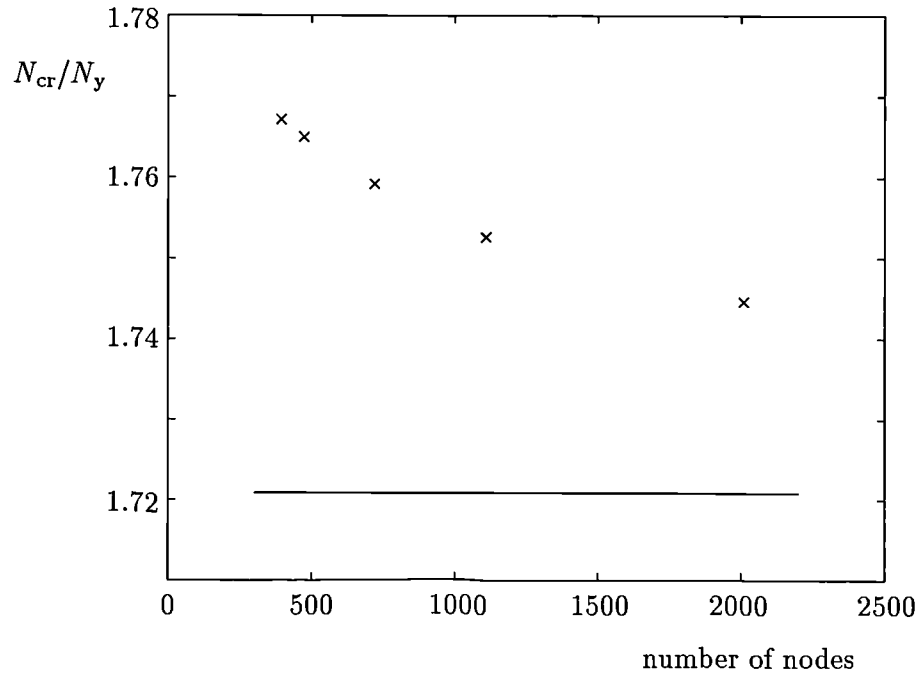

Figure 5.5: Elastic critical buckling force.

example (t_f = 8 mm, c = 100 mm, f_y = 300N/mm^2, E = 210kN/mm^2) and using eq. 5.4 the ratio σ_{cr}/f_y = 1.72085. Fig. 5.5 shows the relation between the finite element analysis and theoretical solution obtained from eq. 5.4. The points repre-

senting the finite element analysis create the curve, which tends to converge to the line representing the theoretical solution. The difference between the smallest value of critical buckling stress obtained from finite element analysis and the theoretical solution is only about 1.4% and it is on the safe side of the theoretical line.

For the finite element analysis of a compressed flange attached to a corrugated web, models with approximately 300 elements and 1000 nodes were used (with a similar geometry), which gives the uncertainty of the results up to about 2%, according to model PLATE–4.

5.2 Local buckling of a compressed flange attached to a corrugated web

5.2.1 Model creation

The design of a specimen for experimental study (explained later in Chapter 6) was the basis for the model for finite element analysis. The model consists from two flanges – one in compression the other in tension (see Fig. 5.6 (c)) and a corrugated web between the flanges which has three half–waves. The notation for the geometry of the model is shown in Fig. 2.1. It is listed in Table 5.3 and it is the same as the design of the geometry of specimen CW1 described in Section 6.2. The length of the model was 675 mm.

$b_{fc} = b_{ft}$	$t_{fc} = t_{ft}$	h_w	t_w	b	d	α
mm	mm	mm	mm	mm	mm	°
200	8	440	3	180	45	45

Table 5.3: Geometrical dimensions of the models used for finite element analysis.

Parabolic quadrilateral shell elements were used. The numbers of elements and nodes are given in Table 5.4. The different number of elements in tension and compression flanges was chosen to decrease the time for running the solution (see Fig. 5.6 (d)).

The boundary conditions are shown in Fig. 5.6 (b) and (c). The compression

	flanges		web	total
	tension	compression		
nodes	265	833	1124	2122
elements	76	254	351	681 + 4

Table 5.4: Number of elements and nodes in the model.

force was chosen as the yield force (estimated from yielding of the compressed flange assuming the steel with $f_y = 300$ N/mm^2). The membrane edge load on the compression flange was calculated as $n_y = 2400$ N/mm. In the laboratory the specimens were loaded by a combination of compression force and bending moment which

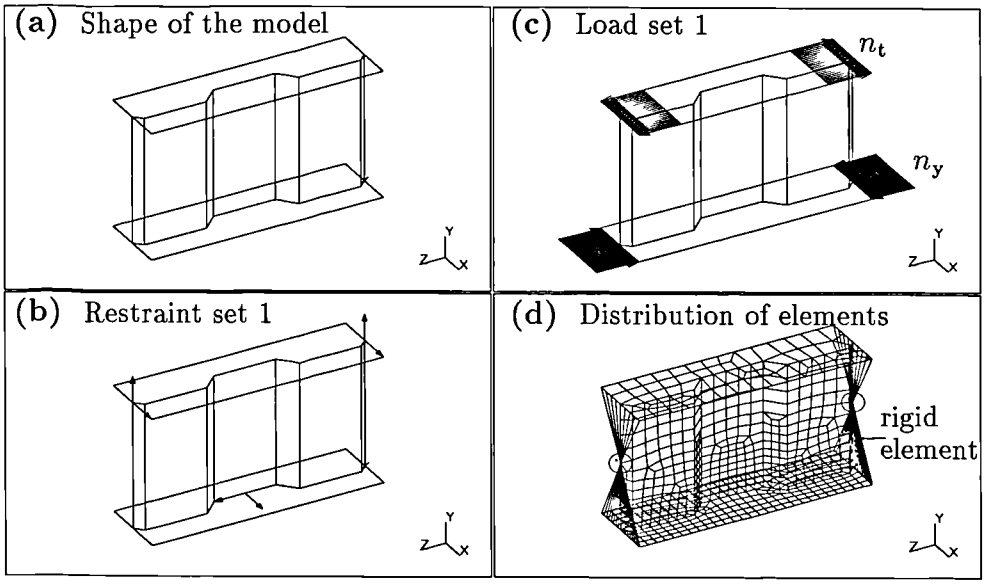

Figure 5.6: Model of test specimen.

moved the neutral axis towards the tension flange. To achieve approximately the same conditions in the computations, the longitudinal force applied to the tension flange was $n_t = -1735$ N/mm. This load set (named Load set 1) ensured that the loading of the model was applied as a combination of compression and bending (Fig. 5.6 (c)).

The ends of the test specimens were welded to 20 mm thick plates to avoid out–

of–plane deformation of end cross–sections. In finite element modelling, two models were created for the end plates. In Table 5.5 the line called 'Restraint set 1 — rigid elements' represents the model shown in Fig. 5.6 (d) where four rigid elements were placed in the planes of the end plates, connected to all nodes in the end cross–sections. The rigid element has no material and no physical properties. The existence of a rigid element implies that the motion of all the nodes on the element are to be related to each other as if they were connected by an infinitely rigid beam. The line called 'Restraint set 1 — shell elements' represents the modelling of the end plates by parabolic quadrilateral shell elements of thickness 20 mm with all material and physical properties.

The longitudinal plate stiffness (parallel to flanges) of a corrugated web panel is very small in comparison with its vertical plane stiffness (perpendicular to flanges). This assumption was checked by creating another load set, where the membrane edge load n_t would have arbitrary value. Say $n_t = 0$, so there is only the loading $n_y = 2400$ N/mm on the compression flange (Load set 2) on the same model. The buckling load factor should be the same for both of these load sets.

The same assumption enabled the creation of a model similar to the one in Fig. 5.4 and shown in Fig. 5.7 (a). Here the web and tension flange are omitted and only the compression flange is modelled. The restraints in the vertical (y–axis) direction simulate a corrugated web (Fig. 5.7 (b)). The advantage of this model compared with modelling the whole specimen is mainly in saving computing time, or in having a more accurate solution for the local buckling of the compression flange because finer mesh can be used for the same amount of computing time. The geometry of this model is the same as the geometry of the compression flange of the whole model.

Restraint set 1 (Fig. 5.6 (b)) for the whole model consisted of the three point restraints, which restricted rigid body movement, and had four rigid elements to keep the end cross–sections in one plane (Fig. 5.6 (d)). Restraint set 2 of the whole model included restraints for all nodes on the shorter edges of the compression flange in the y–axis direction, thus avoiding the usage of rigid elements or end plates modelled by shells (Fig. 5.8 (b)). So the restraint conditions were assumed to be the same as

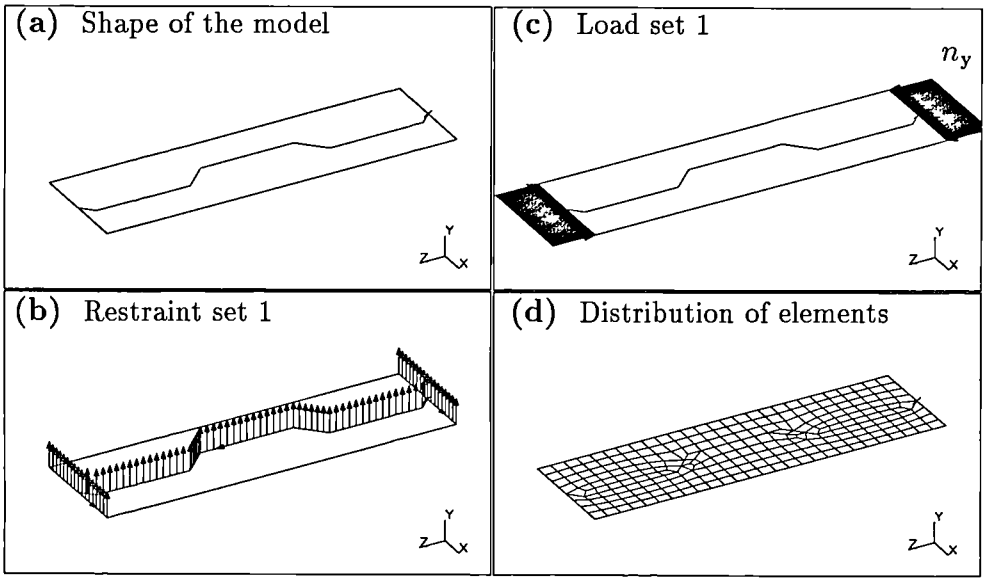

Figure 5.7: Model of compression flange.

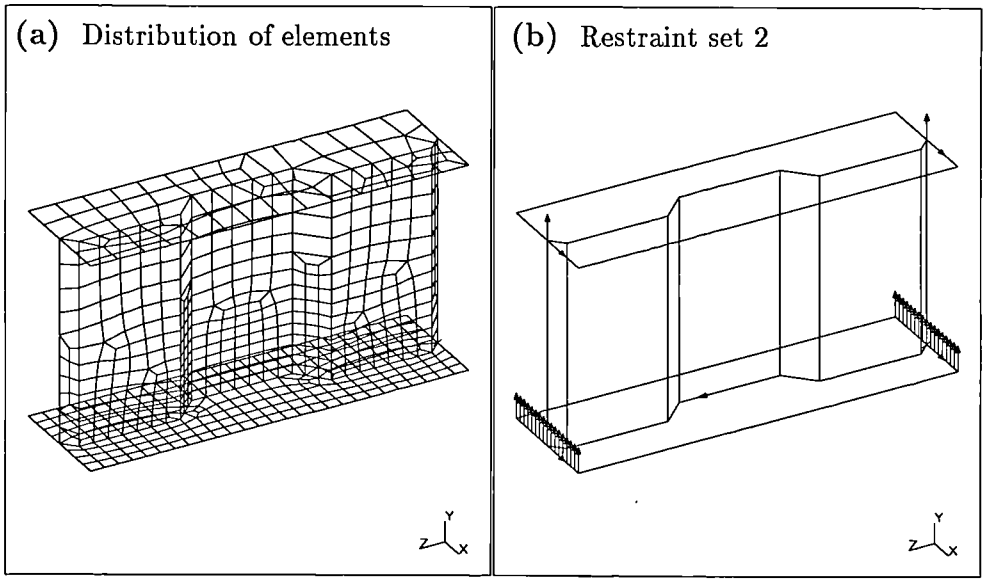

Figure 5.8: Omitted end plates.

for the Flange model (compare Fig. 5.7 (b) and Fig. 5.8 (b)).

The results – buckling load factors – of all the above mentioned analyses are given in Table 5.5.

	Whole model		Flange model
	Load set 1	Load set 2	
Restraint set 1 — rigid elements	2.701	2.707	—
Restraint set 1 — shell elements	2.703	—	—
Restraint set 2	2.320	—	2.372

Table 5.5: Buckling load factors of the models.

Let us assume Whole model and Restraint set 1 with rigid elements only loaded by Load set 1 and Load set 2. The difference is only about 0.2 %. That means that the position of the neutral axis has no influence on elastic critical buckling force of the compressed flange. The loading of the tension flange can be therefore omitted.

There is only 0.07 % difference between the solution given by modelling the end plates using the rigid elements and shell elements, which is negligible. For the buckling analysis it is more convenient to use the rigid elements, because they do not need any additional nodes, and the nodes connected to rigid elements have some of their degree of freedoms restrained by rigid elements. This decreased the total number of degrees of freedom and cut down the computation time.

Comparison of the two restraint sets modelled for the whole model (Table 5.5) gives a difference of 14.1 %. The solution of the model with restraint set 2 is closer to the solution of the flange model. The difference here is only 2.2 %. The reason is obviously in defining the boundary conditions. For the restraint set 1 the rigid elements restricted the rotation of the short edges of compression flange around the x–axis (this is not total restriction in rotation because it depends on rotation of the whole plane of end cross–section). Thus the first buckling mode gives the buckle in the middle of the compression flange with $\lambda_b = 2.701$. The restraint set 2 and the flange model have no such restriction. The rotation of short edges about the x–axis is possible. Thus buckles are more free to develop in either of the large outstand locations. The first buckling mode with value of $\lambda_b = 2.372$ developed the buckles in two side large outstands. For the buckling mode, where the buckle was developed

in the middle (the same as for the restraint set 1), the buckling load factor in the flange model was $\lambda_b = 2.749$, which is 1.7 % higher than the buckling load factor for the restraint set 1 in the whole model.

In real structures beams with a corrugated web will have web stiffeners (which could be represented by rigid elements) only in the cross–sections above the supports or under a concentrated load. They will have more corrugations than the three halfs modelled here. So the restraints considered in the models do not exactly represent the real situation. The restraint sets are considered to be the limiting states of a part of the real structure. That means that the real solution would lie between the results given by the whole model with the restraint set 1 and the flange model. Because the first one gives larger values of λ_b, the second one is more critical, and therefore was chosen for analyses of local buckling of the compression flange. Two per cent difference between the whole model with the restraint set 2 and the flange model is considered to be negligible.

5.3 Local buckling of a compressed flange

The following sections contains eight different sets of analyses where one geometrical dimension of the web is changed at a time. The buckling load factor is then found by finite element analyses.

5.3.1 Effects of changes in b

The wavelength of the buckling mode is fixed by the corrugations. The buckle is more likely to develop on the largest outstand of a flange. Therefore the influence of the change in width of a flat part of a corrugated web, b, was investigated here. The angle of the sloping part of a corrugation, α, as well as its projection on the longitudinal direction, d, were unchanged. Nor was the geometry of the flange changed, except its length, which depended on the width of a flat part of a corrugated web.

According to the theory developed by Easley and McFarland [11] the limiting value in choosing the range of b for investigation is given by the ratio $D_y/D_z > 50$, where D_y and D_z are a corrugated plate stiffnesses in the z and y directions,

respectively, given in Section 1.2.5 by eqs. 1.11 and 1.12. For $b = 0$ mm and the given geometry $\Rightarrow D_y/D_z = 63.28$, and for the maximum considered $b = 250$ mm $\Rightarrow D_y/D_z = 92.78$. Thus b was chosen within the limitations given by theory.

The models are listed in Table 5.6. The last three lines of Table 5.6 represent the

$b_f = 200$ mm, $\alpha = 45°$, $d = 45$ mm, $f_y = 300$ N/mm^2						
Set				**1** ($t_f = 8$ mm)	**2** ($t_f = 6$ mm)	
b	$\frac{b}{(b_f+d)/2}$	nodes	elements	λ_b	λ_b	A_{ratio}
mm	mm					
0	0	1053	328	5.304	3.124	0.113
50	0.408	931	288	4.044	2.396	0.153
100	0.816	991	306	3.075	1.811	0.172
120	0.980	976	301	2.874	1.670	0.177
150	1.224	1047	324	2.592	1.505	0.183
180	1.470	833	254	2.397	1.388	0.188
200	1.633	1044	324	2.281	1.318	0.190
220	1.796	1049	322	2.193	1.259	0.192
250	2.041	985	300	2.074	1.187	0.195
plane web models						
∞	$c_L = 122.5$ mm			1.491	0.839	
∞	$c_A = 100$ mm			2.237	1.258	
∞	$c_S = 77.5$ mm			3.725	2.095	

Table 5.6: Change in b.

large, average and small outstand of a flange assuming a plane web. The buckling load factors, λ_b, for these three cases were calculated from eq. 5.4. The graph which summarises these results is shown in Fig. 5.9. From this diagram it is obvious that with increasing value of b the buckling load factor decreases, so does the critical buckling load. The horizontal dashed lines represent the large, average and small outstand of a flange assuming a plane web (dashed for thickness 8 mm; dot–dashed for thickness 6 mm).

From the drawing the conclusion can be made that the design should be on the safe side if the small outstand of a flange is chosen for calculating the critical buckling load when the ratio $2b/(b_f + d) < 0.5$, and the large outstand has to be used for ratios $2b/(b_f + d) > 1.7$. In between those ratios the average outstand is

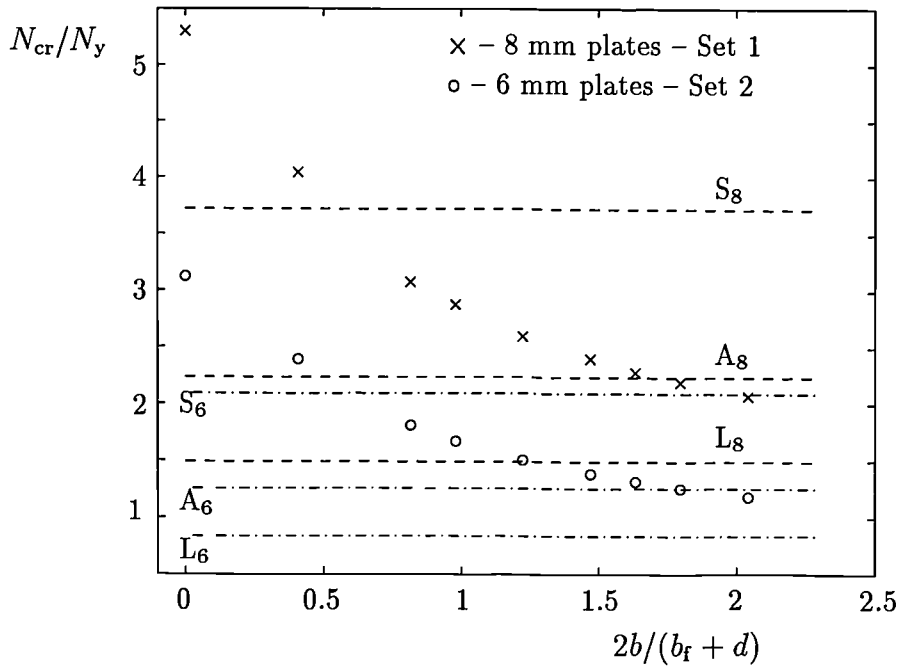

Figure 5.9: Change in b.

safe to use in design when finding the critical buckling load of a compression flange. This is valid for the angle of sloping part of a corrugated web $\alpha = 45°$.

The same analysis was performed with thickness of a flange $t_f = 6$ mm. The results are listed in Table 5.6 and plotted in Fig. 5.9. They give the same conclusion as the previous set of results.

5.3.2 Effects of changes in d

This section deals with the question, how big is an influence of change of the depth of a corrugation, $d \tan \alpha$, on the local buckling of a compression flange attached to a corrugated web.

The models were created on a base of the compression flange of specimen CW1. The value of d was 45 mm in the test. From this value d was decreased and increased, keeping b and α constant. The results are listed in Table 5.7 and they are plotted in Fig. 5.10.

The horizontal dashed line represents the average outstand of a flange where the

$b_f = 200$ mm $f_y = 300$ N/mm^2			$t_f = 8$ mm				
Set	d	D_z/D_y	$\frac{b}{(b_f+d)/2}$	nodes	elements	λ_b	A_{ratio}
	mm	mm					
	$b = 180$ mm ($b/b_f = 0.9$)		$\alpha = 45°$				
	20*	18.49	1.636	920	291	2.623	0.091
	30*	41.31	1.565	773	230	2.565	0.131
	45	91.92	1.469	833	254	2.397	0.188
3	60	161.62	1.385	444	131	2.218	0.240
	80	283.22	1.286	543	162	1.837	0.306
	100	436.51	1.200	587	176	1.518	0.368
	150	952.14	1.029	702	213	0.961	0.516
	200	1648.4	0.900	890	271	0.568	0.655
	$b = 180$ mm ($b/b_f = 0.9$)		$\alpha = 30°$				
	20*	6.14	1.702	533	160	2.408	0.053
	30*	13.66	1.657	821	252	2.395	0.076
	45*	30.45	1.593	549	164	2.340	0.108
4	60	53.56	1.534	655	198	2.230	0.139
	80	94.02	1.462	605	180	2.006	0.177
	100	145.25	1.397	729	220	1.722	0.213
	150	319.27	1.256	975	298	1.225	0.298
	200	557.31	1.141	989	300	0.909	0.378
	$b = 120$ mm ($b/b_f = 0.6$)		$\alpha = 45°$				
	20*	18.36	1.091	457	136	3.094	0.088
	30*	40.85	1.043	485	144	3.063	0.125
	45	90.42	0.980	642	195	2.895	0.177
5	60	158.21	0.923	637	192	2.522	0.225
	80	275.77	0.857	785	240	2.076	0.286
	100	423.17	0.800	825	252	1.718	0.344
	150	916.39	0.686	1023	314	1.108	0.482
	200	1580.59	0.600	919	282	0.685	0.615
	$b = 120$ mm ($b/b_f = 0.6$)		$\alpha = 30°$				
	20*	6.08	1.135	541	164	2.758	0.051
	30*	13.53	1.104	545	164	2.748	0.072
	45*	29.98	1.062	555	166	2.650	0.102
6	60	52.58	1.023	745	228	2.439	0.130
	80	92.03	0.975	710	215	2.118	0.165
	100	141.90	0.931	603	182	1.846	0.198
	150	311.08	0.837	741	224	1.330	0.278
	200	542.63	0.761	845	256	0.995	0.355

Table 5.7: Change in d.

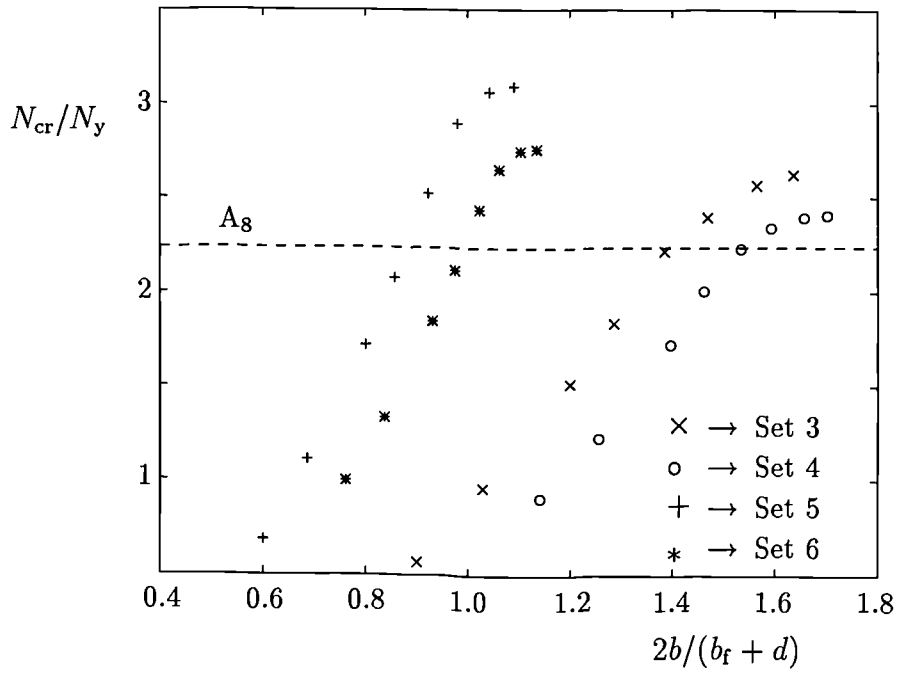

Figure 5.10: Change in d.

web is assumed to be straight. This value was taken from Table 5.6.

The models marked by an asterisk in Table 5.7 do not satisfy the requirement that $D_y/D_z > 50$ [11], but they are listed here to show the whole shape of the curves, which represent the ratio of buckling load factor and $2b/(b_f + d)$. They have no practical usage.

From Fig. 5.10 it is obvious that with increasing d, where b and α are constants, the buckling load factor decreases. The large and small outstands are changing here as well. Therefore the comparison is given only with the average outstand of a flange. It is not possible to define from Fig. 5.10 the values of the ratio $2b/(b_f + d)$ for which to use the large, average or small outstand in a design. However, in Section 5.3.1 it is suggested to use the average outstand in a design when $0.5 < 2b/(b_f + d\tan\alpha) < 1.7$, for $\alpha = 45°$. But according to Fig. 5.10 - Set 3 for $0.5 < 2b/(b_f + d\tan\alpha) < 1.4$ the average outstand would be unsafe. The ratio $2b/(b_f + d)$ is therefore not a suitable characteristic to define the safe usage of the average or small outstand in a design.

5.3.3 Effects of changes in α

The change in the angle of a sloping part of a corrugated web has a considerable influence on design. The practical range of angle α was estimated to be from 30° to 60°. In practice, the smaller the angle α, the less material is needed for manufacturing a corrugated web. $\alpha = 45°$ was chosen for most of the analyses and experiments made here, as the mean value of the given boundaries.

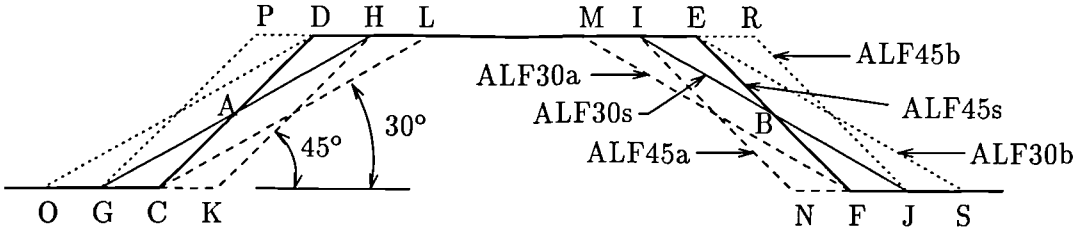

Figure 5.11: Change in α.

However, the research for α other than 45° was performed by computer analyses. The geometry of a compression flange was assumed to be the same (cross-section 8 mm × 200 mm). As a basis for the web geometry the one listed in Table 5.3 was used. It is represented by the thick line in Fig. 5.11 (ALF45s = CDEF). The

Moving line from → to	model	defining points
GH → CL JI → FM	ALF30a	CLMF
GH → OD JI → SE	ALF30b	ODES
CD → KH FE → NI	ALF45a	KHIN
CD → GP FE → JR	ALF45b	GPRJ

Table 5.8: Models for analysing the influence of α.

sloping parts are rotated around their mid-points (points A and B) to the position of $\alpha = 30°$ to create the model ALF30s (points GHIJ). From these two models all the others listed in Table 5.8 are created.

Thin shell parabolic quadrilateral elements were used again. Steel with estimated yield stress $f_y = 320$ N/mm^2 was considered in these analyses. The results are shown in Table 5.9. For the later comparison with the other analyses the results were recalculated for $f_y = 300$ N/mm^2 by the formula $\lambda_{b,300} = 320\lambda_{b,320}/300$.

Set 7 $b_f = 200$ mm $t_f = 8$ mm $d\tan\alpha = 45$ mm						
model	b	d	nodes	elements	λ_b	
	mm	mm				
yield stress in N/mm^2					320	300
ALF45a	147.05	45	762	233	2.464	2.628
ALF45s	180	45	833	254	2.247	2.397
ALF45b	212.95	45	935	286	2.087	2.226
ALF30a	114.12	77.95	723	220	2.032	2.167
ALF30s	147.06	77.95	821	250	1.945	2.075
ALF30b	180	77.95	908	277	1.890	2.016
plane web models						
$c_S = 77.5$ mm					3.492	3.725
$c_A = 100$ mm					2.097	2.237
$c_L = 122.5$ mm					1.398	1.491

Table 5.9: Change of α.

It may seem from Fig. 5.11 that after model ALF45a, which is the best design from the point of view of local buckling of a compression flange, model ALF30a would be considered as the second one. As Table 5.9 shows, it is not true. All three models with the angle of a sloping part of a corrugation $\alpha = 45°$ have the critical buckling load factor higher than the ones with $\alpha = 30°$. Comparing these results with the theoretical solution given by eq. 5.4 for large, average and small outstands listed in the last three lines of Table 5.9 leads to the conclusion that for all the above mentioned models with $\alpha = 30°$, the critical buckling load of a compression flange has to be based on the large outstand. A similar analysis, as in section 5.3.1, was performed for a corrugation with $\alpha = 30°$ to find the boundary for ratio $2b/(b_f + d\tan\alpha)$, which would lead to some design suggestions.

Set 8 in Table 5.10 differs from Set 1 listed in Table 5.6 in the value of $\alpha = 30°$,

Set 8 $b_f = 200$ mm $d = 77.95$ mm				$t_f = 8$ mm $\alpha = 30°$		
b	$\frac{b}{(b_f + d\tan\alpha)/2}$	nodes	elements	λ_b		A_{ratio}
mm						
yield stress in N/mm^2				320	300	
0	0	498	151	3.672	3.917	0.113
50	0.408	473	142	2.529	2.698	0.140
80	0.653	471	142	2.234	2.383	0.151
100	0.816	536	163	2.112	2.253	0.156
114.12	0.932	723	220	2.032	2.167	0.160
147.06	1.200	821	250	1.945	2.075	0.167
180	1.470	908	277	1.890	2.016	0.173

Table 5.10: Change in b.

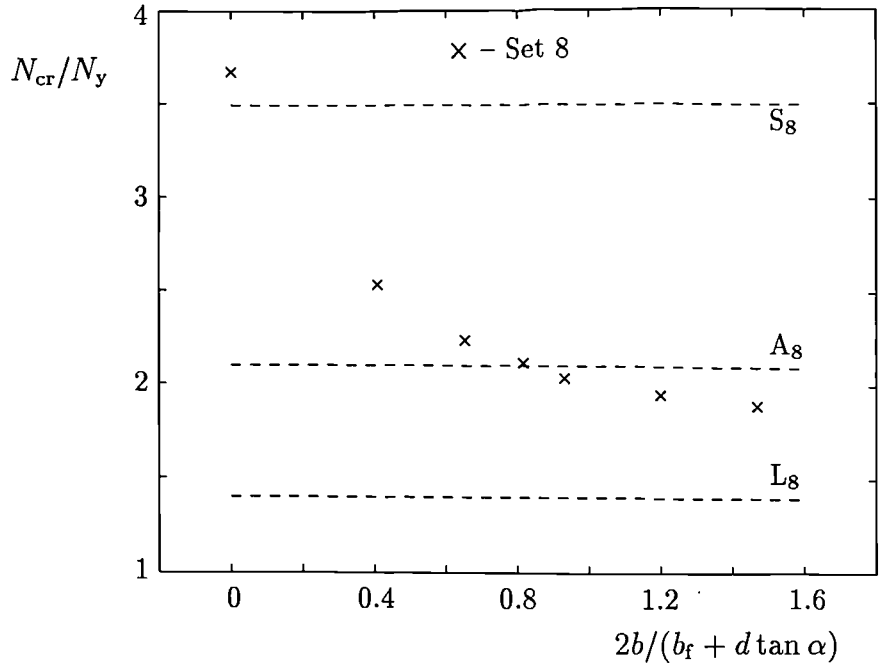

Figure 5.12: Change in b for $\alpha = 30°$.

rather than 45°. According to Fig. 5.12 a design of a compression flange attached to a corrugated web can be done based on an average compressed flange outstand if the ratio $2b/(b_f + d\tan\alpha) < 0.9$. A small outstand can be considered only where $2b/(b_f + d\tan\alpha) < 0.1$.

5.3.4 Overall results

In Sections 5.3.1, 5.3.2 and 5.3.3 one of the geometrical dimensions of the corrugated web was changing at a time. The results of each analysis were treated separately. The ratio $2b/(b_f+d\tan\alpha)$ was believed to characterise the geometry of the corrugated web. It is not suitable for comparison of all analyses together since each section gives a completely different result. Therefore it was necessary to find some other characteristic of the web shape, which can be used for all analyses to be plotted in one diagram.

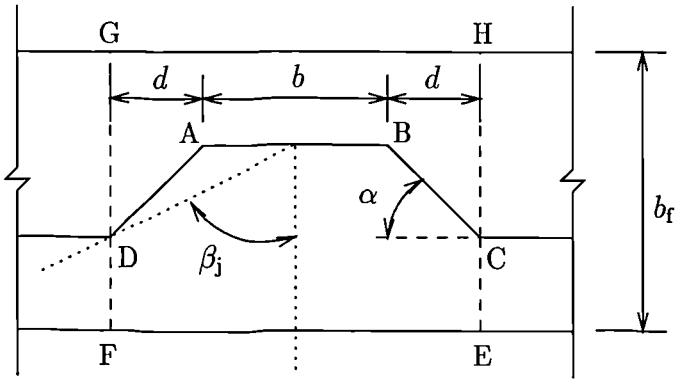

Figure 5.13: Shape of a corrugated web.

Several attempts were made to find the most appropriate ratio for the x axis. For example, $\tan\beta_j$ (see Fig. 5.13) or the ratio $(b + 2d\sec\alpha)/(b + 2d)$ gave rather disorganised diagrams, which did not lead to a single value which could be used in design. Although the ratio of the area ABCEFD to b_f results in a graph which put all the results approximately into one curve, it was not a possible basis for a design rule. This ratio was not non–dimensional, thus it would be probably different for structures of different sizes.

However, the idea of using the flange area cut by the corrugations of the web led

to the ratio

$$A_{\text{ratio}} = A_{\text{ABCD}}/A_{\text{EFGH}} = \frac{(b+d)d\tan\alpha}{(b+2d)b_{\text{f}}}. \tag{5.5}$$

Fig. 5.14 is plotted using the results of all analyses given in Sections 5.3.1, 5.3.2 and 5.3.3 except Set 7. Set 7 is partly included in Set 1 and Set 8 therefore its points

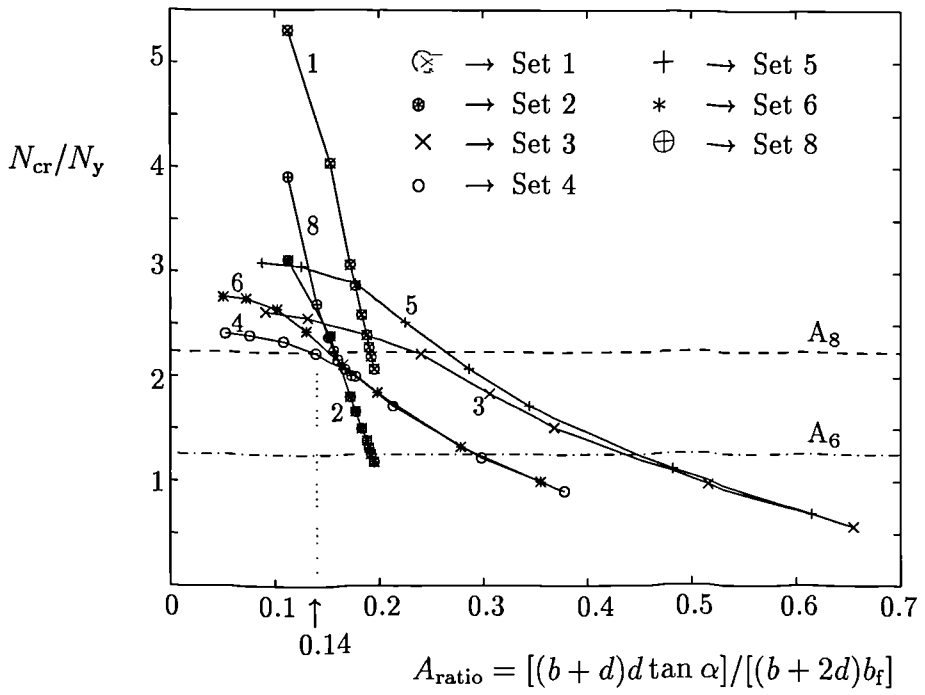

Figure 5.14: Local buckling of the compressed flange.

are not plotted in Fig. 5.14. The models of Sets 1,3,4,5,6,8 have the thickness of the flange $t_{\text{f}} = 8$ mm; for Set 2 $t_{\text{f}} = 6$ mm.

From Fig. 5.14 the intersections of the curves for each set with the line representing the buckling of the flange attached to a plane web with the average outstand were found and they are listed in Table 5.11. The minimum A_{ratio} suggests the

Set	1	2	3	4	5	6	8
A_{ratio}	0.191	0.191	0.236	0.14	0.262	0.167	0.162

Table 5.11: Intersections of the set curves with the line for the average outstand.

limiting value. The design of the flange for buckling will be safe using the average

outstand when $A_{\text{ratio}} < 0.14$. This condition is in good agreement for Sets 4,6,8 where $\alpha = 30°$, and it is conservative for Sets 1,2,3,5 where $\alpha = 45°$. This is understandable, because for larger α the sloping part of the corrugation provides larger restraint against buckling and decreases the buckling wavelength.

5.4 Summary on local buckling

Elastic buckling solver of I-DEAS software for finite element analysis was used. Eight different sets of the analyses were compared and as the result, the ratio A_{ratio} defined by eq. 5.5 was found which suggests that if $A_{\text{ratio}} < 0.14$ than the average outstand of the compressed flange attached to a corrugated web can be safely used when designing for local buckling. This conclusion is conservative for $\alpha > 30°$ and it would be unsafe for $\alpha < 30°$. In a design α will not be less than 30°, because of the condition made for plate stiffnesses: $D_y \gg D_z$.

The extreme situations for the ratio A_{ratio} would be as follows:

1. $A_{\text{ABCD}} = 0 \Rightarrow A_{\text{ratio}} = 0$ which is less than 0.14, thus the flange will be treated for average outstand which is in agreement, because when $A_{\text{ABCD}} = 0$ then web is plane. This can happen when either $\alpha = 0$ or $d = 0$. For $\alpha = 0$ the web is plane. For $d = 0$ and $\alpha \neq 0$ then the sloping part of the corrugation is perpendicular to b and $\alpha = 90°$. In this case the numerator of eq. 5.5 has to be really $b \times d'$ where d' is the perpendicular distance between the flat parts of the corrugations. From this condition either $b = 0$ or $d' = 0$. b can not be 0 for $\alpha = 90°$. If $d' = 0$ the web is flat.

2. $A_{\text{ABCD}} = A_{\text{EFGH}} \Rightarrow A_{\text{ratio}} = 1$. This can only happen when $d = 0$, $\alpha = 90°$ and $d' = b_f$. This is a situation when the buckling wavelength is equal to b and the flange has to be treated for the large outstand $c_L = b_f$ which does agree with the above condition.

Chapter 6

Tests on plate girders with corrugated webs

6.1 Introduction

By localising the problem to be studied, the designs of the test rig and specimens were simplified. The object was to study a behaviour of a compression flange in bending when it is a part of a continuous composite beam with a corrugated web.

Fig. 6.1 shows a part of a typical continuous beam at an internal support, where the negative bending moment may cause local buckling of the bottom flange.

It is assumed that the corrugated web does not contribute to resisting the bending moment, and that the flange does not contribute to resisting the shear force. Therefore the design of the loading for the first two specimens (CW1 and CW2) was aimed to subject them to pure bending and compression . The following three specimens (CW3 to CW5) were loaded by a combination of bending, compression and shear. For simplicity of writing the combination of compression and bending in specimens is referred as bending only.

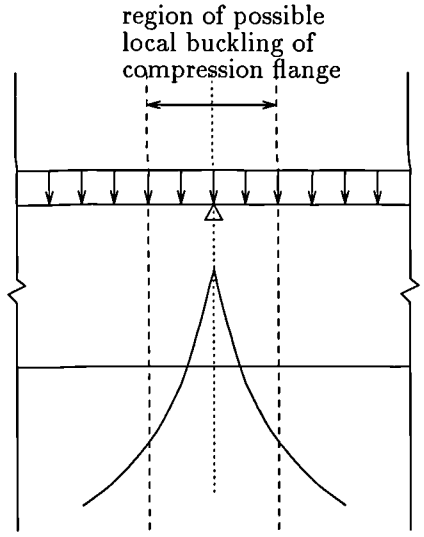

Figure 6.1: Bending moment above the internal support.

6.2 Design of the test specimens

Specimens CW1 to CW3 were fabricated by Rowecord Engineering, Newport, and CW4 and CW5 by Cleveland Structural Engineering, Darlington.

6.2.1 Specimen CW1

From the study of the work done on corrugated webs and panels ([3, 10, 11, 43]) the geometrical dimensions of the corrugated web were chosen so that the following ratios are within the ranges given, where the symbols are as in Fig. 2.1:

- $d/t_w = (5; 30)$
- $b/t_w = (30; 80)$
- $h_w/t_w = (200; 500)$
- $\alpha = (30°; 60°)$

To be able to weld the web to the flanges the minimum thickness of the web was taken as $t_w = 3$ mm for all specimens. From the above ratios the following dimensions were chosen:

- $d/t_w = 15 \Rightarrow d = 45$ mm
- $b/t_w = 60 \Rightarrow b = 180$ mm
- $\alpha = 45°$

For the minimum h_w/t_w ratio, and to minimise the amount of steel used, h_w should be approx. 600 mm. But the system of loading the specimen, which is described in Section 6.4, applies bending in a way which moves the neutral axis closer to the tension flange. The effect on the compression flange was chosen to be the same in this set up, as it would be for $h_w = 600$ mm in pure bending. This allowed h_w to be reduced to 440 mm.

Two of the bridges already built in France have web thicknesses between 8 mm and 12 mm, and the thickness of flanges between 25 and 50 mm. For the present specimen the thickness of the flanges, t_f, was chosen to be 8 mm, to give a similar ratio.

Design of the flange width was based on the EC3 classification [55] of the cross-section for class 3/4 boundary assuming a plane web in the middle of the flange. The ratio $c/t_f \leq 14\epsilon$, where $\epsilon = \sqrt{235/f_y}$. Taking $f_y = 300$ N/mm^2, the outstand of the flange will be $c = 99$ mm. Hence $b_f = 2 \times c + t_w + 2\times$ weld $= 2 \times 97 + 3 + 2 \times 3 = 207$. So the width was chosen to be 200 mm.

To resist warping of the end cross-sections of the specimens the two end plates were designed with a thickness of 20 mm. The remaining dimensions of the end plates were chosen to suit the design of the test rig, as described in Section 6.3.

To minimise the heat input to the weld needed between the web and the flanges, an intermittent fillet weld of 3 mm thickness was used (Fig. 6.2).

The final shape of the specimen can be seen in Fig. 6.12.

6.2.2 Specimen CW2

Only one variable was changed for the next specimen. Because the maximum load in specimen CW1 was close to its yield load, which was estimated from an assumed yield stress ($f_y = 300$ N/mm^2) by elastic theory, it was decided to make the com-

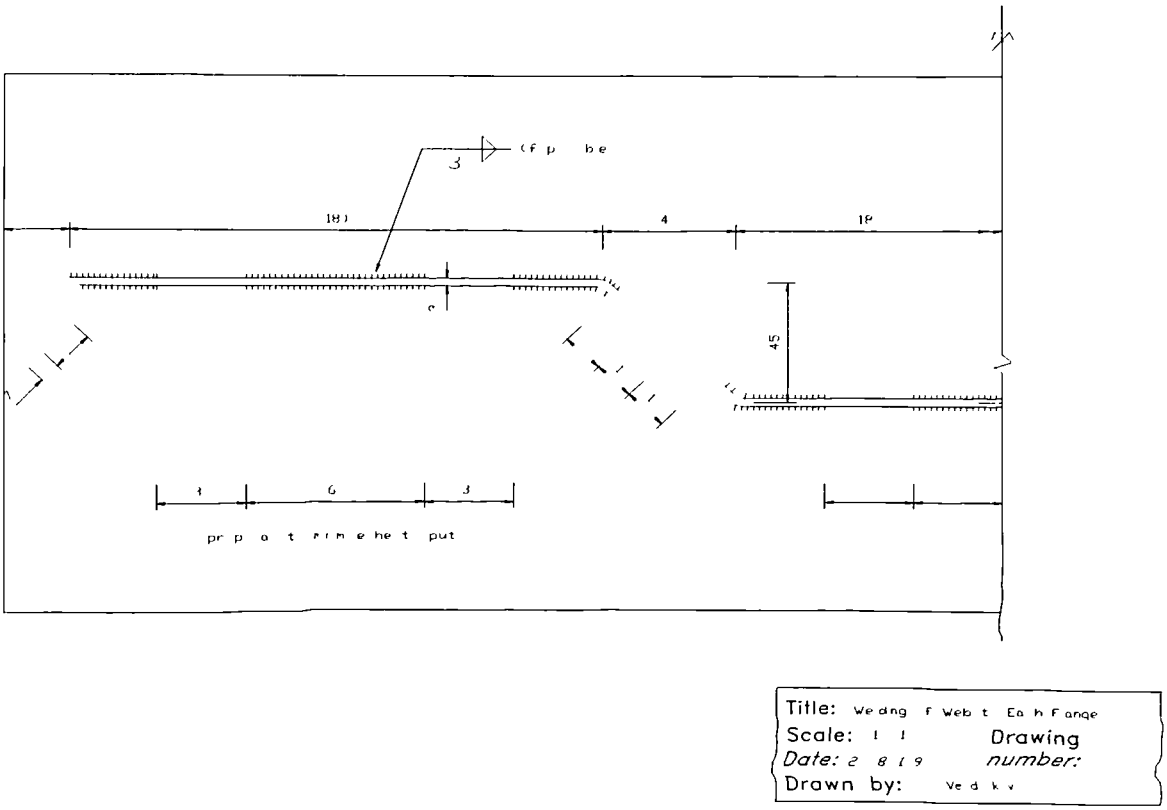

Figure 6.2: Weld design between web and flanges for specimens CW1 and CW2.

pression flange more slender. Its thickness was chosen to be 6 mm.

6.2.3 Specimens CW3, CW4, and CW5

Since the height of the specimens was fixed by the dimensions of the re–usable end plates, placed between a specimen and the main beams of the test rig (for its description see Section 6.3), as shown in Figs. 6.4 or 6.5, the remaining possible variables were the width and thickness of the compression flange and the geometry of the web corrugation. The web thickness as well as the angle of the sloping part of the corrugation were chosen to be constant for all tests, to minimise the number of variables.

The first test, CW1, showed the effect of local buckling of the flange on the web. Its flat part was deformed by bending caused by the rapid increase of flange deformation after buckling. The question arose whether there would be some interaction between local flange buckling and shear buckling of the web. Therefore it was decided to introduce shear loading (described in Section 6.4) for specimens

CW3, CW4, and CW5.

The width of the flat part of each web corrugation was changed from 180 to 250 mm to enable observation of any differences in local buckling of the compressed flange caused by this change.

The flange thicknesses for specimen CW3 were $t_{fc} = t_{ft} = 8$ mm (as specimen CW1). Specimen CW4 had $t_{fc} = 6$ mm and $t_{ft} = 8$ mm (as specimen CW2).

Design of specimen CW5 was based on the geometry of CW4 with the aim of changing only one geometrical dimension of the web. To study the influence of the depth of a web corrugation on local buckling of the flange, d was changed from 45 mm to 63 mm ($b/(d\tan\alpha) = 4$ for CW1 and CW2; $b/(d\tan\alpha) = 3.96$ for CW5).

The weld between web and flanges for specimens CW3, CW4, and CW5 was designed as continuous because of the presence of the shear force.

6.3 Test rig

The general arrangement of the test rig for specimens CW1 and CW2 is shown in Figs. 6.3 and 6.4. Two beams 533 × 210 UB × 82 of overall length 3120 mm (ap-

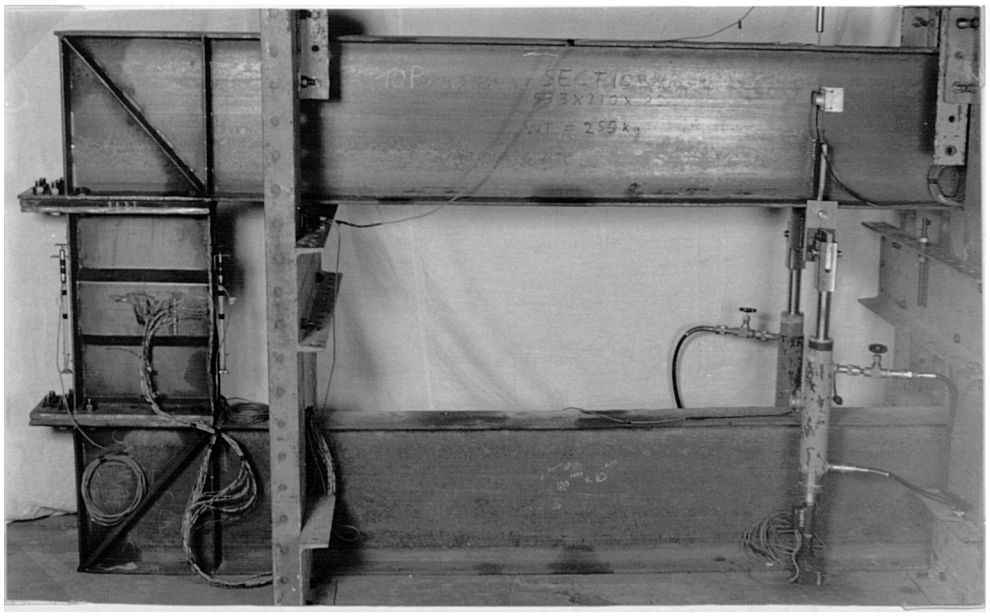

Figure 6.3: Test CW1.

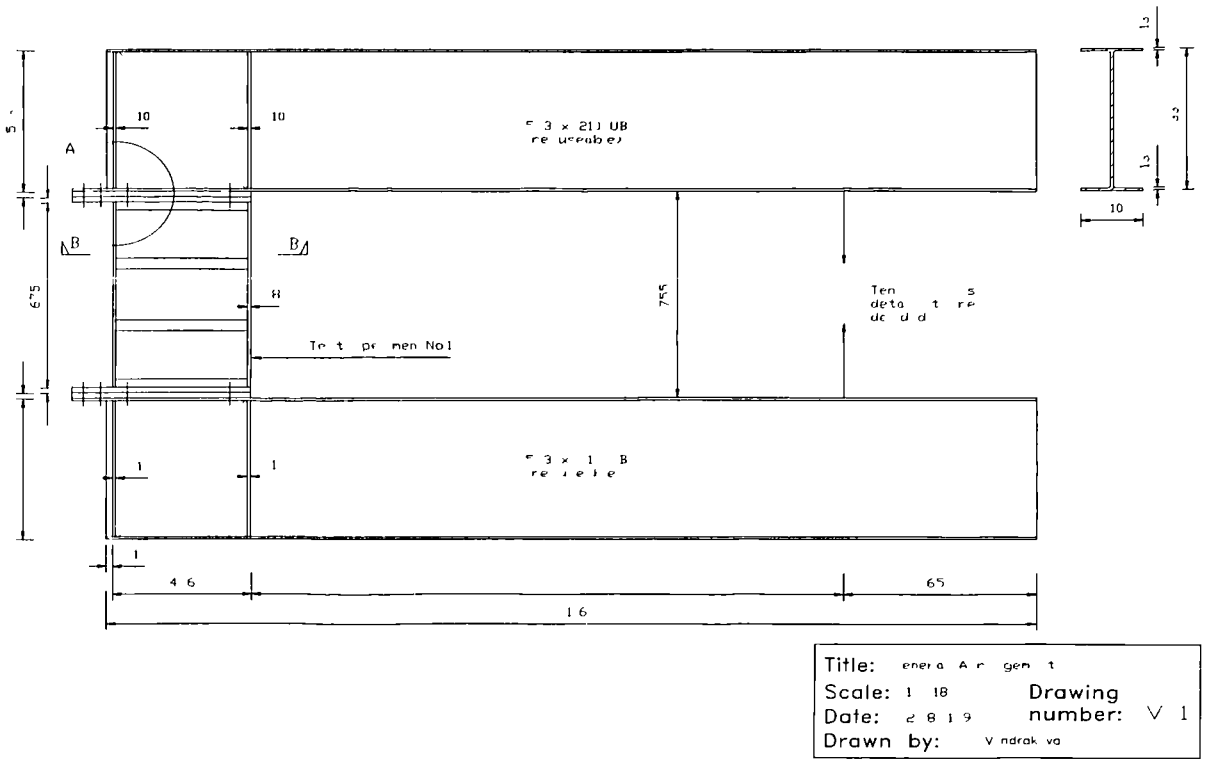

Figure 6.4: General arrangement of tests CW1 and CW2.

prox.) were used. They were pulled together near one end, which creates a combination of bending moment and compression in a specimen. Fig. 6.5 shows the connection between the test specimen and the two beams through the end plates. Their dimensions were chosen slightly larger than needed for test CW1, for possible re-usage for future tests which may need higher loading. The same reason applied to the overall length of the two beams (650 mm was left beyond the location of the tension jacks) and to the design of the bolts connecting a specimen to the beams. The assumed load for design of the test rig was chosen as 2.0 times that needed for the first test.

The shear loading of the specimens CW3, CW4, and CW5 was added as shown in Fig. 6.6.

To avoid lifting and sliding of the bottom beam in the test rig, it was necessary to fix it to the strong floor. The detail of this is shown in Fig. 6.7. Additionally a stop was put at the other end of the bottom beam to prevent its sliding.

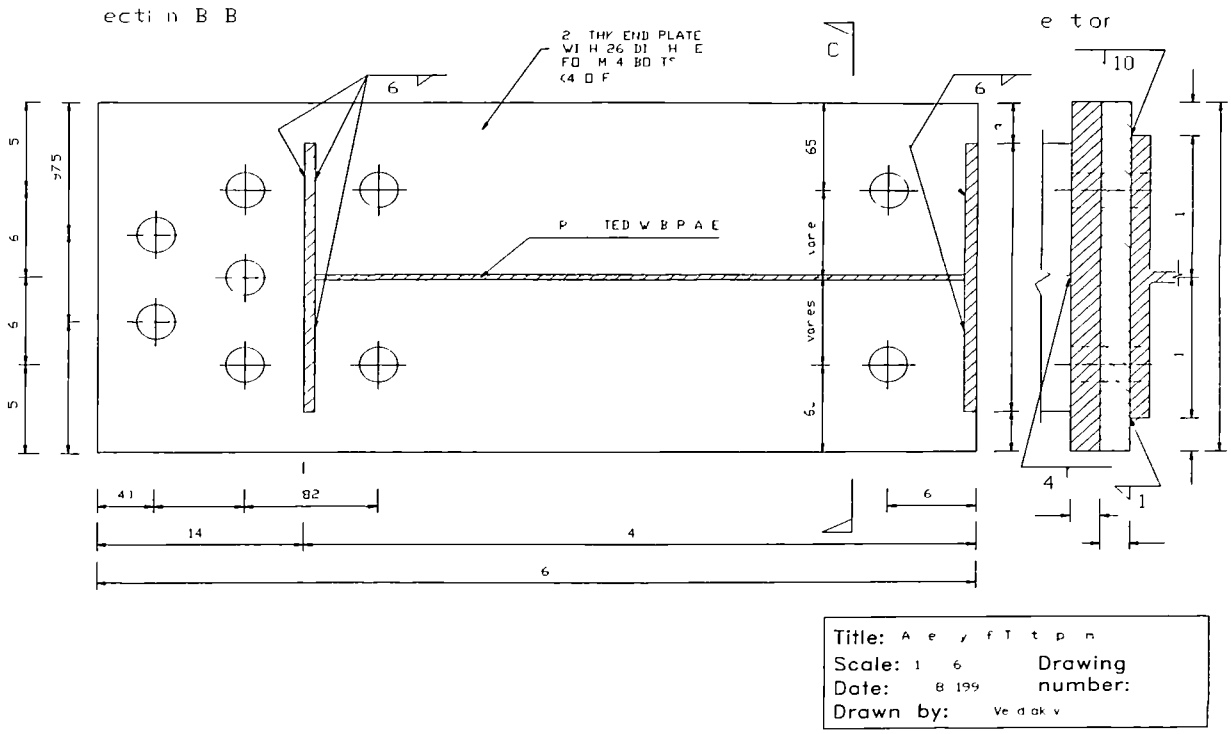

Figure 6.5: Assembly of test specimen to two beams.

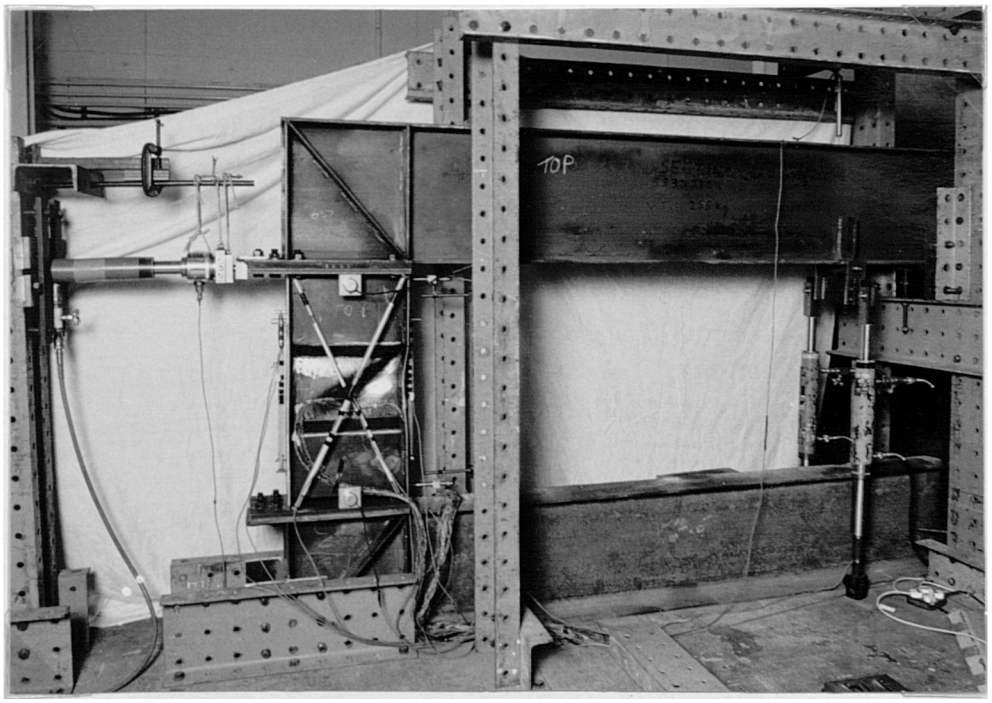

Figure 6.6: Test CW4.

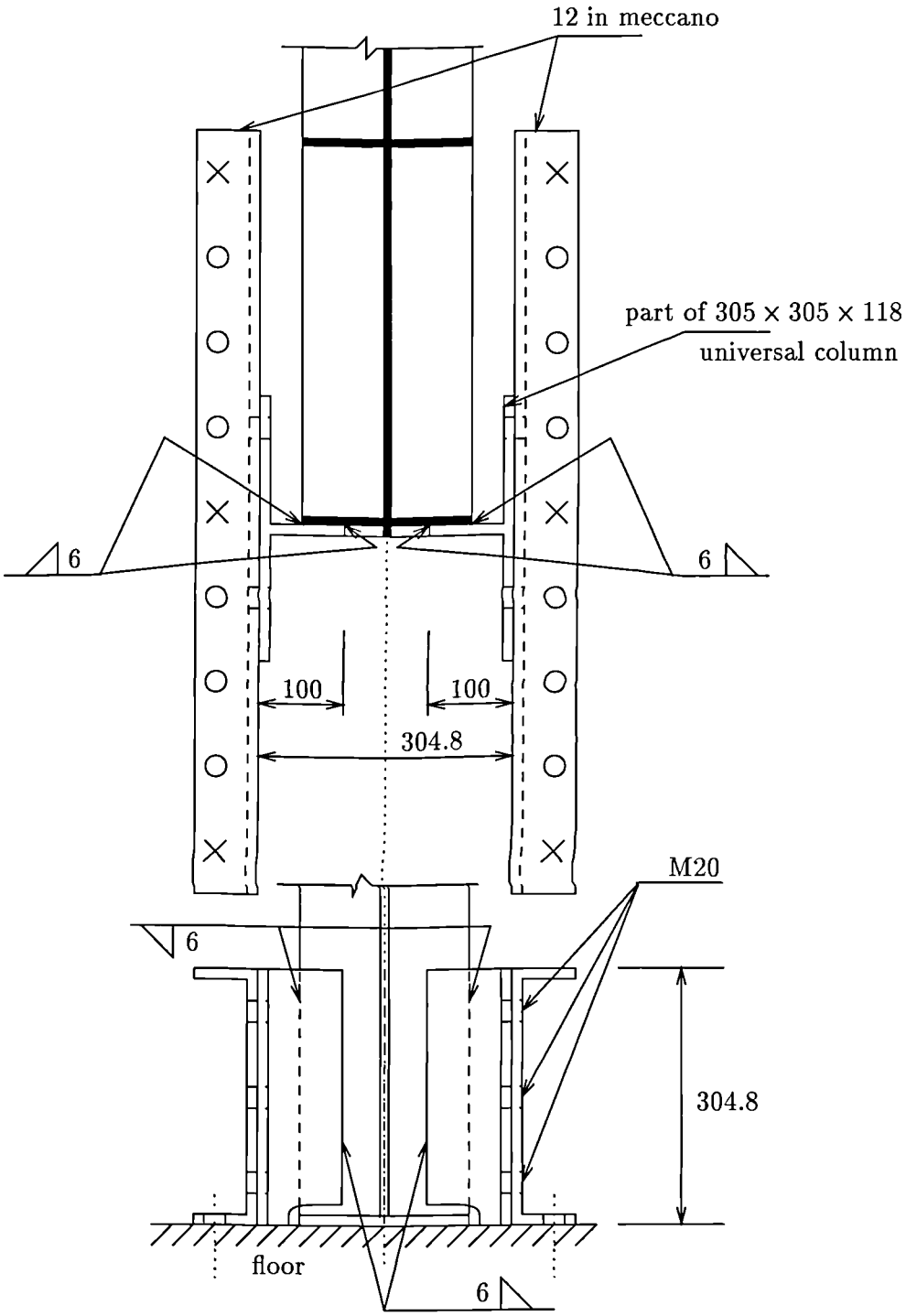

Figure 6.7: Detail of fixing the bottom beam to the floor.

6.4 Loading the specimens

Two 10–tonne tension jacks were available. This enabled the distance between the load point and the nearer face of a specimen to be chosen. Considering the simplified equilibrium of forces acting on the upper beam, shown in Fig. 6.8, and assuming force C_{pr} to be double the yield force for the compression flange, the dimension l

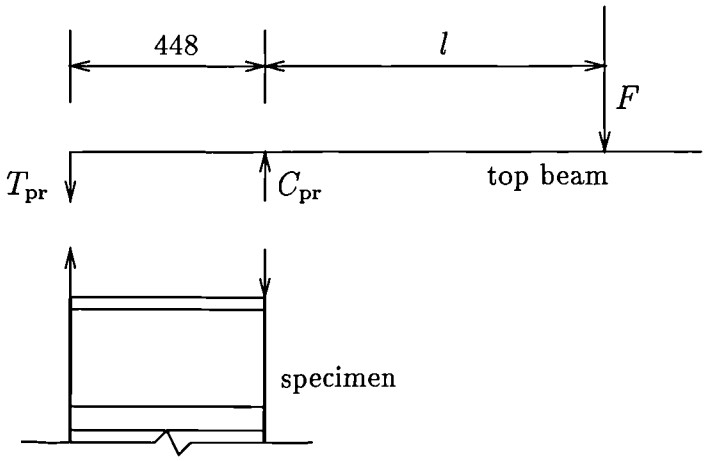

Figure 6.8: Simplified forces acting on the upper beam.

was chosen as 2000 mm.

Details at the tension jacks are shown in Fig. 6.9. The design enables longitudinal and transverse rotation of the top beam to occur. The pieces shown in Fig. 6.9 were designed for the maximum possible load from the jacks which was 180 kN (limited by load cells). The joint between each jack and the floor included a ball joint.

The expected maximum value of load for specimen CW2 was about 70 kN. Therefore it was more accurate to change the load cells from 9–tonne ones to 4.5–tonne. Additional shear in specimens CW3, CW4, and CW5 also created bending in the specimens, so there was no need for bigger load cells and the 4.5–tonne ones were re–used.

For applying the shear force a 25–tonne compression jack and load cell were used. The detail at the point of application of the shear force (the attachment between the end plates of a specimen and the top beam) is shown in Fig. 6.10.

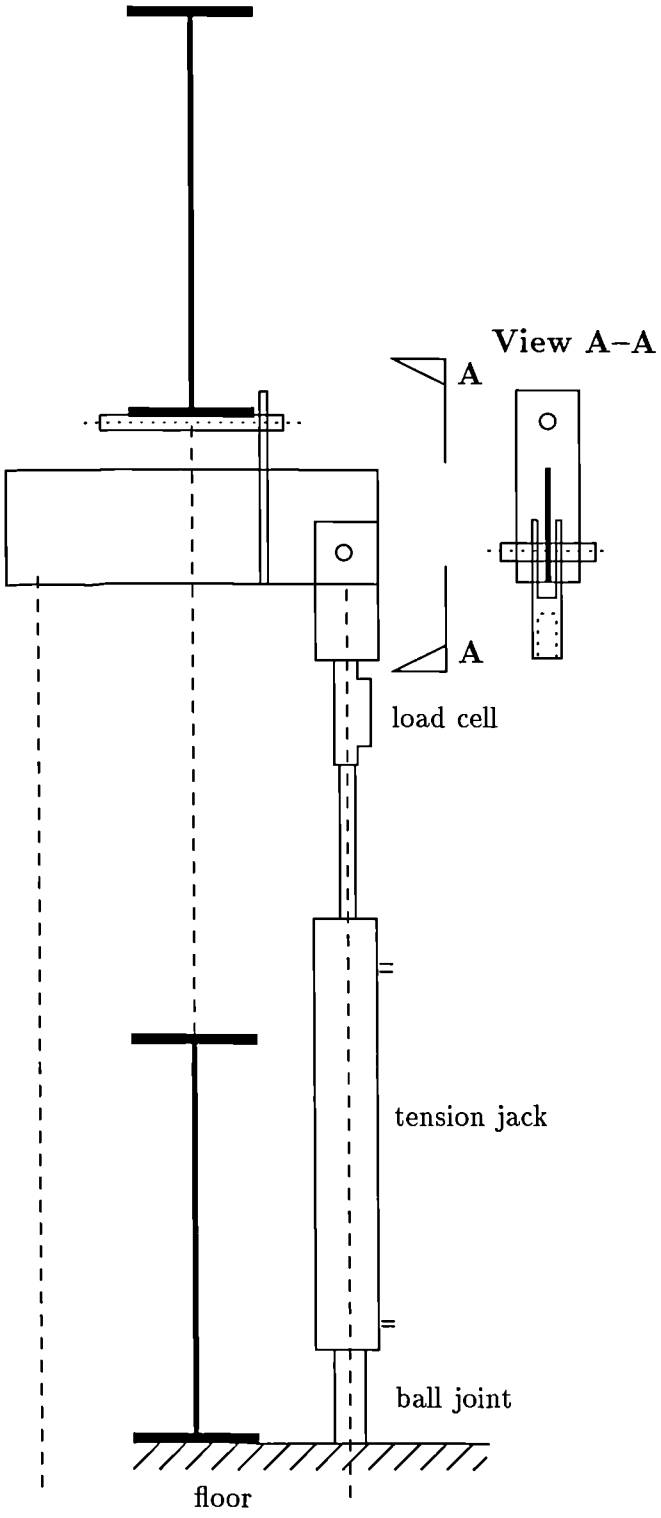

Figure 6.9: The arrangement for loading the upper beam.

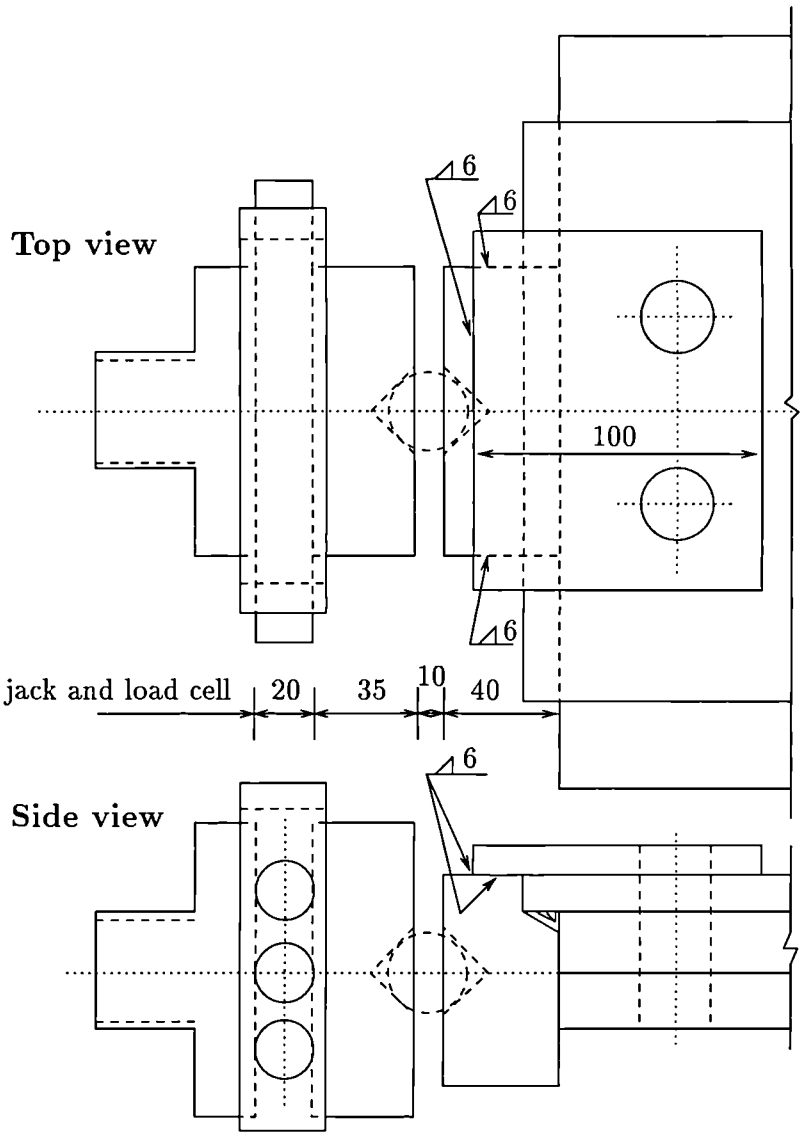

Figure 6.10: Detail of applying the shear force.

6.5 Instrumentation

6.5.1 Load cells

The load was measured using strain gauge load cells (LC):

- two 9–tonne LCs type EM50MR for test CW1
- two 4.5 tonne LCs type DS600 for tests CW2, CW3, CW4, and CW5 on the *bending* side
- 25–tonne LC type 403 for tests CW3, CW4, and CW5 on the *shear* side

The 9 tonne LCs and 4.5–tonne LCs were calibrated on a 40–tonne Amsler testing machine and a Tensometer 'E', respectively. Both of them have a precision ± 0.1 % as it is given in their specifications. Linear regression of calibration curves gave the correlation coefficients above 0.99.

The 25–tonne LC was calibrated on a Denison 300T testing machine for the range 0 to 250 kN, and on a Tensometer 'E' for the range 0 to 100 kN. The expected maximum load was up to 200 kN for all tests, where the LC was used, therefore only the first calibration curve was used. Its linear regression gave the correlation coefficient above 0.99. The specification of this LC declares the accuracy to be better than 0.25 % of the applied load.

It was not possible to perform the equilibrium checks after the tests, because the strong floor was involved in restraining the loads. Re–calibration of the LCs was done after the last test and it showed negligible change.

6.5.2 Linear variable displacement transducers

Shortening of the compression flange and extension of the tension flange were measured by linear variable displacement transducers (LVDT). The compression LVDT (compr in Fig. 6.11) was fixed to the compression flange on its centreline, while the tension LVDTs (tensA and tensB in Fig. 6.11) were attached to the flange near its edges (see also Figs. 6.6, or 7.12, or 7.13 in Section 7.4.1.2).

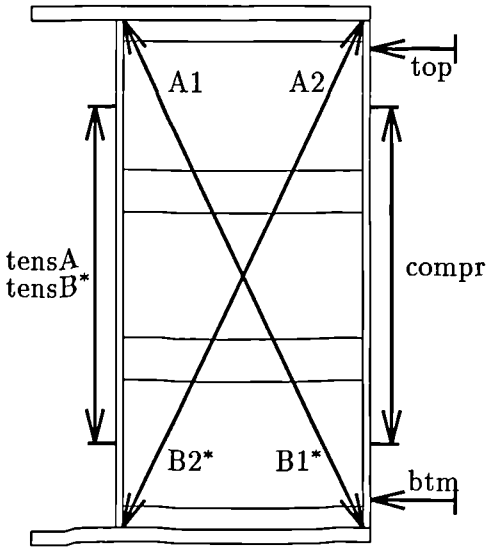

* – LVDTs are on the back side

Figure 6.11: Placing of the LVDTs on the specimens.

For the tests CW1 and CW2 the compression and two tension LVDTs were the only ones attached to the specimens. All three of them were of type HS25 with the non–linearity given in their specification as 0.1 % FS (full scale).

In order to determine the shear strain for specimens CW3, CW4, and CW5, diagonal LVDTs were placed on both sides of the specimens (in Fig. 6.11 the numbers 1 and 2 indicate LVDTs in compression and tension respectively; the letters A and B indicate the sides of a specimen). In test CW3 they were fixed to the inside surface of flanges, which was found to be unsatisfactory, because once the compression flange yielded, the glue used for fixing was not strong enough, and the compression LVDTs, labelled by A1 and B1, dropped off at the bottom corner of the specimen. For the following two tests they were attached to the end plates. All four of them were of type HS50 with non–linearity 0.1 % FS.

The horizontal displacement of the specimens along the test rig beams was measured in tests CW4 and CW5 only. It was decided to add these two LVDTs of type HS50 (top and btm in Fig. 6.11) to check the shear strain obtained from the diagonal measurements.

The calibration of each of the LVDTs was done three times over a range 0 to

10 mm and the mean values of three measurements were considered for defining the calibration curve. The correlation coefficient in all cases was above 0.99.

An LVDT of type HS100 was used to measure the vertical displacement of the top beam above the tension jacks (see Figs. 6.3 or 6.6). The non–linearity of this LVDT was 0.2 % FS. The calibration was done over a range 10 to 90 mm and the correlation coefficient was above 0.99.

Before every test all LVDTs were checked by slip gauges.

6.5.3 Clinometers

The possible rotation of the two loading beams about their longitudinal axis due to asymmetry of a specimen web was measured by two Accustar electronic clinometers placed in the vertical plane of loading on both top and bottom beams (see Fig. 6.3) in tests CW1, CW2, and CW3 only. Because there was no significant rotation of the loading beams observed, the clinometers were replaced and they were located on the top and bottom end plates as shown in Fig. 6.6.

The specification give the repeatability of 0.05° and non–linearity $\pm 0.1°$ over a range 0 to 10°. The clinometers were calibrated over a range of 0 to 3° and the correlation coefficient exceeded 0.99.

6.5.4 Strain gauges

For specimens CW1 and CW2 only, post–yield strain gauges type YL–20 placed on the compression flange measured the strains near the predicted buckling places. Two strain gauges of type PL–20 were placed in the middle of the flat part of the corrugated web on both sides (Fig. 6.12) to check if the stresses were zero, as expected.

The positioning of strain gauges for tests CW3 is shown on Fig. 6.13 and for tests CW4 and CW5 on Fig. 6.14. The gauges were of type :

- YL–20: SG1, SG3, SG27
- PL 20: SG5, SG29, SG31, SG19, SG33, SG35

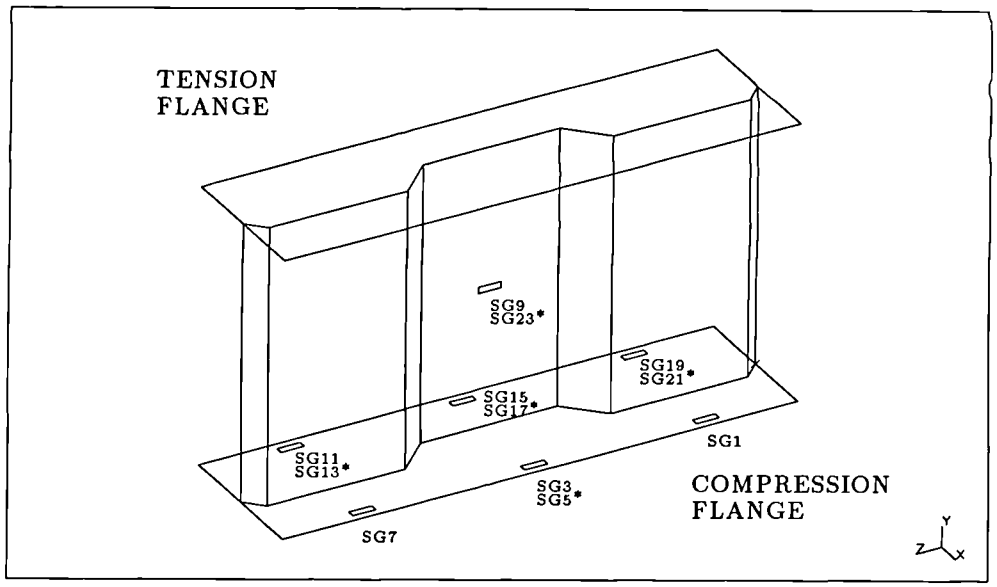

* strain gauges are on back side

Figure 6.12: Strain gauges for tests CW1 and CW2.

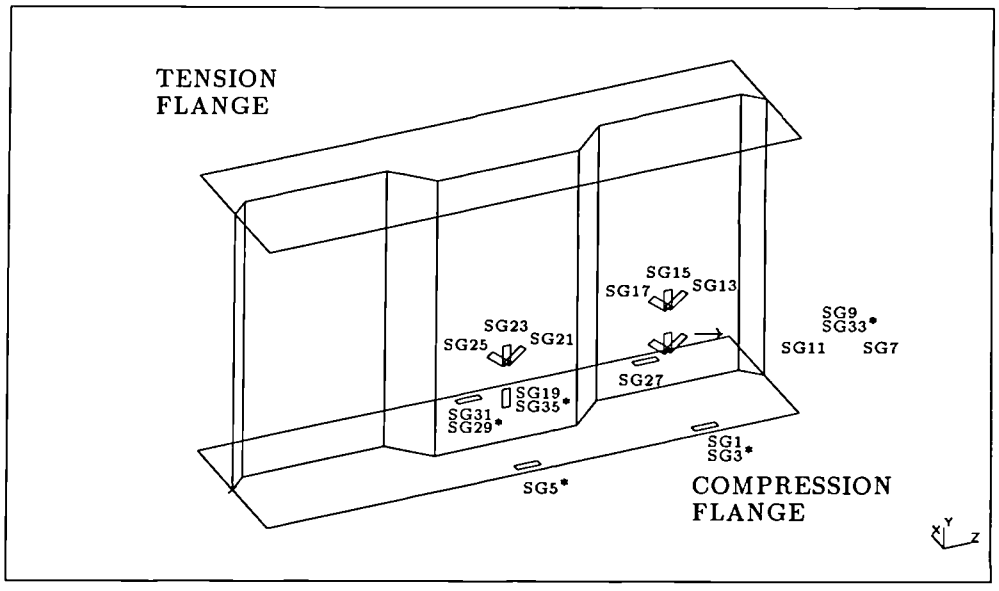

* strain gauges are on back side

Figure 6.13: Strain gauges for test CW3.

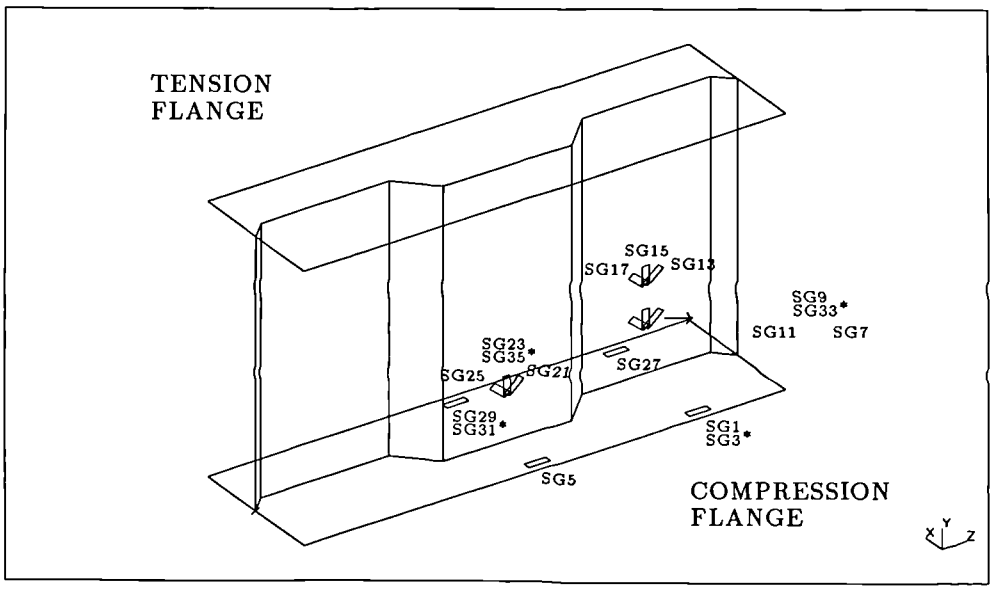

* strain gauges are on back side

Figure 6.14: Strain gauges for tests CW4 and CW5.

- PRS–10: SG7–9–11, SG13–15–17, SG21–23–25

6.6 Testing procedure

6.6.1 Tests CW1 and CW2

Each of the tests CW1 and CW2 was carried out within two days. The bending loading of the top beam was done simultaneously from two jacks in order to ensure that the top beam was pulled down vertically. In the elastic region a constant load increment of 5 kN was used. When the inelastic range was reached, the load was controlled mainly by the displacement of compressed flange, with increments of about 0.1 mm. Readings were taken immediately after applying the load and, in the inelastic phase, after a few minutes, when the rate of reduction of the load was less than 0.5 kN per minute. The test was stopped when the load had fallen to approximately 80 % of the maximum load. The specimens were then gradually unloaded.

6.6.2 Test CW3

Three days were needed for the test on specimen CW3. It was loaded with alternate increments on the *bending* jacks and the *shear* jacks. Fig. 6.15 shows the variation

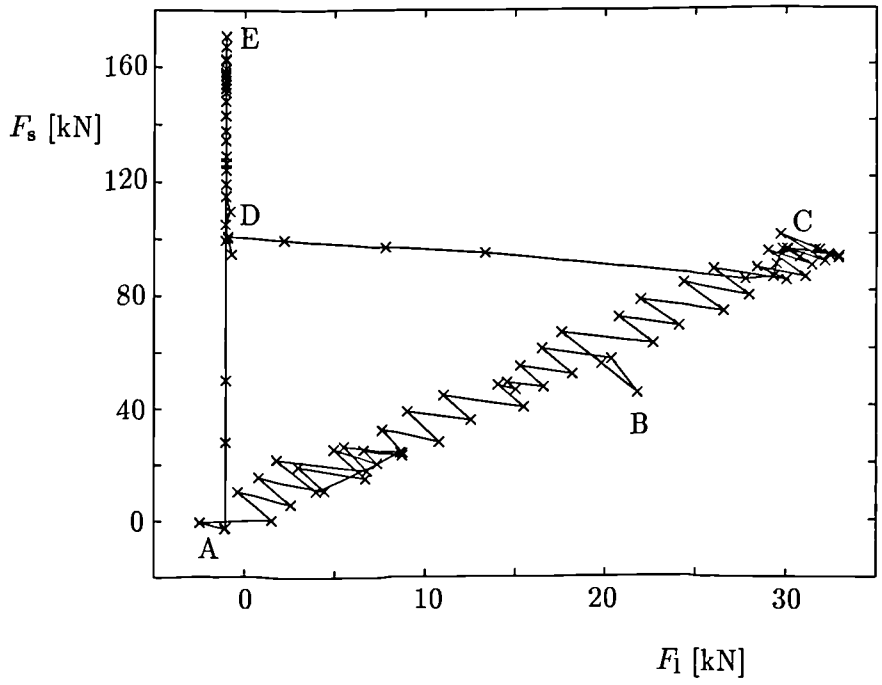

Figure 6.15: Loading procedure for test CW3.

of two applied forces, where F_l represents the bending force applied by two tension jacks and F_s is the shear force applied by a compression jack. In an elastic range (from point A to C) the shear force increment was approximately 10 kN, which after applying the bending force increment 2 kN, fell to about 5 kN. The reason for this method of loading was the attempt to keep the ratio of shear force to bending force constant, equal to 2.81. The ratio was as the estimated ratio of shear critical load to flange critical load, both calculated from estimated yield stress of compression web and flange (assumed steel with $f_y \approx 300$ N/mm^2). When the inelastic behaviour of the compressed flange started (near point C), bending only was applied to the specimen. When the bending load dropped to about 90 % of maximum load, the bending was released completely to zero (point D), which caused a slight increase in shear force. At the third day of testing the shear was then increased up to the

maximum shear force $F_{s,max} = 170$ kN when the web failure occurred (point E). This caused the shear force drop to about 160 kN. The specimen was then gradually unloaded (back to point A).

In very early stages the load readings were negative. This was caused by using the calibration line, which did not start exactly at the zero point. This feature can be seen clearly in Fig. 6.15 between points E and A, where there was no bending force applied at all, but the diagram shows approximately -1 kN.

The specimen was left loaded during the first night, with bending force 20.3 kN and shear force 56.5 kN. Next day the bending force was 21.8 kN and the shear force was 44.3 kN, which is shown in point B.

6.6.3 Tests CW4 and CW5

For tests CW4 and CW5 it was decided to load the specimens first by bending only up to approximately 85 % of the predicted critical load, which was calculated from

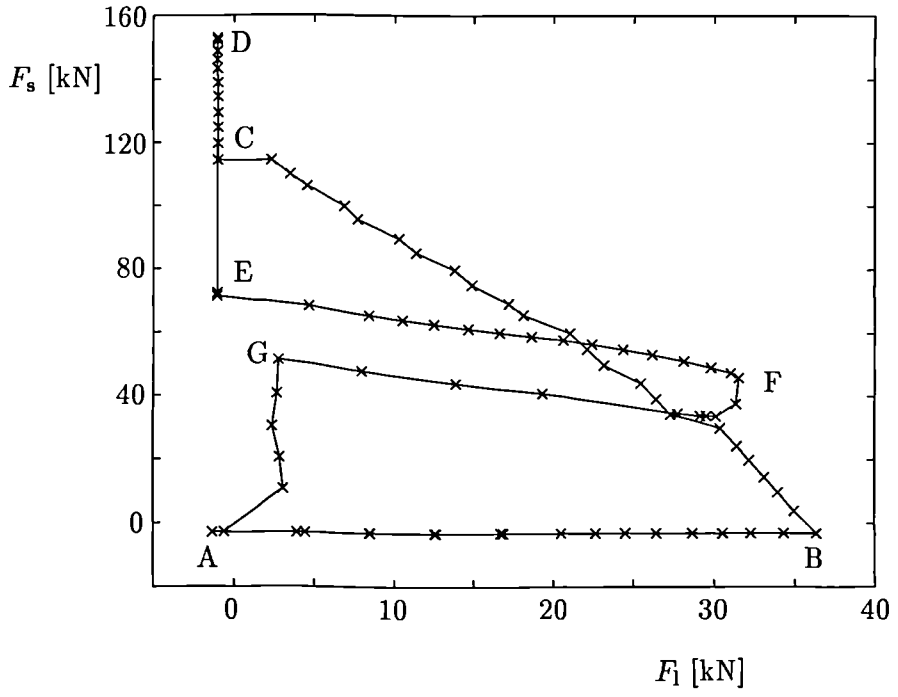

Figure 6.16: Loading procedure for test CW4.

estimated yielding of compression flange (assumed steel, where $f_y \approx 300$ N/mm^2).

The 85 % was chosen according to the maximum load reached in test CW3, and the intention was to keep the stress in the compressed flanges approximately 15 % below the expected critical stress. In Fig. 6.16 the loading sequence is described. From point A to point B, bending only was applied. Then increase in shear force caused decrease in bending (from point B to C). To avoid negative bending loading, the tension jacks were removed and only shear force was increased up to its maximum value of 153 kN (point D), in which the sudden shear failure of the web occured, which brought the shear force down to 72 kN (point E). The failure was unexpected, because the predicted critical shear force, based on the information given by the fabricator, was about 30 % higher. However, the sudden shear failure was explained later by material testing, which showed the yield stress of the web to be about 40 % less than the reported one. Bending was applied to the specimen again up to flange failure (point F). However, it was already deformed from web buckling, so the maximum bending force did not even reach the 85 % of the predicted critical load.

The specimen was gradually unloaded first from bending (points F to G) and then from shear (points G to A).

A similar sequence of loading a specimen was used for test CW5 as can be seen in Fig. 6.17. It was loaded by bending only (points A to B), and then the shear was increased, which caused bending to decrease. The specimen failed first in local flange buckling (point C) followed by sudden web failure, which decreased the shear load from 140 kN down to 62 kN. It caused a slight increase in bending force (point D). The specimen was gradually unloaded first from shear (points D to E) and then from bending (points E to A).

The same reason applies for the occurrence of negative values of loads as was explained for test CW3 in the previous section.

In the inelastic region for the tests CW3, CW4, and CW5 readings were taken only after few minutes, when the load was dropping no more than 0.5 kN per minute.

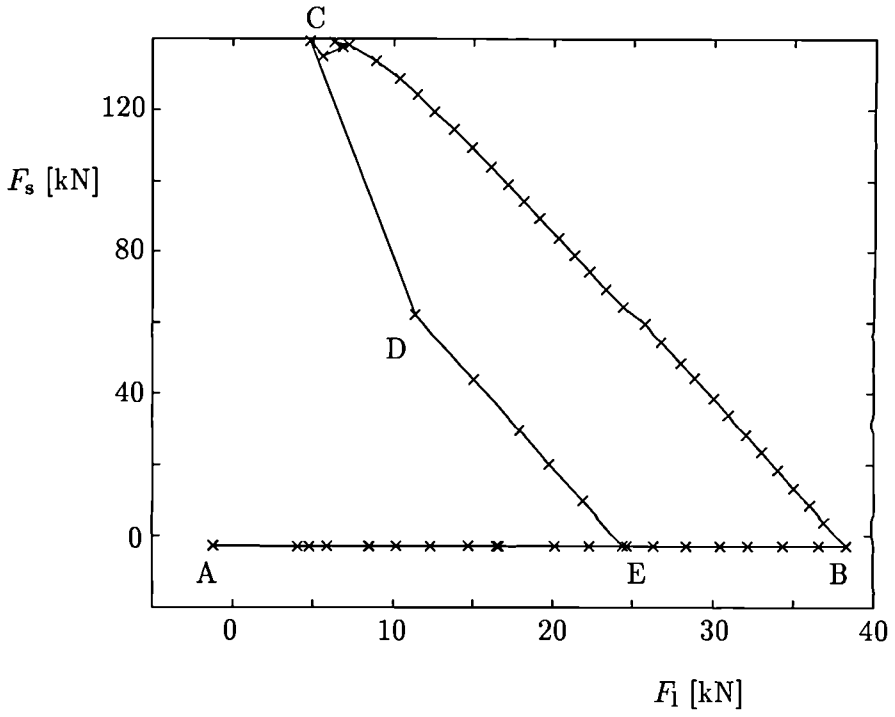

Figure 6.17: Loading procedure for test CW5.

Chapter 7

Results from tests

7.1 Measured dimensions of the specimens

The final average values of major geometrical dimensions, calculated as the mean values of measured ones (they were taken in three cross–sections of each specimen, located in the middle of the flat parts of the corrugated webs), are shown in Table 7.1. The notation is explained in Fig. 2.1. All measurements were taken before the tests.

		CW1	CW2	CW3	CW4	CW5
b_{ft}	mm	201.66	201.10	201.00	201.40	200.50
t_{ft}	mm	8.25	8.00	8.07	7.83	7.72
b_{fc}	mm	201.51	200.80	200.30	200.60	200.43
t_{fc}	mm	8.39	6.00	8.10	6.08	6.00
t_w	mm	3.06	3.29	3.26	2.97	2.97
h	mm	448.68	444.92	445.26	444.46	444.16
h_w	mm	440.36	437.92	437.18	437.51	437.30
b	mm	180	180	250	250	250
d	mm	45	45	45	45	63
α		45°	45°	45°	45°	45°

Table 7.1: Geometrical dimensions of test specimens.

The measurements of web thicknesses taken before each test were inaccurate since all four edges of a web were attached to either flanges or specimen's end plates. The

values listed in Table 7.1 are therefore based on measurements of coupon samples, which were cut from specimens after the tests were completed (see Table 7.3).

The weight of the upper part of test rig (top beam plus all added parts above a specimen) was estimated at $F_w = 3.5$ kN. The distance of the bending force F_1 from the outside surface of the compression flange was $l_1 = 2000$ mm, and the distance of F_w from the compression flange was estimated for $l_2 = 1097$ mm.

Before each test also the dimensions shown in Fig. 7.1 were measured. They are summarised in Table 7.2. Side A is the visible side in Fig. 7.1.

		CW1	CW2	CW3	CW4	CW5
l_{compr}	mm	439	453	591	591	634
l_{tb}	mm	—	—	—	*820*	882
c_{top}	mm	21	20.2	21	20	20.5
c_{btm}	mm	22	20.2	13	24	14
$l_{endplates}$	mm		*672.3*	*884.8*	*884.3*	*938.5*
Side A						
l_{tens}	mm	432	453	582	591	629
t_{top}	mm	20	21.2	21	21	20.5
t_{btm}	mm	21	19.5	21.5	22	21.5
d_1	mm	—	—	909	940	990
d_2	mm	—	—	902	943	992
Side B						
l_{tens}	mm	428	451	582	592	625
t_{top}	mm	20	20.5	21.5	20	21.5
t_{btm}	mm	20	18	26	21	24
d_1	mm	—	—	901.5	945	994
d_2	mm	—	—	905	941	989

Table 7.2: Measurements taken before each test.

7.2 Material testing

7.2.1 Introduction

Test specimens CW1, CW2, and CW3 were delivered without the required samples of steel used for their fabrication. We were informed later that there was no control

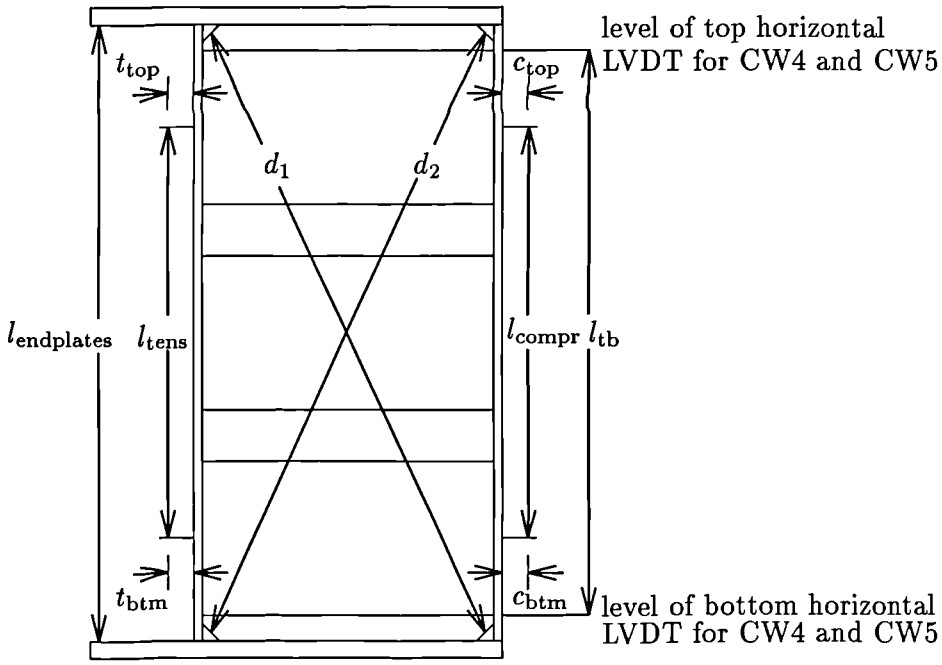

Figure 7.1: Notation for measurements taken before each test.

or checking of the offcuts used when fabricating them, and that no samples could be provided. The specimens CW4 and CW5 had arrived with three 300 × 140 mm plates of 3, 6, and 8 mm thicknesses, to be used for material testing.

7.2.2 Test samples

When tests CW1, CW2, and CW3 were completed, six samples were taken from each specimen, located as shown in Figs. 7.2, and 7.3, respectively. To minimise the heat input into the pieces they were located as far as possible from the welds, and plasma air cutting was done close to these welds. A minimum distance of 50 mm from cut or weld was required.

Material testing of the test specimens CW4 and CW5 was based on tensile test pieces, which were cut from plates as shown in Fig. 7.4. There were two more coupons cut out from the web of specimen CW4 (Fig. 7.5). The coupons were of non proportional dimensions satisfying the requirements of BS EN 10002 [59].

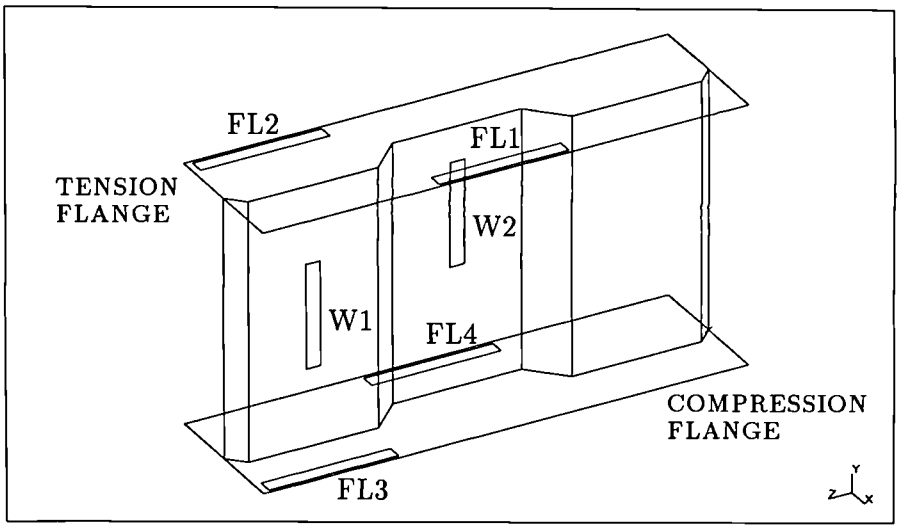

Figure 7.2: Places on specimens CW1 and CW2 from where coupons for the tensile test were taken.

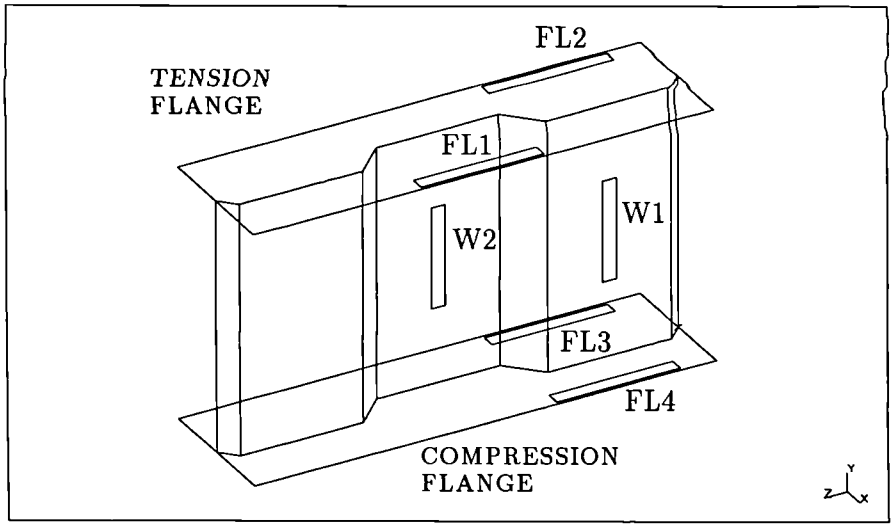

Figure 7.3: Places on specimen CW3 from where coupons for the tensile test were taken.

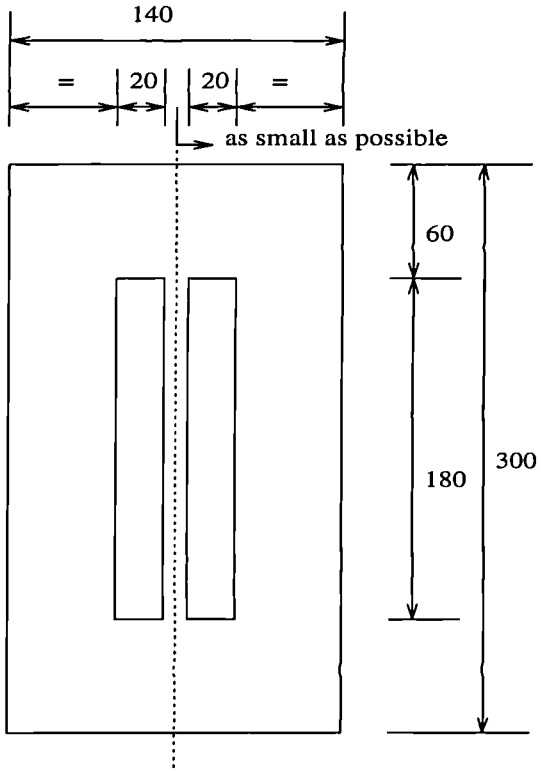

thickness of the plate	coupon number
3 mm	CW4-W1 CW4-W2
6 mm	CW4-FL3 CW4-FL4
8 mm	CW4-FL1 CW4-FL2

Figure 7.4: Plates for tensile test coupons for specimens CW4 and CW5.

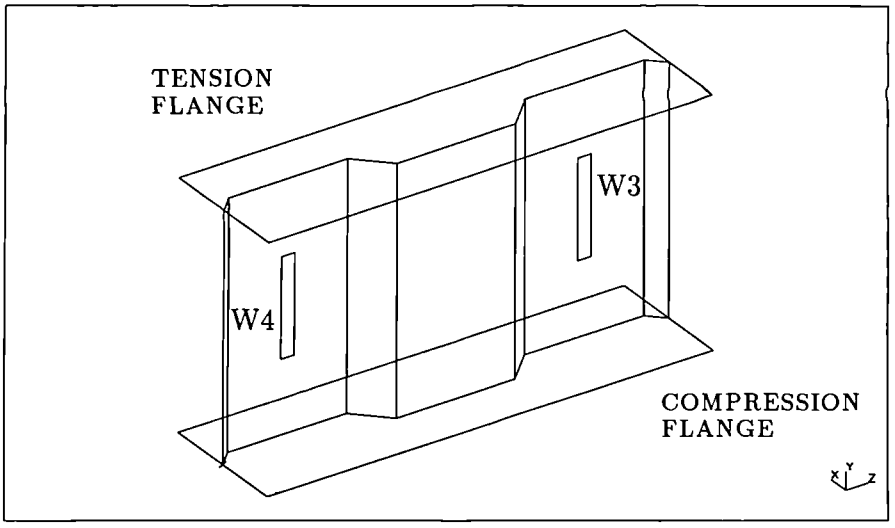

Figure 7.5: Places on specimen CW4 from where coupons for the tensile test were taken.

7.2.3 Testing the samples

Twenty six coupons were tested in a Monsanto tensometer type 'E' 100 kN testing machine. The predicted yielding load for each test sample was estimated, to get enough readings from the extensometer (Lindley No.1) for plotting the stress–strain relation. One division on the extensometer represents 5×10^{-5} inches in extension over 2 inches of original extensometer gauge length which is 25 $\mu\epsilon$. For safety reasons the extensometer was removed before the pieces were loaded to fracture.

7.2.4 Results and discussion

The plots obtained straight from the testing machine were not suitable for estimating the yield stress of the steel because they included slip at the grips.

Each test sample was measured in its width and thickness in five cross-sections. The average values gave the cross-sectional areas, which are listed in Table 7.3.

Figs. 7.6 shows a typical stress-strain relationship. According to the BS [59], the

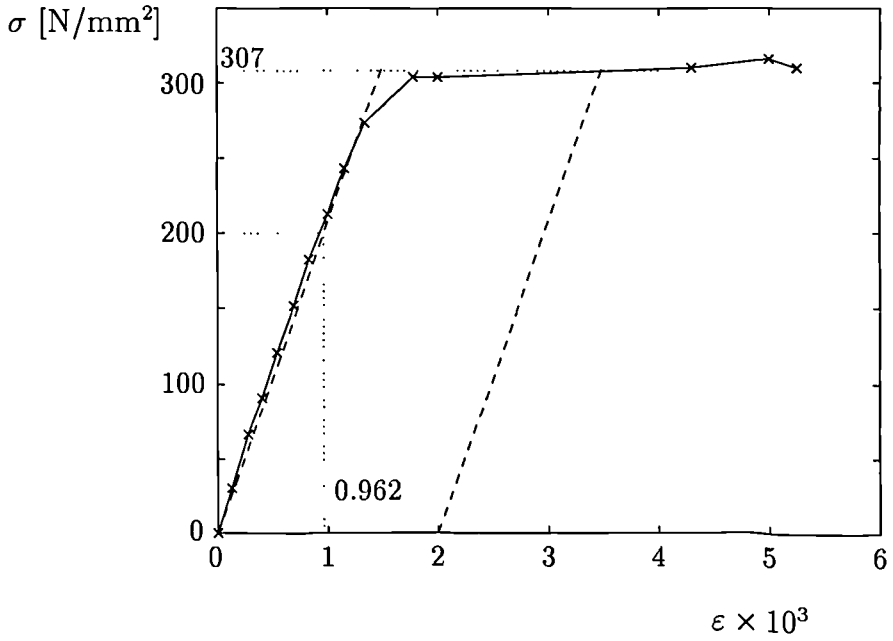

Figure 7.6: Stress–strain curve for test coupon CW1-FL1.

estimation of the yield stress for the type of curve obtained in these tests is done

as a proof strength, which is: (clause 4.9.3.) *"Stress at which a non-proportional extension is equal to a specified percentage of the extensometer gauge length"*. The specified percentage was assumed to be 0.2 %.

The results are given in Table 7.3. The ultimate tensile stress (UTS) was taken as a maximum load reached during the testing.

It was not possible to estimate the yield stress from Fig. 7.7 (a similar diagram was achieved for sample CW1–FL3). It can be seen that there is no elastic behaviour

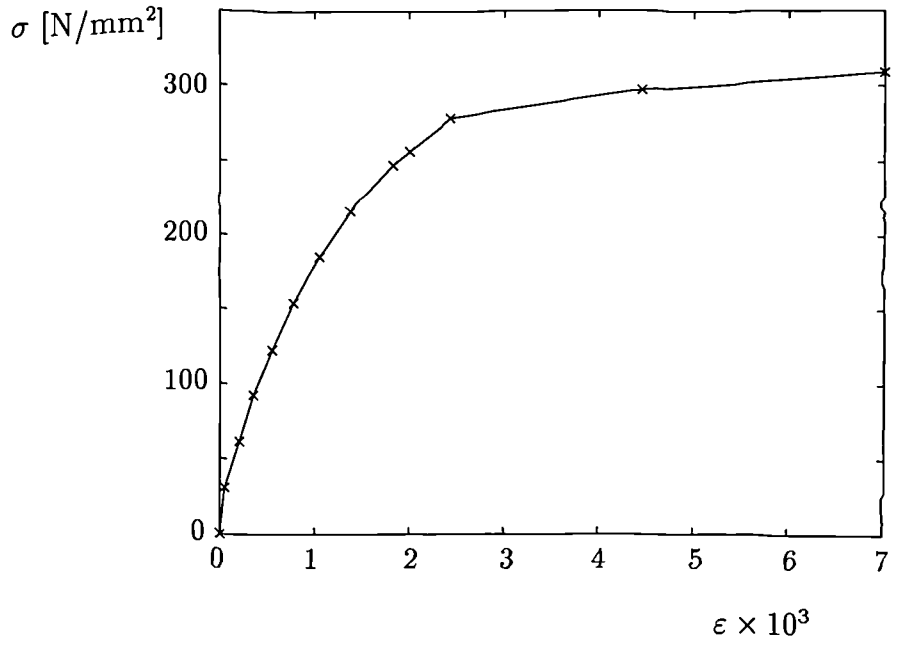

Figure 7.7: Stress–strain curve for test coupon CW1–FL4.

at all. The samples were taken from the compression flange of test specimen CW1. This immediate non–linear behaviour is assumed to be due to a slip in extensometer. The two samples were therefore not considered for defining the yield stress and Young's modulus (see Table 7.3). Their UTSs are almost the same as the ones for the samples CW1–FL1 and CW1–FL2, respectively, therefore the values of yield stress and Young's modulus of these samples were considered for the compression flange of specimen CW1 when analysing the results.

The tensile tests on samples CW4–W1 and CW4–W2 gave very low values of

Test coupon	Thickness	Area	Yield stress	Young's modulus	UTS
	mm	mm^2	N/mm^2	N/mm^2	N/mm^2
CW1–FL1	8.28	164.5	307	208	498
CW1–FL2	8.20	163.3	306	212	505
CW1–FL3	8.17	163.0	—	—	497
CW1–FL4	8.08	161.8	—	—	504
CW1–W1	3.07	60.9	318	204	489
CW1–W2	3.05	60.8	324	204	486
CW2 FL1	8.06	161.8	255	220	408
CW2 FL2	8.02	160.4	270	226	411
CW2–FL3	5.86	117.3	410	216	503
CW2–FL4	5.86	117.2	418	199	499
CW2 W1	3.29	63.3	322	211	468
CW2–W2	3.29	65.7	302	202	441
CW3–FL1	8.05	160.9	224	236	329
CW3–FL2	7.99	159.6	219	243	318
CW3 FL3	7.94	158.7	212	234	318
CW3–FL4	7.94	158.8	220	231	320
CW3–W1	3.26	65.2	281	206	436
CW3–W2	3.25	65.1	286	207	440
CW4–FL1	7.76	154.7	388	218	520
CW4–FL2	7.71	153.7	390	214	523
CW4 FL3	6.00	120.1	359	213	481
CW4–FL4	6.02	120.5	364	213	481
CW4–W1	2.94	58.7	218	198	351
CW4–W2	2.95	59.0	222	194	346
CW4 W3	2.97	61.0	227	202	354
CW4–W4	2.97	59.5	254	184	366

Table 7.3: Yield stresses, Young's modulus, and UTS.

yield stress and UTS, as can be seen in Table 7.3. Therefore it was decided to cut two more pieces straight from the test specimen CW4 (test pieces CW4–W3 and CW4–W4 in Fig. 7.5). The results from these two additional tests only confirmed the previous results.

All flange samples and some web ones failed within the extensometer gauge length as expected. Both the web samples from test CW1 and one from test CW2 (CW2–W2) failed within the top grip. The aim of these tests was not to find the maximum stress or elongation, in which case the failure in the grip might have affected results. For the estimation of yield stress the behaviour of the samples during the tests was sufficient.

7.2.5 Summary of tests on materials

For the further analysis of the test results the values in Table 7.4 were used.

	f_y [N/mm^2]			E [kN/mm^2]		
	compression flange	tension flange	web	compression flange	tension flange	web
CW1	306		320	210		210
CW2	414	263	312	208	223	207
CW3	216	222	284	232	240	207
CW4	362	389	222	213	216	198
CW5	362	389	222	213	216	198

Table 7.4: Yield stresses and Young's modulus used in analysis.

The value of yield stress obtained for the compression flange of specimen CW2 seems to be very high. Comparing the UTS (see Table 7.3) the type of steel used for the compression flange in CW2 seems to be the same as steel used for flanges in CW1. If so, the alternative value for the yield stress is 306 N/mm^2. Only the measured value, 414 N/mm^2, has been used here.

7.3 Measured initial imperfections

The specimens were subjected to measurements of imperfections caused by the heat input during the welding of flanges to a web. The measurements are summarised in Table 7.5. The places, where and how they were taken are shown in Fig. 7.8. The

	CW1	CW2	CW3	CW4	CW5
compressed flange					
A	0.9	1.3	1.8	3.2	2.8
B	2.6	3.3	3.7	5.6	6.8
C	1.1	1.5	2.6	2.5	3.3
D	1.9	2.5	4.2	5.6	6.2
E	1.7	2.2	2.4	2.6	3.6
F	1.6	2.2	3.5	5.2	5.8
tension flange					
A	—	1.4	3.5	2.2	2.1
B	—	2.5	5.7	4.3	5.0
C	—	1.4	2.5	2.7	2.1
D	—	2.2	5.9	3.9	3.6
E	—	1.6	4.7	2.8	2.9
F	—	1.8	5.4	3.6	4.1

Table 7.5: Initial imperfections of the specimens.

measurements are in mm. From the Table 7.5 it is obvious that the more heat is input to a specimen, the more distortion it has. Specimens CW1 and CW2 had only intermittent welds between a web and flanges, as shown in Fig. 6.2.

The longitudinal imperfections of compression flanges were measured along the outside surfaces of the specimen flanges over the length of the 24 in ruler. The largest imperfection was observed for specimen CW1 — 1.6 mm. All the other specimens had this initial imperfection measured within 0.3 mm.

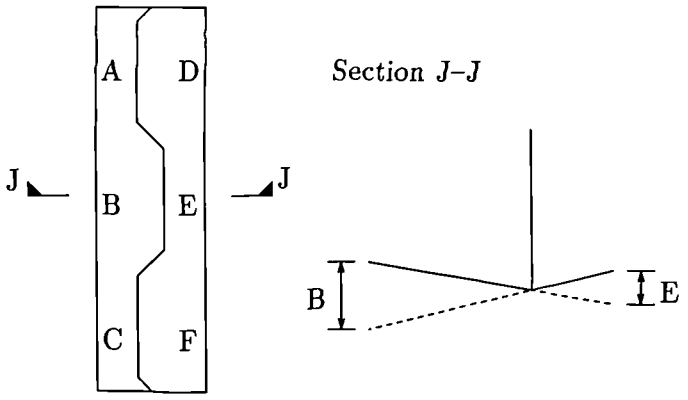

Figure 7.8: Places on a flange where the measurements for imperfections were taken.

7.4 Behaviour of the specimens

7.4.1 Loading without shear

7.4.1.1 General

The local buckling of the compressed flange appeared significantly in two places — near strain gauges SG3–5 and SG19–21 (Fig. 6.12), as described in detail below.

There was also a buckle near gauges SG11–13, not so obvious as the two previous ones, but evident, by comparison with a straight edge, after finishing the test.

The flat parts of the web, which were attached to the buckled portion of the compressed flange, showed clearly the bending deformations near the flange. The bending of the web was indicated by strain gauge measurements (two strain gauges placed on the web), which showed no strain in the web before the buckles in the flange appeared.

The measurements of the twisting of the loading beams showed that this was negligible.

7.4.1.2 CW1

The yielding of the compressed flange was predicted as for steel with $f_y = 300$ N/mm^2, from which the load in the tension jacks was estimated as 95 kN. The maximum load was 87.9 kN. As Fig. 7.9 shows, the non–linear behaviour of the flange started

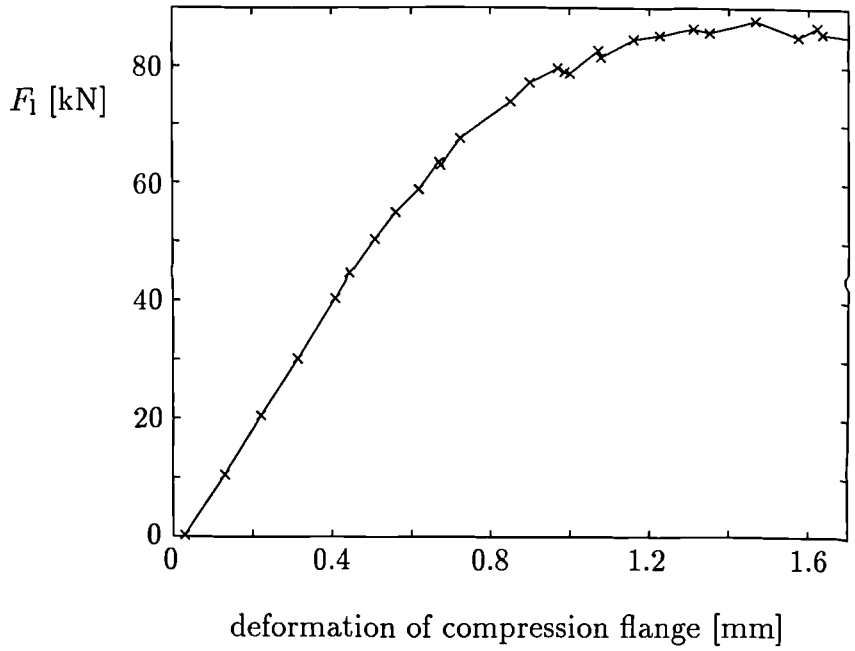

Figure 7.9: Deformation of compression flange versus applied load for CW1.

at about 60 kN. This is supported by Fig. 7.10, where the measured values of strain are plotted against the applied load. The place, where these two strain gauges were placed, showed the first local buckle of the flange. The second visible buckle was indicated by strain gauges SG3 and SG5 (Fig. 7.11). It had finally a larger deformation than the buckle near gauges SG19–21. This could be explained by the influence of an end plate on the development of the buckle near gauges SG19–21.

Figs. 7.12 and 7.13 show the specimen with buckled flange. It can be clearly seen that the flange of the specimen buckled at the large outstands. On the side A it was the bottom part of the specimen; while on the side B it was the middle part. The buckle which developed in the top part of the specimen's flange on the side A, was not so significant.

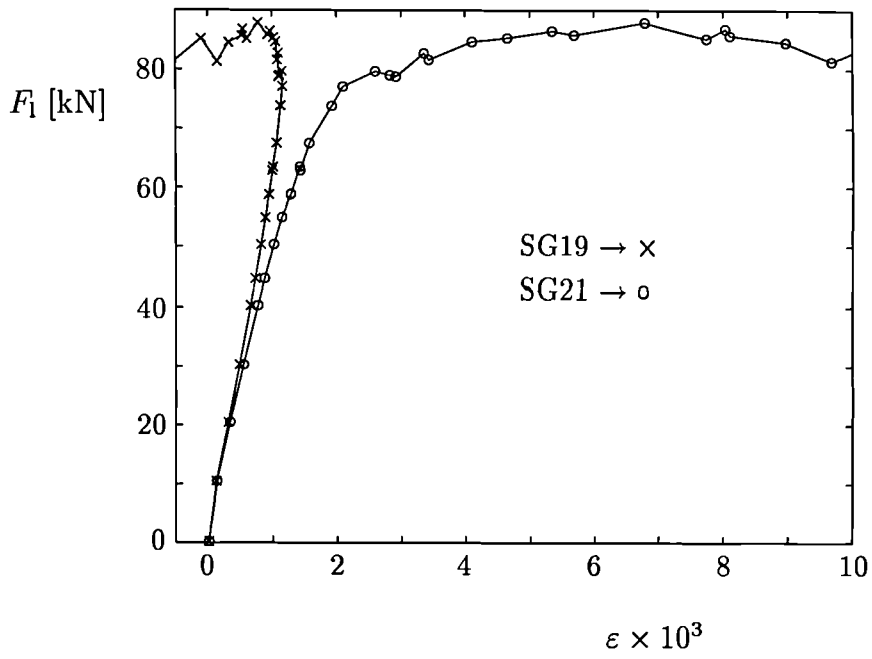

Figure 7.10: Measurements of SG19 and SG21 versus applied load for CW1.

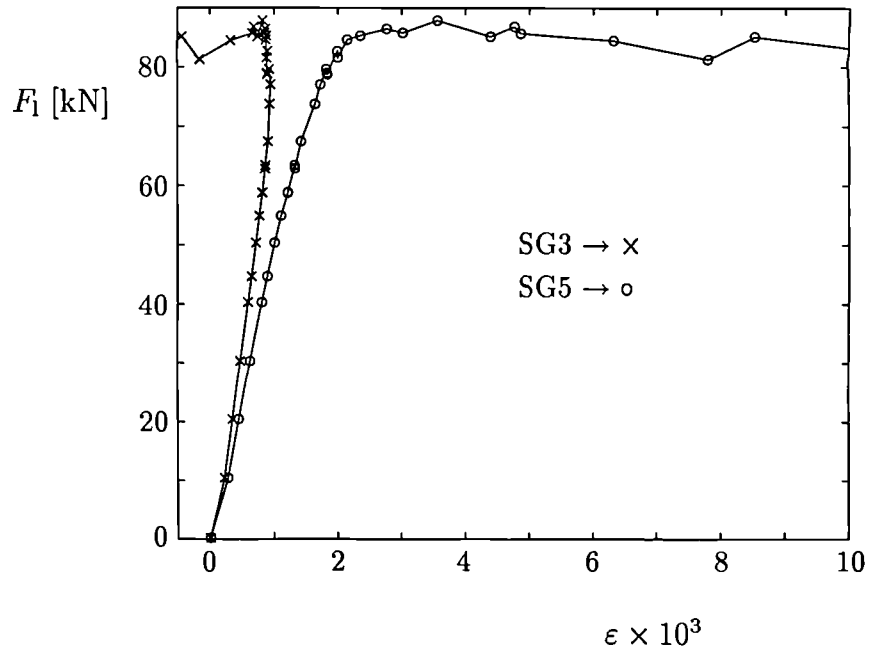

Figure 7.11: Measurements of SG3 and SG5 versus applied load for CW1.

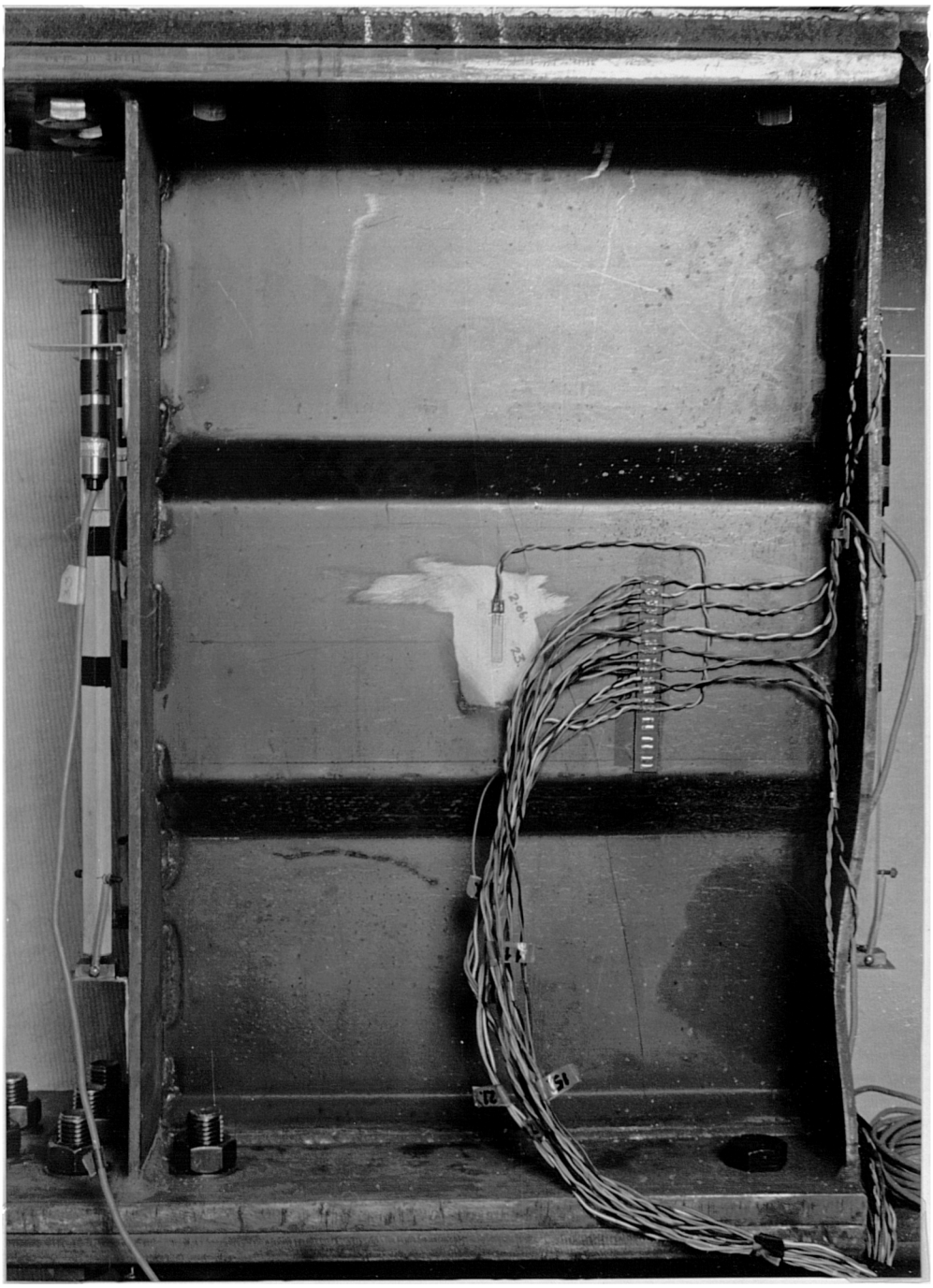

Figure 7.12: Specimen CW1 from side A.

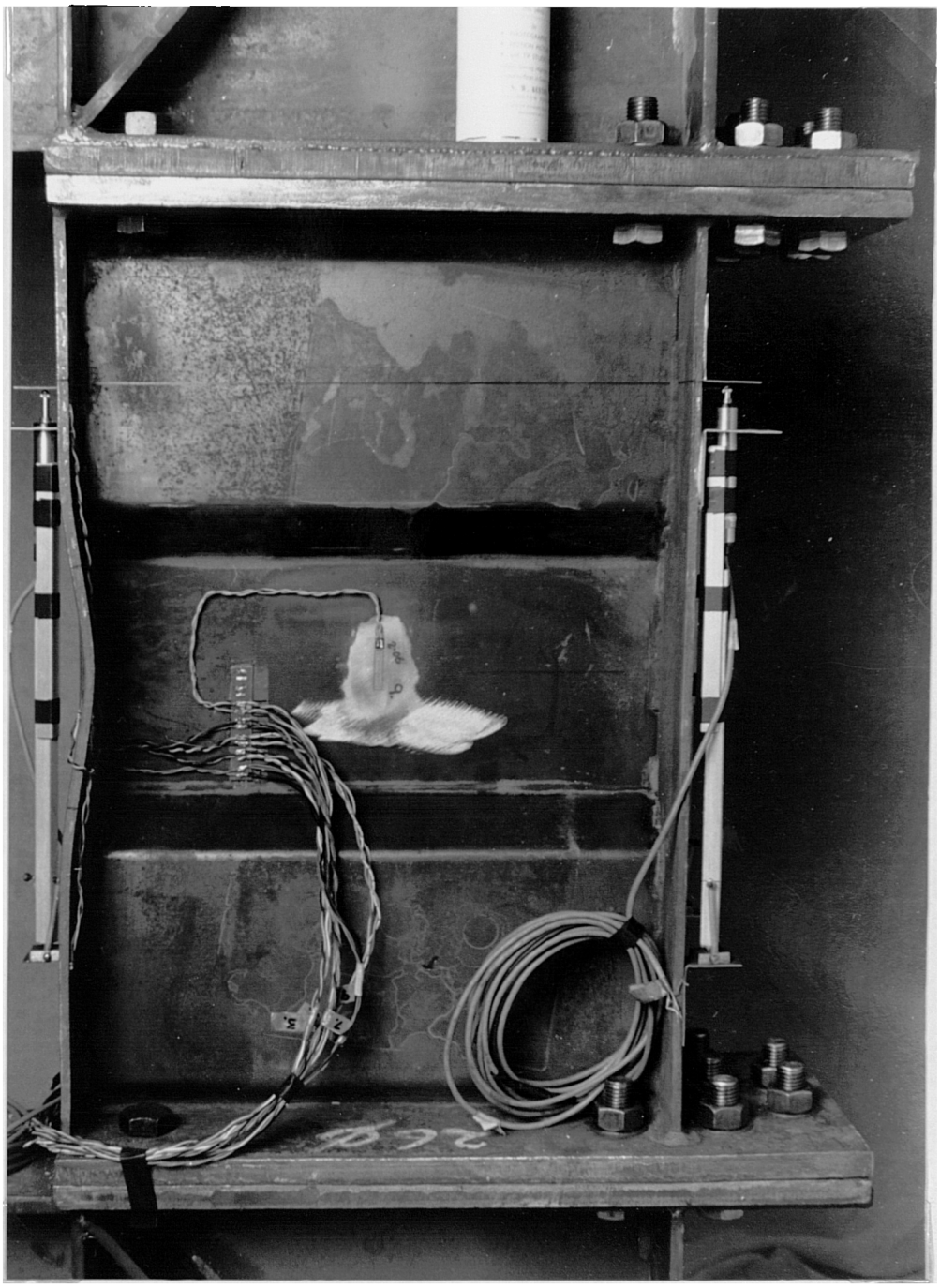

Figure 7.13: Specimen CW1 from side B.

7.4.1.3 CW2

Figs. 7.14 and 7.15 show the non–linear behaviour from about 35 kN, while the

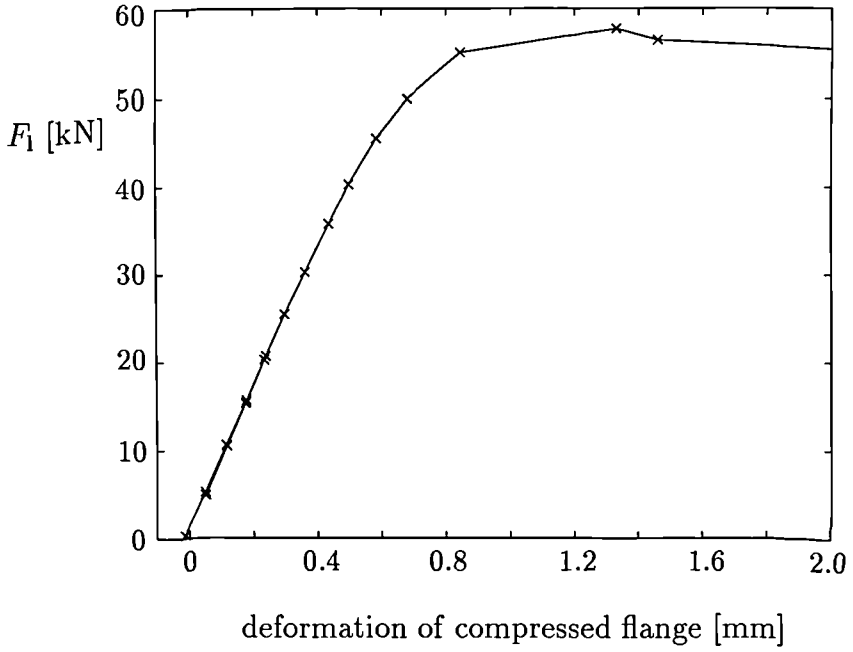

Figure 7.14: Deformation of compressed flange versus applied load for CW2.

predicted yielding was estimated for 65 kN. The maximum load was 57.7 kN.

Figs. 7.16 and 7.17 show the specimen with a buckled flange on both sides of the specimen. The deformed shape of the flange is compared with the ruler put vertically next to the flange edge.

7.4.2 Loading with shear

7.4.2.1 CW3

The shortening of the compression flange over the gauge length can be seen in Figs. 7.18 and 7.19. The deformation of the compressed flange was increased by both bending and shear force. The predicted yielding of the flange was about 46 kN of bending force. From Fig. 7.18 the nonlinear behaviour started approximately when the bending force reached about 25 kN. The maximum bending force was

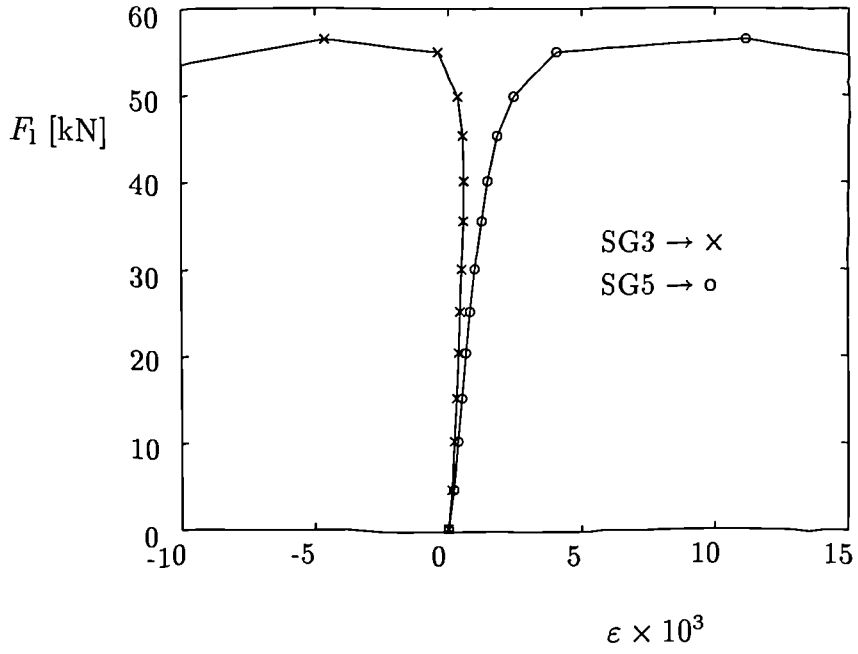

Figure 7.15: Measurements of SG3 and SG5 versus applied load for CW2.

32.9 kN. Once the bending was released (points C to D in Fig. 7.18), a decrease on deformation and small increase in shear force were observed (points C to D in Fig. 7.19). The increase of shear force with zero bending force extended the deformation of the flange (points D to E in both figures). The big increment in deformation was observed, when the web buckled suddenly in shear (points E to F in Fig. 7.19).

The local buckling of the flange appeared in the place where strain gauges SG1 and SG3 were located (Fig. 6.13). Fig. 7.20 clearly shows the creation of the buckle, when the strain in SG1 changed direction of its increments (point B). This behaviour was expected since the shear force creates a larger bending moment at the location of SG1–3 than at the place of SG29–31. The line CD in Fig. 7.20 represents a part of the unloading process during the test.

The details of the deformed specimen are shown in Figs. 7.21 and 7.22. Fig. 7.21 shows the side of the specimen where the large outstand of the flange was in the middle. There is no significant local deformation of the compressed flange when com-

Figure 7.16: Specimen CW2 from side A.

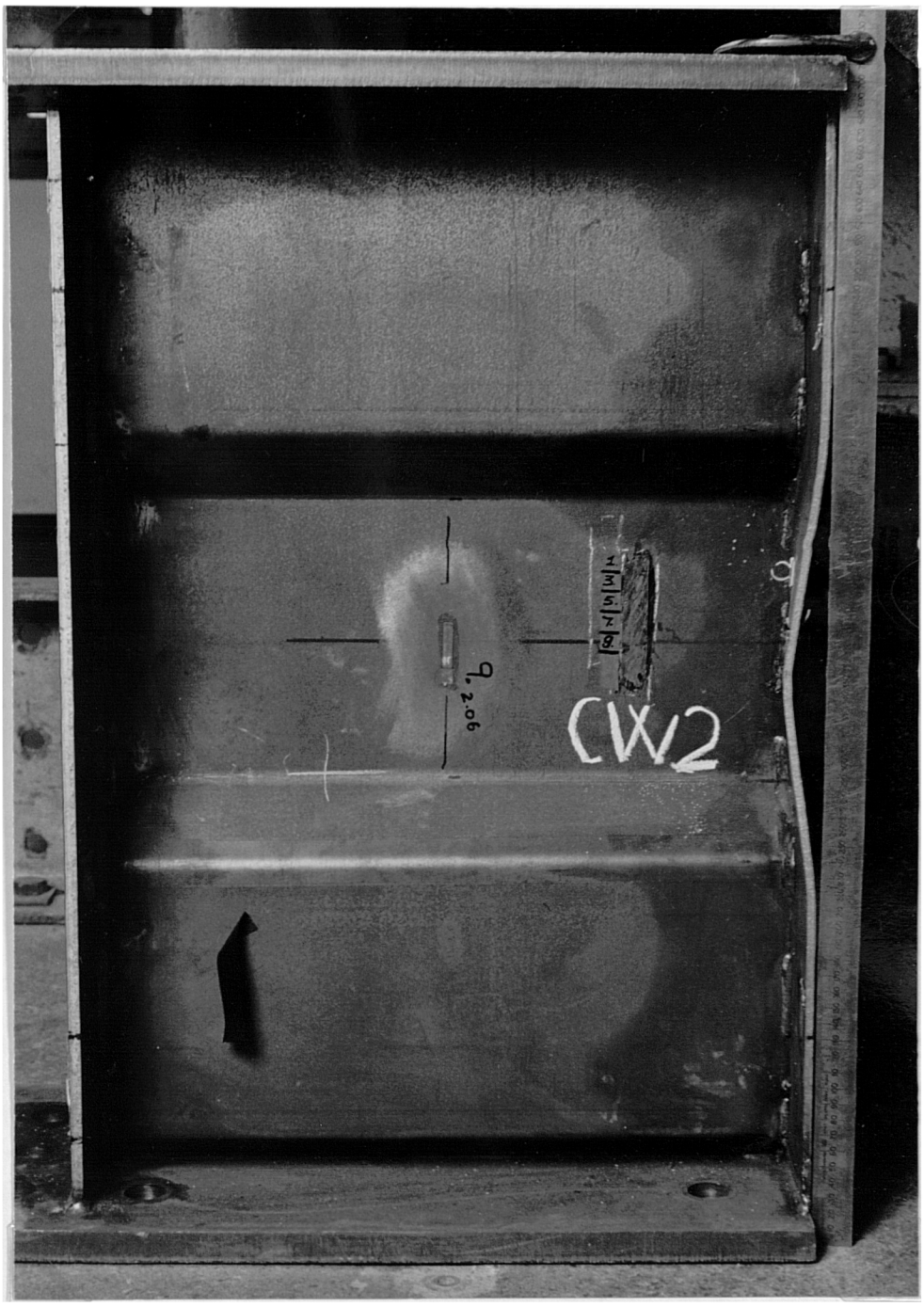

Figure 7.17: Specimen CW2 from side B.

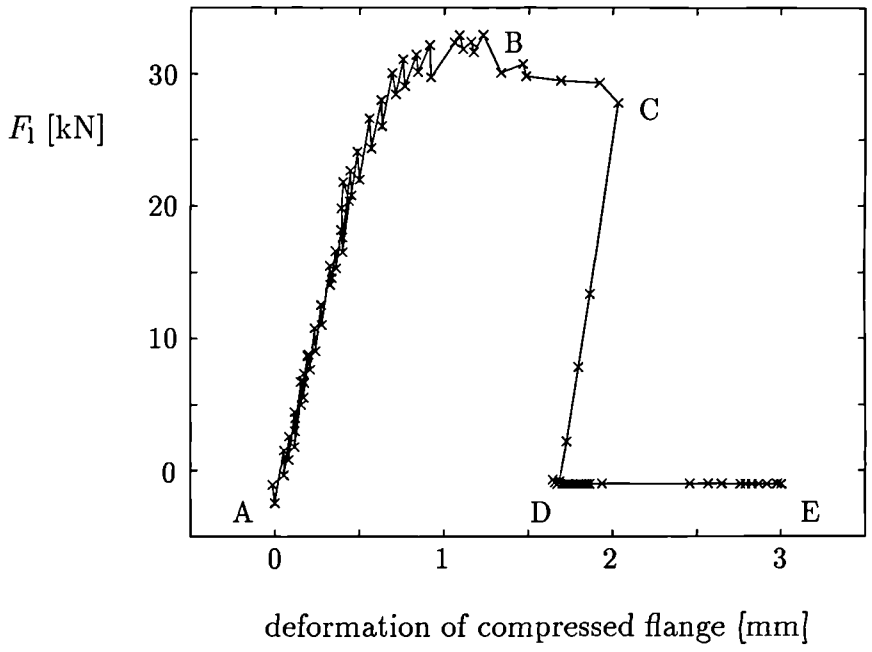

Figure 7.18: Deformation of compressed flange versus bending force for CW3.

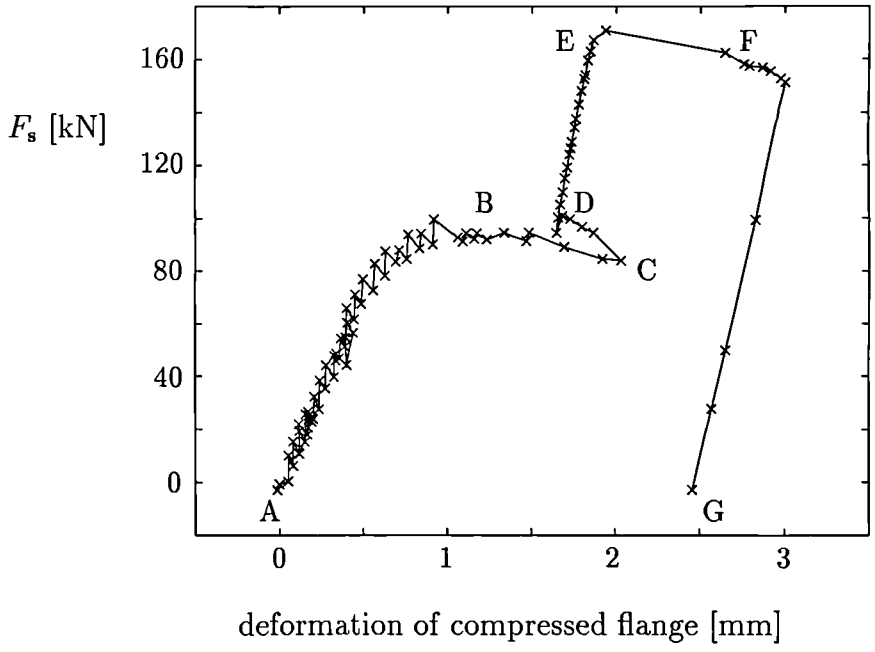

Figure 7.19: Deformation of compressed flange versus shear force for CW3.

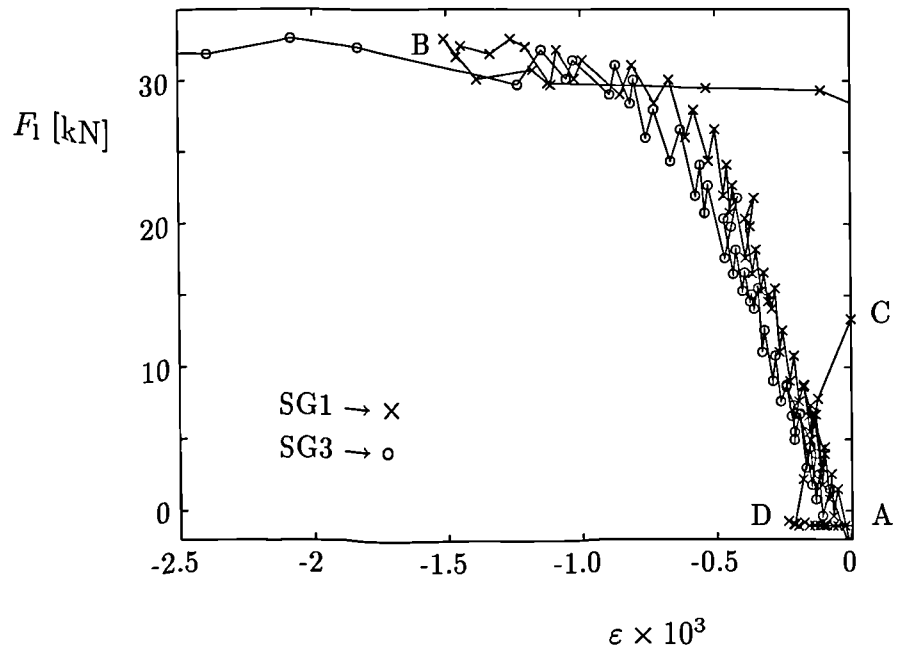

Figure 7.20: Measurements of SG1 and SG3 versus bending force for CW3.

paring it with the ruler in Fig. 7.21. On the other side of the specimen, Fig. 7.22 shows a clear local buckle in the bottom part of the compression flange (the comparison is again shown with the ruler). The stresses were higher in the cross–section of the bottom half–wave of the corrugation of specimen CW3 due to the way of loading – the shear load was applied perpendicular to the specimen length on its top "free" end thus the bending moment was linearly increased towards the bottom of the specimen where it was "fixed".

The web behaviour can be observed in Figs. 7.23 and 7.24. The strain gauges SG7, SG11, SG13, and SG17 were oriented on the web in the predicted directions of principal stresses (see Fig. 6.13). In Fig. 7.23 the loading sequence for SG7 is through points A, B, C, D, E, F and back to A. For SG11 it is A, K, G, H, I, and J. Strain gauges SG11 and SG17 were in compression (points A to K in Fig. 7.23 and A to F in Fig. 7.24), SG7 and SG13 were in tension (points A to B in the both figures) in the first part of the test before flange buckling. Once the local buckle on the flange started to develop, it forced the web panel to bend. The rate of increase

Figure 7.21: Specimen CW3 from side A.

Figure 7.22: Specimen CW3 from side B.

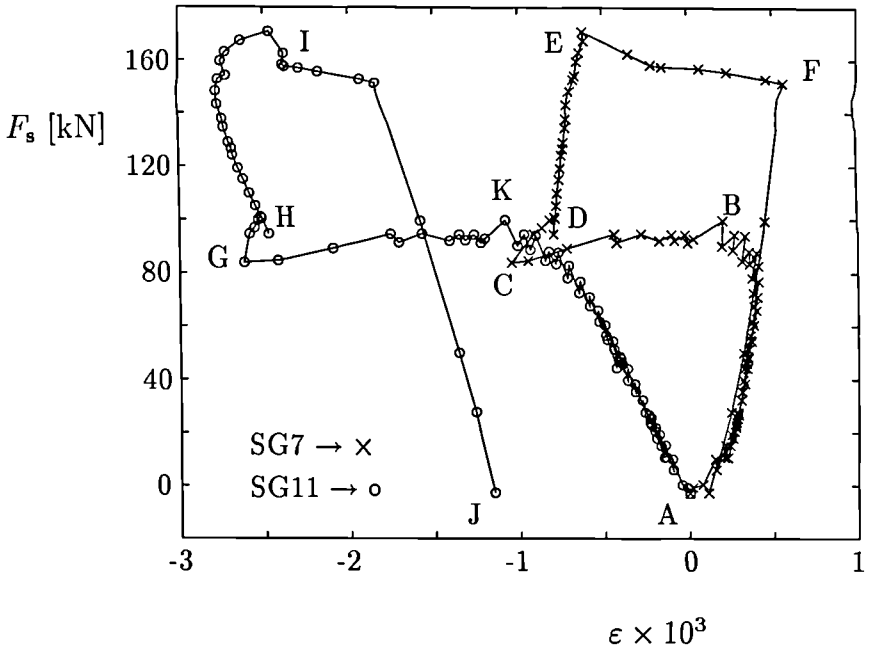

Figure 7.23: Measurements of SG7 and SG11 versus shear load for CW3.

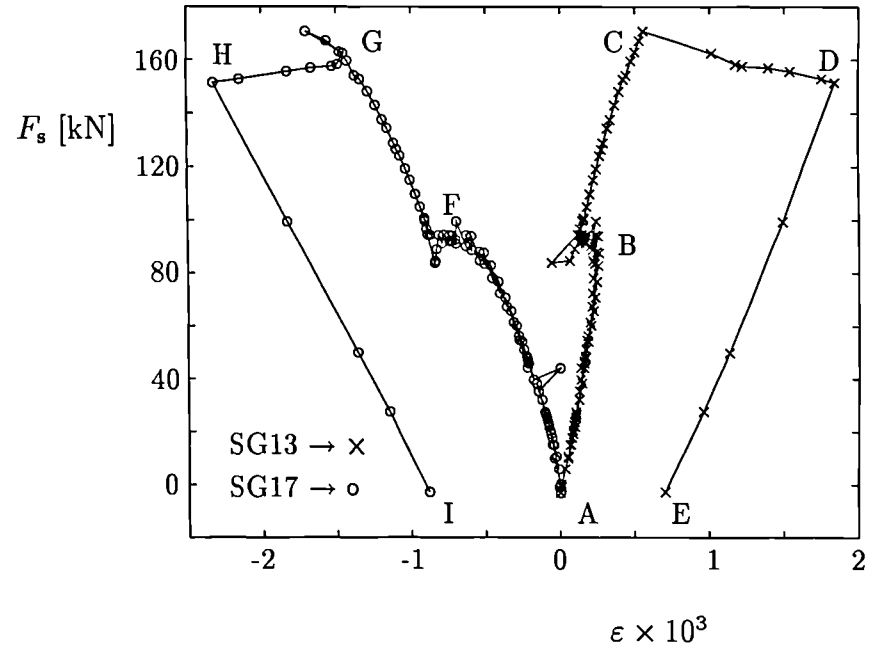

Figure 7.24: Measurements of SG13 and SG17 versus shear load for CW3.

in strain in all four strain gauges shown (either in positive or negative direction) changed, which indicated the bending of the web panel (from place K to G, and from B to C in Fig. 7.23, and around B and F in Fig. 7.24). It is more significant for SG7 and SG11, because these two strain gauges were placed closer to the buckled flange.

After releasing the bending force to zero (this is indicated in Fig. 7.23 between points G—H and C—D) the shear force was increased until the web buckled. This was more dramatic than the flange failure. The first indication of nonlinear behaviour of the web was observed on strain gauge SG11 (Fig. 7.23) at about 145 kN of shear force. The maximum shear force reached in this test was about 171 kN.

The lines between points F—A, I(approx.)—J in Fig. 7.23, and D—E and H—I in Fig. 7.24 represent the influence of the unloading process on SG7, SG11, SG13, and SG17, respectively.

7.4.2.2 CW4

Fig. 7.25 shows the changes in the compressed flange of the specimen. It displays

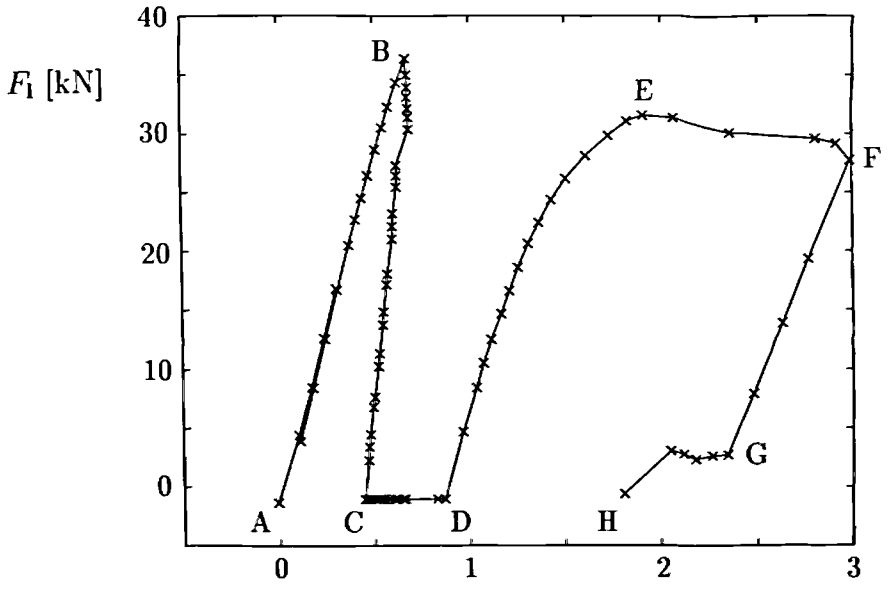

Figure 7.25: Deformation of compressed flange versus bending force for CW4.

linear behaviour up to about 32–33 kN and an indication of beginning of non–linear performance. Between points A to B bending only was applied to the specimen. The increasing of shear force slightly decreased the deformation of the compression flange (points B to C). Once the bending force was released completely the deformations of the compressed flange started to rise with increasing shear force again (points C to D). Shear buckling of the web increased the deformation by 0.2 mm. The maximum bending force after reloading the specimen by bending was 30.5 kN (point E). Lines FG and GH represents the unloading the specimen from bending and shear, respectively.

Fig. 7.26 shows clearly the nonlinear behaviour of the flange in the middle (points

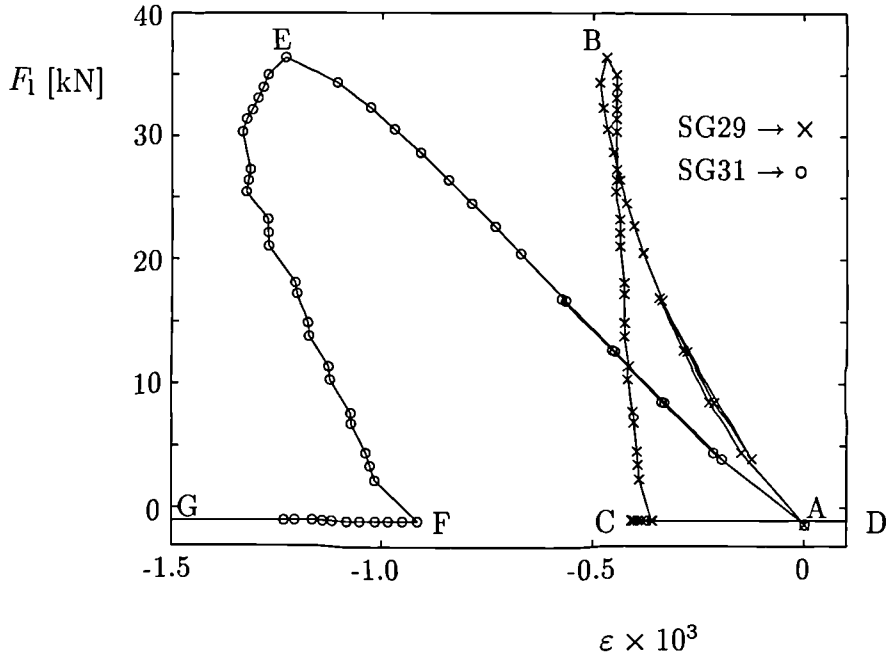

Figure 7.26: Measurements of SG29 and SG31 versus bending force for CW4.

A to E for SG31 and A to B for SG29). That was the reason to change the method of loading, already at 80 % of the predicted critical bending force, and start with shear loading of the specimen. Releasing the bending force and increasing the shear force did not change the strains in this place very much (the lines EF and BC are almost vertical) until the sudden web failure, which happened under the shear loading only. It is indicated by lines FG and CD, where the sudden failure is significant behind

the last measurement shown in this figure. The shear buckling deformed the flange significantly and made it yield in this place, as shown in Fig. 7.26 by lines FG and CD running out of the diagram. To enable the diagram to be drawn at a convenient scale the measurements of SG29 and SG31 taken after web failure are not shown.

The shear behaviour of the middle web panel is shown in Fig. 7.27. All three

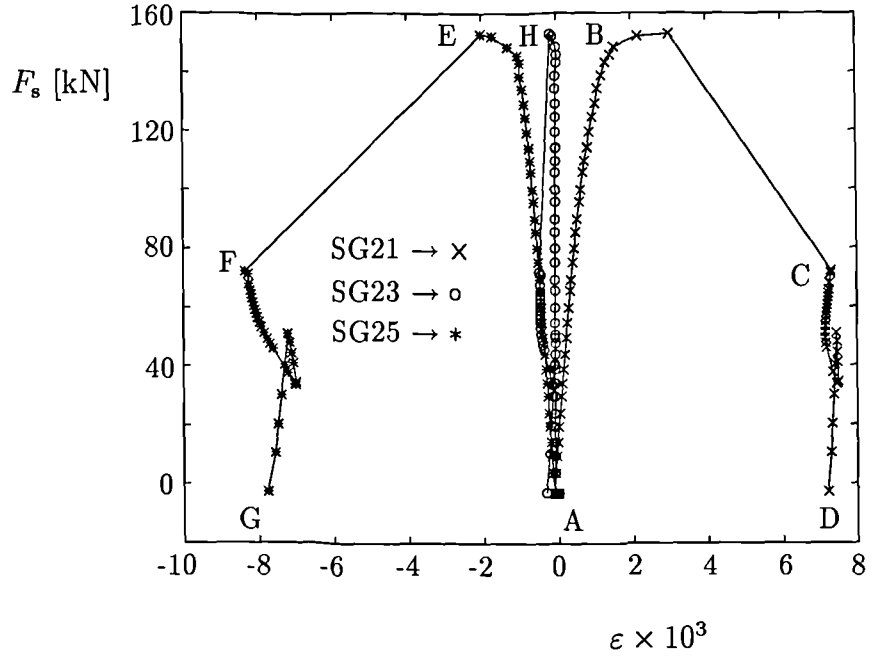

Figure 7.27: Measurements of SG21, SG23, SG25 versus bending force for CW4.

displayed strain gauges show no large increase in compressive strain during the bending loading only (point A). SG23 was placed in a vertical position to measure any bending of the web, caused by local flange buckling. Since the flange did not buckle first, the strains in SG23 remained almost zero (line AH) until the web failure. Strains from SG21 and SG25 increased linearly with increasing shear force, as expected (lines AB and AE respectively). The nonlinear performance was first observed, when the load reached about 110 kN. After about 150 kN the load started to drop rapidly, when at the load of 153 kN the sudden failure appeared (lines BC and EF). The bending reloading, as well as the total unloading, had no influence in large changes in strains measured by SG21, SG23, and SG25, as seen in Fig. 7.27 between points F and G, and C and D.

The details of the deformed specimen are shown in Figs. 7.28 and 7.29. The deformations of the flange were developed due to shear buckling of the web, which can be observed on the photographs. They were taken on both sides of the specimen.

7.4.2.3 CW5

The local buckling of the flange at the location of the strain gauges SG1 and SG3 occurred first in this test, as shown in Figs. 7.30 and 7.31. In Fig. 7.30 the curve AB and AG represent the bending loading only. Lines AB and AF in Fig. 7.31 stand for bending only. At 38 kN of bending force the loading from tension jacks was stopped and loading by shear force started, which decreased the bending force (see curves BCD and GHI in Fig. 7.30, or BCD and FGH in Fig. 7.31). The significant non–linear behaviour of the compressed flange started at about 17 kN of bending force (near points C and H in Fig. 7.30) and 100 kN of shear force (near points C and G in Fig. 7.31). The later web failure at shear load of 139 kN did not change the strain in SG3 (lines IJ in Fig. 7.30 or IH in Fig. 7.31), but it had influence on SG1 (lines DE in the both figures). Lines EF and JK (Fig. 7.30) or EA and IJ (Fig. 7.31) represents the unloading of the specimen first by shear then by bending forces.

At shear force of 139 kN a sudden web failure occured. The indication of shear buckling of the bottom web panel was given by the strain gauges SG7 and SG11, as shown in Fig. 7.32. The bending force had no significant influence on strain gauges placed on the web (point A). Increasing shear force increased strains in SG7 – in tension and SG11 – in compression. Lines BC and DE represent sudden web failure.

The photograph of the deformed flange of the specimen is shown in Fig. 7.33. It is compared with the straight edge of the white painted wood.

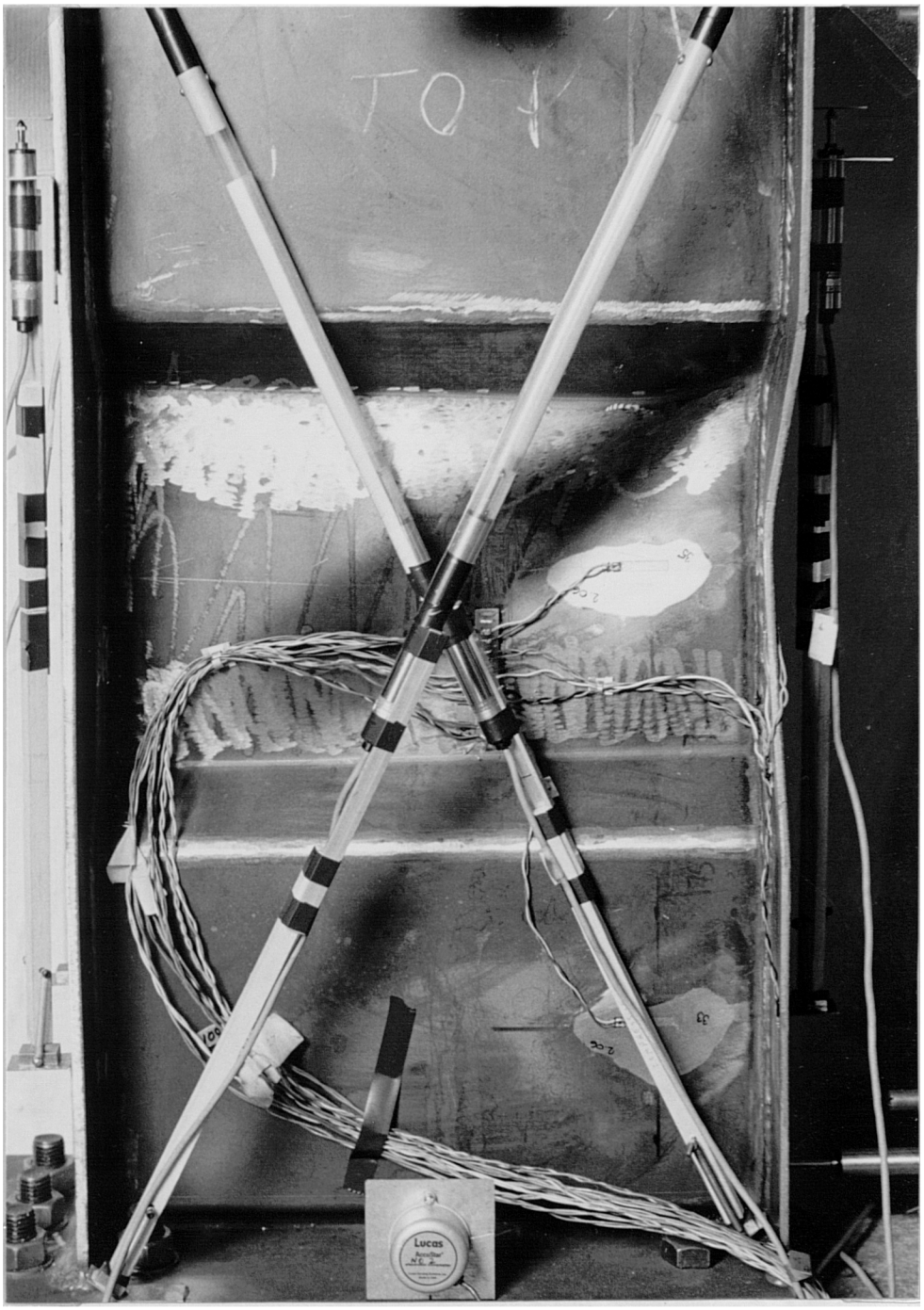

Figure 7.28: Specimen CW4 from side A.

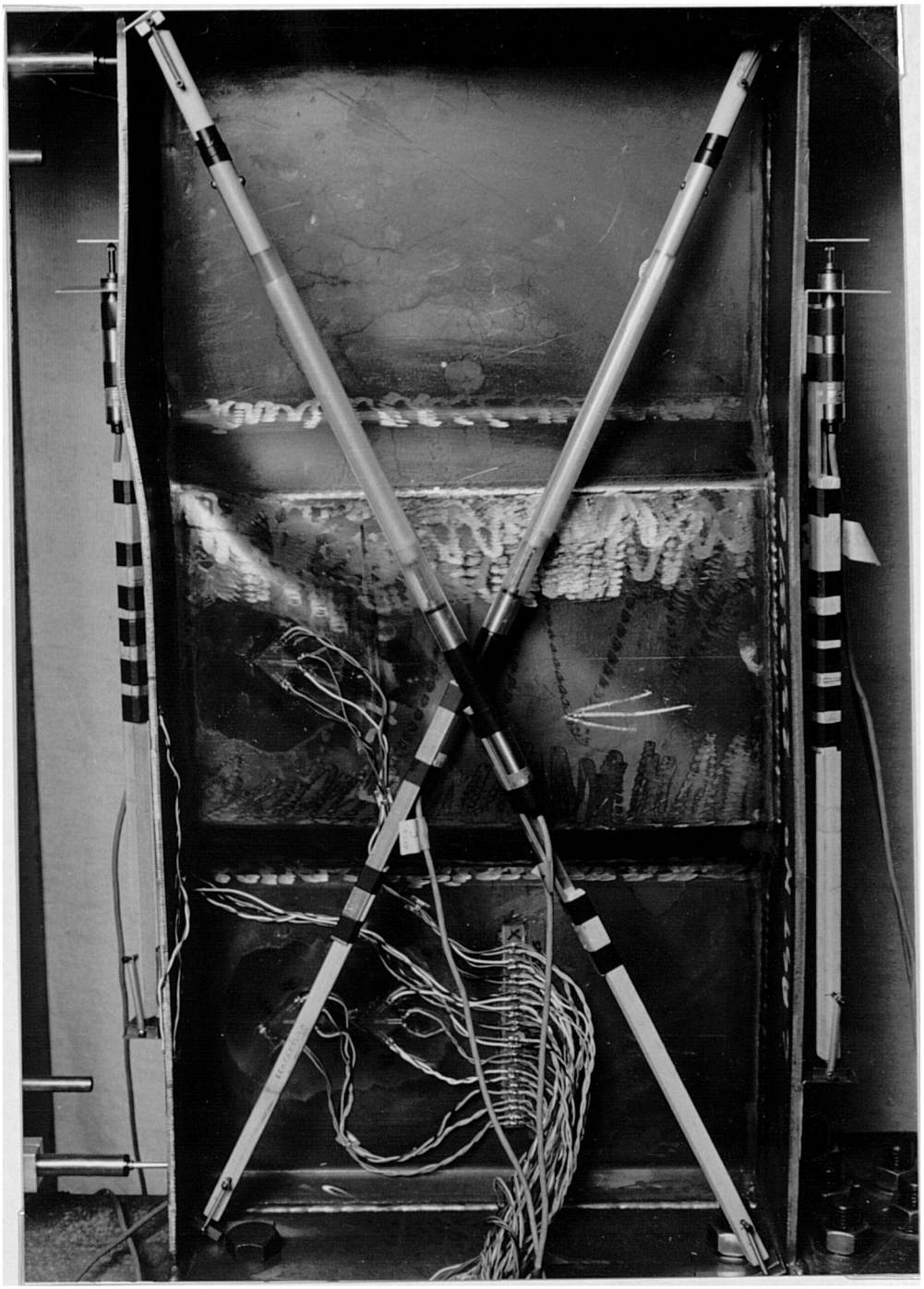

Figure 7.29: Specimen CW4 from side B.

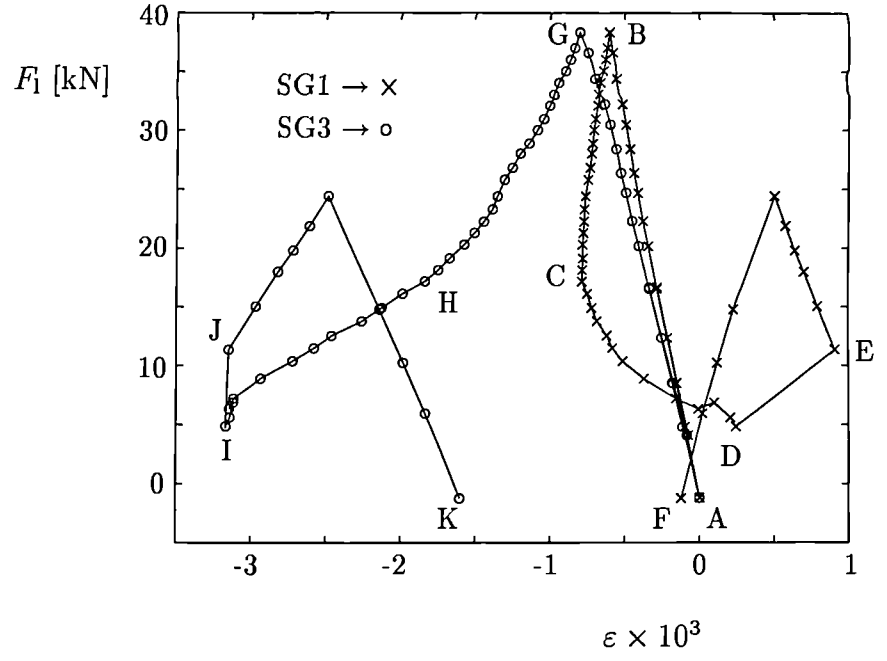

Figure 7.30: Measurements of SG1 and SG3 versus bending force for CW5.

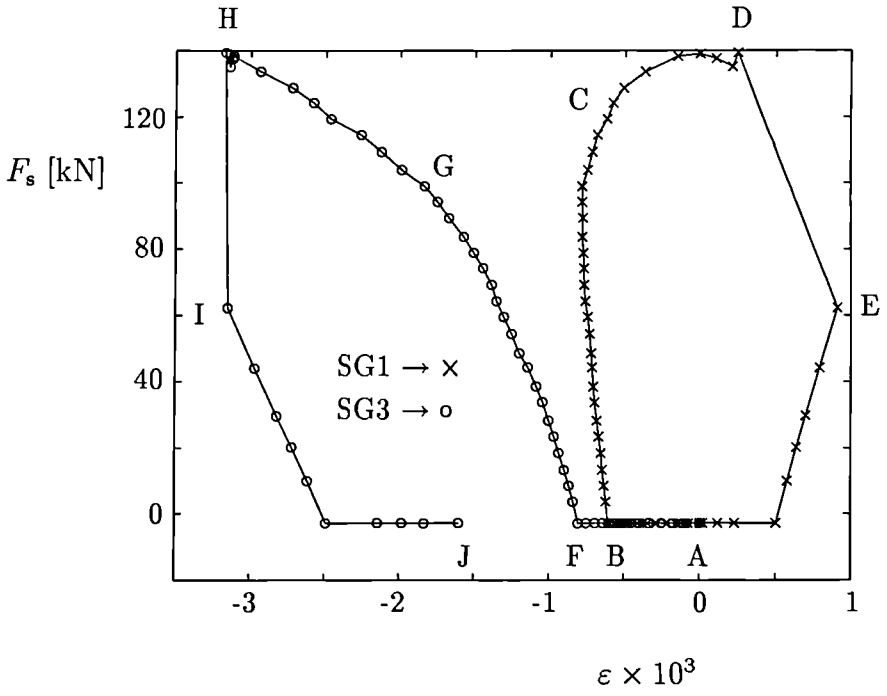

Figure 7.31: Measurements of SG1 and SG3 versus shear force for CW5.

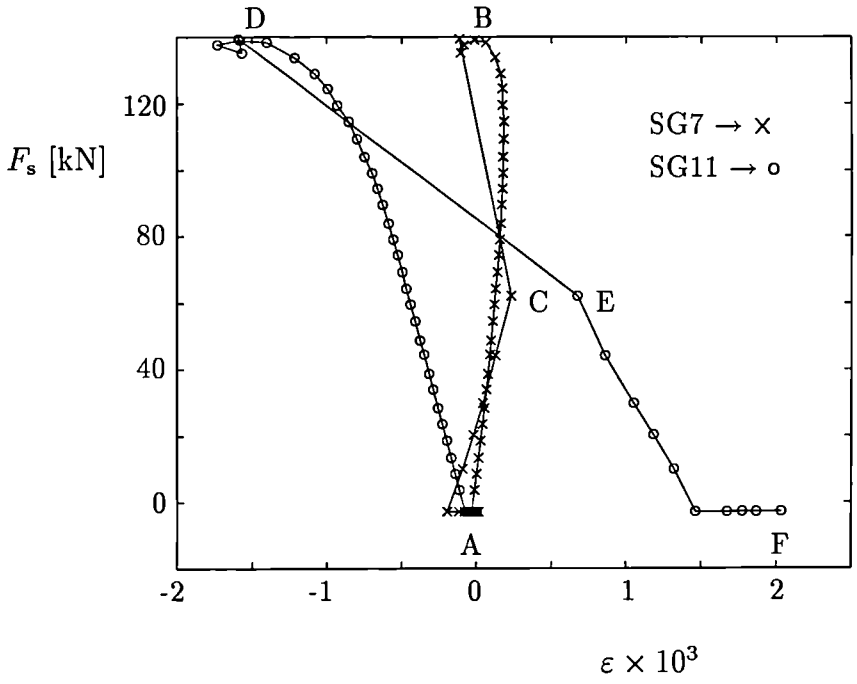

Figure 7.32: Measurements of SG7 and SG11 versus shear force for CW5.

Figure 7.33: Specimen CW5 from side B.

Chapter 8

Analysis and discussion

8.1 Basic theory for analysing the results

8.1.1 The compression flange analysis

8.1.1.1 Effective thickness of flanges

Chapter 2 suggests to use the design assumption that a corrugated web does not contribute to resisting compression or bending being applied to the beam. However, in reality a small part of the web does contribute to resisting compression and bending. Assuming flanges only without any web between them leads to the idea of introducing some effective thickness of the flanges, to include the contributing part of the web into design.

Ten models, given in Table 8.1, with different corrugated web geometry were analysed by finite element analysis. Linear quadrilateral elements were used. The notation for the geometry is shown in Fig. 2.1. The flange width was taken constant: $b_{ft} = b_{fc} = b_f = 200$ mm, and flange thicknesses were assumed to be equal: $t_{ft} = t_{fc} = t_f$. All models have three corrugations in a web. They were intended to be similar to the test specimens. All models were loaded first by pure bending – tension in the top flange and compression in the bottom flange – with equal absolute values of the forces, and then by compression only.

Deformations over a half wave of a corrugated web were found, which gave the

No.	b	d	α	t_w	t_f	$\epsilon_f \times 10^4$
	mm	mm	°	mm	mm	—
1	180	45	45	3	8	2.89
2	100	45	45	3	8	2.97
3	180	100	45	3	8	2.89
4	180	45	30	3	8	2.84
5	180	45	45	6	8	2.80
6	250	100	45	3	6	3.77
7	250	100	45	3	8	2.86
8	250	100	30	3	8	2.83
9	250	45	45	3	6	3.73
10	250	45	45	3	8	2.81

Table 8.1: Geometry of the models for finding the effective thickness of flanges.

1	2	3	4	5	6	7	8
No.	$\frac{b_f+d\tan\alpha}{2b}$	$I_{eff} \times 10^{-8}$	$t_{f,I}$	$\frac{(t_{f,I}-t_f)b_f}{t_w h}$	A_{eff}	$t_{f,A}$	$\frac{(t_{f,A}-t_f)b_f}{t_w h}$
	—	mm^4	mm	—	mm^2	mm	—
1	0.681	1.65	8.544	0.081	3295.4	8.239	0.036
2	1.225	1.61	8.329	0.049	3206.7	8.017	0.003
3	0.833	1.65	8.544	0.081	3295.4	8.239	0.037
4	0.628	1.68	8.724	0.108	3353.5	8.384	0.057
5	0.681	1.71	8.850	0.063	3456.2	8.641	0.048
6	0.600	1.27	6.501	0.075	2525.5	6.313	0.047
7	0.600	1.67	8.678	0.101	3333.5	8.334	0.050
8	0.516	1.69	8.757	0.113	3367.0	8.418	0.062
9	0.490	1.28	6.578	0.086	2554.0	6.385	0.057
10	0.490	1.70	8.806	0.120	3384.4	8.461	0.069

Table 8.2: Effective thicknesses of flanges of an imaginary beam, without any web between the flanges.

mean values of compression strains in the centre–plane of a compression flange. They are listed in the last column of Table 8.1 as ϵ_f. The effective second moment of area can be calculated from

$$I_{eff} = \frac{Mh}{2E\epsilon_f} \tag{8.1}$$

where M is the pure bending moment applied to the models; h is the distance between the centre–planes of the top and bottom flanges; E is Young's modulus. I_{eff} is listed in the third column of Table 8.2.

Neglecting the web between the two flanges with effective thickness $t_{f,I}$ the effective second moment of area can be defined as:

$$I_{eff} = \frac{1}{6}b_f t_{f,I}^3 + \frac{1}{2}t_{f,I}b_f\left(h - t_{f,I}\right)^2 \tag{8.2}$$

from which the cubic equation can be written for $t_{f,I}$:

$$t_{f,I}^3(4b_f) + t_{f,I}^2(-6hb_f) + t_{f,I}\left(3b_f h^2\right) - 6I_{eff} = 0 \tag{8.3}$$

The fourth column of Table 8.2 lists the solutions of eq. 8.3 for each model.

Similarly the effective thickness of a flange was developed from compression analysis of the models. The effective cross–sectional area was calculated from

$$A_{eff} = \frac{F}{E\epsilon_f} \tag{8.4}$$

The effective thickness of flanges replacing a corrugated web is

$$t_{f,A} = \frac{A_{eff}}{2b_f} \tag{8.5}$$

These are listed in the sixth and seventh columns of Table 8.2.

From the values found for effective thicknesses of flanges the ratios shown in the second, fifth and eight columns were calculated and the results were plotted in Fig. 8.1. Those ratios were chosen to show the relationship between the geometry of the beam with and without a corrugated web. If we consider the ratio $(b_f + d\tan\alpha)/2$ to b, which is plotted on the x–axis, if b is zero, the ratio tends to infinity and t_{eff} for

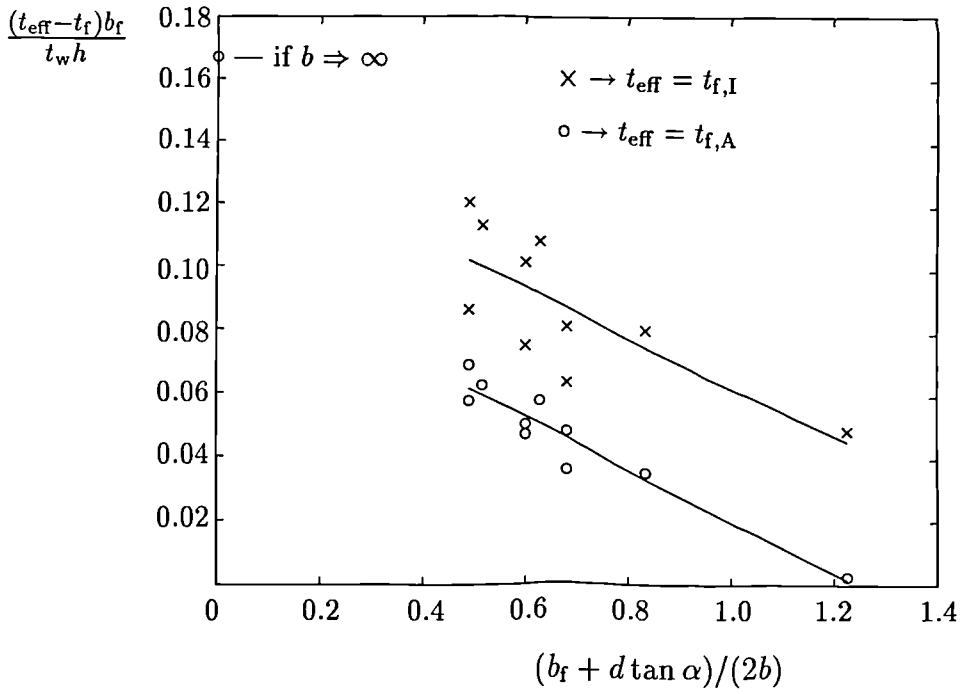

Figure 8.1: Effective thicknesses of flanges.

either bending or compression should tend to t_f. If $b \Rightarrow \infty$, the ratio plotted on the x–axis is zero, and a corrugated web becomes a straight one, which gives the value of the ratio $(t_{eff} - t_f)b_f$ to $t_w h$ equal 0.167, shown in Fig. 8.1. The linear regression was performed for both of the sets of points shown. From these linear relationships the effective thicknesses of flanges of the imaginary beam without any web between the flanges can be calculated from the following equations:

– for bending effects:

$$t_{f,I} = \left(0.14 - 0.076\frac{b_f + d\tan\alpha}{2b}\right) t_w h/b_f + t_f \tag{8.6}$$

– for compression effects:

$$t_{f,A} = \left(0.10 - 0.081\frac{b_f + d\tan\alpha}{2b}\right) t_w h/b_f + t_f \tag{8.7}$$

According to Fig. 8.1, a beam with corrugated web is less stiff in pure compression than in pure bending (the line for pure bending is above the one for pure

compression). The reason is believed to be in the different boundary conditions applied to the sloping parts of a corrugated plate. While in pure bending a sloping part of a web is twisted, in pure compression the whole part is rotated about a vertical axis. Because the angles between the sloping and flat parts of the web stay constant, the compression in mid-depth of the beam in pure compression causes more out of plane deformation of width b of the flat part of the web, than occurs in pure bending. The compressive strain across the flat part of the web is then less than if it stayed flat.

8.1.1.2 Longitudinal stresses and strains in flanges

According to the set up of the experiments (Fig. 8.3) and considering the imaginary beam consisting only of two flanges with thicknesses t_{ft} and t_{fc} (Fig. 8.2) the

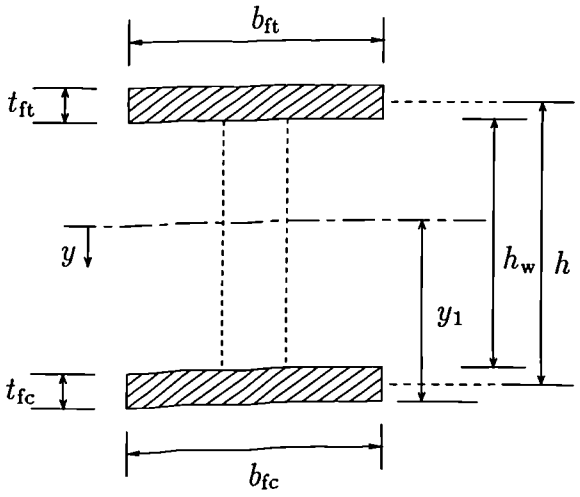

Figure 8.2: Effective cross-section.

longitudinal stresses can be obtained from

$$\sigma = \frac{F}{(A_{ft} + A_{fc})} + \frac{M_1}{I_1} y \tag{8.8}$$

where A_{ft}, A_{fc} are the cross-sectional areas of tension and compression flanges, respectively; y_1 and I_1 are given by

$$y_1 = \frac{t_{fc}}{2} + \frac{A_{ft}h}{(A_{ft} + A_{fc})} \tag{8.9}$$

$$I_1 = \frac{1}{12}\left(A_{fc}t_{fc}^2 + A_{ft}t_{ft}^2\right) + A_{fc}\left(y_1 - \frac{t_{fc}}{2}\right)^2 + A_{ft}\left(h - y_1 + \frac{t_{fc}}{2}\right)^2 \tag{8.10}$$

F is the load applied parallel to the length of the specimen at a distance $(l + y_1)$ from the neutral axis (eq. 8.11); and y is distance of the studied surface from the neutral axis. According to Fig. 8.3, F, l and M_1 are defined as follows:

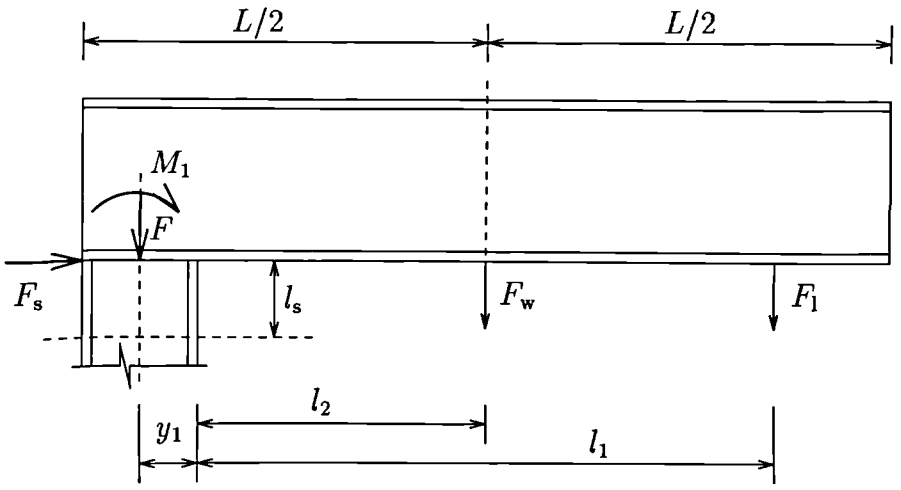

Figure 8.3: System of loading the specimens.

$$F = F_w + F_l \tag{8.11}$$

$$l = \frac{F_l l_1 + F_w l_2}{F_l + F_w} \tag{8.12}$$

$$M_1 = F_w(l_2 + y_1) + F_l(l_1 + y_1) + F_s l_s \tag{8.13}$$

The mean strains were determined in the following way:

- compression flange

$$\varepsilon_c = \frac{\Delta c}{l_{compr}} \tag{8.14}$$

where Δc was taken from measured deformations by LVDT over the gauge length of l_{compr};

- tension flange

$$\varepsilon_t = \left(\frac{\Delta t_A}{l_{tensA}} + \frac{\Delta t_B}{l_{tensB}}\right)/2 \tag{8.15}$$

where Δt_A was the extension measured by LVDT - tensA over the length l_{tensA}; and Δt_B was the extension measured by LVDT - tensB over the length l_{tensB}. The lengths l_{compr}, l_{tens} are defined in Fig. 7.1.

8.1.1.3 Slenderness of flange outstands

The elastic critical theory for compression outstands given by [28] gives the critical stress as

$$\sigma_{cr} = k\left[\frac{\pi^2 E}{12(1-\nu^2)(c/t_f)^2}\right] \tag{8.16}$$

where $k = 0.425$ for one edge simply supported, the other free. The slendernesses $\overline{\lambda}$ for small, average, and large outstands of the flange of specimens can be determined from the elastic theory critical curve given by

$$\overline{\lambda} = \sqrt{\frac{f_y}{\sigma_{cr}}} \tag{8.17}$$

8.1.1.4 Moment rotation relationship

Fig. 8.4 shows the loading of the beam by a combination of compression and shear forces and bending moment, as in the tests, and by pure bending moment, respectively. The steel flanges in both cases are assumed to be identical. The curvature is then defined by

$$\phi = \frac{M_1}{EI_1} = \frac{M_2}{EI_2} \tag{8.18}$$

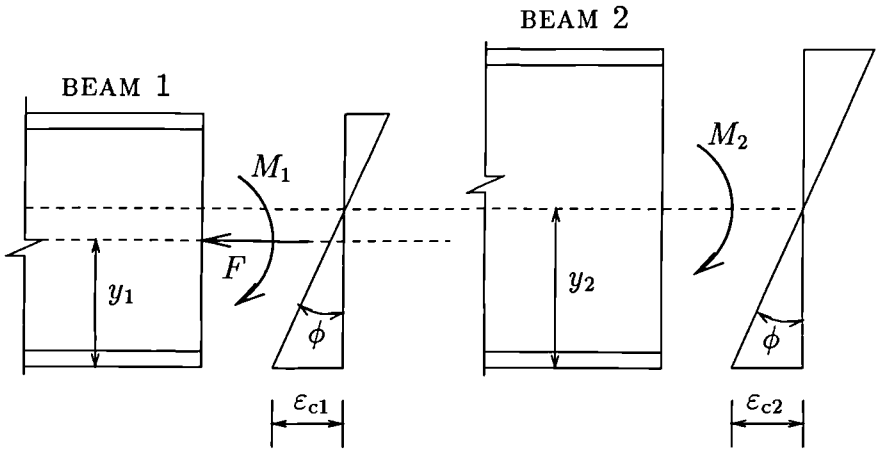

Figure 8.4: Beams under different loading conditions but same curvature.

where I_1, I_2 are the second moments of area of beams 1 and 2, respectively; and moment M_1 is (assuming eqs. 8.11 and 8.12)

$$M_1 = F(l + y_1) + F_s l_s. \tag{8.19}$$

The ratio between M_1 and M_2 is

$$\frac{M_2}{M_1} = \frac{I_2}{I_1} \tag{8.20}$$

Longitudinal strains at the outside surface of the compression flange of beam 1 are defined by

$$\varepsilon_{c1} = \phi y_1 + \frac{F}{(A_{fc} + A_{ft})E} \tag{8.21}$$

where A_{fc} and A_{ft} are cross–sectional areas of the compression and tension flanges, respectively, and y_1 is the geometrical neutral axis of the real cross–section (defined by eq. 8.9).

Longitudinal strains at the outside surface of the compression flange of beam 2 are

$$\varepsilon_{c2} = \phi y_2 \tag{8.22}$$

Based on the condition of equal curvature for both beams

$$\varepsilon_{c1} = \varepsilon_{c2}. \tag{8.23}$$

Hence

$$\phi y_2 = \phi y_1 + \frac{F}{(A_{fc} + A_{ft})E}. \tag{8.24}$$

Substituting eq. 8.18 into 8.24

$$y_2 = y_1 + \frac{F}{M_1}\frac{I_1}{(A_{fc} + A_{ft})} \tag{8.25}$$

Substituting eq. 8.19 into 8.25 the neutral axis of the imaginary beam 2 loaded by pure bending is

$$y_2 = y_1 + \frac{FI_1}{(A_{fc} + A_{ft})[F(l + y_1) + F_s l_s]} \tag{8.26}$$

where for $F_s = 0$ (tests CW1 and CW2)

$$y_2 = y_1 + \frac{I_1}{(A_{fc} + A_{ft})(l + y_1)} \tag{8.27}$$

8.1.2 Shear in a web

8.1.2.1 Shear in a web from diagonal deformations

The mean shear stresses in a web are obtained from:

$$\tau = \frac{F_s}{h_w t_w} \tag{8.28}$$

If bending, compression and shear deformations of a web are separated, the difference between the changes of length of the diagonals of a web is zero for bending and compression. This difference is influenced only by shear deformations of a web panel. From the geometry of the Fig. 8.5 it can be written:

$$d_{2\gamma}^2 = (l_n + l_p \cot \Omega)^2 + l_p^2 \tag{8.29}$$

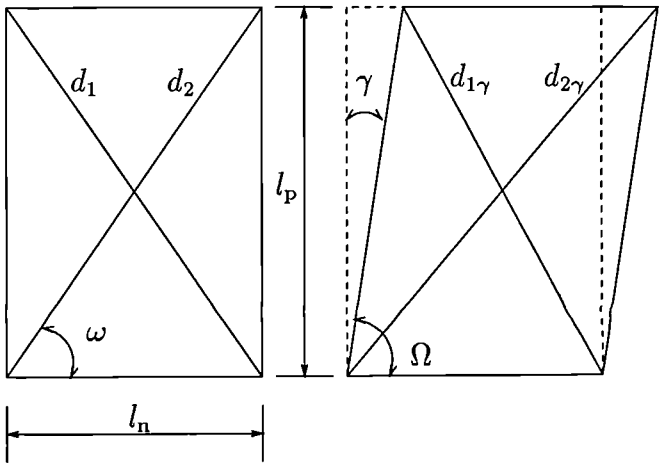

Figure 8.5: Shear deformation based on the diagonals measurements.

$$d_{1\gamma}^2 = (l_n - l_p \cot \Omega)^2 + l_p^2 \tag{8.30}$$

Subtracting these two equations

$$\cot \Omega = \frac{d_{2\gamma}^2 - d_{1\gamma}^2}{4 l_p l_n} = \tan \gamma \approx \gamma \tag{8.31}$$

where

$$d_{2\gamma} = d_2 + \Delta d_{2\gamma} \tag{8.32}$$

$$d_{1\gamma} = d_1 + \Delta d_{1\gamma} \tag{8.33}$$

Assuming $d_1 = d_2 = d$ and $(\Delta d_{2\gamma})^2 - (\Delta d_{1\gamma})^2 = 0$, then from eqs. 8.32 and 8.33

$$d_{2\gamma}^2 - d_{1\gamma}^2 = 2d(\Delta d_{2\gamma} - \Delta d_{1\gamma}) + \left[(\Delta d_{2\gamma})^2 - (\Delta d_{1\gamma})^2\right] = 2d(\Delta d_{2\gamma} - \Delta d_{1\gamma}) \tag{8.34}$$

Substituting eq. 8.34 into eq. 8.31

$$\gamma = \frac{2d(\Delta d_{2\gamma} - \Delta d_{1\gamma})}{4 l_n l_p} \tag{8.35}$$

For $l_n = d\cos\omega$ eq. 8.35 can be written as

$$\gamma = \frac{\Delta d_{2\gamma} - \Delta d_{1\gamma}}{2l_p \cos\omega}. \tag{8.36}$$

8.1.2.2 Shear in a web from horizontal deformations

Another possible way to check the shear modulus is to consider a specimen acting as a cantilever with a clamped end on the bottom (held by the bottom beam, which was rigidly fixed to the floor) and a free end at the top of the specimen (where the attachment to the top loading beam was made) as shown in Fig. 8.6. The elastic bending deformation of the cantilever at its free end loaded by a force and a moment,

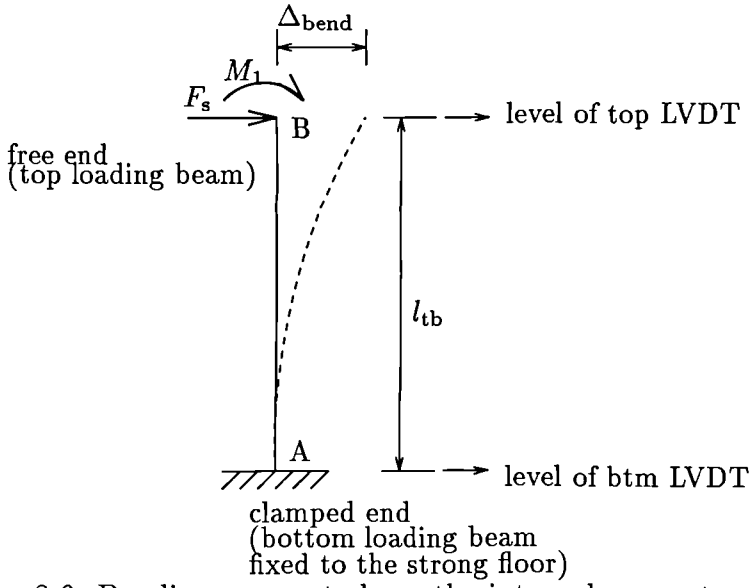

Figure 8.6: Bending moment above the internal support.

both located at the free end is given by

$$\Delta_{bend} = \frac{F_s l_{tb}^3}{3EI_1} + \frac{M_1 l_{tb}^2}{2EI_1} \tag{8.37}$$

where Δ_{bend} is considered at the level of the top LVDT (see also Section 6.5), so that the bending moment is calculated from eq. 8.13 where l_s is the distance of the level of the top LVDT from the level of the applied shear force F_s. I_1 are defined in Section 8.1.1.4.

The attachment to the bottom loading beam was not perfectly rigid. Therefore it cannot be assumed that the specimen was clamped at its bottom end. The rotation in this place (point A in Fig. 8.6) was measured by clinometer placed in the middle of a specimen depth on the end plate (see Fig. 6.6) in tests CW4 and CW5 and it gives additional horizontal deformation at the free end equal to $\theta_{\text{btm}} l_{\text{tb}}$.

Finally there is also shear deformation

$$\Delta_{\text{shear}} = \Delta_{\text{z}} - \Delta_{\text{bend}} \tag{8.38}$$

where $\Delta_{\text{z}} = \delta_{\text{top}} - \delta_{\text{btm}} - \theta_{\text{btm}} l_{\text{tb}}$ is the whole deformation, and $\delta_{\text{top}} - \delta_{\text{btm}}$ is defined as the difference of top and bottom horizontal deformations measured along the loading beams.

The shear strain is then

$$\gamma = \frac{\Delta_{\text{shear}}}{l_{\text{tb}}} \tag{8.39}$$

The effective shear modulus of a corrugated web is then given by

$$\tau = G_{\text{eff}} \gamma \tag{8.40}$$

8.2 The compression flange analysis

8.2.1 Shortening of flanges

Test results are compared with simple elastic theory in stress-strain diagrams (Figs. 8.7 to 8.11). For the x–axis the mean strains were calculated from measurements of the deformation of compressed flange over the length l_{compr} in the level of the compression LVDT. The eq. 8.14 was used for this purpose. For the y–axis the longitudinal mean values of compression stress were adopted, derived from the eq. 8.8, where y represents the distance of the LVDT level from the neutral axis. When divided by the yield stress, f_{y}, of compression flange given in Table 7.4, it can represent the relative mean stress.

The straight lines in Figs. 8.7 to 8.11 represent the elastic theory for the com-

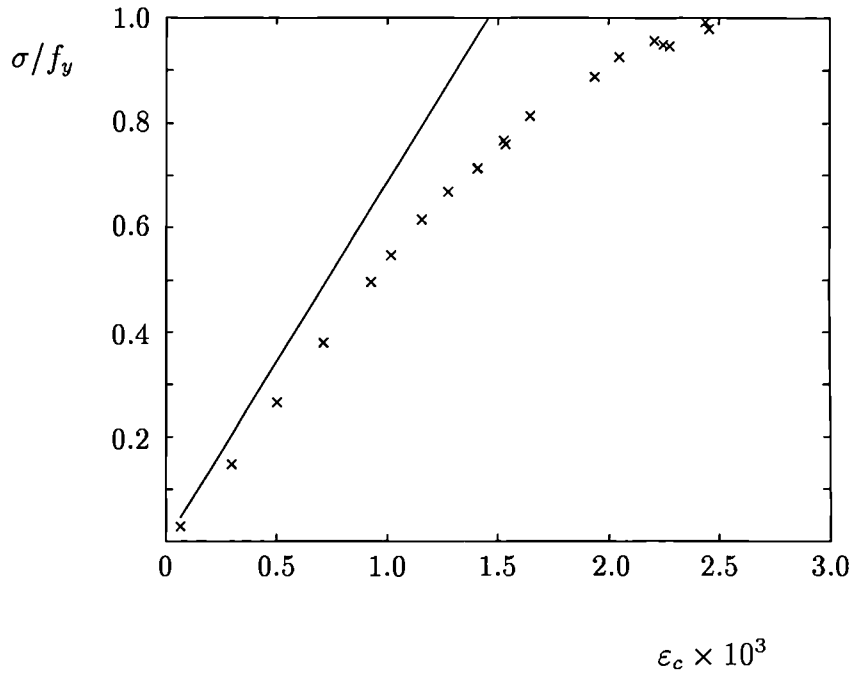

Figure 8.7: Mean stress — mean strain in the compression flange of CW1.

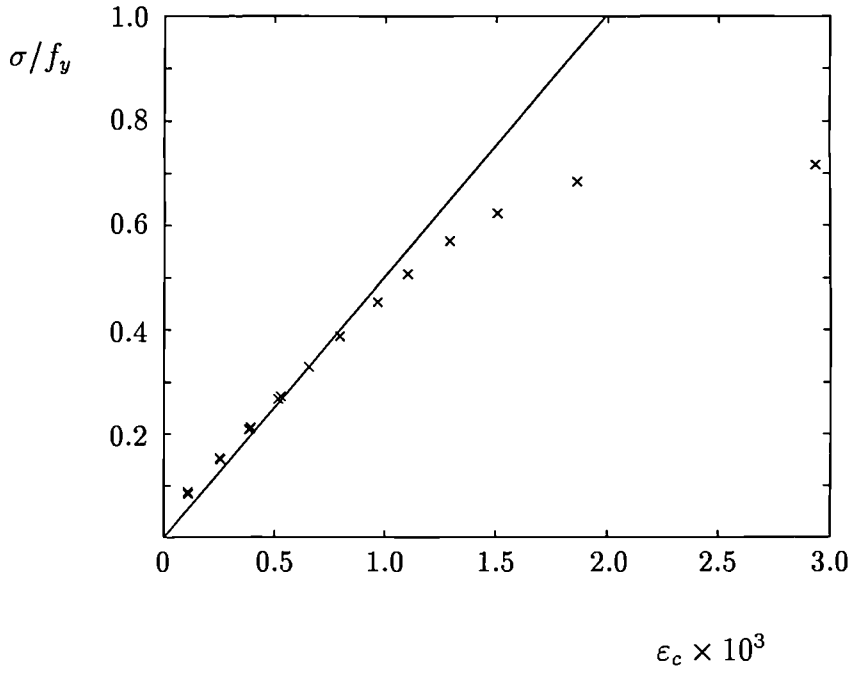

Figure 8.8: Mean stress — mean strain in the compression flange of CW2.

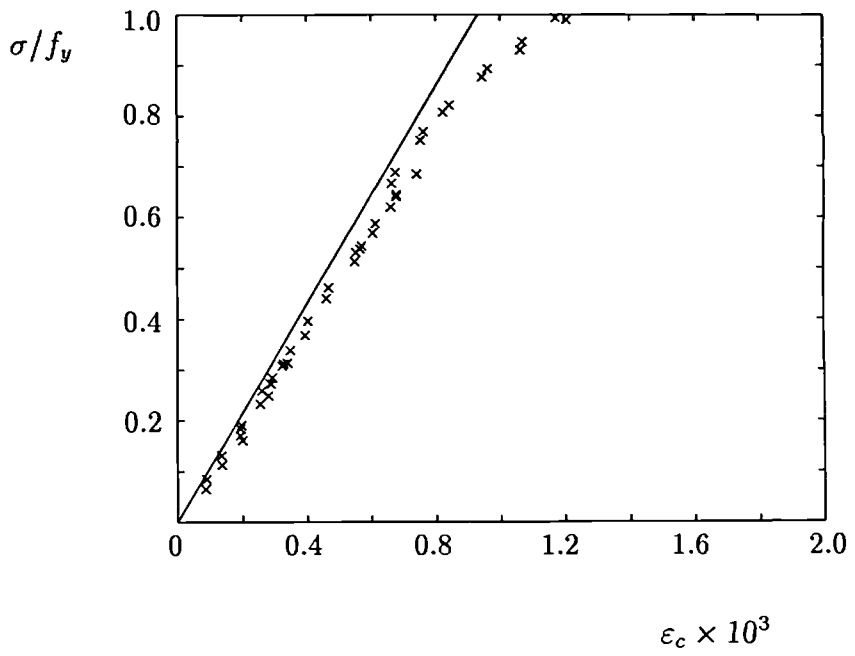

Figure 8.9: Mean stress — mean strain in the compression flange of CW3.

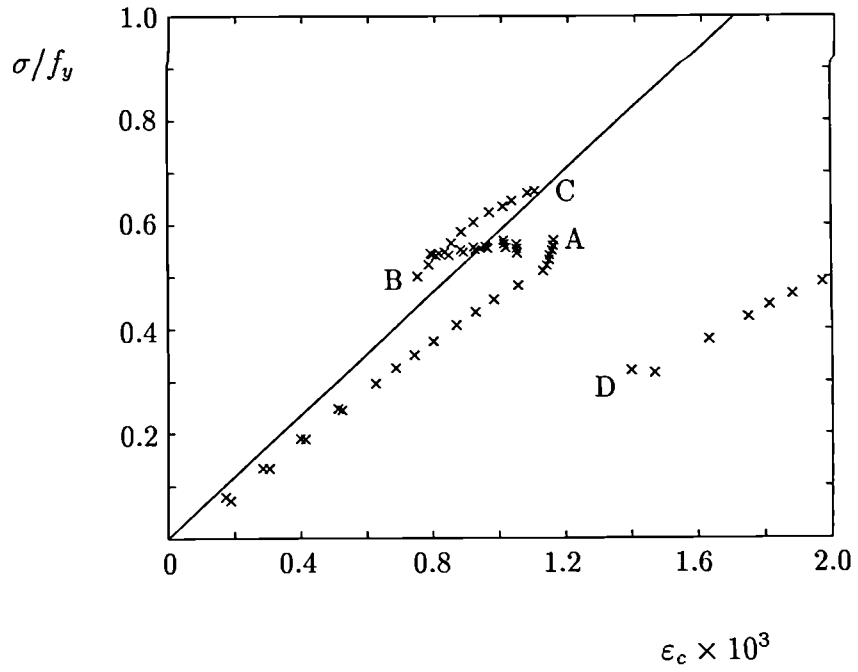

Figure 8.10: Mean stress — mean strain in the compression flange of CW4.

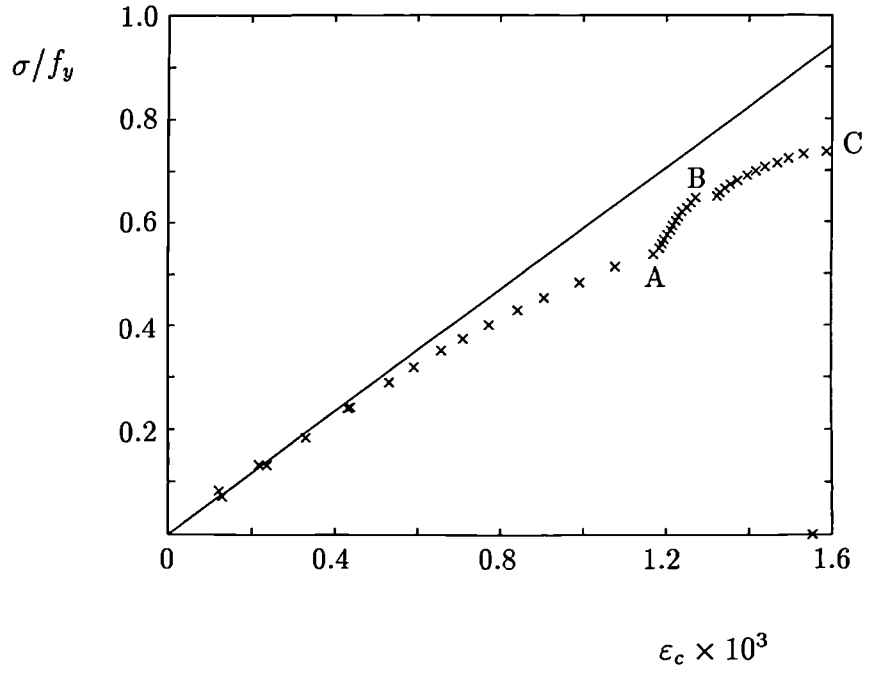

Figure 8.11: Mean stress — mean strain in the compression flange of CW5.

pressed member. The final equation of this linear function is

$$\varepsilon_{\text{theory}} = \frac{f_y}{E}\left(\frac{\sigma}{f_y}\right) \tag{8.41}$$

Table B.1 in Appendix B gives the effective geometrical dimensions calculated from measured values shown in Table 7.1, using eqs. 8.6, 8.7. The values of A_{eff}, $I_{1,\text{eff}}$, $y_{1,\text{eff}}$, and A, I_1, y_1 are *effective* and *measured* values of the specimens' cross-sectional properties, respectively.

Originally, it was believed that use of the effective thicknesses of the compression and tension flanges would give better agreement with the elastic theory. However, it was found that using the measured values from Table 7.1 and the third part of Table B.1 to calculate the mean values of compressive stress given by eq. 8.8 for plotting the diagrams in Figs. 8.7 to 8.11 agreed with elastic theory much better. The measured values are therefore used in these figures. The finite element modelling analyses models with perfect geometry and perfectly rigid end plates. This is not the case for the real specimens. Although their end plates are 20 mm thick, which

can be approximately considered as rigid, in reality they also deform. This creates different boundary conditions which may cause the above mentioned discrepancies.

Basically, all five diagrams give very good agreement between the theory and test results in the elastic region. The largest discrepancy in the slopes given by theory and test is observed in Fig. 8.7 for test CW1. It is believed to be the result of the large longitudinal imperfection described in Section 7.3.

In Fig. 8.10, when the test curve reached point A, the stress in the compression flange was approx. 165 N/mm^2. The shear load started to be applied to the specimen, which decreased the bending load and released the compression strains in the flange (see also Section 6.6.3). When the force from the bending jack was reduced to zero – point B – applied shear loading increased the compressive strain in the flange again (from B to C). The specimen's web buckled suddenly in shear, which decreased the mean stress to approx. 0.3 f_y (point D). Then the specimen was re–loaded by bending, so the increase of the test curve can be observed again starting from point D.

8.2.2 Local buckling of flanges

The local buckles of compression flanges appeared in all five tests in a large outstand of the flange. In tests CW1 and CW2 the bending moment was constant through the whole length of the specimens. Therefore buckles developed in all three large outstands, but were not as visible in the top outstand as in the other two. In experiments CW3, CW4 and CW5 the bending moment in the specimens was increasing from the top to bottom, which was caused by applied shear force. That means that the maximum compression force was in the bottom large outstand, where the buckles finally appeared in tests CW3 and CW5. Specimen CW4 buckled first in shear in the middle flat part of the web, which caused the deformation and yielding of the compressed flange in this place as well.

According to eqs. 8.16 and 8.17 the slendernesses of the large, average and small outstands of the specimens were calculated and they are summarised in Table 8.3.

The compressive stresses, σ_{max}, in the flanges of the specimens were calculated

according to eq. 8.8, using the measured geometrical values from Table 7.1 and Appendix B. For specimens CW1 and CW2 it is not important in which cross-section of the three flat parts of the web the stresses σ_{max} is calculated. For the remaining specimens the stress was determined in the cross-section in the middle of the bottom flat part of the web. This cross-section is defined by the variable l_s (see Fig. 8.3). The compressive stresses, σ_{max}, were calculated on the outside surface

	units	CW1	CW2	CW3	CW4	CW5
c_S	mm	72.33	71.03	71.13	73.17	64.17
$\sigma_{cr,S}$	N/mm^2	1085.4	570.1	1155.6	564.9	715.3
$\bar{\lambda}_S$		0.531	0.852	0.432	0.800	0.711
$\sigma_{d,S}$	N/mm^2	306.0	360.4	216.0	328.1	351.6
c_A	mm	96.00	95.73	95.22	95.50	95.50
$\sigma_{cr,A}$	N/mm^2	616.1	313.9	644.9	331.6	323.0
$\bar{\lambda}_A$		0.705	1.149	0.579	1.045	1.059
$\sigma_{d,A}$	N/mm^2	298.6	291.3	216.0	273.5	270.8
c_L	mm	119.67	120.43	119.30	117.83	126.83
$\sigma_{cr,L}$	N/mm^2	396.5	198.3	410.8	217.8	183.1
λ_L		0.878	1.445	0.725	1.289	1.406
$\sigma_{d,L}$	N/mm^2	261.2	242.9	207.5	232.9	217.2
F_l	kN	87.9	57.7	32.94	0	8.87
F_s	kN	0	0	92.06	152.94	133.72
σ_{max}	N/mm^2	296.37	276.5	219.42	226.32	254.46
σ_{max}/f_y		0.969	0.668	1.016	0.625	0.703
A_{ratio}		0.186	0.187	0.195	0.195	0.262

Table 8.3: Slendernesses, forces and stresses for the compression flanges.

of the compression flanges. Thus the value $y = y_1$ (see also Fig. 8.2) was used in eq. 8.8. Designers would use the maximum values of compression stresses in flanges for bridge design and not the mean values, which would appear in the centre-plane of the compression flange. The values of σ_{max} for each specimen are listed in Table 8.3. This table also shows the forces F_l and F_s used in eq. 8.8. For specimens CW1 and CW2 they are obviously the maximum bending forces, $F_{l,max}$. The maximum compression stress in the flange of specimen CW3 was reached with the maximum bending load $F_{l,max} = 32.94$ kN. The shear force at that moment was $F_s = 92.1$ kN.

The maximum compression stresses, σ_{max}, for specimens CW4 and CW5 were not reached when $F_l = F_{l,max}$. $F_{l,max}$ in both tests was reached when $\sigma = \sigma_A$ in Figs. 8.10 and 8.11. Then the bending force was gradually released by increasing shear force – curve AB. The compression stress in the flange was not released. It continued to rise with increasing shear loading until point C. Thus Table 8.3 shows the values of F_l and F_s when σ_{max} was reached, which does not necessarily mean, that one of the bending or shear load has to be the maximum.

The yield compressive stress, f_y, and Young's modulus, E, were taken from Table 7.4 for compression flange only, since local buckling is observed in the compression flange only.

The variables $\sigma_{cr,S}$, $\sigma_{cr,A}$ and $\sigma_{cr,L}$ are critical stresses computed from eq. 8.16 for c_S, c_A and c_L, which are small, average and large outstands of the compression flange, respectively. The outstands were measured on the inside surfaces of the specimens' compression flanges at the cross–sections in the middle of each flat part of a corrugated web. Thus each specimen had three values for small, average and large outstands. The values c_S, c_A and c_L in Table 8.3 represent the mean values of the above mentioned three measurements, measured from weld.

The results from Table 8.3 are plotted in Fig. 8.12, where S_i, A_i and L_i represent the small, average and large outstands of the flanges for specimens i = 1 to 5, respectively, together with the elastic critical curve given by eq. 8.17 and the design curve taken from EC3 for class 4 outstands.

The design curve taken from EC3 for class 4 cross–section is defined by the reduction factor χ, which is obtained from the following:

- when $\overline{\lambda}_p \leq 0.673$:
  $\chi = 1$
- when $\overline{\lambda}_p > 0.673$:
  $\chi = (\overline{\lambda}_p - 0.22)/\overline{\lambda}_p^2$

where $\overline{\lambda}_p$ is the plate slenderness given by eq. 8.17. The design value of the com-

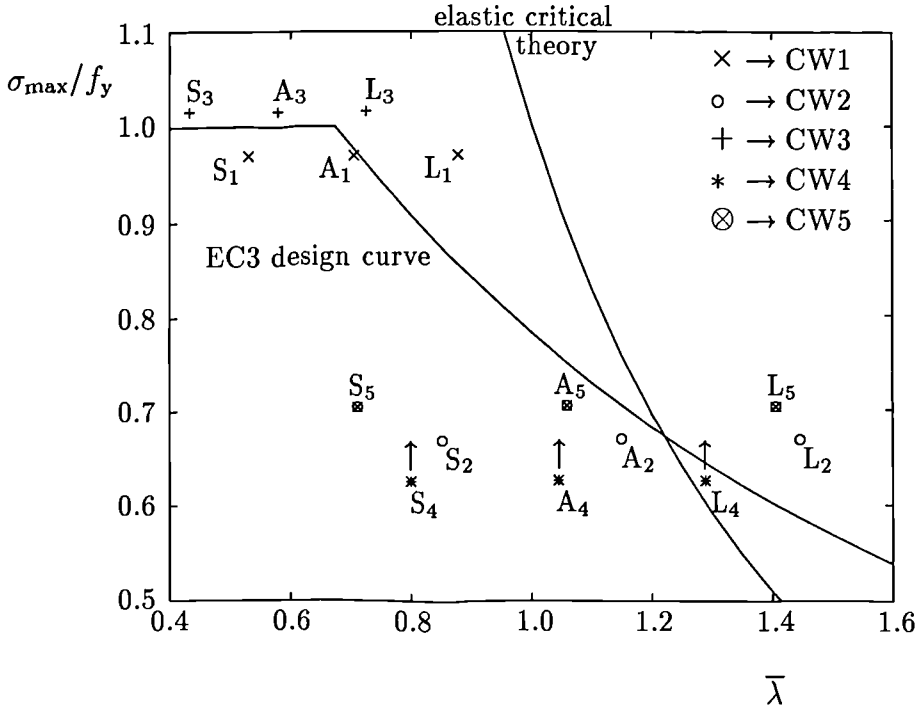

Figure 8.12: Comparison of the tests results with the theory and design rules.

pression stress, σ_d, is then calculated from

$$\sigma_d = \chi f_y \tag{8.42}$$

The values are given in Table 8.3 for each outstand of each specimen.

Specimens CW1 and CW3 differs in the width of the flat part of the corrugated web. Their width–to–thickness ratios of compression flanges are approximately the same. The values of maximum relative stresses in the flanges are close (both values of $\sigma_{max}/f_y \approx 1$). They differ only by about 4 %. The same applies for the specimens CW2 and CW5. Their width–to–thickness ratios of compression flanges are also very similar (33.52 for CW2 and 33.42 for CW5 with the difference 0.3 %). The difference between $(\sigma_{max}/f_y)_{CW2}$ and $(\sigma_{max}/f_y)_{CW5}$ is about 5 %, which is still in a good agreement. Specimen CW4 buckled unexpectedly in shear first, thus the maximum compression stress in the specimen flange was not reached. It is assumed that the value of $(\sigma_{max}/f_y)_{CW4}$ would be close to the value of the same stress ratio of specimen CW5, since $(b_{fc}/t_{fc})_{CW4} = 33.13$. The difference between $(b_{fc}/t_{fc})_{CW4}$

and $(b_{fc}/t_{fc})_{CW5}$ is 1.16 %, but the difference between the stress ratios is 11.1 %.

The last line of Table 8.3 give the values of A_{ratio} defined in Section 5.3.4. All these values indicates that a large outstand should be used in a design of the compression flange because they are all larger than 0.14 which is the upper limit for using the average outstand.

Nevertheless, the angle α of all specimens was 45°. This condition is better than if $\alpha = 30°$. It is explained in Section 5.3.4 that for $\alpha = 45°$ the boundary for A_{ratio} would be slightly higher. For using the average outstand it would rise to $A_{ratio} < 0.19$. This means that CW1 and CW2 would satisfy the condition for using the average outstand in a design. In Fig. 8.12 point A_1 of the average outstand for specimen CW1 is almost on the design curve taken from EC3. Point A_2 is close to the design curve. $(\sigma_{max}/\sigma_{d,A})_{CW2} = 0.95$ where $\sigma_{d,A}$ is given in Table 8.3 for specimen CW2.

Specimen CW3 reached the maximum compression stress which is larger then the yield stress, f_y, obtained from tensile tests. Therefore the design curve from *EC3* does not pass between any of the points S_3, A_3 or L_3. The ratio A_{ratio} suggests to use the large outstand for the buckling design of the compression flange. If $\sigma_{max} < f_y$ the design curve would pass between A_3 and L_3 which would perfectly agree with limitation given by A_{ratio}.

For specimen CW5 the EC3 design curve is passing between the points for average, A_5, and large, L_5, outstands. Thus the large outstand has to be used in a design. This conclusion supports the finite element results given in Section 5.3.4. $(\sigma_{max}/\sigma_{d,A})_{CW5} = 0.94$.

As it was mentioned above, specimen CW4 buckled prematurely in shear, which significantly deformed the compression flange. Thus the maximum compression stress in the flange could not be reached. This explains why point L_4 for large outstand of the flange is below the EC3 design curve.

8.2.3 Inelastic rotation

The mean value of curvature can be calculated from

$$\phi_{\text{mean}} = \frac{\varepsilon_c + \varepsilon_t}{h_w + t_{fc} + t_{ft} + \Delta_{\text{compr}} + \Delta_{\text{tens}}}. \tag{8.43}$$

where ε_c and ε_t are given by eqs. 8.14 and 8.15.

The inelastic rotation θ_i (due to yielding and buckling) is defined by

$$\theta_t = \theta_i + \int_0^{l_{\text{gauge}}} \frac{M_{(x)}}{EI} dx = \phi_{\text{mean}} l_{\text{gauge}} \tag{8.44}$$

where l_{gauge} is either the length over which the deformations of flanges in tests CW1 and CW2 were measured and, taken as an average value of l_{compr} and l_{tens}, or the length of the specimens CW4 and CW5.

The rotation θ_i is assumed to result from an inelastic curvature ϕ_i. For tests CW1 and CW2 it is considered to be constant over the length l_{gauge}, which is one wave of corrugated web, because of the assumed constant bending moment in the specimens. So θ_i is defined by

$$\theta_i = \phi_i l_{\text{gauge}} \tag{8.45}$$

where ϕ_i is determined from

$$\phi_i = \phi_{\text{mean}} l_{\text{gauge}} - \phi_e l_{\text{gauge}} \tag{8.46}$$

where ϕ_e is the elastic curvature. This inelastic rotation defined over the wave of the corrugated web for tests CW1 and CW2 had obtained two full buckles in both tests. That means that one buckle would occur in each half–wave of corrugated web. So the final inelastic rotation is half of the one given by eq. 8.45.

A different situation arose for tests CW3, CW4 and CW5. The buckles occured outside of the length l_{gauge}, as it was defined for tests CW1 and CW2. The bending moment cannot be assumed constant along the length of the specimens. For those reasons, the inelastic rotation could not be calculated as described above. In tests CW4 and CW5 the rotations of the end plates were measured so the total rotation

is determined from

$$\theta_t = \theta_{top} - \theta_{btm} \tag{8.47}$$

Assuming the constant stiffness EI the integral from eq. 8.44 can be evaluated.

Fig. 8.13 shows the inelastic rotation of specimens CW1, CW2, CW4 and CW5.

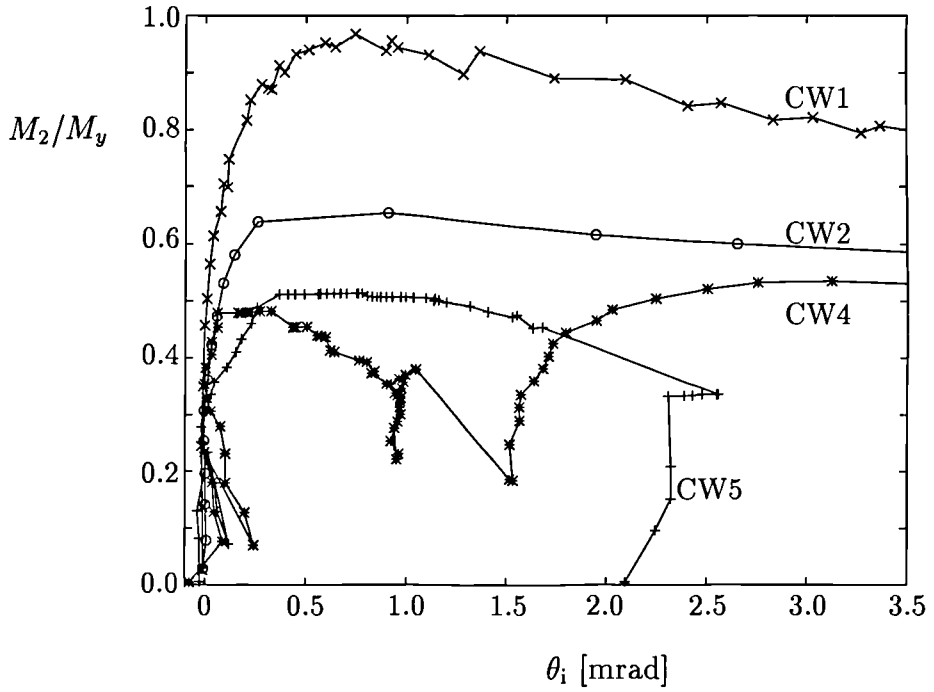

Figure 8.13: Inelastic rotation.

It was not possible to determine the inelastic rotation of specimen CW3, because the rotations of the end plates were not measured and the buckle occurred outside of the range where the compression deformation of the flange was monitored. The y-axis in Fig. 8.13 represents the bending moment M_2 defined by eq. 8.20.

The inelastic rotation given in Fig. 8.13 is rather conservative. It was calculated on the base of real geometrical values of cross-sections (as described in Section 8.1.1.4). Using the effective values developed in Section 8.1.1.2 would increase the second moment of area, I_1, and thus increase the inelastic rotation calculated from eq. 8.44.

8.3 Shear analysis

8.3.1 Effective shear modulus of a corrugated web

8.3.1.1 Results from tests CW3, CW4 and CW5

For the mean shear stress – mean shear strain diagram (Figs. 8.14 to 8.16) eq. 8.28 was used for the y–axis, and eqs. 8.36 and 8.39 were used for the x–axis. Crosses

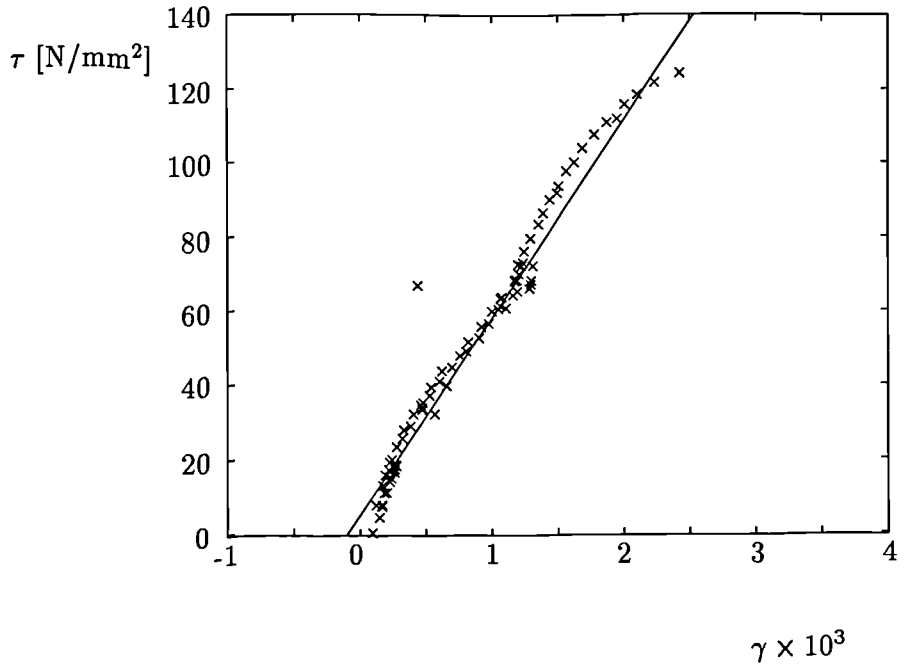

Figure 8.14: Mean shear stress – mean shear strain diagram for test CW3.

are used to show the γ — τ relation for γ derived from eq. 8.36 and circles for γ derived from eq. 8.39. The diagram for specimen CW3 (Fig. 8.14) does not give the shear stress–strain relation expressed by eq. 8.39, because the horizontal movement of the specimen was not measured during this test.

Section 7.1 gives the values of a length of a diagonal LVDT measured between the points of ball joints (see Fig. 8.17) as d_1 or d_2 for both sides of the specimens. The mean strain calculations were based on measured lengths l_{d1} and l_{d2}, listed in Table 8.4, rather than on d_1 and d_2 (l_{d1} and l_{d2} are the average values of the measured diagonals from both sides of a specimen). An angle ω used in eq. 8.36 was then

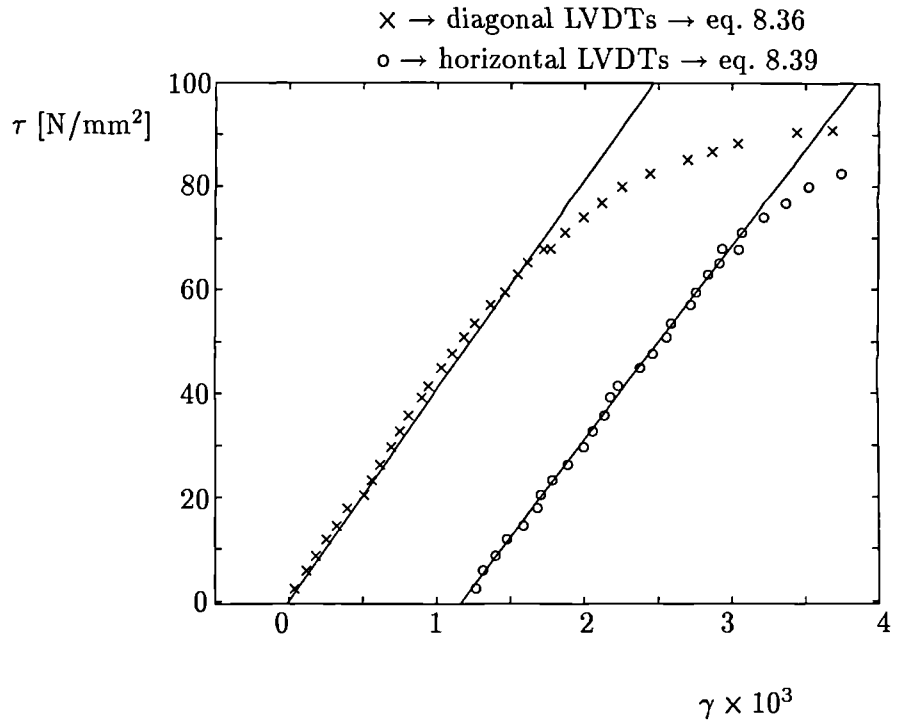

Figure 8.15: Mean shear stress – mean shear strain diagram for test CW4.

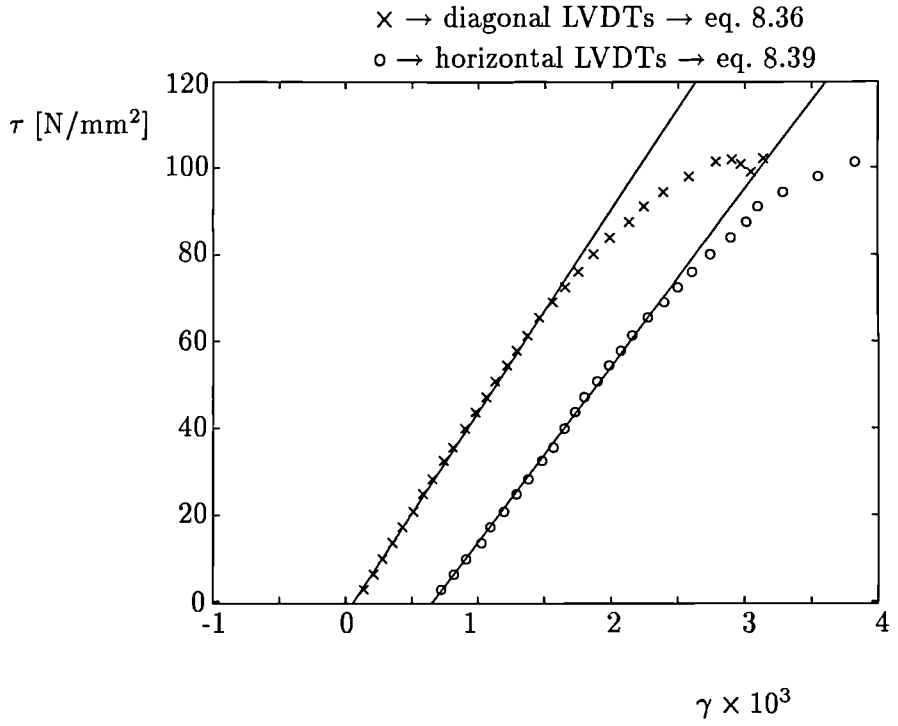

Figure 8.16: Mean shear stress – mean shear strain diagram for test CW5.

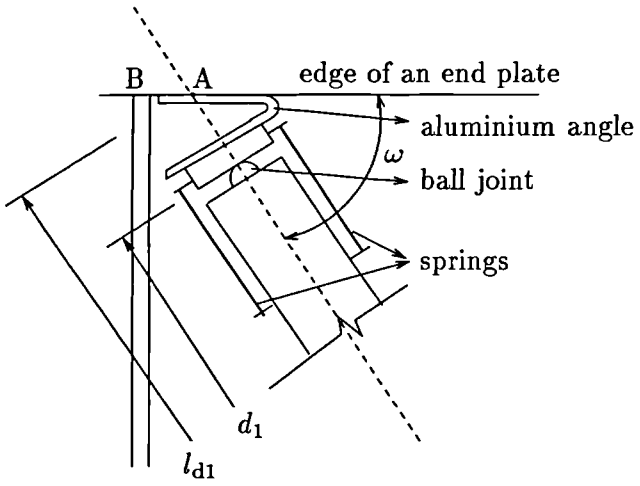

Figure 8.17: Fixing a diagonal LVDT to the end plate.

	CW3	CW4	CW5
l_{d1}	952.17 mm	979.48 mm	1026.17 mm
l_{d2}	973.64 mm	976.19 mm	1027.69 mm
ω_1	68.32°	64.53°	66.14°
ω_2	65.33°	64.94°	65.95°
ω	66.83°	64.74°	66.05°

Table 8.4: Angles ω for CW3, CW4 and CW5.

calculated from right-angle triangles with an adjacent $l_{\text{endplates}}$ and a hypotenuse l_{d1} (or l_{d2}). The angle ω used in eq. 8.36 is taken as the mean value of ω_1 and ω_2 given in Table 8.4. The length l_{p} in eq. 8.36 is given by $l_{\text{endplates}}$ listed in Table 7.2.

In Figs. 8.15 and 8.16 there is an offset of the curves created by circles. This non-zero shear strain comes from eq. 8.38. Before the tests started all instrumentation was zeroed. Thus $\Delta_{\text{z}} = 0$ (because $\delta_{\text{top}} = \delta_{\text{btm}} = \theta_{\text{btm}} = 0$. However, $\Delta_{bend} \neq 0$. because it is calculated from eq. 8.37 where although $F_{\text{l}} = F_{\text{s}} = 0$. self weight of the upper part of the test rig is not zero ($F_{\text{w}} \neq 0$ in equation for M_{l} . This constant value of Δ_{bend} was not subtracted from the final value of the shear strain because it had no influence on the slope of the linear part of shear stress-strain curve. Thus the curve created by circles is not plotted over the curve created by crosses. so the diagrams are clearer to analyse.

The straight lines in Figs. 8.14 to 8.16 indicate the elastic behaviour of the specimens. They were obtained by linear regression of points in the linear region. The inclination of these lines gives the values of the effective shear modulus of corrugated panels of the specimens. These values are listed in Table 8.8, and conclusions are given in Section 8.3.1.4.

8.3.1.2 Finite element analysis of shear stresses in a web with *different* boundary conditions

The finite element software I-DEAS was used to analysed the shear stresses in a web. The models listed in Table 8.5 have the geometry based on the geometry of specimen CW4. The only difference between the two models is that Model 1 has a plane web and Model 2 has a corrugated web. Linear quadrilateral shell elements were used for the both models.

We first consider Model 1 and load it by shear only see Fig. 8.18 . The boundary conditions to apply shear to the model were chosen in two different ways. Fig. 8.18 (a) assumes restraints along both longitudinal edges of the web in the z-axis direction and along one of the vertical edges in the y-axis direction. Thus the restraints represents the infinitely large cross-section area of two flanges and one of the end plates. The loading is performed by nodal forces acting vertically on

	Model 1 and Model 2		Model 1	Model 2
b_{ft}	200 mm	b	—	250 mm
t_{ft}	8 mm	d	—	45 mm
b_{fc}	200 mm	α	—	45°
t_{fc}	6 mm	E_{ten}	216 kN/mm^2	
h_w	440 mm	E_{com}	213 kN/mm^2	
t_w	3 mm	E_{web}	198 kN/mm^2	
end plates	cross–section: 200 × 20 mm^2			

Table 8.5: Geometrical dimensions of models for shear finite element analysis.

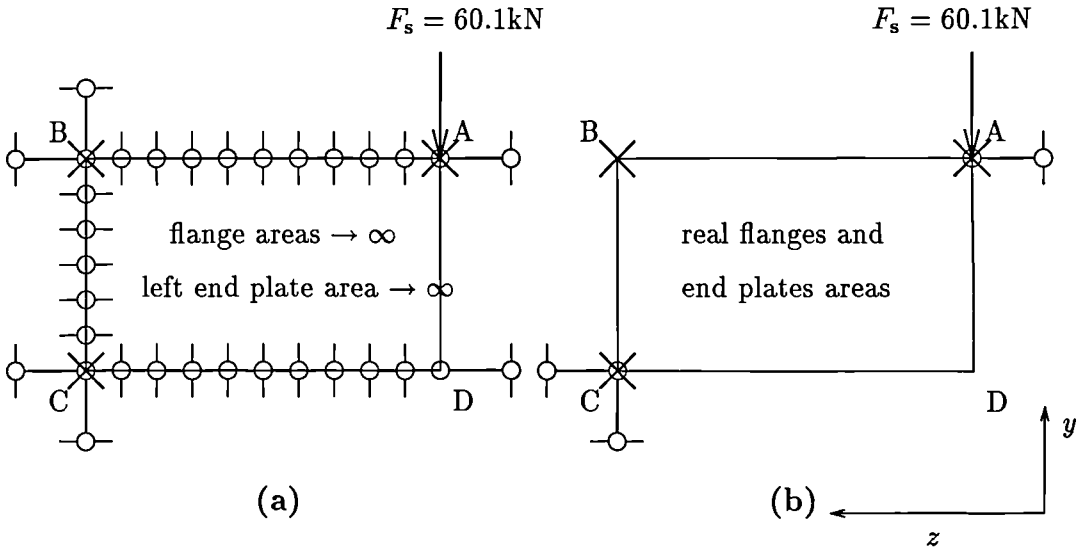

Figure 8.18: Boundary conditions applied to Model 1.

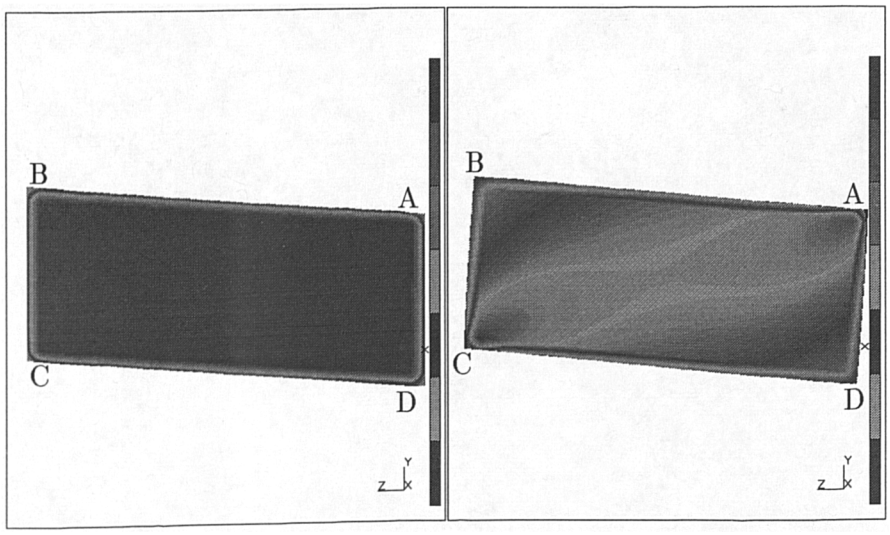

(a) (b)

Figure 8.19: Distribution of yz–shear stress in the web of Model 1 undertaking different boundary conditions.

the shorter edge of a flange on the side of the model where no y–axis restraints were applied. This set up applies distributed shear load along the sides of the web.

The second set up (Fig. 8.18 (b)) has the restraints at points A, B and C only. Point A is restrained in the x and z directions, point B is restrained in the x direction only, and point C is held in all three directions. The real cross–section areas of flanges and end plates are used. The loading of the model is the same as in figure 8.18 (a).

The distributions of the yz–shear in the web on its deformed geometry for Model 1 are shown in Fig. 8.19. For Fig. 8.19 (a) the boundary conditions are shown in Fig. 8.18 (a); for Fig. 8.19 (b) the boundary conditions are shown in Fig. 8.18 (b). It is obvious that for the (a) case the distribution is uniform over the whole area of the web and that the edges remained straight. In the (b) case because the points along the edges of the web can move freely and the model is restrained only at three discrete points, a large concentration of the yz–shear stress is observed near points A and C. This stress is not uniform over the web area. The maximum yz–shear stresses are around a line in the direction of diagonal AC. The minimum

case	(a)			(b)		
coordinates	x	y	z	x	y	z
A	0	-0.528	0	0	-1.152	0
B	0	0	0	0	-0.027	-0.175
C	0	0	0	0	0	0
D	0	-0.514	0	0	-1.143	0.217

Table 8.6: Deformations of web corners after loading Model 1.

yz–shear stresses are around the corners B and D. The flanges and the end plates surrounding the web are not stiff enough to keep the edges of the web straight, and so to transfer the loading into the web in pure shear. That is why the (b) case is not pure shear.

The deformations in these two cases are also different. Table 8.6 lists the deformations of the corners after the loading of Model 1 in (a) and (b) cases. Using the formula 8.36: $\gamma_{(a)} = 5.89 \times 10^{-4}$ and $\gamma_{(b)} = 8.43 \times 10^{-4}$. The applied load was 60.096 kN which gives the mean shear stress in a web $\tau = 60096/(440 \times 3) = 45.53$ N/mm^2. From the basic theory of elasticity, where the shear modulus is given from Young's modulus: $G = E/(2(1+\nu)) = 198/2.6 = 76.15$ kN/mm^2, the shear strain should be: $\gamma = \tau/G = 45.53/76150 = 5.97 \times 10^{-4}$ which matches very well with the case (a) and confirms the above conclusion that the web in case (b) is not in a state of pure shear.

In real plate girders with unstiffened webs this *shear effect* has less influence on the effective shear modulus than in the test specimens because the flanges are relatively larger and the boundary conditions are different.

8.3.1.3 Model of specimen CW4 analysed by finite elements

A similar situation as in Section 8.3.1.2 was created in the following analyses. Models 1 and 2 in Table 8.5 represent specimen CW4. The restraint set and the load set applied to match the test conditions are shown in Fig. 8.20. One of the measured stages during the test was taken as a loading for the models. The shear force was therefore chosen to be $F_s = 60.096$ kN; and bending was represented by compression

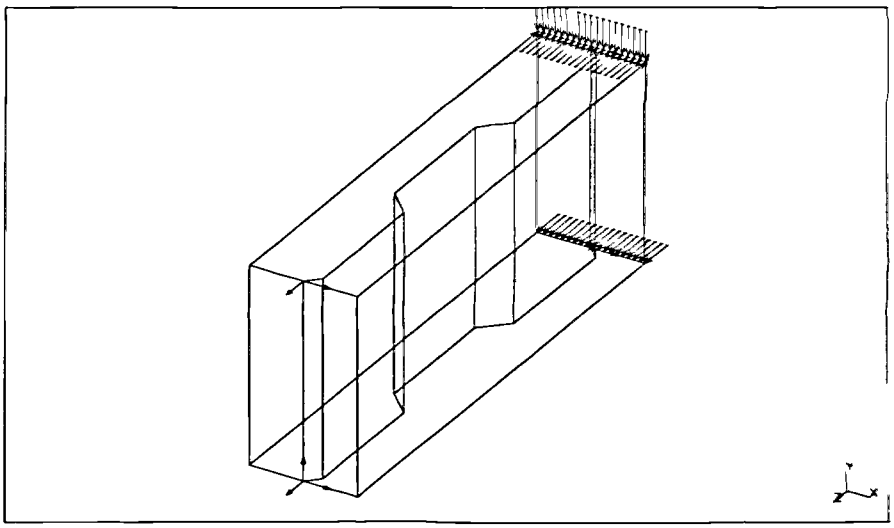

Figure 8.20: Boundary conditions for Models 1 and 2 to match the conditions in the test.

force $C = 115.232$ kN and tension force $T = 94.208$ kN. All three forces were evenly distributed on the free end flange edges. The designed sizes of the flanges and end plates were modelled by shell elements.

	Model 1 plane web			Model 2 corrugated web		
coordinates	x	y	z	x	y	z
A	0	-1.956	-0.468	0	-2.138	-0.493
B	0	-0.030	0	0	-0.032	0
C	0	0	0	0	0	0
D	0	-1.943	0.631	0	-2.124	0.706

Table 8.7: Deformations of web corners of Models 1 and 2.

Table 8.7 summarises the deformations of the web corners after the load was applied to the models. Because of the boundary conditions applied to the models, and the shear effect noted in Section 8.3.1.2, the shear modulus of Model 1 with the plane web will be less than theoretical elastic shear modulus, G. However, the theory of elasticity is still valid. Neglecting the shear effect (described in Section 8.3.1.2)

in the models, the estimated value of shear modulus, G_{est}, can be calculated. Using the eq. 8.36 and assuming the uniform distribution of mean shear stress over the whole web area, the estimated shear modulus will be $G_{est} = \tau\ \gamma$. The results are summarised in Table 8.8.

8.3.1.4 Conclusions on shear modulus investigations

Table 8.8 summarises all shear investigations made during the test analysis. The

PLANE WEB				
G_{est} using eq. 8.36 (see Section 8.3.1.3)	47.6			A
CORRUGATED WEB				
	CW3	CW4	CW5	
G_{eff} from finite element analysis using eq 8.36	—	43.4	—	B
G_{eff} from tests using eq 8.36	53.29	40.52	46.75	C
G_{eff} from tests using eq 8.39	—	37.45	40.75	D
G_{eff} using eq. 8.48 where $G = G_{est}$ for plane web	44.77	44.77	43.94	E

Table 8.8: Effective shear modulus of a corrugated web, in kN/mm^2.

effective shear modulus of corrugated web can be calculated from eq. 2.18. For $\alpha = 45°$ and assuming $G = G_{est}$ as an estimated value obtained from finite element analysis described in Section 8.3.1.3 (as given in Table 8.8 — line A), the effective shear modulus of corrugated web is then

$$G_{eff} = G_{est}\frac{b+d}{b+d\sqrt{2}} \tag{8.48}$$

for each specimen. These effective values are given in line E of Table 8.8. The comparison with the finite element analysis of the numerical model of specimen CW4 — given in line B of Table 8.8, gives the difference about 3 %. This is assumed to be caused by numerical approximations made during the computations.

Comparisons between theory (eq. 8.48) and test results are given by comparing lines C with E; and D with E. The differences between those numbers for each specimen are up to approximately 16 %. The reason is in modelling the test specimen for computer analysis. As was shown in Section 8.3.1.2, the boundary conditions applied to the models play an important role in the final results. The test specimens were bolted to the loading beams by 9 bolts at each end. In finite element modelling these connections were modelled by fixing one end of the model at two points only.

The geometry of the model used in the finite element analysis had its values rounded in contrary with the specimens, where the real values of the specimens' geometry were used to calculate the effective shear module.

The obtained results indicate the validity of the formula 8.48. The three tests done with shear loading were not designed to investigate the shear modulus of a corrugated web. Therefore the discrepancies between the theoretical and experimental results are not considered to be unsatisfactory and the conclusion can be drawn that although formula 8.48 cannot allow for different boundary conditions of specimens used either in tests or in finite element analysis it is good enough for practical use, where an accurate value for G_{eff} is rarely needed.

8.3.2 Shear stresses in the webs of specimens

The investigation of shear stresses was not the main objective of the present tests. However, specimen CW4 buckled in shear in the middle flat part of the corrugated web before the local buckling of the flange was fully developed. Obviously, this behaviour needs an explanation.

Table 8.9 lists the shear stresses calculated for specimens CW3, CW4 and CW5 using the measured geometrical dimensions and material properties. $\tau_{\text{cr,loc}}$ is the critical local buckling shear stress defined by eq. 1.5 where $k_{\text{f}} = 1.0$; τ_{f} is the design

		CW3	CW4	CW5
$\tau_{cr,loc}$	N/mm^2	170	135	135
τ_y	N/mm^2	164	128	128
τ_f	N/mm^2	150	118	118
$F_{s,max}$	kN	170	153	140
$h_w t_w$	mm^2	1425	1299	1299
τ	N/mm^2	119	118	108

Table 8.9: Shear stresses of specimens CW3, CW4 and CW5.

local buckling shear stress to EC3 given by eq. 1.7 with factor 1.1 omitted where $\tau_y = f_y/\sqrt{3}$ and f_y is given in Table 7.4. τ is the maximum shear stress reached in the tests. It was calculated from $\tau = F_{s,max}/(t_w h_w)$ where t_w, h_w were taken from Table 7.1.

Specimen CW3 and CW4 were made by different fabricators. Their webs were therefore made from completely different plates which can also be seen from the web thicknesses. They differ by 9 % (see Table 7.1). Their yield stresses differ by about 22 %; and their maximum shear stresses reached in the tests differ by about 0.8 %. The shear stress in the web of specimen CW3 when local flange buckling occurred was $\tau = 67$ N/mm^2 (for $F_s = 92.06$ kN from Table 8.3) which is only 56 % of the maximum shear stress reached later. This is believed to be the reason why specimen CW3 did not buckle in shear before local flange buckling. Shear buckling of specimen CW3 occurred at the shear stress $\tau = 119$ N/mm^2 which was 79 % of the critical design local buckling shear stress τ_f. It was obviously influenced by flange deformations after the flange buckling.

The webs of specimens CW4 and CW5 differed only in d. The flat parts of their corrugated webs were the same size. In the following, their behaviour is compared using principal stresses calculated from strain gauge measurements. Fig. 6.14 shows the locations of the strain gauges on specimens CW4 and CW5. The principal stresses are then calculated from the formula

$$\sigma_{princ} = \frac{E}{2(1-\nu)}(\epsilon_1 + \epsilon_3) \pm \frac{E}{\sqrt{2}(1+\nu)}\sqrt{(\epsilon_1 - \epsilon_2)^2 + (\epsilon_2 - \epsilon_3)^2} \qquad (8.49)$$

where ϵ_i are measured strains in the rectangular rosette where the axes of the three gauges are spaced at 45° intervals such that the gauges 1 and 3 are perpendicular to each other (for more detailed information about developing eq. 8.49 see [9]). Table 8.10 lists the gauges from which measurements were used in eq. 8.49 for calculating the principal stresses in Figs. 8.21 to 8.27.

Figs. 8.21 to 8.24 are plotted for the principal stresses in the middle parts of the corrugated webs of specimens CW4 and CW5. Eq. 8.49 is valid in the elastic region only. It means that Figs. 8.21 to 8.24 (and 8.25, 8.27 shown later) are valid only up to the point where the difference between the principal stresses is less then von-Mises yield stress which is approximately equal to $1.15f_y$. For specimens CW4 and CW5 it is then 255 N/mm^2 (f_y = 222 N/mm^2 from Table 7.4). The elastic region in Figs. 8.21 to 8.27 is marked by joining the points, while the separate points would be only valid for unlimited yield strength and therefore they are unreliable. They are plotted for better understanding of the behaviour of specimens CW4 and CW5.

i in ϵ_i	1	2	3	specimen
Fig. 8.21	21	23	25	CW4
Fig. 8.22	21	23	25	CW4
Fig. 8.23	21	23	25	CW5
Fig. 8.24	21	23	25	CW5
Fig. 8.25	7	9	11	CW4
Fig. 8.27	7	9	11	CW5

Table 8.10: Strain gauges used for calculating the principal stresses.

In specimen CW4 during the bending loading the principal stresses remained almost zero – curve OA in Fig. 8.21. When shear load was applied the principal stresses separated and they were increasing linearly (in the opposite direction) up to over 100 N/mm^2 each – curves AB, AD in Figs. 8.21 and 8.22. At points B and D the bending load was zero. Increasing the shear load increased the principal stresses, both in compression and tension, so their difference exceeded 255 N/mm^2 – points C and E in Figs. 8.21 and 8.22, which caused the buckling of the web. The reason for this *unexpected* web failure was in wrong predictions of shear stresses before the

tests. The thickness of the web was measured inaccurately, which influenced the calculations of predicted shear stresses significantly. Table 7.1 shows the values of the web thicknesses, which correspond with measurements taken after the tests from coupons CW1–W1, CW1–W2; CW2–W1, CW2–W2; CW3–W1, CW3–W2; CW4 W3 and CW4–W4 shown in Table 7.3. These values are believed to be the correct ones since the coupons were taken from the actual webs.

The middle flat part of the web of specimen CW5 was bent during the bending loading due to deformations of the large outstand of the flange. This is clearly seen as curve OA in Fig. 8.23 and it indicates the start of non–elastic behaviour of the flange. From point A only the shear loading was increased. This decreased the bending load – curves AB and AE in Figs. 8.23 and 8.24. Buckling of the flange occurred – points B and E in both figures, followed by shear buckling in the bottom flat part of the web – lines CD and EF in Fig. 8.23. The specimen was then unloaded. The principal stresses in the middle flat part of the web did not exceed 150 N/mm^2 during the test. Their difference did not reach 255 N/mm^2 so the middle part of the web did not yield as can be clearly seen in Fig. 8.24.

A comparison of the principal stresses in the bottom flat parts of the web of specimens CW4 and CW5 is given in Figs. 8.25 and 8.27. The large outstand of the flange of specimen CW5 was greater than for specimen CW4. Comparing Figs. 8.26 and 7.31 first, one can see that while applying shear load only, the flange buckling of specimen CW5 developed clearly – points G and C in Fig. 7.31. This was not the case for specimen CW4. Flange buckling started to develop – curves BC and FG in Fig. 8.26, but it was interrupted by shear buckling in the middle of the web – lines CD and GH. Looking at Fig. 8.27 again, points B and E show clearly the bending of the bottom flat part of the web of specimen CW5 – both curves AF, AC bend in the same direction. Due to bending of the web the compressive principal stress exceeded the yield stress (222 N/mm^2) and the difference between the principal stresses exceeded 255 N/mm^2. The specimen buckled in shear almost immediately after complete flange failure. As mentioned above, the inelastic behaviour of specimen CW4 started in the compression flange. It can be seen at point D in Fig. 8.25 as a very slight change in direction of curve AD. This indicates the bending of the web panel due to

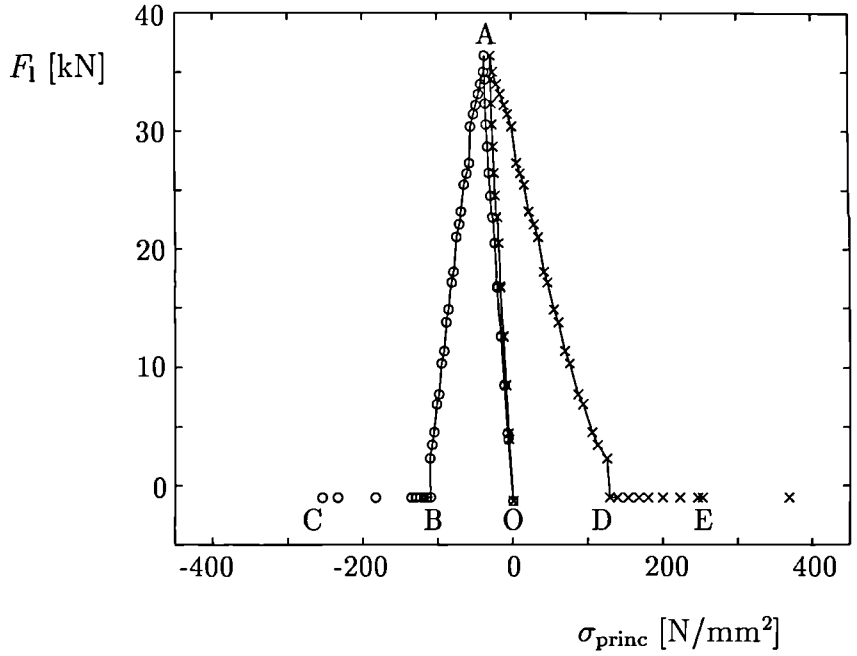

Figure 8.21: The principal stresses in the middle panel of specimen CW4.

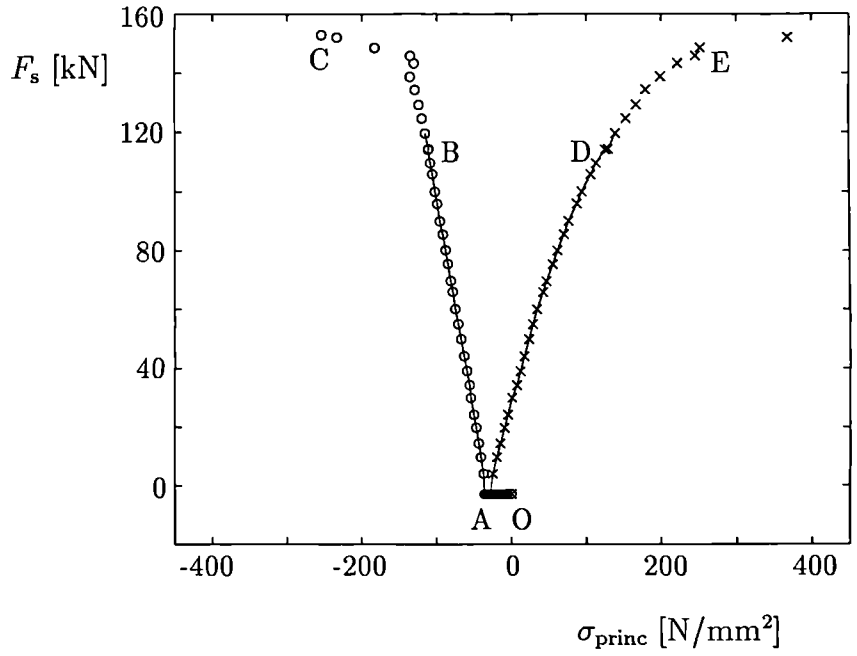

Figure 8.22: The principal stresses in the middle panel of specimen CW4.

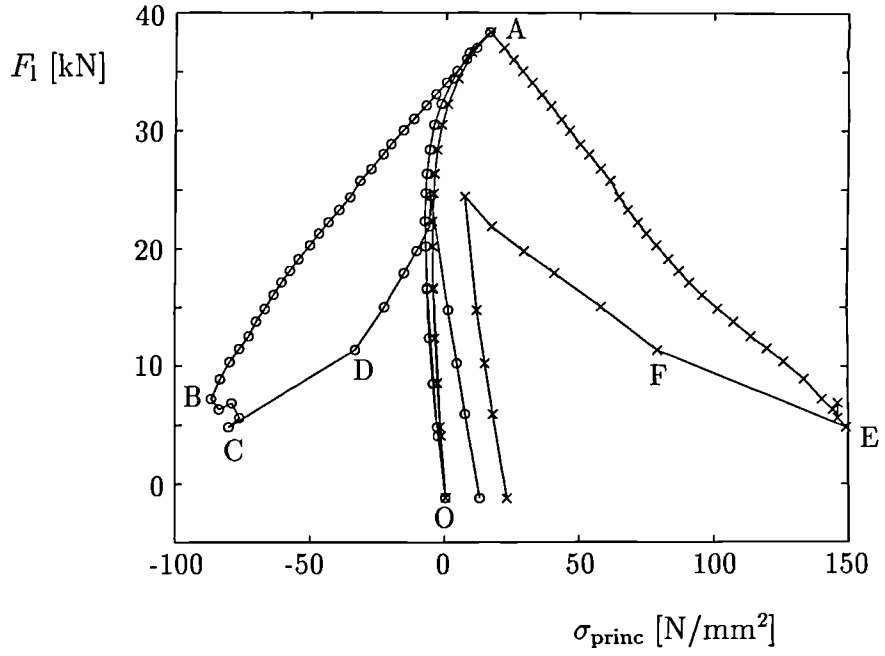

Figure 8.23: The principal stresses in the middle panel of specimen CW5.

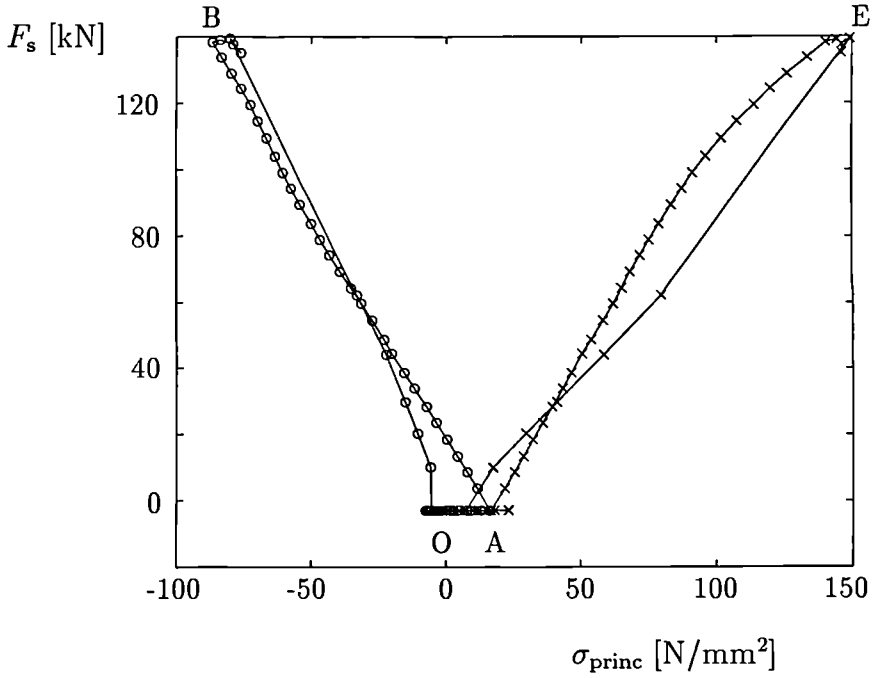

Figure 8.24: The principal stresses in the middle panel of specimen CW5.

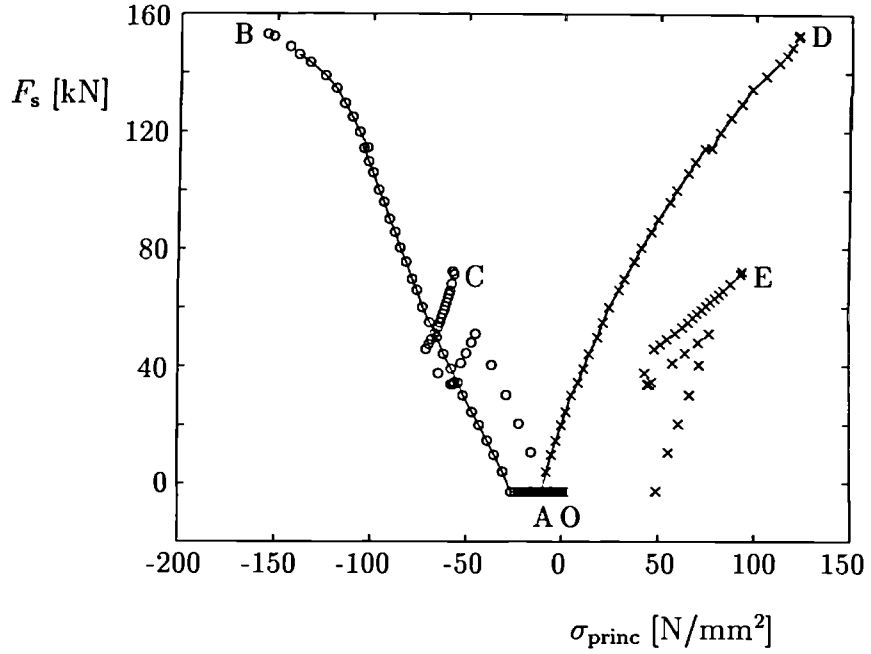

Figure 8.25: The principal stresses in the bottom panel of specimen CW4.

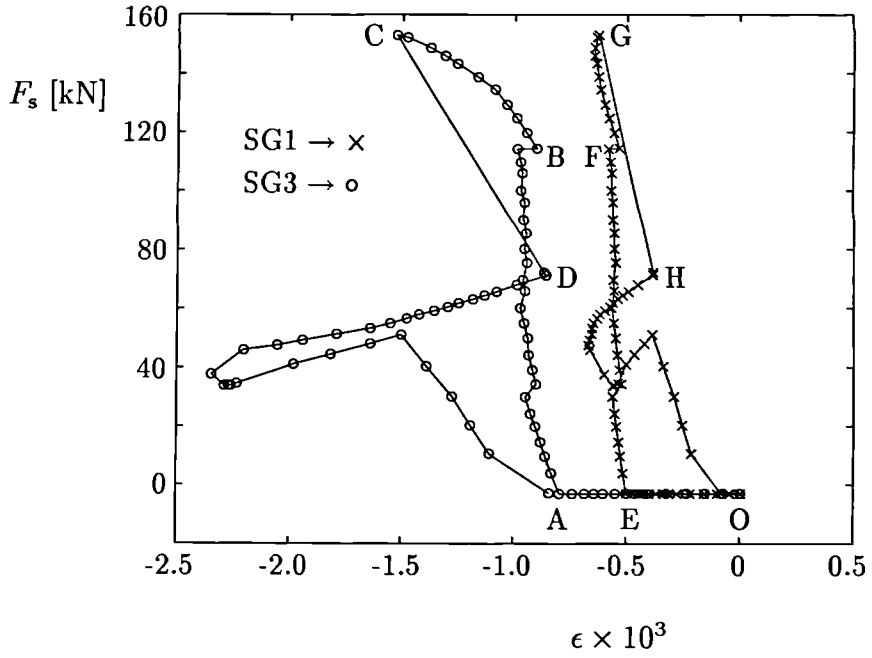

Figure 8.26: Measurements of SG1 and SG3 versus shear force for specimen CW4.

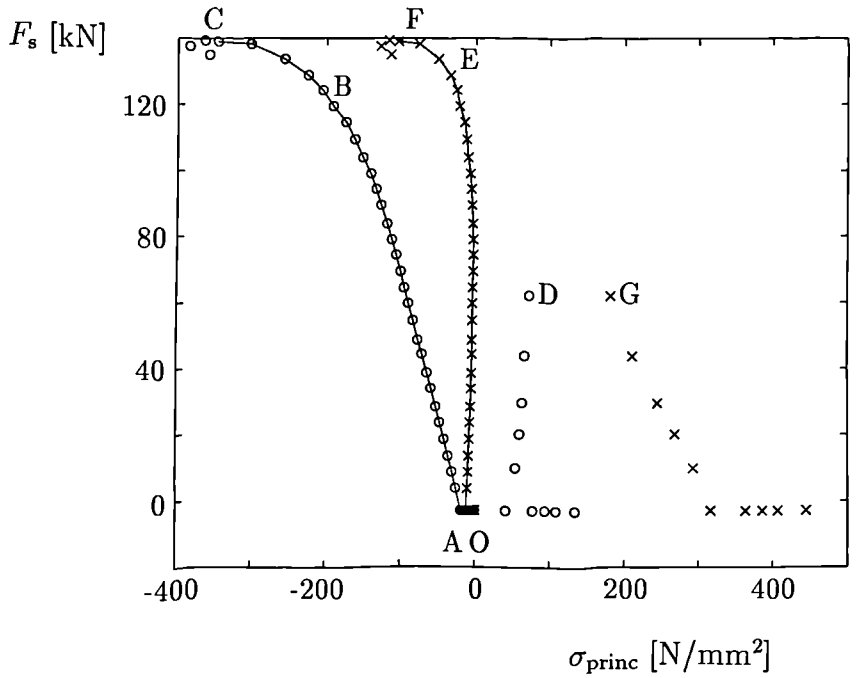

Figure 8.27: The principal stresses in the bottom panel of specimen CW5.

deformations in the flange. At this point the bottom web panel was already yielding since the difference of the principal stresses exceeded 255 N/mm^2. However, the web buckled first in shear in the middle panel, as explained above, thus the buckling of the flange was not fully developed.

The flanges of specimens CW4 and CW5 were approximately the same size. However, the large outstand of specimen CW5 was greater, thus its critical buckling stress was less than for specimen CW4. This is why the buckling of the flange of specimen CW5 could fully develop before a shear failure.

From the above comparisons it is believed that both flange and web buckling were interacting and appeared almost immediately one after the other. Thus the shear buckling was strongly influenced by the flange buckling in the tests where the compression buckling occurred first and vice versa. This is believed to be a reason why the maximum shear stresses in specimens CW3 and CW5 are less by 20 % and 8.5 %, respectively, than the design local buckling shear stress τ_f. Specimen CW4 buckled exactly at τ_f.

8.4 Summary on the tests

The tests were carried out on samples of steel beam with I–cross–section and three half–wave corrugated web. The samples were considered to be a part of a composite plate girder of either a simply supported or a continuous bridge structure. The yield stresses of the steel use for the tests specimens varied from 222 N/mm^2 to 414 N/mm^2. Hand welding between a web and flanges was performed in the case of each specimen. The welds were required to be as small as possible to minimise the heat input. The following conclusions summarise the achievements of the experimental work.

1. Mean stress — mean strain diagrams plotted from the test measurements agreed well with the theoretical assumption in the elastic region of the specimens' behaviour (Figs. 8.7 to 8.11).

2. The test results support the conclusion given in Section 5.4 drawn by computer analyses where for $A_{\text{ratio}} > 0.14$ the large outstand of the compressed flange should be considered for local buckling verifications. However, $\alpha = 45°$ for all five specimens. For this angle the average outstand can be considered when $A_{\text{ratio}} < 0.19$. Specimens CW1 and CW2 has their ratios close to this value (see Table 8.3) and their points for the average outstands lays close to the EC3 design curve (Fig. 8.12). This definitely shows a good agreement between the computer analysis and experimental work.

3. The conclusion 3 in Section 2.6 is supported by experimental tests on specimens CW3, CW4 and CW5. Initially all five specimens were designed to investigate the local buckling of a compression flange. When it was later decided that some shear investigations would be performed on tests CW3, CW4 and CW5, it was not possible to modify the tests conditions to the theoretical assumptions of pure shear. Therefore the discrepancies between the theoretical and experimental results for shear modulus (found with approximately 16 % difference) are not considered to be unsatisfactory and the conclusion can be drawn that although the conclusion 3 in Section 2.6 cannot allow for differ-

ent boundary conditions of specimens used either in tests or in finite element analysis it is good enough for practical use, where an accurate value for G_{eff} is rarely needed.

4. Why did specimen CW4 buckle in shear before local buckling of the compressed flange could have been fully developed? The flanges of specimens CW4 and CW5 were approximately the same size and their loading procedures were similar. Specimen CW4 had a higher critical local buckling stress for the flange than specimen CW5 because the large outstand of specimen CW5 was greater. Thus the buckling of the flange of specimen CW5 could fully developed before its shear failure. The full explanation of this behaviour is in Section 8.3.2.

5. Tests CW4 and CW5 clearly show that for a region where both the web and the nearby flange are both fully stressed, the interaction between local buckling of the flange and web can not be ignored in a design. The flange buckling causes the deformations of the web and vice versa which significantly decreases the critical buckling stresses of the web (or the flange if web buckles first).

Chapter 9

Conclusions on corrugated webs

Corrugated panels are widely used in applications such as side walls, roofing, aircraft or in off–shore structures, because of their excellent shear response. However, as webs of beams, corrugated panels are very rarely chosen. Using corrugated webs in bridge girders may significantly improve shear and torsional conditions and save on the volume of steel used. Bearing this in mind, the author has tried to look at corrugated webs in a way which might cause problems in designing a bridge girder.

Since corrugated panels are used to a large extent, as mentioned above, a lot of research, done by many authors referenced here, was undertaken to define critical shear stresses in the panels. Using results of these investigations the relationship between the geometrical properties of a corrugated web and the shear stresses is defined (eq. 2.3). This relationship can suggest the optimum geometrical values when designing this type of the web.

The way of dealing with bending and shear stiffnesses of an I–beam with a corrugated web was shown here using analytical solutions and finite element analyses. Since the corrugated web has almost zero bending stiffness when bent in its plane, it is suggested that the bending stiffness of a beam with a corrugated web is calculated as a bending stiffness of a beam where the cross–sectional area of the web is not taken into consideration. The effective shear modulus of a corrugated web is in the same ratio to the shear modulus of the material as the ratio of the length of the sheeting to its unfolded length. The additional stresses in flange tips due to bimo-

ment effects depend on the type of bridge structure and geometry of the corrugated web. It has been shown here that these stresses can be limited to less than 10 % of the direct stress coming from hogging bending moment above an internal support or at a fixed end by a suitable and careful choice of geometrical dimensions.

Cambering a bridge girder is a common practice. There are two possible ways of cambering a beam of uniform depth with a corrugated web. A beam of approximately 14 m in length is considered. The first way is to cut the flat plate into a camber before it is corrugated. The second way is to create the camber by bending an already corrugated plate in a plane parallel to the flat panels of the plate. The forces needed for the second method to pull the top corners of the plate apart while fixing the bottom corners are typically less than 0.5 kN. By forming a corrugated plate into a cambered shape by either of the above mentioned methods, the gaps created between the top or bottom surfaces of the corrugated plate and flanges are sufficiently small so as not to cause difficulties in welding the flanges to the web. This is not the case of a girder with curved soffit. Corrugated plates are not recommended for use in bridge girders with a curved soffit, unless a better method of fabrication can be devised, than cutting the bottom longitudinal edge of the web plate to a circular arc before corrugating it.

An error that arises from the maximum likely deviation of a pair of folds is within the allowed range but it is cumulative for extra folds and therefore it is necessary to monitor carefully the fabrication of folds when manufacturing a corrugated plate.

The investigations into fabrication of a cambered beam of uniform depth with a corrugated web was undertaken using both, the analytical solutions applying known mathematical methods and by finite element analyses. The results were compared. A large discrepancy was shown between the analytical solution using energy methods and finite element analyses when finding the bending stiffnesses of a corrugated panel. The main aim of this part of the work was to find approximate values for the forces needed to pull the top corners of a corrugated plate apart while fixing the bottom corners thereby creating the required camber. These forces then indicate what type of tension jack is needed. Since both methods generated bending stiffnesses to the same order of magnitude, the forces could be still considered as

a reasonable estimate. The author is confident that the analytical solution given in Appendix C is correct. It is believed that the type of elements used in finite element analysis is the reason for the discrepancies mentioned above. It appears that the shell elements used for the bending analysis were not the best choice since they were designed to model thin smooth surfaces under membrane stresses. Using different types of elements may prove this assumption to be correct. The foldings between flat and sloping panels of corrugations can be for example modelled by solid elements and joined to either plate or shell elements which would model the flat and sloping parts of the corrugation itself. An experiment on bending a corrugated plate would not be difficult to perform. The corrugated plate could rest horizontally on the floor; two "bottom" corners would have to be fixed and the forces required to pull the "top" corners of the plate apart would be not large as shown in Section 3.3. The problem could arise of avoiding any out of plane deformations of the plate. In the presented computer analyses these out of plane deformations were prevented by restraining each sloping panel of the plate in the x–direction (see Fig. 3.5). The forces in these restraints were found to be negligible. Therefore in an experiment it would be necessary to place some plane plates on each side of a corrugated plate, or only on one side if the corrugated plate is resting horizontally on the floor. The details would have to be solved when performing the test. Neither the test nor the finite element analyses with the alternative types of elements were undertaken because of the lack of time and because the forces found are considered to be a reasonable estimate and the formulae given by analytical solution (Appendix C) are assumed to be sufficient to be used in practice.

The re–design of a plate girder of Avon Bridge shows that the theoretical saving on the volume of steel used for the web when comparing plane and corrugated webs can be about 16 %. However, the corrugated web makes no contribution to carrying the bending stresses whatsoever thus the flange volume has to be increased. No overall saving on the volume of steel used was found for this plate girder structure. However, for composite box–girder bridges the situation would be different as the new web would increase distortional stiffness, which would lead to other savings, and an increase in the area of flanges would probably be less. It could be shown

by a re–design of a typical box–girder. Nevertheless, box–girder bridges were not considered in the present work.

The main topic of the thesis is the local buckling of a compressed flange attached to a corrugated web. The results of the finite element analyses on this subject suggest the use of the ratio, A_{ratio}, defined by eq. 5.5, when designing the compressed flange for its local buckling. If $A_{\text{ratio}} < 0.14$ the average outstand of the flange can be safely used for a design of the local buckling of the flange. This condition is true for $\alpha > 30°$ where α is the oblique angle between the flat and sloping panels of the corrugated web. As α increases the condition becomes more conservative, because for larger α the sloping parts of the corrugation provide larger restraint against buckling and decreases the buckling wavelength. The tests results presented in this thesis support this conclusion. All tests have $A_{\text{ratio}} > 0.14$. From Fig. 8.12 all tests should be strictly designed for large outstand of the compression flange. However, $\alpha = 45°$ for all test specimens. This would therefore increase the limitation to $A_{\text{ratio}} = 0.19$. Specimens CW1 and CW2 have $A_{\text{ratio}} = 0.186$ and 0.187, respectively, which is just below the given limitation. Points A_1 and A_2 in Fig. 8.12 are just below the design curve.

All tests were carried out on samples of steel beam with I–cross–section and a corrugated web. Web crippling and fatigue were not considered. The yield stresses of the steel used for the test specimens varied from 222 N/mm^2 to 414 N/mm^2. The test specimens CW1, CW2 and CW3 were delivered without the required samples of steel for their fabrication. The material testing was therefore performed with the samples taken from the specimens after the tests were finished. The results of the material testing for these specimens could have been influenced by the tests. However, these results (given in Table 7.4) are the best which could be obtained from the test specimens. The detailed summary of the test results and conclusions are given in Section 8.4. The tests were initially designed to investigate the local buckling of the compressed flange only. Therefore the test rig was constructed to load the specimens only by bending. Shear loading was added later to investigate any possible interaction between bending and shear effects of a beam with a corrugated web. Although the conditions for the shear loading were not ideal with the existing

test rig, all accessible results of shear behaviour were used. The effective shear modulus of the corrugated web found from the test measurements was compared with the effective shear modulus found from analytical and finite element analyses. The differences were within 16 %. This difference is explained by having different boundary conditions applied in the tests and in the finite element models. The approximation in modelling the restraint conditions for the finite element method had to be taken into account. To investigate the shear behaviour of the corrugated webs, the experiments would have to be designed in a different way, e.g. such as the tests undertaken in Sweden. Nevertheless, the present thesis does not consider the shear behaviour as the major topic of the investigation since there is a vast amount of this type of work performed by other authors, as shown in the literature review.

From the conclusions discussed above it can be seen that there are many areas within the analysing of corrugated webs which need more attention and many of them which were not investigated in the present thesis. The designer would probably try to design a corrugated web with the angle α as small as possible. Therefore the experimental work on panels with $\alpha = 30°$ similar to the tests shown in the thesis is suggested as a possible further reaserch. It was found that the corrugated webs would have better use in box girders. Distortional behaviour of the such girders is another proposed research. The author did not considered a fatigue of web–to–flange welds which might play an important role in the design of a bridge girder with a corrugated web.

Part II

Lateral restraints in composite bridges

Chapter 10

General overview of the problem

10.1 Introduction

Plate girders for composite continuous bridges in the U.K. have to be checked for lateral torsional buckling to BS 5400. The design method of Part 3 [56] is based on an extended analogy between lateral buckling, without distortion of the cross–section of the member, and the Euler critical buckling of an axially loaded strut. A steel bottom flange in compression near an internal support of a continuous composite beam is susceptible to lateral buckling. The method is rather conservative because this type of buckling occurs mainly in a region of steep moment gradient. This is when there is a variation in stress along the flange, which is not a case for a uniformly compressed strut. Also lateral torsional buckling can occur only if cross–sections distort which is again not exactly the case for composite bridge plate girders where a concrete slab provides restraint to distortion of beam.

The above mentioned design method leads to often unnecessarily heavy restraints. These are considered compulsory in term of the rigidity of a structure, to stabilise the longitudinal girders against buckling. The rules also seem to be difficult to apply to continuous and half–through types of bridges.

Therefore there is a need to revise the existing codified rules. The subject of this second part of the present thesis is numerical second–order elastic analyses of appropriate parts of typical simplified steel and composite bridges. The objective

is to find relationships between lateral deformations at braced points and forces in bracings as functions of the following: stiffness bracings; types of loading on the structure; magnitude and type of geometrical imperfections of the members.

10.2 Design rules as in BS 5400: Part 3

A typical U–frame system is shown in Fig. 10.1 which is taken from BS 5400: Part 3

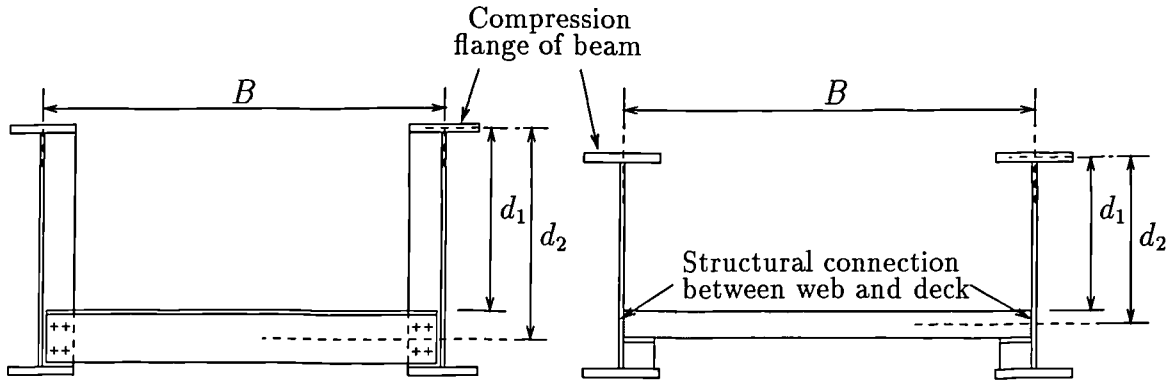

(a) Main beams restrained by U–frames (see **9.6.5**)

(b) Main beams continuously restrained by deck (see **9.6.6**)

Figure 10.1: Figure 8 of BS 5400.

– Figure 8 [56]. It is relevant to a simply supported girder where instability of the compression flange would occur mainly in the middle region of the girder. In a continuous bridge girder the U–frame is inverted, and it has to be placed in a hogging moment region near an internal support.

Compression flanges tend to buckle laterally. BS 5400: Part 3 deals with restraining the compression flange by either discrete or continuous U–frames. The lateral stability of the compression flange is therefore almost dependent on the rigidity of the U–frames, which consist from three main components: the transverse beam bending in the plane of the frame, the girder webs with any associated stiffeners as a vertical members in lateral bending and the joints connecting the two.

Clause 9.6 of BS 5400: Part 3 gives rules for defining the effective length, l_e, for

beams subjected to lateral torsional buckling. This clause assumes certain conditions for lateral and torsional restraints to be satisfied. Clause 9.12 then deals with the required strength of U–frames and their component parts. Traditionally all systems of restraint have to be designed so that they will be sufficiently strong to resist transverse wind loading and other applied loads as well as the forces generated as a result of their bracing function. Therefore F_u and F_c forces are introduced (Clause 9.12.2) for intermediate discrete U–frame restraint, and similarly in Clause 9.12.3 f_u and f_c forces per unit length for continuous restraint provided by the deck. These forces are assumed to act at the tips of the U–frames as a result of their restraining action on the compression flange.

The requirements for restraints at supports are given in Clause 9.12.4 by defining the force F_R.

A common procedure, given in design codes, is to design bracing to resist a certain percentage of the compressive force in the braced member. A typical value is 2.5 %. This will be referred to as the 2.5 % *strength rule.* The treatment in clause 9.12 is simplified. The derivation of F_u forces assumes the initial imperfections to be 50 % larger than those given by BS 5400: Part 6 [57] as $l_e/1000$. A constant force of $P = A_{fc}\sigma_{fc}$ (where A_{fc} is the area of compression flange; σ_{fc} is the maximum compressive stress in the flange) is considered to be present along the entire length l_e, which is not the case in real bridge girders. In practice this constant force would only exist over a relatively short length. F_c forces represent the forces developed at the tips of the frame as the results of deformations of cross beams under the applied load. The assumptions made in their development consider the joint between a cross beam and a vertical member to be perfectly rigid, and the tip of the U–frame to be positionally restrained by compression flange continuity, which means that the compression flange can rotate but not move laterally within the plane of the frame.

All the above mentioned assumptions indicate that the present design rules given by BS 5400: Part 3 [56] are unnecessarily conservative, and need to be revised.

10.3 U–frame design to Eurocode 4: Part 1.1 (EC4)

The draft european code deals with the problem of lateral buckling of a steel compression flange in a building (the other than the one attached to the concrete slab) in EC4, Part 1.1, Clause 4.6 [23]. It differs in detail from the method given in EC3, Part 1.1, Clause 5.5.2 [55], because the model for lateral buckling of a steel beam neglects distortion of the cross–section. The EC3 mode of buckling is prevented in composite bridge girders by a concrete slab. The design must therefore take account of bending of the web.

The method given in Clause 4.6.3 of EC4 considers flanges in compression generally in situations where the elastic critical bending moment, M_{cr}, can be determined. The method based on a continuous inverted U–frame model is then given in Annex B of EC4. Thus the real distribution of the bending moment along the beam, the moment gradient, is considered when determining the elastic critical bending moment. Factor C_4 is introduced for this reason. However, the design method of Annex B is too approximate for short lengths of beam between lateral bracings. The reason is that the factor C_4 is dependent on a length between braced points. It was computed as a minimum of a curve and becomes too inaccurate when the distance between braced points is much less than a span.

No rules are given in EC3 or EC4 on the minimum force required for a bracing to restrain the compression flange laterally. There is guidance given in BS 5950: Part 1 [58] which states that a discrete restraint should be designed using the 2 % strength rule. Experimental work supports the suggestion that the design force can be reduced to 1 % of the force in the flange for a composite beam.

Although the design methods of Eurocode seem to be less conservative than those in BS 5400: Part 3, they are within the limited scope. The design rules of the both above mentioned codes are therefore under revision.

10.4 Literature review

The need to revise the Standards has led to extensive research work, especially in the United Kingdom. Study of a few codes from different countries showed that most of the countries had no codified requirements for support restraints in continuous composite bridges. In German and Danish rules, for example, only principles are stated. The Czechoslovakian code considers this problem only for truss through bridges, where there are rules given for top compression chords of truss main girders [61].

One of the earliest work on elastic lateral bracings was presented by Winter [53]. He developed a very simple theory considering a compressed simply supported imperfect strut with a spring in the middle such that the continuity at the mid–point was neglected. This paper gives a good basis for the analyses presented here. Some of the ideas of this paper are described in Section 12.1.

Aadnesen [1] worked on the problem of compression chords for through bridges by solving the differential equations using a Fourier series. The equations were based on energy method. A straight bar was subjected to axial loading, and supported laterally along its length by a uniform elastic medium. The energy equation consisted of the work done in bending and twisting, on the elastic medium, and by the axial loading during the buckling of the bar. All three expressions then contained functions of the deflected and rotated form of the bar. Rather complicated equations were simplified by making many assumptions, which had to be satisfied in applications of the theoretical results to the design of actual bridges. The assumption of linear elastic behaviour, for example, was close to reality for welded structures. This might not be true for bolted or riveted connections, although the author had undertaken some experimental work on aluminium models which gave results close to his theoretical solution. The method neglected imperfections of the chords. This was not true in common practice, and any initial deflection might have led to serious reductions of the buckling loads. The lateral stiffness of U–frames was considered to be replaced by an equivalent elastic medium which meant that U–frames needed to be of the same stiffness, and evenly spaced along the girder. This assumption led to over–conservatism since there was no need to consider any moment gradient.

A specially developed finite element program was presented by Wang and Nethercot [50, 51]. The program was used for study of the behaviour of braced beams. The authors had concluded that for a single bracing system 1 % of the axial force in a flange at failure was a reasonable upper bound requirement for bracing strength. However, for multiple bracing systems this value could be unsafe, especially for very slender beams. The authors therefore suggested that the value of 2 % might be more appropriate as a total figure, with a maximum value of 1 % for each brace.

In his paper Jeffers [18] showed the difficulties of BS 5400 rules, mentioned above. Jeffers suggested an alternative design method to alleviate these difficulties and he proposed further research to be undertaken. Since it was shown that U–frame bridge girders often failed in a different mode of buckling than classical lateral torsional buckling, Jeffers suggested that computer elasto–plastic finite element analyses with geometrical and material non–linear facilities should be done. The results would review the value $\theta = 1.0$ (Clause 9.7.2) for the moment gradient effects in the hogging regions of continuous composite bridges. He also recommended analytical and experimental research on the flexibility of corner joints of U–frames.

Comments on Jeffers' paper were made by Hayward (Cass Hayward & Partners) and Tubman (Scott Wilson Kirkpatrick) [19]. They both supported Jeffers' suggestions on *necessity for background to the Code criteria and for further investigations*, to make the Code rules simpler and less conservative.

Hayward's contribution on the commentary explained the origin of BS 5400. It had taken over the rules for U–frame treatment from BS 153 in 1953, where U–frame restraint had been applicable to simply supported half–through bridges with rigid end U–frames. Designers often used these rules from BS 5400 for bridges with other configurations (e.g. continuous composite bridges where the U–frames were inverted) and this created a new situation.

Tubman's background approach to the problem underlined numerous difficulties which were arising using BS 5400 in a design. The numerical factor 2.5 given in BS 5400: Part 3, Clause 9.6.5 was believed to be based on the theory of a beam on an elastic foundation as an approximation of $\pi/\sqrt{2}$, which is 2.22. This was a conservative rounding up. In connection with the treating of non–uniform bending

moment, BS 5400 does not have an equivalent to the m–factor of BS 5950 [58], which is considered to be less conservative than the θ–*factor in BS 5400 (Clause 9.7).* Tubman supported the idea that the maximum force in a bracing rarely exceeds 1 % of the compression flange squash load, assuming that the axial stiffness of the brace is slightly greater than that strictly required for stiff restraint.

Experimental work was carried out at the University of Warwick by Johnson and Fan [27]. The authors tested realistically scaled models of T–beams and inverted U frames, with slendernesses at the class 2–3 boundary (as defined in EC3 [55]). The maximum hogging bending moments at internal supports were observed. The results were compared with predictions by five different methods: BS 5400; Bradford & Johnson (ref. 11 in [27]); Weston & Nethercot (ref. 12 in [27]); SCI (ref. 14 in [27]) and Eurocode 4. The authors concluded that the maximum hogging moments in the tests exceeded the predictions of the EC4 method by 23 % to 33 %, while in comparison with BS 5400 the predictions were over 200 % larger than test results.

The inappropriate nature of the present BS 5400: Part 3 was shown also by Weston, Nethercot and Crisfield's analytical research [52]. A large deflection elasto–plastic finite element analysis was used. The results provided the basis for derivation of the equation for an approximate lower bound to the slenderness for lateral–torsional buckling as a function of three geometrical parameters (span of the girder, clear web depth between flanges and web thickness). This equation was for use in the design of continuous composite bridges in which the girders were of steel grade 43 or 50. The failure by lateral buckling of the compression flange near the internal supports occured in the finite element analyses at values of applied support moment four to five times higher than the ones predicted by BS 5400.

Stanway, Chapman and Dowling [44, 45] used buckling and non linear elasto–plastic critical buckling finite element analysis to model an initially imperfect column with an intermediate elastic restraint at three different positions within the length of the column. The authors paid particular interest to restraint position, column slenderness and column imperfection shape and magnitude, since these factors were relevant to the design of the restraint. Their results suggested again the revision of BS 5400. The proposal for a 1 % strength rule was supported here and columns

with multi–restraint were advised to be investigated further.

In more experimental work at the University of Warwick Johnson and Chen [25, 26] tested two half–scaled twin double cantilever girders with class 4 webs. One of the girders had the compression steel flange restrained by continuous U–frame action, the other one by discrete U–frames. These tests provided the bases for tentative design rules for stiffness, diagonal tension cracking of the slab, and local yielding of the steel flange.

All the above mentioned analytical and experimental work suggests that BS 5400: Part 3 needs to be revised. Many design rules have been suggested, but none of them has been codified so far. Many of these suggestions were made on basis of initial assumptions which narrowed the range of their use. That means that they could not be generalised for codified rules. They would not cover all possible situations. In 1995, the Highways Agency awarded a contract to Scott Wilson Kirkpatrick, consulting engineers, for research on bracing systems of steel and composite bridge girders. Computer analyses presented in this Part II of the present thesis contributed to this research, and should provide a basis for modifying the present design rules.

10.5 Overview of Part II of the thesis

Experimental work done so far on F–forces (as defined in BS 5400), has a very limited scope. It is almost impossible to achieve a validation of the expressions for F–forces by model tests due to the difficulty of fabricating steelwork to maximum permitted imperfections. Numerical studies are therefore more appropriate.

It is believed that F–forces are influenced much more by geometric imperfections and the deflections arisen from loading on transverse members than by residual stresses. To avoid fatigue failure, only elastic behaviour is assumed in bridge design. There is therefore a good case for using a numerical elastic finite element analyses with geometric non–linear facilities. A relevant part of the structure (a compressed flange) that has the maximum allowed geometric imperfections is modelled to determine F–forces. To simplify the model, the flange is created within a hogging moment region, considering only the main member on one side of the support. This

region is assumed to be about 10 to 15 m long (usually 1/5 of a span) with the length 5 m between two bracing points.

This study concentrates particularly on design forces for bracings at the supports of simply–supported and continuous composite UB and plate girder bridges. Half–through, box girder, truss and bowstring bridges are excluded from the present analyses since they require different boundary conditions to be applied. Interaction between horizontal F-forces and vertical shear forces is not considered. That means that the analyses provide the basis for F_2 forces only (as defined in BS 5400).

Neither the lateral guide restraints of sliding metal bearings nor the friction to be overcome in the bearing are considered in the analyses.

The yield stress, f_y, defines the failure axial force, N_{pl} (see Section 12.1 for explanation on using N_{pl} as a failure load). The material in the analyses is assumed to be isotropic and elastic behaviour is assumed. The results are presented as non–dimensional values related to N_{pl}. The value of $f_y = 355$ N/mm^2 is chosen as typical of material used in bridge design.

Chapter 11

Non–linear finite element analysis

11.1 Non–linear package of the I–DEAS Master Series

11.1.1 Overview of non–linear analysis

The I–DEAS Master Series is the latest (1994) version of this software. It was used here for the numerical studies. The non–linear package is an additional to the previous version VI of I–DEAS, which was used in Part I. The package is a structural finite element solver that takes into account geometric and material non–linear behaviour. It is capable of performing the following types of analyses:

- geometric non–linear analysis
- material non–linear analysis
- combined geometric and material non–linear analysis.

Geometric non–linear analysis was chosen for the present analyses. The software uses an Updated Lagrangian formulation. The load history is given as a function of time. This creates the solution time intervals where equilibrium equations are obtained. The software solves for displacements, stresses, strains, element forces, reaction forces and strain energies of a finite element model at these discrete time intervals in the history of the structure.

The finite element equations used in the software are derived from the principle of virtual work which states: *A loaded deformable body is in equilibrium if the total virtual work of the real external forces and moments is equal to the virtual work of the real internal stresses when the body is subjected to any virtual displacement consistent with the constraints.*

For the geometric non–linear analysis, the equations are formed with the respect to the current configuration and are solved by an iterative full Newton–Raphson method, where the tangent stiffness is updated for every iteration except first iteration for a new solution time point.

11.1.2 Elements used in the present analyses

11.1.2.1 Linear beam elements

A linear beam element is topologically a one–dimensional element but it can have displacements in three dimensions. The element has two nodes. Three translational and three rotational degrees of freedom are assigned to each node. It can be loaded by nodal forces and moments in three main directions, and by distributed constant or varying forces and moments along the element.

The material for the beam elements is assumed to be isotropic. The cross–section area and surface area per unit length of the linear beam are assumed to be constant.

Cross–sectional properties include *stiffness properties* such as cross–section area, y & z second moments of area where x axis is along the element, y & z shear area ratio, torsional constant, warping constant and warping restraint factor (not used in these analyses).

For more detailed information reference may be made to the on–line manual in the Master Series.

11.1.2.2 Node–to–ground translational spring elements

A node–to–ground translational spring element is connected to one node. It has three translational and three rotational degrees of freedom which are assigned to each node. It can be loaded by nodal force only.

It has a null material table. Physical properties are characterised by three translational stiffnesses which represent the forces required to move the node a unit distance in a given direction; and by a stiffness reference coordinate system whose axes define the directions in which the three stiffnesses act.

11.2 Validation of the software

To get familiar with the non–linear statics analysis in I–DEAS software a simple problem with one degree of freedom (shown in Fig. 11.1) was analysed. The example

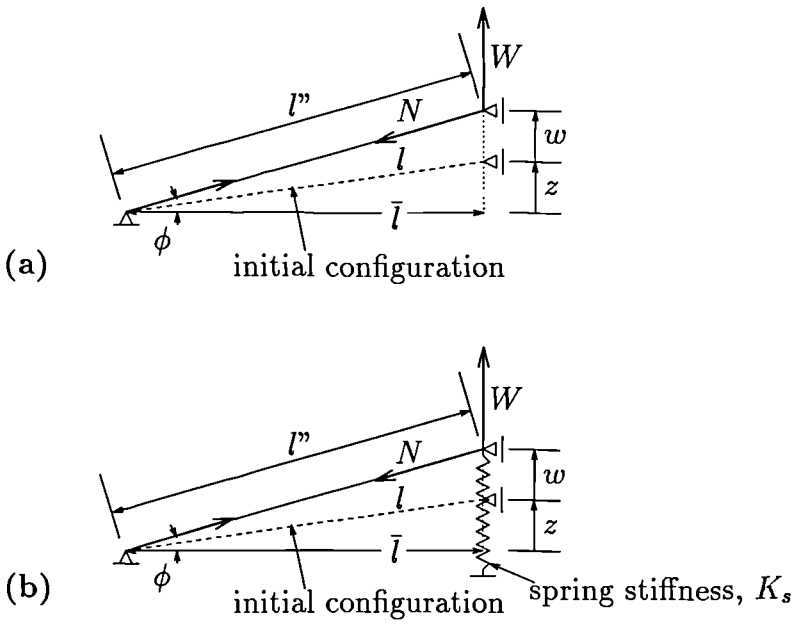

Figure 11.1: Simple problem with one degree of freedom.

was taken from a book written by M.A. Crisfield [8].

The dimensions and properties were:

$EA = 5 \times 10^7$ N; $z = 25$ mm; $l = 2500$ mm; $K_s = 1.35$ N/mm.

The cross–section was circular with diameter $D = 17.84$ mm. Both models (cases (a) and (b) in Fig. 11.1) had 25 linear beam elements of equal length. The spring in case (b) was represented by a translational node–to–ground spring element.

In case (a) the load increment was $\Delta W = -0.18$ N; in case (b) it was $\Delta W =$

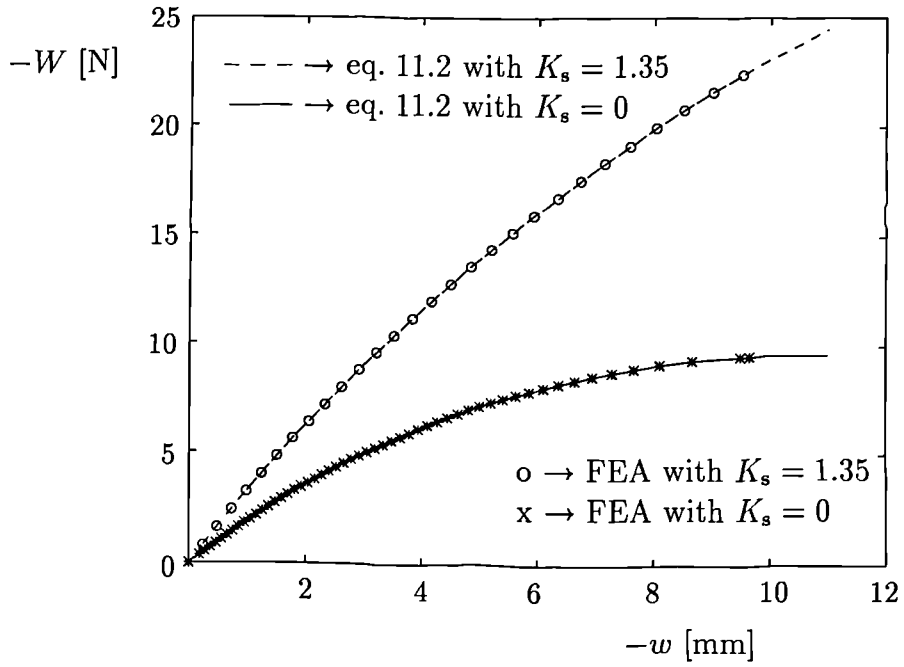

Figure 11.2: Load deflection curve of simple bar problem.

−0.8 N. The results, represented by load–deflection curves, are given in Fig. 11.2. Both solutions stopped when the axial force in the bar reached the Euler critical buckling force. For the given example theoretical value of N_{cr} is

$$N_{cr} = \frac{\pi^2 EI}{l^2} = 1570 \text{ N} \tag{11.1}$$

For case (a) finite element analysis gave the axial force in the bar at the last solution point as $N_a = -1560$ N; for case (b) it was $N_b = -1540$ N. Adding another ΔW would have increase the axial force in the bars above the value -1570 N.

The theoretical load–deflection curve [8] is given by the formula

$$W = \left(\frac{EA}{l^3}\right)\left(z^2 w + \frac{3zw^2}{2} + \frac{w^3}{2}\right) + K_s w. \tag{11.2}$$

The finite element non–linear solution gave very good match with the theoretical solution up to the point when the axial Euler critical force was reached in the model. To overcome this point the deflection history should have been introduced for the

solution — rather than load history. But for the future investigation of compressed flanges there was no need to find the solutions beyond the critical axial buckling force.

11.3 Creating a model

11.3.1 Geometry of a model

The objective of the present analysis was to investigate the behaviour of compressed flanges in continuous bridges, with particular interest in the F_u–forces as defined in BS 5400: Part 3 [56].

F_u forces provide restraint against lateral movements which can arise due to buckling of compressed flange above an internal support, as described in the previous chapter. The contribution of the web to restraining these lateral movements is negligible. Therefore U–frames are introduced at an appropriate spacing. They have to be designed for the restraining F_u–forces. They are modelled as elastic restraints with a stiffness K.

Assuming no web contribution and replacing a U–frame by a spring with stiffness K acting in the horizontal xy plane of the compressed flange, the model shown in Fig. 11.3 was created. Initial imperfections were considered to be as given by

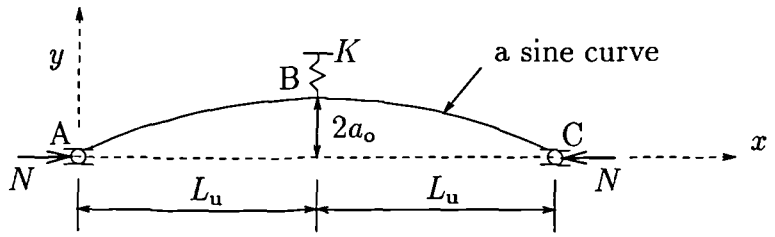

Figure 11.3: A model of compressed flange.

BS 5400: Part 6 [57]. At first, a sine curve was assumed. The maximum amplitude was given by $2a_o = \gamma_M L_G/1000 = 2L_u/667$ where L_G was the overall length of the model; $\gamma_M(= 1.5)$ was a safety factor; L_u was the length between two neighbouring restraints, taken as 5 m.

A cross–section of the flange is shown in Fig. 11.4. The plastic axial force is

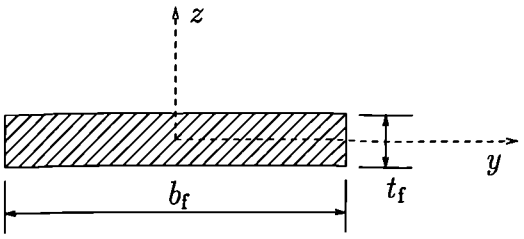

Figure 11.4: Cross–section of the model.

reached when

$$N_{pl} = b_f t_f f_y \tag{11.3}$$

where $f_y = 355$ N/mm^2 is the yield stress of the material. The elastic critical buckling force for a simply supported compressed strut is defined by the Euler force

$$N_{cr} = \frac{\pi^2 EI}{L_{cr}^2} \tag{11.4}$$

where EI is the flexural stiffness of the strut; L_{cr} is a critical buckling length, which is taken as the distance between two braced points.

According to Figs. 11.3 and 11.4 the weaker plane for buckling of this type of strut would be the xz plane. In the real bridge girder the flange would be restrained against buckling in this plane by a web. It will be shown later how these restraints were modelled in analyses. For now, let us assume that the strut will buckle in the horizontal xy plane. In that case the critical second moment of area is I_z defined as

$$I_z = \frac{b_f^3 t_f}{12} \tag{11.5}$$

The slenderness of the strut is defined in EC3 [55] by equation

$$\bar{\lambda} = \sqrt{\frac{N_{pl}}{N_{cr}}} \tag{11.6}$$

For an effective length of the flange equal to the distance L_u between the braced

points substitution of eqs. 11.3, 11.4 and 11.5 into eq. 11.6 gives

$$\bar{\lambda} = \sqrt{\frac{12 f_y L_u^2}{\pi^2 E b_f^2}} \tag{11.7}$$

From eq. 11.7

$$b_f = \frac{L_u}{\pi \lambda} \sqrt{\frac{12 f_y}{E}} \tag{11.8}$$

The width of the cross section is then calculated for the known values L_u = 5000 mm; E = 210 kN/mm^2; f_y = 355 N/mm^2 and $\bar{\lambda}$ = 0.6. In later analyses, the slenderness of the main member $\bar{\lambda}$ will range from 0.4 to 1.0. The thickness of the main member was taken as approximately $b_f/20$.

11.3.2 Boundary conditions

Once the geometry of the model was set, the length was divided into 50 equal linear beam elements. Thus 51 nodes each having 6 degree of freedom had to be considered for applying the boundary conditions. These consisted of a Restraint set and a Load set. Table 11.1 shows the way the nodes were restrained. Nodes A, B and C are as defined in Fig. 11.3. Thus all 51 nodes were restrained in the vertical xz plane

node	restraints					
	translational			rotational		
	x	y	z	x	y	z
A	free	0	0	0	0	free
B	0	free	0	free	free	free
C	free	0	0	0	0	free
all the others	free	free	0	free	free	free

Table 11.1: Boundary conditions in the model.

against any translational movement, to simulate a web which would restrain the flange in a real girder. Because the model was symmetrical, the middle point B was chosen to be restrained in the longitudinal x direction to prevent rigid body movement. Pinned end supports (points A and C) were modelled by restricting

sideways movements of end points. Those two points were also restrained against rotations around the x and y axes to prevent rigid body rotation.

The Load set was created by two forces acting longitudinally and against each other at the end points, causing constant compression in the main member. As explained in Section 11.1.1, the software solves for displacements, stresses etc. at discrete time intervals in the history of the structure. Therefore a linear relation between time intervals and load increments was introduced.

Fig. 11.5 shows the typical load–deflection curve for the strut simply supported

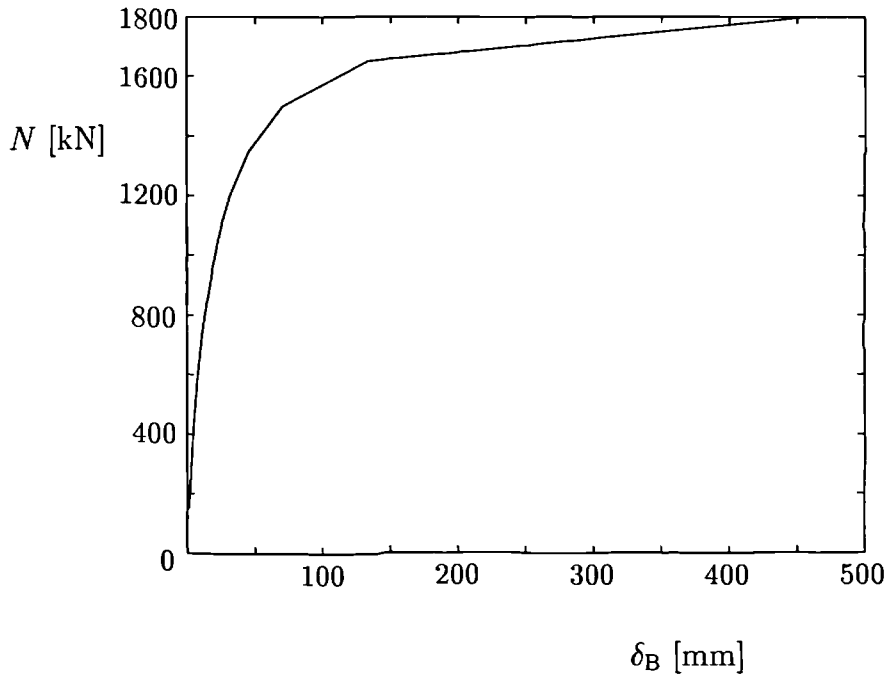

Figure 11.5: Load–deflection curve in non–linear analysis.

at the ends with the geometry given in Fig. 11.3 and 11.4 without a spring in the middle ($K = 0$). δ_B is deformation of the middle point B. The elastic critical force (for a cross–section 20 mm × 378 mm) using eq. 11.4 is $N_{cr} = 1865$ kN. The curve in Fig. 11.5 shows that the highest axial force at which convergence occurred is $N = 1800$ kN. The load increment was 150 kN, thus the next load would have been 1950 kN which was larger then N_{cr}.

Chapter 12

Results of computer analyses

12.1 Introduction

This chapter gives the results of numerical analyses. They are represented by an axial force in the model at first yield, N_y; forces in lateral elastic bracings, F_u; and lateral reaction forces at left and right supports, R_{s1} and R_{s2}, respectively. Unless otherwise stated, forces N_y, R_{s1} and R_{s2} were taken straight from non–linear finite element analyses at the load level at which the maximum stress along the main member reached the yield stress within 0.5 % accuracy. The yield stress was $f_y = 355\text{N/mm}^2$.

The non–dimensional compressive force in the main member is represented by the ratio N_y/N_{pl}, where N_{pl} is defined in eq. 11.3, and is used as a criterion of failure. The plastic axial force, N_{pl}, depends only on the geometrical and material properties of a cross–section. It is not influenced by any codified rules.

The design resisting force, N_R, is used for comparison of the results with a code. This force is defined in EC3 [55]. It is related to N_{pl} as follows

$$N_R = \chi N_{pl} \tag{12.1}$$

where χ is a function of the slenderness, $\bar{\lambda}$, and is given by the curve c of EC3.

F_u forces are calculated from the simple linear relationship, $F_u = K_b \delta_b$, where δ_b is the deformation of the cross–section in the horizontal xy plane at the braced point.

It is taken from finite element analysis at the same load level as the appropriate force N_y.

The bracing is modelled by a spring of stiffness K_b. A compressed imperfect strut, shown in Fig. 12.1, has a stiff bracing in the middle, if the elastic critical

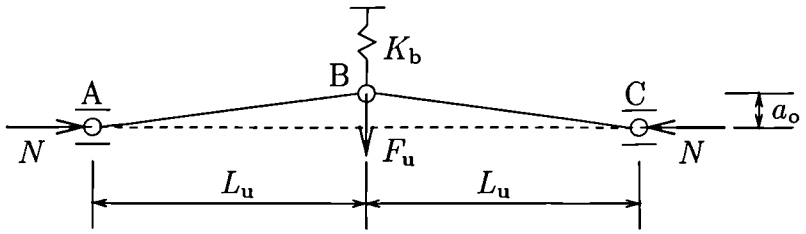

Figure 12.1: Shapes of initial imperfections.

buckling force for the strut (if straight) satisfies eq. 11.4 for $L_{cr} = L_u$. The initial eccentricity of point B relative to the line AC is a_o. Winter's paper [53] has shown that a perfect strut ABC (when $a_o = 0$) buckles at load N_{cr} (eq. 11.4) where

$$k_i \geq 2N_{cr}/L_u. \tag{12.2}$$

where k_i is a constant of the spring which would be sufficient to replace the full bracing thus the strut ABC snaps into the two–half–wave mode.

The force F_u depends on the spring stiffness K_b. Assuming that buckling occurs when $\delta_b = a_o$, where δ_b is a deformation of the spring after applying a compression force N, and neglecting any bending at point B, the condition for the spring stiffness is

$$K_b = 2k_i = 4N_{cr}/L_u. \tag{12.3}$$

The coefficient 4 gives the basic value for the stiffness of intermediate bracing in all following analyses.

12.2 An elastic lateral restraint in the middle of a compressed flange

12.2.1 Shape of initial imperfections

In addition to the simple sine curve explained in Section 11.3.1, curve A in Fig. 12.2, other imperfections were considered. Curve A is represented by function:

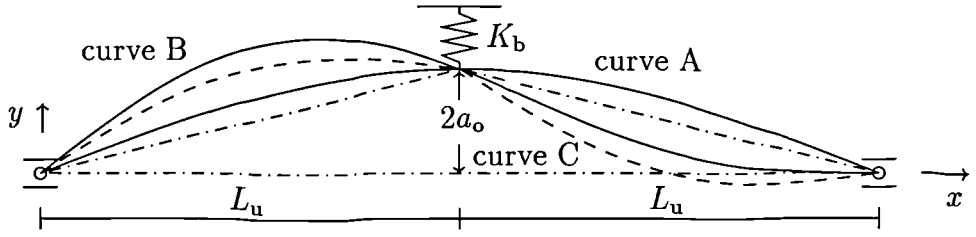

Figure 12.2: Shapes of initial imperfections.

$$y = 2a_o \sin \frac{\pi x}{2L_u} \tag{12.4}$$

The stiffness of a U–frame in a real structure was represented by the stiffness K_b of a spring element (see Fig. 12.2) given in the y–direction.

In the set up as described above the model could buckle generally in two different shapes: symmetrical and antisymmetrical. If the second one was true then the initial shape of imperfections following the antisymmetrical mode of buckling could be more critical. The initial imperfections of second model were presented by curve B (Fig. 12.2) which was the sum of functions:

$$y = 2a_o \sin \frac{\pi x}{2L_u} + a_o \sin \frac{\pi x}{L_u} \tag{12.5}$$

Curve C, dashed curve shown in Fig. 12.2, was used by Stanway [44, 45]. It was a sum of a triangle and the second part of eq. 12.5.

12.2.2 Change in stiffness of a spring

Table 12.1 gives the results of computer analyses for finding the influence of spring

	$K_b L_u/N_{cr}$	N_y	N_y/N_{pl}	N_y/N_R	$R_{s1} = R_{s2}$	R_{s1}/N_{pl}
		[kN]			[kN]	$\times 10^{-3}$
1	0	1352	0.504	0.641	0	0
2	2/3	2145	0.799	1.018	10.31	3.84
3	2	2460	0.917	1.167	10.75	4.01
4	3	2505	0.933	1.188	10.37	3.86
5	4	2529	0.942	1.200	10.17	3.79
6	5	2541	0.947	1.205	10.06	3.75
7	6	2550	0.950	1.210	9.99	3.72
8	8	2565	0.956	1.217	9.92	3.70
9	∞	2535	0.944	1.203	9.46	3.52
	K_b	δ_b	$\delta_b/2a_o$	F_u	F_u/N_y	F_u/N_{pl}
	[kN/mm]	[mm]		[kN]	$\times 10^{-3}$	$\times 10^{-3}$
1	0	47.68	3.179	0	0	0
2	0.994	20.72	1.381	20.61	9.61	7.68
3	2.984	7.206	0.480	21.50	8.74	8.01
4	4.477	4.630	0.309	20.73	8.28	7.72
5	5.97	3.407	0.227	20.34	8.04	7.58
6	7.46	2.607	0.180	20.12	7.92	7.50
7	8.953	2.232	0.149	19.98	7.84	7.44
8	11.94	1.662	0.111	19.84	7.73	7.39
9	∞	0	0	18.92	7.46	7.05

Table 12.1: Influence of spring stiffness.

stiffness on the strength of a flange. For this reason the slenderness of the flange was kept constant at the value $\bar{\lambda} = 0.6$. Thus the cross-section was then defined from eq. 11.8 as 20 mm × 378 mm (E = 210 kN/mm^2; f_y = 355 N/mm^2; $L_{cr} = L_u$ = 5000 mm). A plastic compression force (eq. 11.3) was N_{pl} = 2684 kN. The elastic critical force (eq. 11.4) was N_{cr} = 7461 kN, where I defined by eq. 11.5. EC3 design value of axial force (eq. 12.1) was N_R = 2108 kN.

12.2.3 Change in slenderness of the main member

The analyses of a compressed flange, where its slenderness was changing, were done for curve B of initial imperfections (see Fig. 12.2). Table 12.2 shows the results of

	λ	cross–section	N_{pl}	N_y	N_R/N_{pl}	N_y/N_{pl}
		[mm×mm]	[kN]	[kN]		
1	0.4	30×567	6038	5360	0.897	0.888
2	0.522	22×434	3389	2880	0.830	0.850
3	0.6	20×378	2684	2190	0.785	0.816
4	0.7	17×324	1955	1510	0.725	0.772
5	0.8	15×284	1512	1085	0.662	0.718
6	0.9	13×252	1163	764	0.600	0.657
7	1.0	12×227	967	580	0.540	0.600

	K_b	δ_b	F_u	F_u/N_y	F_u/N_{pl}	$\delta_b/2a_o$
	[kN/mm]	[mm]	[kN]	$\times 10^{-3}$	$\times 10^{-3}$	
1	30.244	1.223	36.99	6.90	6.126	0.082
2	9.949	2.121	21.102	7.33	6.23	0.141
3	5.97	2.806	16.752	7.65	6.25	0.187
4	3.197	3.848	12.302	8.15	6.29	0.256
5	1.899	4.96	9.419	8.65	6.23	0.331
6	1.15	6.165	7.09	9.28	6.096	0.411
7	0.776	7.37	5.72	9.86	5.92	0.491

Table 12.2: Influence of flange slenderness.

these analyses. The stiffness of spring was kept constant with the non–dimensional stiffness $K_b L_u/N_{cr} = 4$ (see Section 12.1 for explanation). The values of $\chi = N_R/N_{pl}$ were taken from EC3–curve c for appropriate slendernesses $\bar{\lambda}$ which varied from 0.4 to 1.0. They defined the cross–sections, as described in Section 11.3.1.

12.3 More than one elastic lateral restraint

12.3.1 Shape of initial imperfections

A strut of length $3L_u$ was analysed. When choosing a shape of initial imperfections, three "basic" shapes and two of their combinations were considered, as shown in

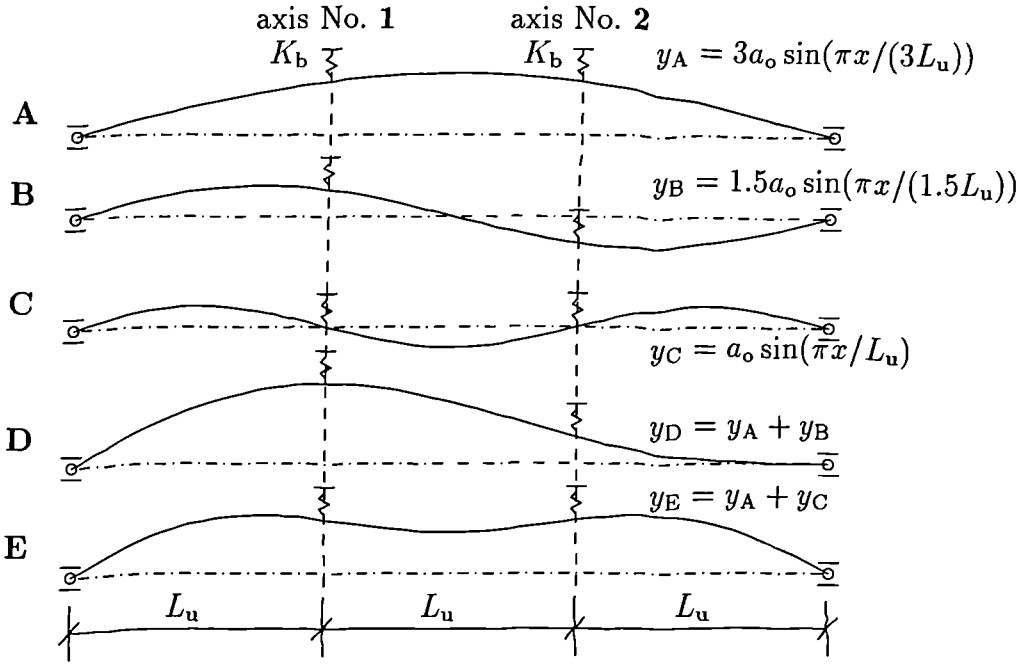

Figure 12.3: Shapes of initial imperfections.

Fig. 12.3. All of them were variations of a sine curve. The basic maximum amplitude a_o was $L_u/667$ (see Section 11.3.1). L_u was taken to be 5 m.

The elastic lateral bracings were represented by *two spring elements of stiffness* $K_b = 4N_{cr}/L_u$ at the third points, as indicated in Fig. 12.3. The reason for number 4 in the stiffness definition is given in Section 12.1.

The following values were common for all five models in the first shape analysis: slenderness of the main member $\bar{\lambda} = 0.6$; cross–section 20 mm × 378 mm; plastic axial force $N_{pl} = 2684$ kN where yield stress was taken as $f_y = 355$ N/mm^2; design value of axial force based on EC3 – curve c, $N_R = 2108$ kN; Euler elastic critical force $N_{cr} = 7461$ kN.

Load increments of 150 kN were used. The objective was to find which of these shapes of initial imperfections were the most adverse; meaning lower N_y/N_{pl}, or higher $K_b\delta_b/N_y$, where δ_b was a deformation of a spring.

Table 12.3 shows the results of the first shape analysis. The lower boundary values for shapes A, B, C, D and E represent the highest stage of loading before the first yield in a section was reached. Adding a load increment of 150 kN to axial force the first yield in the section was overcome and this stage of loading was

then represented by higher boundary values. The axial force at first yield was then approximately calculated by interpolation between the lower and higher boundaries

overall length of the main member slenderness of the main member stiffness of the springs			$3L_u$ $\bar{\lambda} = 0.6$ $K_b = 4N_{cr}/L_u$			
shape	lower boundary		higher boundary		interpolation	
	N_l	σ_l	N_h	σ_h	N_y	N_y/N_{pl}
	[kN]	[N/mm^2]	[kN]	[N/mm^2]	[kN]	
A	2550	349.05	2700	369.74	2593	0.966
B	2250	332.66	2400	355.88	2394	0.892
C	2250	348.85	2400	378.80	2281	0.850
D	2250	337.62	2400	361.26	2360	0.879
E	2250	353.86	2400	379.21	2257	0.841
F					2422	0.903
shape	$\delta_{b1,l}$	$\delta_{b2,l}$	$\delta_{b1,h}$	$\delta_{b2,h}$	$\delta_{b,max}$	$K_b\delta_{b,max}/N_y$
	[mm]	[mm]	[mm]	[mm]	[mm]	$\times 10^{-3}$
A	1.962	1.962	2.091	2.091	1.999	4.60
B	2.742	-2.74	2.991	-2.99	2.982	7.44
C	-2.43E-5	-2.43E-5	-2.73E-5	-2.73E-5	2.492E-5	6.52E-5
D	4.451	-1.03	4.826	-1.16	4.727	11.96
E	1.709	1.709	1.835	1.935	1.715	4.54
F					3.761	9.27

Table 12.3: Results of the first shape analysis.

using the formula:

$$N_y = N_l + \left(\frac{\sigma_y - \sigma_l}{\sigma_h - \sigma_l}\right)(N_h - N_l) \tag{12.6}$$

The maximum deformation in a spring $\delta_{b,max}$ was calculated in the same way using the larger absolute value of the deformations δ_{b1} or δ_{b2}, where δ_{b1} and δ_{b2} were the deformations of the springs along the axis No. 1 and 2 in Fig. 12.3, respectively.

A shape F was created later for the second set of shape analyses. It was shape D scaled down by the ratio 513/667. The results, shown in Table 12.3, were taken from finite element analyses in the same way as explained in Section 12.1 in contrast with the results for the other shapes obtained by the approximate interpolation.

Table 12.4 compares results for the shapes D, E (from Fig. 12.3) and F (scaled

as described above) where the slenderness of the main member was changed to $\bar{\lambda} = 1.0$ (cross–section: 12 mm × 227 mm; $K_b = 4N_{cr}/L_u = 0.776$ kN/mm).

overall length of the main member slenderness of the main member stiffness of the springs				$3L_u$ $\bar{\lambda} = 1.0$ $K_b = 4N_{cr}/L_u$		
shape	N_y	N_y/N_{pl}	$\delta_{b,max}$	$F_{u,max}$	$K_b\delta_{b,max}/N_y$	$K_b\delta_{b,max}/N_{pl}$
	[kN]		[mm]	[kN]	$\times 10^{-3}$	$\times 10^{-3}$
D	666	0.689	15.99	12.408	18.63	12.83
E	600	0.620	3.902	3.028	5.05	3.13
F	698	0.722	13.77	10.686	15.31	11.05

Table 12.4: Results of the second shape analysis.

12.3.2 Change in stiffness of springs

Shape D of Fig. 12.3 had the highest value of $K_b\delta_{b,max}/N_y$. This shape was therefore considered as the most adverse (see detailed explanation in Section 13.3.1). It was used as the basic shape of a compressed flange. The two springs were of the same stiffness K_b, which varied from 0 to infinity. The results are listed in Table 12.5. a_{b1} is an initial imperfection of the flange in xy plane where the spring 1 is placed (see vertical axis No. 1 in Fig. 12.3); δ_{b1} is its deformation along axis No. 1. The same applies for a_{b2} and δ_{b2} along axis No. 2. For shape D, $a_{b1} = 29.23$ mm and $a_{b2} = 9.74$ mm. $F_{u,max}$ is the larger of the two lateral forces created in the springs due to their deformations. R_{s1} and R_{s2} are reactions at the end supports counting from left to right, respectively.

12.3.3 Change in number of springs within a constant length

The beam of length $3L_u$ and of cross–section 20 mm × 378 mm with shape D of initial imperfections was divided into n equal lengths. Springs of stiffnesses $k_n = 2K_b/(n-1)$, where $K_b = 4N_{cr}/L_u$, were applied at $(n-1)$ internal nodes (see Fig. 12.4). The deformations of the springs and their stiffnesses are given in Table 12.6.

overall length of the main member slenderness of the main member		$3L_u$ $\bar{\lambda} = 0.6$				
stiffness of springs						
$K_{b1} = K_{b2} = K_b$	[kN/mm]	0	2.984	5.97	11.94	∞
$K_b L_u / N_{cr}$		0	2	4	8	∞
axial force at first yield						
N_y	[kN]	712.5	2258	2355	2423	2445
N_y / N_{pl}		0.266	0.843	0.879	0.904	0.912
deformations of springs						
δ_{b1}	[mm]	132	8.579	4.713	2.628	0
δ_{b1} / a_{b1}		4.516	0.293	0.161	0.090	0
δ_{b2}	[mm]	126.6	-1.306	-1.119	-0.699	0
δ_{b2} / a_{b2}		12.998	-0.134	-0.115	-0.072	0
maximum spring force						
$F_{u,max}$	[kN]	0	25.60	28.14	31.38	30.94
$F_{u,max} / N_R$	$\times 10^{-3}$	0	12.16	13.37	14.91	14.70
$F_{u,max} / N_y$	$\times 10^{-3}$	0	11.34	11.95	12.95	12.65
$F_{u,max} / N_{pl}$	$\times 10^{-3}$	0	9.55	10.5	11.71	11.54
reaction forces at pinned end supports						
R_{s1}	[kN]	0	15.77	16.53	17.09	17.32
R_{s2}	[kN]	0	5.935	4.924	4.371	3.702
R_{s1} / N_y	$\times 10^{-3}$	0	6.98	7.02	7.05	7.08
R_{s1} / N_{pl}	$\times 10^{-3}$	0	5.88	6.16	6.37	6.45

Table 12.5: Change in stiffnesses of springs.

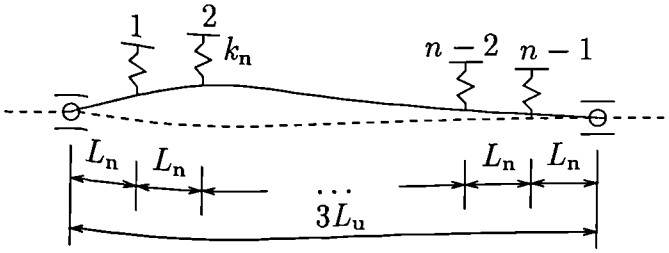

Figure 12.4: Multiple lateral elastic restraints.

overall length of the main member slenderness of the main member		$3L_u$ $\bar{\lambda} = 0.6$			
n		3	4	6	8
k_n	[kN/mm]	5.97	3.98	2.388	1.706
L_n	[mm]	5000	3750	2500	1875
axial force at first yield					
N_y	[kN]	2355	2430	2407	2415
N_y/N_{pl}		0.8787	0.9067	0.8981	0.9011
deformations and locations of springs					
δ_{b1}	[mm]	**4.713**	**5.677**	5.072	4.276
x_{b1}	[mm]	5000	3750	2500	1875
δ_{b2}	[mm]	-1.119	2.426	**6.056**	**6.518**
x_{b2}	[mm]	10000	7500	5000	3750
δ_{b3}	[mm]		-2.246	2.686	5.813
x_{b3}	[mm]		11250	7500	5625
δ_{b4}	[mm]			-1.402	2.84
x_{b4}	[mm]			10000	7500
δ_{b5}	[mm]			-2.385	-0.565
x_{b5}	[mm]			12500	9375
δ_{b6}	[mm]				-2.501
x_{b6}	[mm]				11250
δ_{b7}	[mm]				-2.102
x_{b7}	[mm]				13125
maximum forces in springs					
$F_{u,max}$	[kN]	28.14	22.6	14.46	11.12
$F_{u,max}/N_{pl}$	$\times 10^{-3}$	10.48	8.42	5.39	4.14
reaction forces at pinned end supports					
R_{s1}	[kN]	16.53	19.54	20.87	21.47
R_{s2}	[kN]	4.924	3.774	3.065	2.894
R_{s1}/N_{pl}	$\times 10^{-3}$	6.16	7.28	7.78	8.00

Table 12.6: Multiple lateral elastic restraints.

12.3.4 Elastic buckling analysis

Linear elastic critical buckling analyses were performed on models with multiple lateral elastic restraints as shown in Fig. 12.4. It was decided to perform three sets of solutions for three types of initial imperfections – no imperfection, shape C and shape D from Fig. 12.3.

Number n was a number of equal lengths within the overall length $3L_u$ separated by lateral elastic restraints of following stiffnesses: $k_{n=2}$ = 11.94 kN/mm; $k_{n=3}$ = 5.97 kN/mm; $k_{n=4}$ = 3.98 kN/mm; $k_{n=6}$ = 2.388 kN/mm; $k_{n=8}$ = 1.706 kN/mm. Thus the overall lateral stiffness of each model was unchanged.

The boundary conditions for elastic buckling analysis were different from the ones used in non–linear analysis. Rotational restraints in the x and y–directions were added to each node. The reason was to avoid the singularity of stiffness matrix formulation when solving the eigenvalue problems. The first modes of buckling shapes of the models are shown in Fig. 12.5. According to the manual for I–DEAS software: *The buckled shape is normalised such that the maximum displacement is one metre or maximum rotation is one radian.* In the presented results all models were governed by maximum displacement.

Table 12.7 shows the results of the linear buckling analyses. The eigenvalue λ_{buck}

	shape of initial imperfections					
	none		shape C		shape D	
n	λ_{buck}	N_{cr}	λ_{buck}	N_{cr}	λ_{buck}	N_{cr}
1	5.519	828	5.519	828	5.519	828
2	21.967	3295	21.968	3295	21.968	3295
3	49.032	7355	49.031	7355	49.030	7355
4	60.687	9103	60.686	9103	60.684	9103
6					58.077	8712
8					56.484	8473

Table 12.7: Results of buckling analysis.

is the buckling load factor given by computer analysis which multiplied by applied load (which was 150 kN) gives the value of elastic critical buckling force N_{cr}.

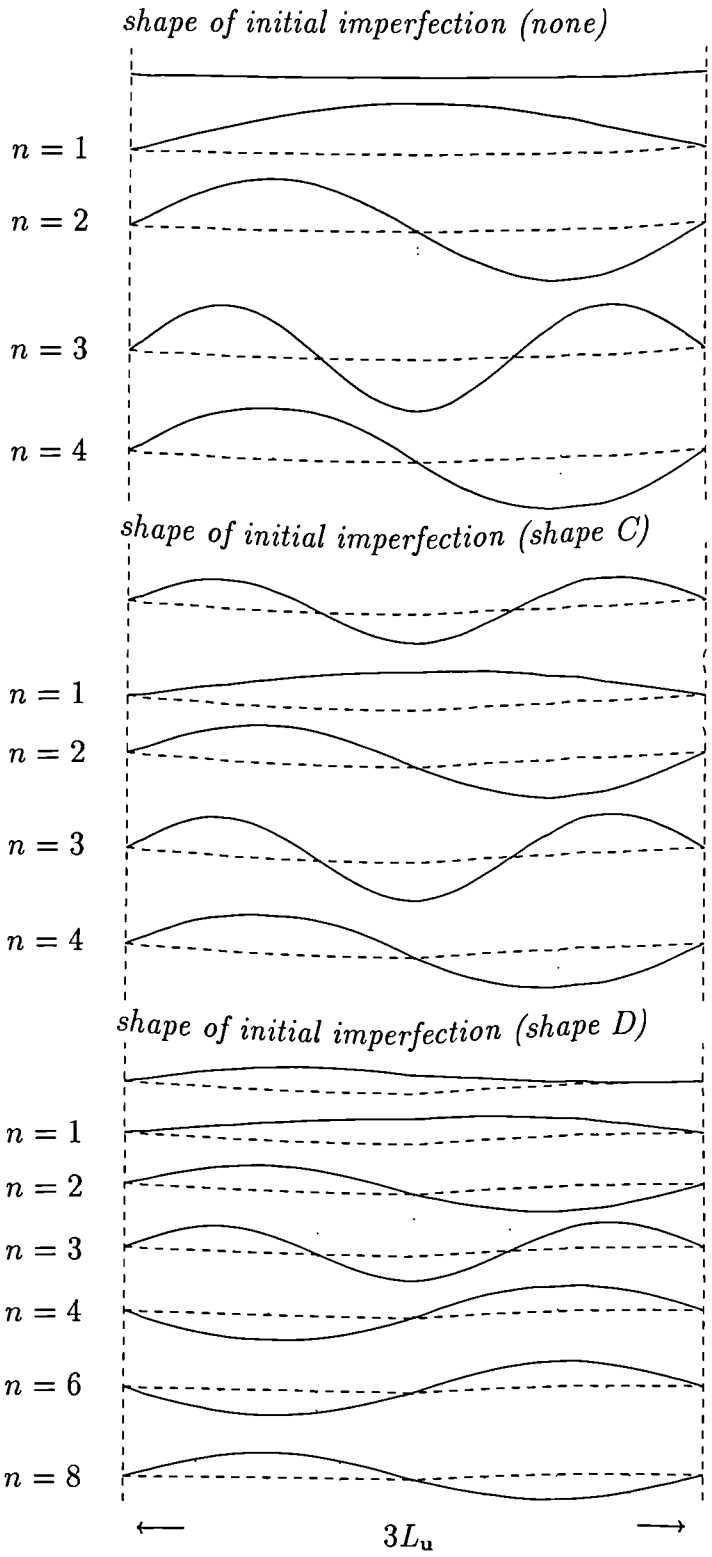

Figure 12.5: The first modes of buckling shapes.

12.4 Elastic lateral end supports

The model represented by curve B in Fig. 12.2 was considered again. The boundary conditions of the end supports were changed such that, in the y–direction the restraints were elastic with stiffness $K_1 = K_2 = 2K_b$, where K_b was the stiffness of the elastic restraint placed in the middle of the model as given in the heading **2** of Tables 12.8 to 12.13. Frequently, designers have the stiffness of lateral bracings at the supports at least ten times the value of the stiffness for intermediate bracings. This is not necessary since there is no evidence of the need for such a high ratio. Clearly, the support bracings need to be stronger than the intermediate bracings and so for simplicity an initial guess of 2:1 was chosen. Reffering to Tables 12.8 to 12.13 (and as explained in Section 13.4) there is very little difference between using either a low or high ratio. The heading **1** of Tables 12.8 to 12.13 shows the cardinal characteristics of the main member.

The values of F_u marked by an asterisk were not calculated from $F_u = K_1\delta_1$, because they represent the reaction force at a pinned support where $\delta_1 = 0$ (δ_1 is a deformation in the left hand support in contrast with δ_{b1} which was a deformation of the first bracing counting from the left, where the multiple elastic restraints were applied). The minus sign in values δ_y means that the deformation of an end point was in the negative direction along the y axis. The minus sign in the 'difference' column represents the decrease in a lateral force when changing the elastic supports to pinned ones.

Table 12.8 gives the comparison between the models using elastic supports at end points where the stiffnesses of the supports are $K_1 = K_2 = 2K_b$ and $K_1 = K_2 = \infty$, respectively, where $K_b = 4N_{cr}/L_u$. Table 12.9 shows the same comparison for $K_b = 2N_{cr}/L_u$. The slenderness of the main member is $\bar{\lambda} = 0.6$.

For Table 12.10, the overall length is increased from $2L_u$ to $3L_u$; other data are as in Table 12.8.

Tables 12.11 to 12.13 give the same comparisons for beams with one intermediate lateral elastic bracing as in Table 12.8, for slendernesses of the main member $\bar{\lambda} =$ 0.4 to 1.0.

1	overall length of the main member			$2L_u$	
	slenderness of the main member			$\bar{\lambda} = 0.6$	
	cross–section			20 mm × 378 mm	
	stiffness of internal spring			$K_b = 4N_{cr}/L_u$	
2			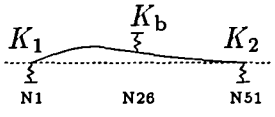	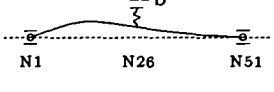	difference [%]
	K_b	[kN/mm]	5.97	5.97	
	$K_1 = K_2$	[kN/mm]	11.94	∞	
	axial force at first yield				
	N_y	[kN]	2175	2190	0.69
	σ_y	[N/mm^2]	354.49	355.03	
	displacements along the main member				
	$\delta_{x,N1}$	[mm]	6.908	6.951	
	$\delta_{x,N26}$	[mm]	0	0	
	$\delta_{x,N51}$	[mm]	-6.863	-6.909	
	deformations perpendicular to the main member (y–direction)				
	$\delta_{y,N1}$	[mm]	-0.701	0	
	$\delta_{y,N26}$	[mm]	2.804	2.806	
	$\delta_{y,N51}$	[mm]	-0.701	0	
	lateral forces (y–direction)				
	$F_{u,N1}$	[kN]	8.37	8.375*	0.06
	$F_{u,N26}$	[kN]	-16.74	-16.752	0.07
	$F_{u,N51}$	[kN]	8.37	8.375*	0.06

Table 12.8: Change of restraint conditions at supports (a).

1	overall length of the main member		$2L_u$		
	slenderness of the main member		$\bar{\lambda} = 0.6$		
	cross–section		20 mm × 378 mm		
	stiffness of internal spring		$K_b = 2N_{cr}/L_u$		
2			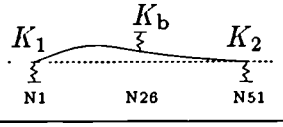	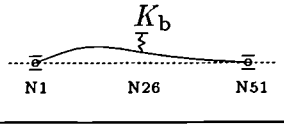	difference [%]
	K_b	[kN/mm]	2.985	2.985	
	$K_1 = K_2$	[kN/mm]	5.97	∞	
	axial force at first yield				
	N_y	[kN]	2115	2138	1.09
	σ_y	[N/mm^2]	354.27	354.13	
	displacements along the main member				
	$\delta_{x,N1}$	[mm]	6.744	6.804	
	$\delta_{x,N26}$	[mm]	0	0	
	$\delta_{x,N51}$	[mm]	-6.684	-6.751	
	deformations perpendicular to the main member (y–direction)				
	$\delta_{y,N1}$	[mm]	-1.403	0	
	$\delta_{y,N26}$	[mm]	5.611	5.610	
	$\delta_{y,N51}$	[mm]	-1.403	0	
	lateral forces (y–direction)				
	$F_{u,N1}$	[kN]	8.376	8.372*	-0.05
	$F_{u,N26}$	[kN]	-16.749	-16.746	-0.02
	$F_{u,N51}$	[kN]	8.376	8.372*	-0.05

Table 12.9: Change of restraint conditions at supports (b).

1	overall length of the main member			$3L_u$	
	slenderness of the main member			$\bar{\lambda} = 0.6$	
	cross–section			20 mm × 378 mm	
	stiffness of internal springs			$K_b = 4N_{cr}/L_u$	
2			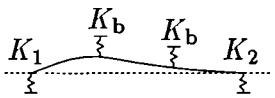	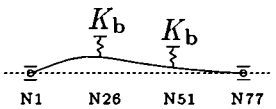	difference [%]
	K_b	[kN/mm]	5.97	5.97	
	$K_1 = K_2$	[kN/mm]	11.94	∞	
	axial force at first yield				
	N_y	[kN]	2347	2355	0.34
	σ_y	[N/mm^2]	355.08	354.25	
	displacements along the main member				
	$\delta_{x,N1}$	[mm]	11.14	11.17	
	$\delta_{x,N26}$	[mm]	3.699	3.711	
	$\delta_{x,N51}$	[mm]	-3.713	-3.724	
	$\delta_{x,N77}$	[mm]	-11.10	-11.14	
	deformations perpendicular to the main member (y–direction)				
	$\delta_{y,N1}$	[mm]	-1.417	0	
	$\delta_{y,N26}$	[mm]	4.732	4.713	
	$\delta_{y,N51}$	[mm]	-1.040	-1.119	
	$\delta_{y,N77}$	[mm]	-0.429	0	
	lateral forces (y–direction)				
	$F_{u,N1}$	[kN]	16.92	16.53*	-2.36
	$F_{u,N26}$	[kN]	-28.25	-28.13	-0.43
	$F_{u,N51}$	[kN]	6.21	6.68	7.57
	$F_{u,N77}$	[kN]	5.12	4.924*	-3.98

Table 12.10: Change of restraint conditions at supports (c).

1	overall length of the main member			$2L_u$	
	slenderness of the main member			$\bar{\lambda} = 0.4$	
	cross–section			30 mm × 567 mm	
	stiffness of internal spring			$K_b = 4N_{cr}/L_u$	
2			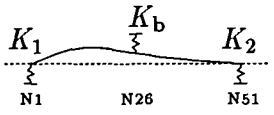	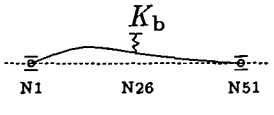	difference [%]
	K_b	[kN/mm]	30.244	30.244	
	$K_1 = K_2$	[kN/mm]	60.488	∞	
	axial force at first yield				
	N_y	[kN]	5350	5360	0.19
	σ_y	[N/mm^2]	355.014	354.58	
	displacements along the main member				
	$\delta_{x,N1}$	[mm]	7.503	7.515	
	$\delta_{x,N26}$	[mm]	0	0	
	$\delta_{x,N51}$	[mm]	-7.486	-7.499	
	deformations perpendicular to the main member (y–direction)				
	$\delta_{y,N1}$	[mm]	-0.301	0	
	$\delta_{y,N26}$	[mm]	1.203	1.223	
	$\delta_{y,N51}$	[mm]	-0.301	0	
	lateral forces (y–direction)				
	$F_{u,N1}$	[kN]	18.207	18.5*	1.61
	$F_{u,N26}$	[kN]	-36.384	-36.988	1.66
	$F_{u,N51}$	[kN]	18.207	18.5*	1.61

Table 12.11: Change of restraint conditions at supports (d).

1	overall length of the main member			$2L_u$	
	slenderness of the main member			$\bar{\lambda} = 0.8$	
	cross section			15 mm × 284 mm	
	stiffness of internal spring			$K_b = 4N_{cr}/L_u$	
2			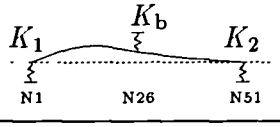	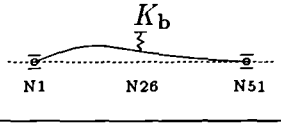	difference [%]
	K_b	[kN/mm]	1.899	1.899	
	$K_1 = K_2$	[kN/mm]	3.798	∞	
	axial force at first yield				
	N_y	[kN]	1078	1085	0.6
	σ_y	[N/mm^2]	354.48	353.76	
	displacements along the main member				
	$\delta_{x,N1}$	[mm]	6.174	6.203	
	$\delta_{x,N26}$	[mm]	0	0	
	$\delta_{x,N51}$	[mm]	-6.071	-6.107	
	deformations perpendicular to the main member (y–direction)				
	$\delta_{y,N1}$	[mm]	-1.279	0	
	$\delta_{y,N26}$	[mm]	5.115	4.960	
	$\delta_{y,N51}$	[mm]	-1.279	0	
	lateral forces (y–direction)				
	$F_{u,N1}$	[kN]	4.858	4.710*	-3.14
	$F_{u,N26}$	[kN]	-9.713	-9.419	-3.12
	$F_{u,N51}$	[kN]	4.858	4.710*	-3.14

Table 12.12: Change of restraint conditions at supports (e).

1	overall length of the main member			$2L_u$	
	slenderness of the main member			$\bar{\lambda} = 1.0$	
	cross–section			12 mm × 227 mm	
	stiffness of internal spring			$K_b = 4N_{cr}/L_u$	
2			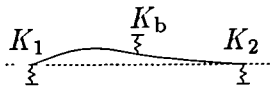	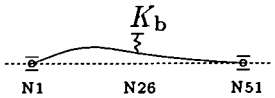	difference [%]
	K_b	[kN/mm]	0.776	0.776	
	$K_1 = K_2$	[kN/mm]	1.552	∞	
	axial force at first yield				
	N_y	[kN]	575	576	0.2
	σ_y	[N/mm^2]	354.174	352.54	
	displacements along the main member				
	$\delta_{x,N1}$	[mm]	5.344	5.346	
	$\delta_{x,N26}$	[mm]	0	0	
	$\delta_{x,N51}$	[mm]	-5.130	-5.150	
	deformations perpendicular to the main member (y–direction)				
	$\delta_{y,N1}$	[mm]	-1.954	0	
	$\delta_{y,N26}$	[mm]	7.815	7.291	
	$\delta_{y,N51}$	[mm]	-1.954	0	
	lateral forces (y–direction)				
	$F_{u,N1}$	[kN]	3.033	2.829*	-7.2
	$F_{u,N26}$	[kN]	-6.064	-5.658	-7.2
	$F_{u,N51}$	[kN]	3.033	2.829*	-7.2

Table 12.13: Change of restraint conditions at supports (f).

12.5 Non–uniform axial force

12.5.1 Distributed force $N/(4L_u)$ per unit length

The model of curve B in Fig. 12.2 was used in analyses where an axial force was not constant along the beam. As shown in Fig. 12.6 the beam was held in position

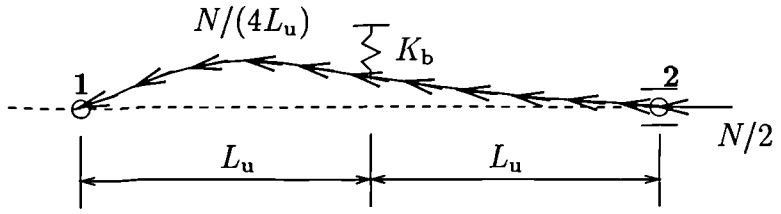

Figure 12.6: Non–uniform axial force along the main member.

at point **1**, thus there were horizontal and vertical reaction forces (N_1 and R_{s1} respectively) at this point. At point **2** the beam was free to move along the length and force $N/2$ was applied. Distributed axial force $N/(L_u)$ per unit length was applied to the main member. N_{y1} represents the axial force at point **1** when first yield occurred anywhere along the main member. The stiffness of the bracing was $K_b = 4N_{cr}/L_u$. The results are given in Table 12.14.

12.5.2 Distributed force $N/(2L_u)$ per unit length

Another loading was applied to the model shown in Fig. 12.6. The distributed force was changed to $N/(2L_u)$ per unit length, thus the axial force at point **2** was zero. Fig. 12.7 shows the variations of force N (and stress N/A_a) in the compressed flange. Thus, results for three types of axial force can be compared. As shown in Fig. 12.8, for loading L_3, where $q = N/(2L_u)$ & $N_2 = 0$, three analyses with $\bar{\lambda} = 0.6$ were done for pinned support at end **1** and three for elastic support at end **1**. The lateral stiffnesses K_2 at end **2** are shown in Fig. 12.8. The results of the analyses are given in Table 12.15.

	λ		0.6		0.8		1.0	
	N_{pl}		2684		1512		967	
	loading		const.	distr.	const.	distr.	const.	distr.
1	pinned supports ($K_1 = K_2 = \infty$)							
	R_{s1}	[kN]	8.375	9.635	4.710	5.657	2.829	3.691
	$R_{\mathrm{s1}}/N_{\mathrm{pl}}$	$\times 10^{-3}$	3.12	3.59	3.12	3.74	2.93	3.82
	N_{y1}	[kN]	2190	2445	1085	1225	576	662
	$R_{\mathrm{s1}}/N_{\mathrm{y1}}$	$\times 10^{-3}$	3.82	3.94	4.34	4.62	4.91	5.58
	difference	[%]	3.1		6.5		13.6	
2	elastic supports ($K_1 = K_2 = 2K_{\mathrm{b}}$)							
	R_{s1}	[kN]	8.37	9.712	4.858	5.822	3.033	3.899
	$R_{\mathrm{s1}}/N_{\mathrm{pl}}$	$\times 10^{-3}$	3.12	3.62	3.21	3.85	3.14	4.03
	N_{y1}	[kN]	2175	2438	1078	1215	575	654
	$R_{\mathrm{s1}}/N_{\mathrm{y1}}$	$\times 10^{-3}$	3.85	3.98	4.51	4.79	5.27	5.96
	difference	[%]	3.4		6.2		13.1	

Table 12.14: Distributed load $N/(4L_{\mathrm{u}})$ per unit length.

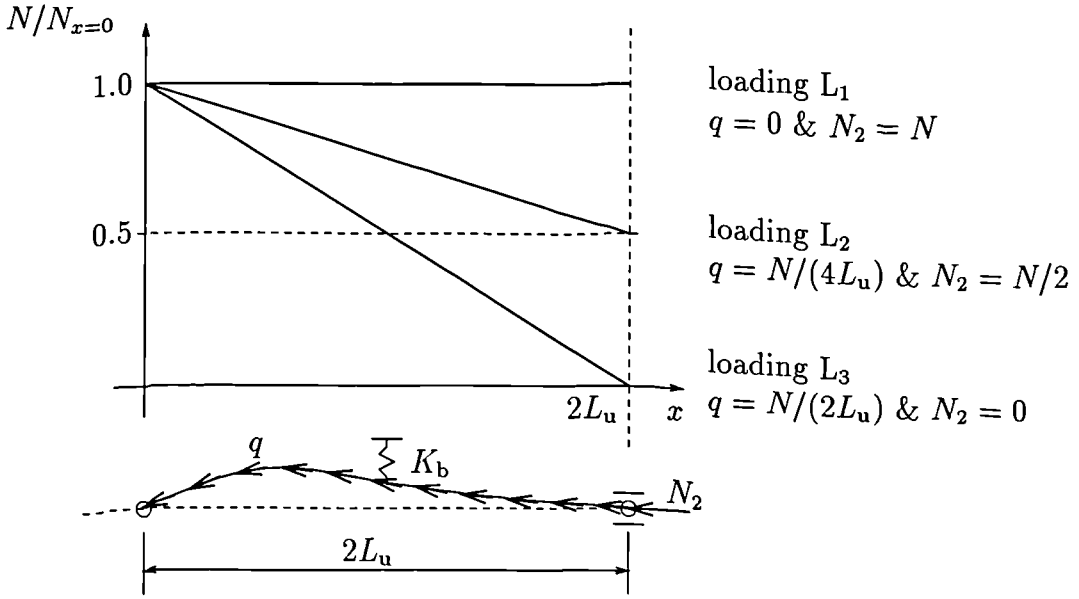

Figure 12.7: Type of axial force applied to models.

	loading		const.	distr.	distr.	distr.	distr.
	type of loading as in Fig. 12.7		L_1	L_2	L_3		
				$N/(4L_u)$	$N/(2L_u)$	$N/(2L_u)$	$N/(2L_u)$
	N_{y2}	[kN]	2190	1222.5	0		
1	pinned support at end **1** ($K_1 = \infty$)						
	conditions for K_2		∞			0	$K_b/100$
	R_{s1}	[kN]	8.375	9.635	10.48	0.692	4.309
	R_{s1}/N_{pl}	$\times 10^{-3}$	3.12	3.59	3.90	0.26	1.61
	N_{y1}	[kN]	2190	2445	2633	2363	2483
	R_{s1}/N_{y1}	$\times 10^{-3}$	3.82	3.94	3.98	0.29	1.74
2	elastic support at end **1** ($K_1 = 2K_b$)						
	conditions for K_2		$2K_b$			0	$K_b/100$
	K_2	[kN/mm]	11.94			0	0.0597
	R_{s1}	[kN]	8.37	9.712	10.639	0.727	4.49
	R_{s1}/N_{pl}	$\times 10^{-3}$	3.12	3.62	3.96	2.71	1.67
	N_{y1}	[kN]	2175	2438	2633	2363	2483
	R_{s1}/N_{y1}	$\times 10^{-3}$	3.85	3.98	4.04	0.31	1.81

Table 12.15: Variation in non–uniform axial force.

12.6 Summary of the results

This chapter lists all results obtained from the non–linear finite element analyses. They are analysed and discused in the following chapter using diagrams which were plotted from the results given in the tables of this chapter. The appropriate number of the table used for the plot is shown in the right top corner of each diagram.

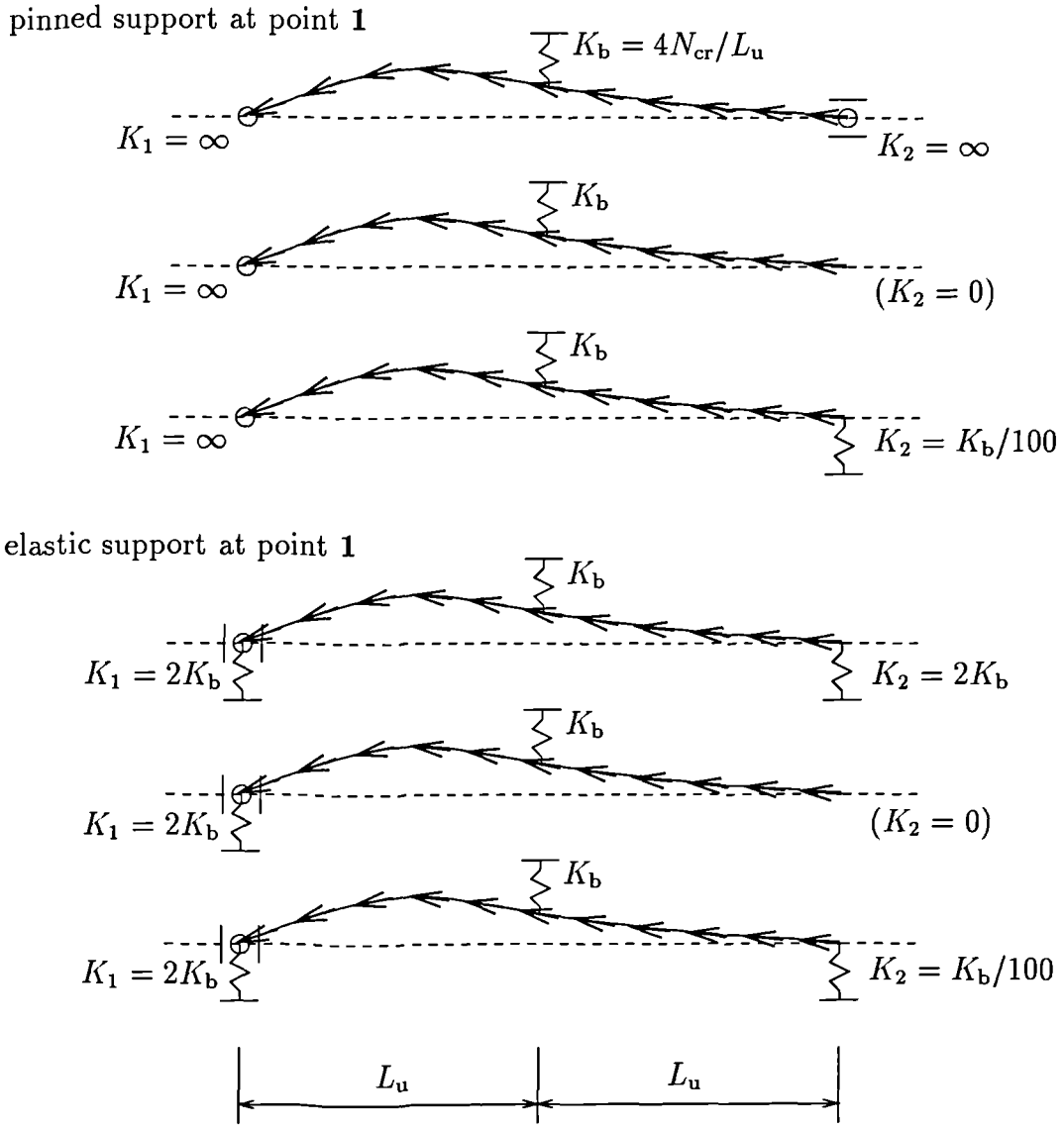

Figure 12.8: Support variation at end points.

Chapter 13

Analyses and discussions

13.1 Introduction

Results given in the tables of the previous chapter are discussed in this chapter. The same numbering and titles of the sections are used. The graphs are plotted using values from the tables in Chapter 12. The numbers of the appropriate tables are given at the top right corners of the graphs.

13.2 An elastic lateral restraint in the middle of compressed flange

13.2.1 Shape of initial imperfections

Comparing curves A and B in Fig. 12.2 the second one was found to be more critical. This is shown by comparing $N_{yA} = 2529$ kN (Table 12.1) and $N_{yB} = 2190$ kN (Table 12.2), where for both curves $\bar{\lambda} = 0.6$ and $K_b L_u / N_{cr} = 4$. The ratio $N_{yB}/N_{pl} = 0.876 < N_{yA}/N_{pl} = 0.942$, as also shown in Fig. 13.1. However, in the following analysis (Section 13.2.2) curve A was used for finding the influence of the stiffness of an intermediate elastic bracing, represented here by a spring, on the value of an axial force at first yield in a section.

13.2.2 Change in stiffness of a spring

In Fig. 13.1 the variation of the axial force at first yield in a cross–section is plotted

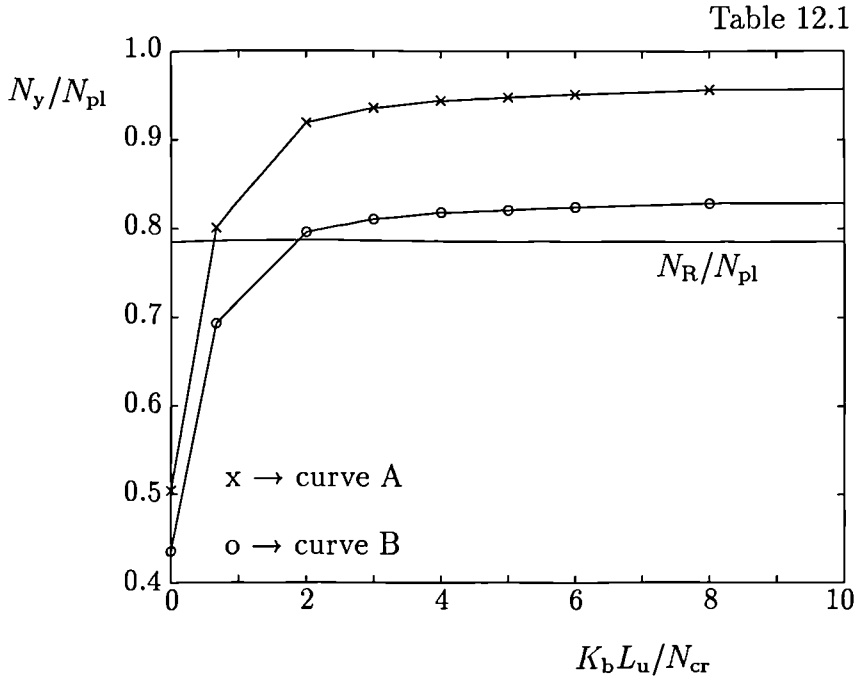

Figure 13.1: Axial force at first yield versus stiffness of a spring.

against the stiffness of a spring at mid–length of the member. The curve marked by 'x' is defined by the values given in Table 12.1 which were obtained from analyses with initial imperfections of type A. For the value $K_b L_u/N_{cr} = 4$ and slenderness $\bar{\lambda} = 0.6$ both curves A and B were used in analyses. The results for curve B are given in Table 12.2. This shape of the curve leads to a more critical value of axial force at first yield by 15 %. Therefore it is assumed that analyses for curve B by the same way as it is done for curve A will give all axial forces at first yield for appropriate values K_b as 15 % less than the values for curve A. The estimated axial forces at first yield for curve B, found in this way, are marked 'o' in Fig. 13.1.

Comparing these results with the design value, N_R, taken from EC3, it can be seen that for $K_b L_u/N_{cr} \geq 2$ the axial force in a compressed beam when the first yield is reached in a cross–section is larger than the design value, when considering the most critical case of initial imperfections allowed by BS 5400: Part 6 and taking to

account the safety factor $\gamma_M = 1.5$. The spring stiffness of 2 (as defined in Fig. 13.1) is well up on the shoulder of the curve, which also agrees exactly with Stanway's results [44].

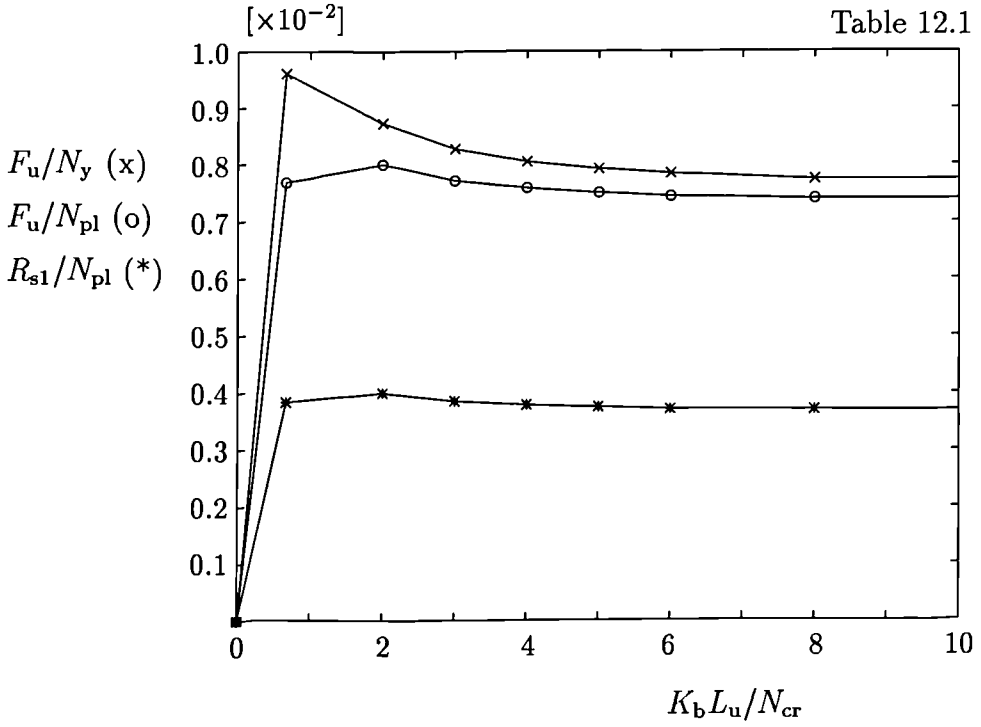

Figure 13.2: Lateral spring force and reaction at end support versus spring stiffness.

Fig. 13.2 shows that F_u is always less than 1 % of either N_y or N_{pl}. The lateral spring force is almost constant at the value 0.0075 N_{pl} for $K_b L_u/N_{cr} \geq 2$. The variation of the reaction force at a pinned end (R_{s1}) is also shown here. From symmetry, it is $0.5F_u$ for each $K_b L_u/N_{cr}$.

In Table 12.1 it can be seen that $\delta_b/2a_o$ passes through 1.0 (the value assumed in the simple theory developed by Winter [53] and explained in Section 12.1) before $K_b L_u/N_{cr}$ reaches 2, and is lower at all higher values of K_b. That suggests a sufficiently stiff system.

13.2.3 Change in slenderness of the main member

Fig. 13.3 shows that the design values of an axial force are below yield (on the safe side) for almost the whole range of slenderness by an amount which is not excessive. For $\bar{\lambda} \leq 0.4$, buckling of a flange is hardly a problem.

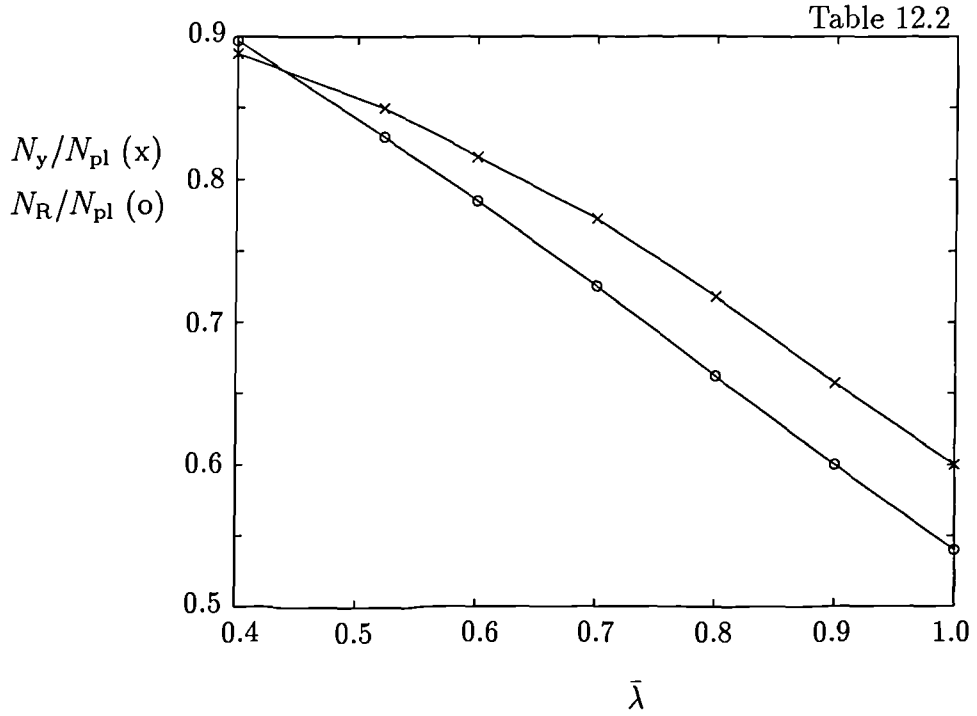

Figure 13.3: Axial force at first yield versus slenderness.

In Fig. 13.4 a spring force is almost constant at $0.006N_{pl}$. This ratio can suggest the design ratio for finding the lateral force in U–frame.

13.3 More than one elastic lateral restraint

13.3.1 Shape of initial imperfections

The results for shapes A, B, C, D and E (Fig. 12.3), shown in Table 12.3, are analysed first. The criterion for finding the most adverse shape is either the lowest value of N_y/N_{pl} or the highest value of $K_b\delta_{b,max}/N_y$. Shape E has the lowest value of the ratio N_y/N_{pl}, 0.957 times the ratio for shape D. The value $K_b\delta_{b,max}/N_y$ for shape D

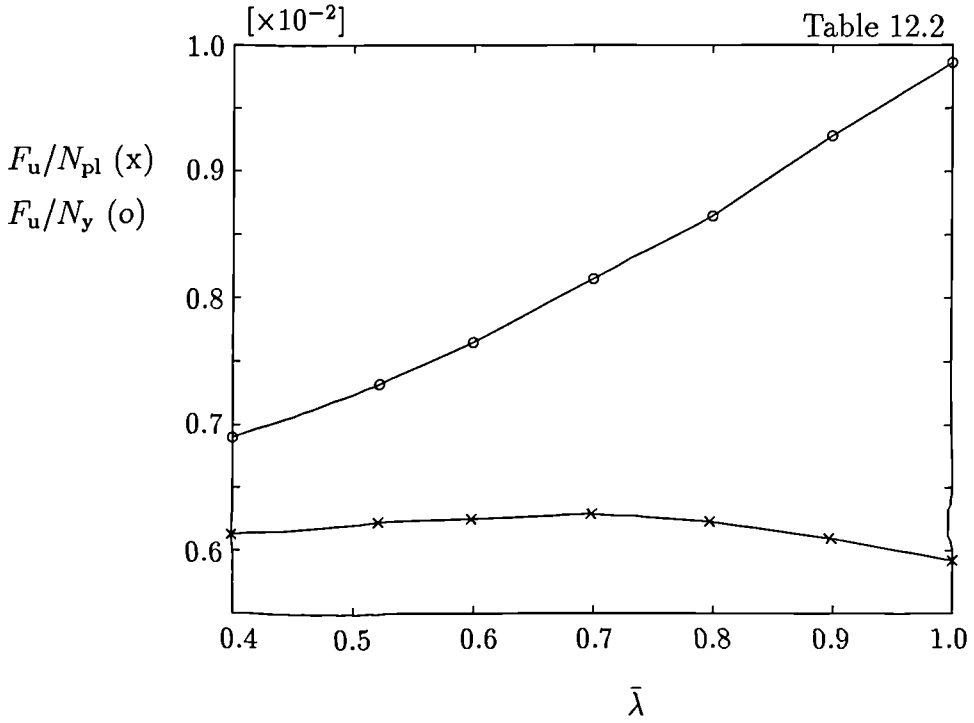

Figure 13.4: Lateral force in a spring versus slenderness.

is 2.63 times greater than the one for shape E. Comparing these differences, shape D has the most critical initial imperfections because the large difference between the values $K_b\delta_{b,max}/N_y$ influences the required resistance of the bracing member.

From Table 12.3 the failure load for shape E was calculated as $N_y = 2257$ kN. The lower boundary value for shape D is $N_l = 2250$ kN. The difference between these two forces is only 0.3 %. But the ratio $(K_b\delta_{b1,l}/N_l)_D/(K_b\delta_{b,max}/N_y)_E = (11.81/4.54) = 2.6$. This shows that having an axial force at the same level for both shapes D and E, the lateral forces in bracings are very different and definitely more critical for shape D.

The interpretation of BS 5400: Part 6 is now discussed. Shape D is perhaps too adverse, because it is the sum of two functions. The first function gives shape A of Fig. 12.3, where the maximum imperfection is measured from the line connecting two end points of the main member of length $L_G = 3L_u$, thus $a_{max,A} = L_G/667 = 3L_u/667 = 22.5$ mm (for $L_u = 5000$ mm). The second function represents shape B of Fig. 12.3, where the maximum imperfection is measured from the line joining an

end and a middle point of the main member of length $L_G = 3L_u$, thus $a_{max,B} = (L_G/2)/667 = 1.5L_u/667 = 11.25$ mm. There is an assumption that the middle point has already the maximum imperfection of shape A. Joining the left end point with the middle point and considering an additional maximum imperfection between those two points as in shape B suggests adding the functions of shapes A and B together. This results in shape D of Fig. 12.3. The maximum imperfection over the length L_G, however is increased to $a_{max,D} = 29.23$ mm, which is approximately $L_G/513$. This value might be considered too large. Nevertheless, this is the initial imperfection considered in the analyses.

Because of the doubt of the adversity of shape D, a shape F was analysed later. The results for shape F show an increase in N_y of about 2.6 % (cf. shape D). Thus shape E also becomes 6.8 % more critical than shape F when *axial* force at first yield is the criterion. However, the ratio $K_b\delta_{b,max}/N_y$ for shape F is still 51.03 % higher than that for shape E, when *lateral* force is the criterion.

From the comparison of the analyses for shapes D and F, it can be said that scaling down the lateral imperfections 1.3 times (from shape D to shape F), brings down the lateral forces by about 22.5 %, while keeping the axial force at first yield at approximately the same level. If we strictly consider the shape, which has the most critical value for *axial* force at first yield between shapes A, B, C, E and F, then shape F would be out of consideration. But both shapes D and F show the most critical *lateral* forces in comparison with all the other shapes of initial imperfection. Thus using shape D is definitely on the safe side, in respect of BS 5400.

Table 12.4 compares the results for models with the following characteristics: slenderness of the main member $\bar{\lambda} = 1.0$; cross–section: 12 mm × 227 mm; $K_b = 4N_{cr}/L_u = 0.776$ kN/mm. The axial force at first yield for shape E gives the most critical value, which is 9.91 % less than that for shape D. But for the lateral force (which for shape E less by 75.6 %), shape D gives the more critical value. The ratio of lateral force to the yield axial force for shape E is $(F_{u,max}/N_{pl})_E = 3.13 \times 10^{-3}$; and for shape D it is $(F_{u,max}/N_{pl})_D = 12.83 \times 10^{-3}$, where $N_{pl} = 967$ kN. Thus basing the design rules for lateral forces on shape D gives the most critical values.

13.3.2 Change in stiffness of springs

Fig. 13.5 shows the variation of axial force at first yield plotted against stiffness of

Table 12.5

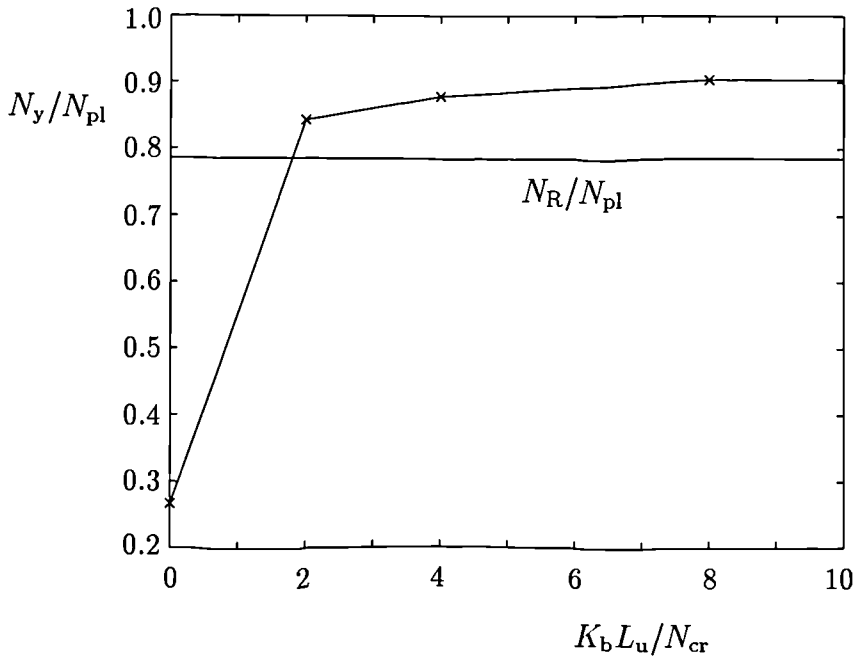

Figure 13.5: Axial force in the main member at first yield.

the springs. As in Section 13.2.2 where there was only one elastic restraint placed in the middle, the axial force of the main member, when the first yield is reached, is well up on the shoulder of the curve for $K_b L_u/N_{cr} \geq 2$.

Fig. 13.6 shows the maximum force in a spring ('x') and the larger reaction at a pinned end ('o') against the spring stiffness $K_b L_u/N_{cr}$. In contrast to the same relationship plotted in Fig. 13.2, the force $F_{u,max}$ in Fig. 13.6 has an increasing tendency with its convergence towards $0.012N_{pl}$. The reaction force at the pinned restraint shows the constant value of about 0.6 % of N_{pl}.

The conclusion of Section 13.2.2 that the lateral force F_u in an elastic restraint is always less than 1 % of N_{pl} seems to be not correct and the ratio, if considered as a basis for finding the design value, has to be increased to at least 1.2 % of N_{pl}. The reason for this increase in lateral force could be the increase in the maximum amplitude of initial imperfections ($a_{max} = 19.5$ mm in Section 13.2.2; $a_{max} = 29.23$ mm

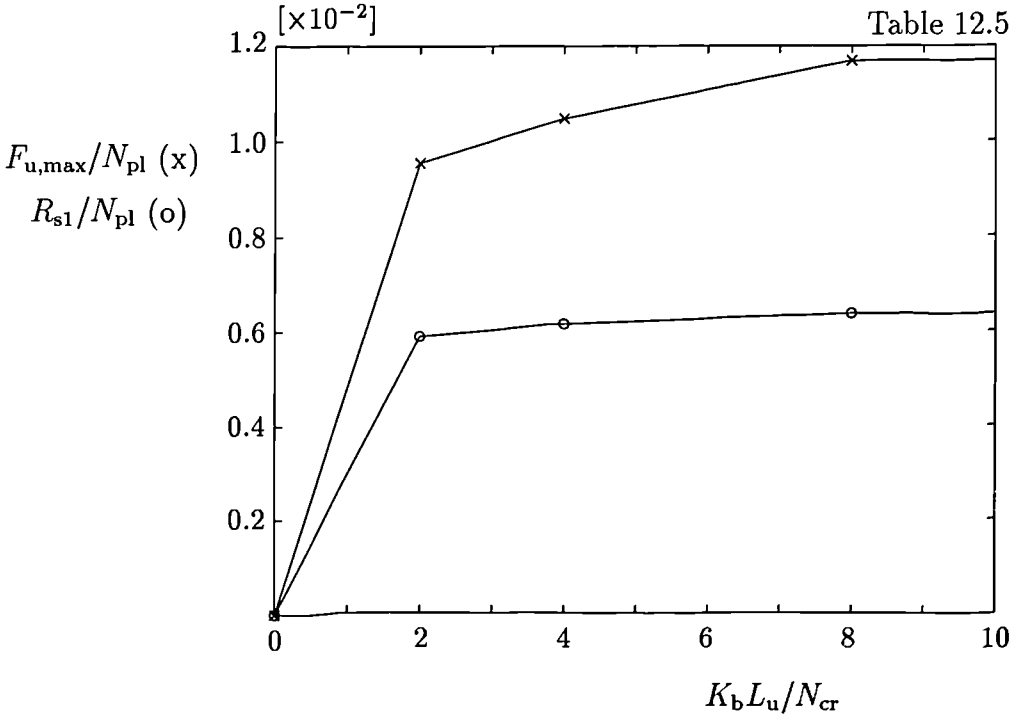

Figure 13.6: Maximum lateral force in a spring versus stiffness of a spring.

here).

13.3.3 Change in number of springs within a constant length

Table 12.6 gives the values of the axial forces at first yield which, as can be seen, are varying within 3.1 % so there is no significant change in N_y. The maximum lateral force in a spring is calculated as $F_{u,max} = k_n \delta_{b,max}$, where $\delta_{b,max}$ is the maximum spring deformation in a model (printed by bold characters in Table 12.6).

The greater of the two reaction forces increases by 23.01 % as the number of intermediate restraints increases from 2 to 7, while the total lateral stiffness of those restraints is constant, as shown in Fig. 13.7. The variable n in Fig. 13.7 is the number of the equal lengths within the overall length of the main member.

13.3.4 Elastic buckling analysis

From simple elastic theory the elastic critical buckling load of the strut is given by eq. 11.4 where L_{cr} is overall length of $3L_u$ for $n = 1$. Thus $N_{cr} = 829.047$ kN.

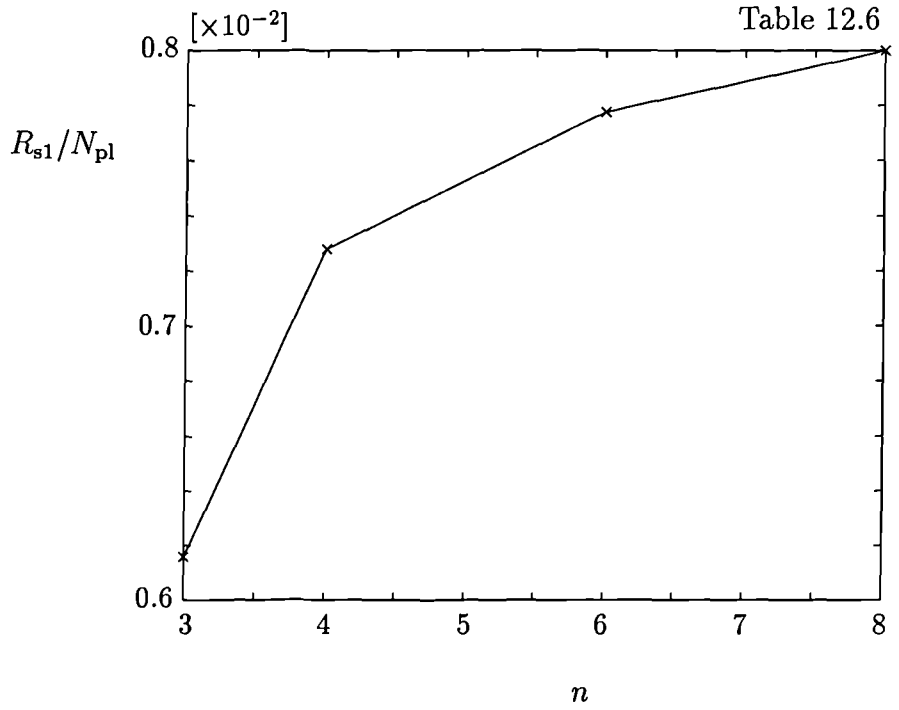

Figure 13.7: Reaction force versus number of intermediate springs.

Comparing this value with the values in Table 12.7, finite element modelling gives the value of 1.43 % lower for all three sets of solutions. This agreement suggest that the finite element analysis is performing well with the accuracy up to 1.5 %.

A strut of a general shape as shown in Fig. 13.8 is loaded by axial force N. Let

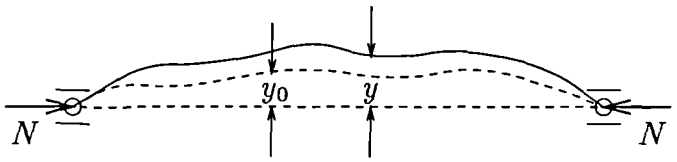

Figure 13.8: Pin–ended strut with initial deformation.

the shape of initial imperfections of the strut when $N = 0$ (the broken curve in Fig. 13.8) be represented by a Fourier series

$$y_0 = \sum_{i=1}^{\infty} a_i \sin \frac{i\pi x}{L} \tag{13.1}$$

where the amplitudes a_i are known. Similarly the displacements of the loaded strut

can be expressed as

$$y = \sum_{i=1}^{\infty} \bar{a}_i \sin \frac{i\pi x}{L} \tag{13.2}$$

where the amplitudes $\bar{a}_i$ are to be found.

The bending moment in the loaded strut is

$$M = Ny = -EI\left(\frac{\mathrm{d}^2 y}{\mathrm{d}x^2} - \frac{\mathrm{d}^2 y_0}{\mathrm{d}x^2}\right) \tag{13.3}$$

which leads to the differential equation

$$\frac{\mathrm{d}^2 y}{\mathrm{d}x^2} + k^2 y = \frac{\mathrm{d}^2 y_0}{\mathrm{d}x^2} \tag{13.4}$$

where $k^2 = N/EI$.

Solving the equation and making the assumptions as given in [2] (Section 2.2.2, p.81 to 83) leads to the displacement for loads close to the Euler load

$$y = \frac{a_1}{[1 - (N/N_{\mathrm{cr}})]} \sin \frac{\pi x}{L} \tag{13.5}$$

where N_{cr} is the Euler elastic critical buckling load, because the amplitude of the first mode becomes very large — larger than all the others, which can be neglected in consequence. The eq. 13.5 shows that the amplitude of the first member of the Fourier series in eq. 13.1 is increased by an amplification factor $1/[1 - (N/N_{\mathrm{cr}})]$, which becomes infinitely large when $N \rightarrow N_{\mathrm{cr}}$ and it is true for any value of a_1.

Thus the elastic critical buckling force is proven to be independent of the shape of the initial imperfection, when small-deflection theory is used. This is believed to be true also for an elastically restrained strut. As expected, the computed critical elastic buckling force for the analysed models is the same as it would be for a straight model (without any imperfections), independent of the initial curve of the model — assuming small deflections (see Table 12.7).

As explained in Section 12.3.4, the overall lateral stiffness of each model was unchanged. $n - 1$ springs were equally distributed along the main member. Their stiffnesses decreased as the number $n-1$ increased. If the stiffness of each individual

spring is high enough then the springs would divide the beam into n critical lengths which define the elastic critical force. Thus using eq. 11.4 the theoretical critical forces are listed in Table 13.1. To calculate these forces the assumption $k_{n=i} = \infty$ is made. The critical length, L_{cr}, used in eq. 11.4, is the distance between two

n	L_{cr}	N_{cr}	$k_n L_{cr}/N_{cr}$
	mm	kN	
1	15000	829	
2	7500	3317	27.0
3	5000	7462	4.0
4	3750	13267	1.12
6	2500	29851	0.2
8	1875	53069	0.08

Table 13.1: Elastic critical forces.

neighbouring lateral restraints. Comparing Table 13.1 with Table 12.7 and Fig. 12.5, the theoretical critical forces are in good agreement with the results of finite element analysis for n = 1,2, and 3 (the difference is only up to 1.5 %). For $n > 3$ the critical elastic forces obtained by finite element analysis are lower than the critical forces calculated for the assumption $k_{n=i} = \infty$. This suggests that the stiffnesses of the springs, where $n > 3$, are not high enough. This conclusion is supported also by the shape of the first mode of buckling (see Fig. 12.5). However, this is expected, since spreading a constant overall lateral stiffness along the beam will decrease the value of $k_n L_{cr}/N_{cr}$ of each spring, as it is shown in Table 13.1. Therefore to perform elastic critical buckling analyses of this type some other assumptions need to be made which was not the aim of the present work.

When $n = 4$ the stiffness of each spring is $k_{n=4} = 3.98$ kN/mm. This is a higher value than $K_b = 2N_{cr}/L_{cr} = 2.984$ kN/mm. Therefore one more elastic critical buckling analysis was performed where $n = 3$ and stiffnesses of the two springs were $K_b = 2N_{cr}/L_{cr} = 2.984$ kN/mm. The elastic critical buckling force, N_{cr}, was equal to 6288 kN which was 15.7 % less than expected if the stiffnesses of the springs were to be considered infinite. The mode of buckling was the same as for all $n > 3$ in the above shown analyses. Therefore the conclusion is that for elastic critical buckling

the stiffness of the lateral restraints is not high enough when $K_b = 2N_{cr}/L_{cr}$. This would be in contrary with the conclusions made in Section 13.2.2 and therefore more investigations are needed in the area of non–linear analyses for the stiffness of the lateral restraint $K_b = 2N_{cr}/L_{cr}$.

13.4 Elastic lateral end supports

The objective of these analyses was to find any significant changes in axial force at first yield and in F_u–forces, when the infinitely stiff end supports in the y–direction were replaced by elastic restraints with finite stiffness $K_1 = K_2 = 2K_b$.

As can be seen from both of Tables 12.8 and 12.9, the axial force at first yield decreased approximately by only 1 % when the pinned end points were replaced by elastic ones. The change in lateral force at end point nodes is not larger than 0.07 % (where the pinned supports were applied, the reaction force in the support was taken as a lateral force).

The same comparison was performed for the beam of length $3L_u$. Results are shown in Table 12.10. The change in the axial force at first yield is about 0.3 %. When the pinned end support is change to elastic, the highest lateral force, $F_{u,N26}$, increases very slightly, and is 1.2 % of N_y. The greater lateral force at support increases by 2.3 % to 0.72 % of N_y.

Tables 12.11 to 12.13 and Table 12.8 compare the main members with one intermediate lateral elastic bracing, for slendernesses of the main member $\bar{\lambda} = 0.4$ to 1.0. The change in axial force at first yield is again only about 0.2 to 0.6 %, but the changes in lateral forces range from -6.7 % to 1.6 %. Fig. 13.9 shows the relation between the slenderness of a beam and the change in lateral forces at support when changing the elastic end supports to the pinned ones. The absolute value of the difference between pinned and elastic restraint forces seems to go up with increasing slenderness of the main member.

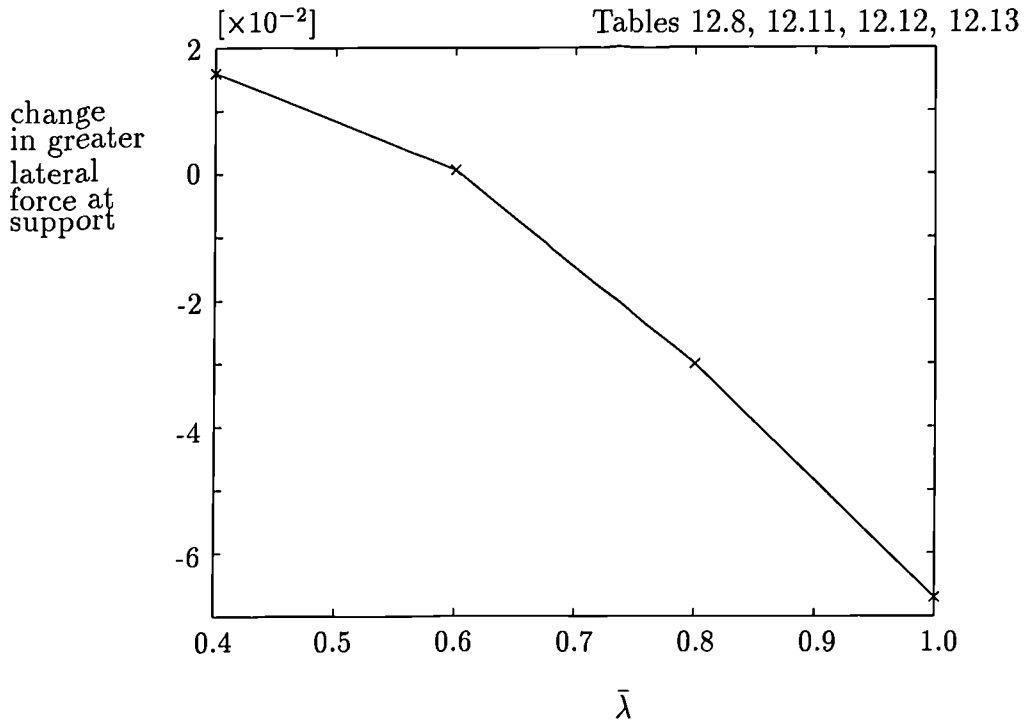

Figure 13.9: Lateral forces, for stiff and elastic restraints, versus slenderness.

13.5 Non–uniform axial force

13.5.1 Distributed force $N/(4L_u)$ per unit length

Table 12.14 and Fig. 13.10 show the increase in lateral force with slenderness, for both uniform axial force N_y, and for distributed axial force along the beam. For $\bar{\lambda} = 0.6$ the change to distributed force increases R_{s1}/N_{y1} by only about 3 %. But as $\bar{\lambda}$ increases the lateral force increases by a larger amount and for $\bar{\lambda} = 1.0$ the increase is about 12 %. Fig. 13.10 also indicates that the variation of the lateral force with varying slenderness of the main member is non–linear when the axial force is distributed along the main member in contrast to the linear variation when the axial force is constant along the main member. This figure was plotted only for the first part of Table 12.14. In the given scale the values of the second part would give the points almost overlapping the ones already plotted.

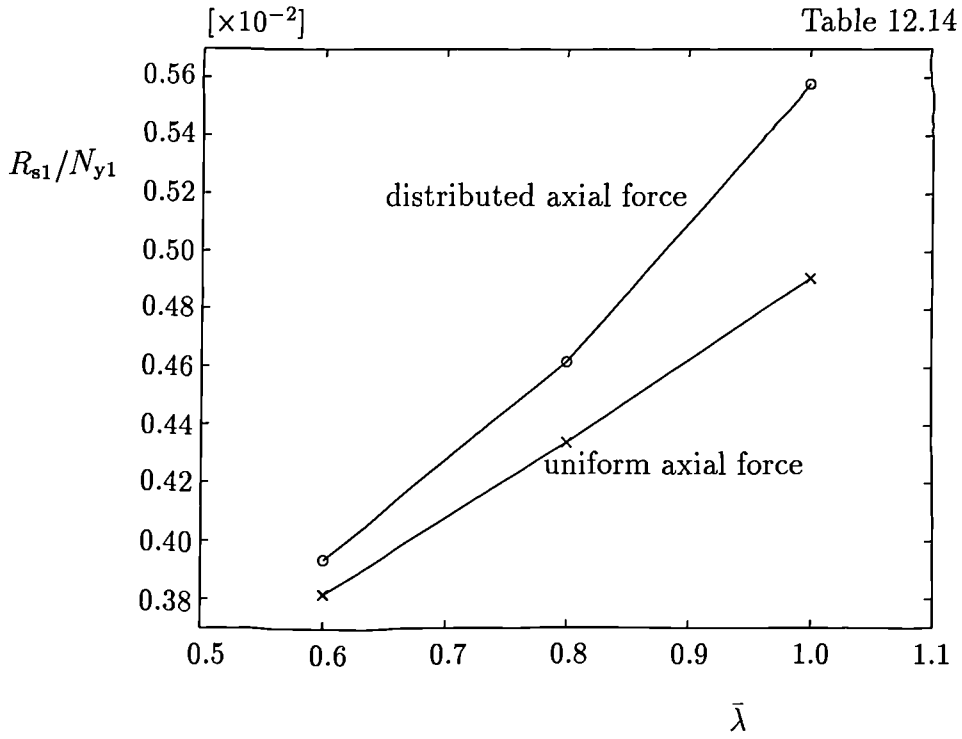

Figure 13.10: Lateral restraint force versus slenderness.

13.5.2 Distributed force $N/(2L_u)$ per unit length

Fig. 13.11 shows the variation of the lateral force as the distribution of axial force per unit length in the main member is varied. R_{s1} changes by 20.1 %, but the increase in the ratio R_{s1}/N_{y1} is only 4 % (Table 12.15).

Keeping the same distribution of axial force along the main member ($N/(2L_u)$ per unit length) and changing only the stiffness of the elastic restraint at point **2** from $2K_b$ to 0 brings the lateral force at the end support **1** (point **1**) considerably down as expected and as shown in Fig. 13.12. Figs. 13.11 and 13.12 are plotted only for the second part of Table 12.15. Comparing the appropriate values of the two parts, the difference between them is negligible at the scale of Figs. 13.11 and 13.12.

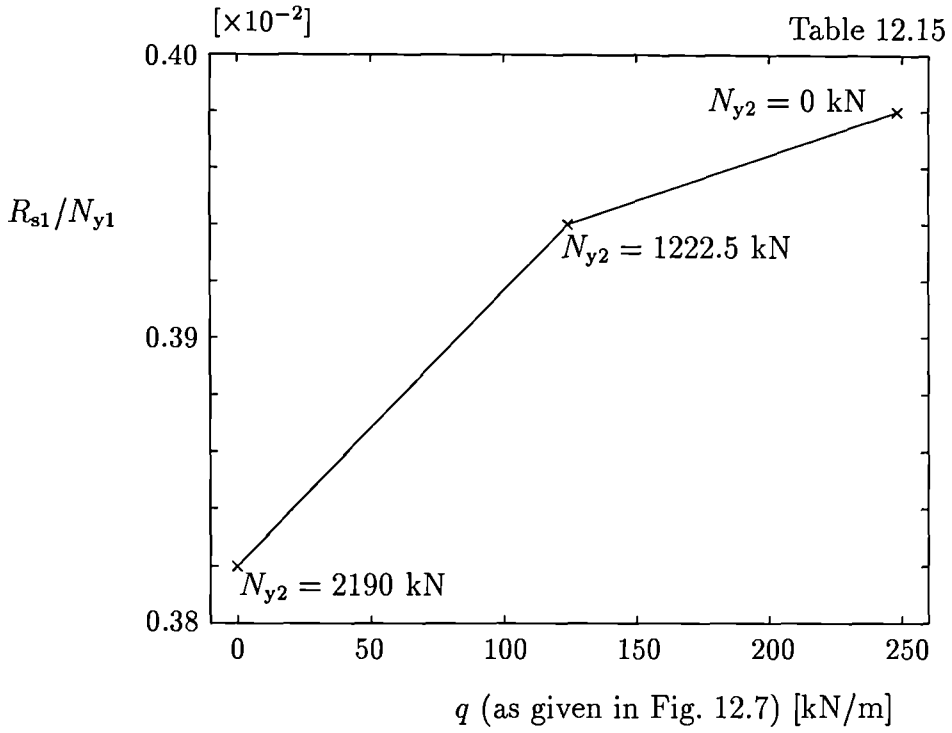

Figure 13.11: Lateral restraint force versus distributed axial force.

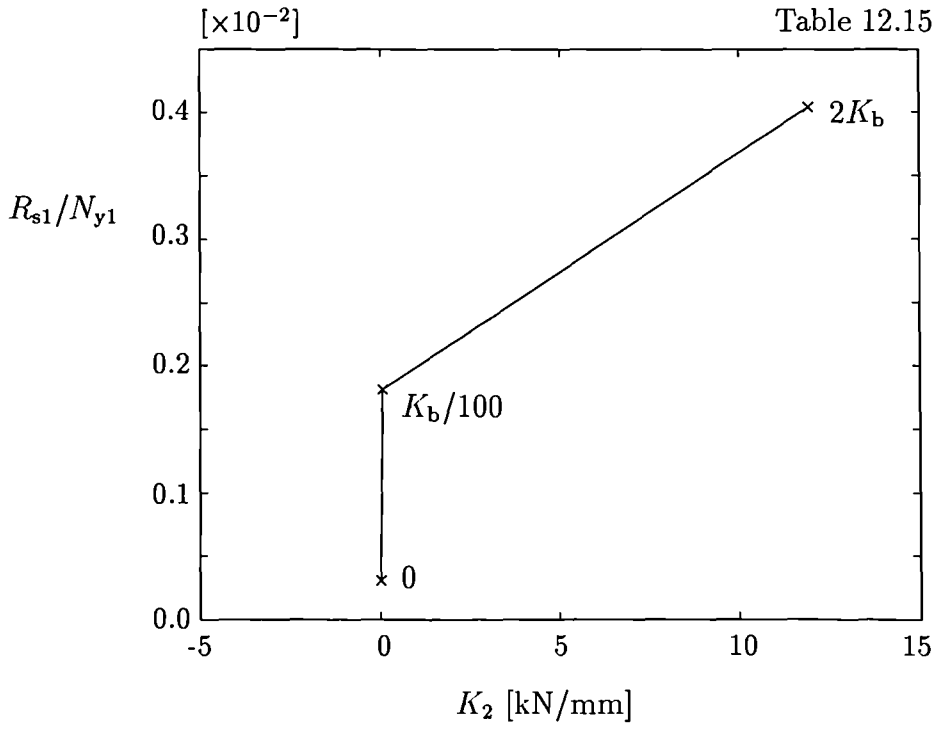

Figure 13.12: Restraint force for elastic support at point **1** versus stiffness of the support at point **2**.

13.6 Summary on the analyses of lateral restraints

The results of all computer analyses of the compressed imperfect strut undertaken within this part of the thesis are summarised in the following points:

1. The antisymmetrical imperfections of the main member influence the lateral force in bracing members, and is less critical especially for higher values of $\bar{\lambda}$, than the lateral force obtained by analysing the model with symmetrical imperfections. Nevertheless, there is little difference between the values of the failure load, assumed to be the axial force at first yield in a cross–section anywhere along the main member.

2. The axial force at first yield, N_y, in the main member is greater than the design force, N_R, taken from EC3 – curve c for slendernesses $0.43 < \bar{\lambda} < 1.0$ when considering the antisymmetrical imperfections of the main member. This is not true for $\bar{\lambda} < 0.43$, but for this range buckling is hardly a problem. Thus the design curve c, which is recommended in EC3 for use for lateral buckling of welded members, is sufficient for the design of braced compression flanges and leads to safe results (Fig. 13.3).

3. Using a spring stiffness $K_b L_u/N_{cr} > 2$ (this represents the stiffness of a bracing member) would be sufficient from both points of view:

   - the yielding load for the main member is larger than the unfactored design value, N_R, and is well up on the shoulder of the curve in Fig. 13.1;
   - the ratio $\delta_b/2a_o$ (Table 12.1) is well below 1.0 which suggests a sufficiently stiff system.

   However, Section 13.3.4 (see also point con6 here) brings the doubt into this conclusion. Therefore it is necessary to perform a few more analyses in the area of non–linear solution for the stiffness of lateral restraints $K_b = 2N_{cr}/L_{cr}$.

4. The maximum lateral force, $F_{u,max}$, in intermediate bracings is found to be 1.3 % of N_y (Table 12.4) for a maximum imperfection $a_{max} = L_G/513$ where

L_G is overall length of the main member. For $a_{max} = L_G/667$ the value of $F_{u,max}$ in an intermediate bracing is up to 1.0 % of N_y (Tables 12.1 and 12.2). These ratios suggest that the increase of lateral force is roughly proportional to the increase of initial imperfections.

5. Spreading the elastic lateral stiffness of the whole system along the main member slightly increases the axial force at first yield in the member, but by less than 3 %. However, there is a large increase in the greater lateral reaction force at a support, 23 %, when two intermediate elastic restraints are replaced by seven, equally distributed along the length while keeping the overall lateral stiffness of the system constant (Fig. 13.7).

6. The elastic critical buckling force is independent of the shape of initial imperfections when assuming small deflection theory. For $n = 3$ the critical buckling force was calculated for the spring stiffnesses $K_b = 4N_{cr}/L_{cr}$ and $K_b = 2N_{cr}/L_{cr}$. The second stiffness showed to be not sufficient for elastic buckling analyses to force the strut to buckle in three sine half–waves.

7. The axial force at first yield, N_y, is reduced when pinned end supports are replaced by elastic ones with stiffness $K_1 = K_2 = 2K_b$ (see Tables 12.8 to 12.13). This reduction is, however, only 1 %, when $K_b = 2N_{cr}/L_u$ (Table 12.9), and only up to 0.7 %, when $K_b = 4N_{cr}/L_u$ (Table 12.8). Thus the reduction is considered to be negligible.

8. The change in lateral bracing force when pinned end supports are replaced by elastic ones with stiffness $K_1 = K_2 = 2K_b$ depends on slendernesses of the main member. For members with slendernesses $0.4 < \bar{\lambda} < 0.7$ this change is within 2 %. For the more slender main members with $\bar{\lambda} > 0.7$ the change in lateral bracing force increases up to 7 % (Fig 13.9).

9. The lateral force at an end support does not exceed 0.6 % of the maximum axial force at first yield for members of the type shown in Fig. 12.6, where an axial force is distributed along the main member. The main member was considered on one side of the support only, with overall length $L_G = 2L_u$ and

with one mid–length elastic bracing with stiffness $K_b = 4N_{cr}/L_u$. The ratio of the lateral force in the spring to the maximum axial force at first yield in the main member, F_u/N_y, did not exceed 1.2 %. However, if comparison is done between the lateral force F_u and the squash load N_{pl} then it can be concluded that F_u is always less than 1 % of N_{pl} for the range of slendernesses (0.6 to 1.0) and stiffness of the intermediate spring $K_b = 4N_{cr}/L_{cr}$.

10. Point 9 suggests that if the axial force at first yield, reached in any cross–section of the main member along its length, is taken as the failure load, the conclusions in points 1 to 8 can be used independently of whether the main member is loaded by constant or linearly distributed axial force.

Chapter 14

Conclusions on lateral restraints

All computer analyses were done for geometrically imperfect plate girder flanges of uniform section which are curved in neither plan nor elevation. They are typically bottom flanges for continuous deck type bridges. The effects of eccentric loads from cross–members are not included. Only computer analyses were performed since it would be almost impossible to achieve the required accuracy in fabricating steelwork to maximum permitted imperfections.

The slenderness, $\bar{\lambda}$, of the modelled flange varied from 0.4 to 1.0. The rectangular cross–sections were calculated according to the rules of EC3 curve c for a compressed strut. Tables 14.1 and 14.2 summarise all computer analyses. Symmetrical (A) and

length $= 2L_u$									
	$K_b L_u/N_{cr}$								
λ	0	2/3	2	3	4	5	6	8	∞
0.4					$B_{r,e}$				
0.522					B_r				
0.6	A_r	A_r	A_r,$B_{r,e}$	A_r	A_r,$B_{r+L2+L3,e+L2+L3}$	A_r	A_r	A_r	A_r
0.7					B_r				
0.8					$B_{r+L2,e+L2}$				
0.9					B_r				
1.0					$B_{r+L2,e+L2}$				

Table 14.1: Analyses with the overall length $2L_u$.

length = $3L_u$					
	$K_b L_u/N_{cr}$				
$\bar{\lambda}$	0	2	4	8	∞
0.6	D_r	D_r	A_r,B_r,C_r,$D_{r,e}$,E_r,F_r	D_r	D_r
1.0			D_r,E_r,F_r		

Table 14.2: Analyses with the overall length $3L_u$.

antisymmetrical (B) shapes of initial imperfections were investigated for the overall length of $2L_u$ with one intermediate elastic lateral restraint. Five different shapes (from A to E) of initial imperfections were considered for the overall length $3L_u$ with two intermediate elastic lateral restraints of equal stiffnesses. Stiffness of the lateral restraints was varied from $K_b = 0$ to $K_b = \infty$ for one set of analyses where $\bar{\lambda} = 0.6$ and the overall length was $2L_u$. In most of the cases it was considered to be $K_b = 4$. Support conditions were either pinned end supports (subscript r in Tables 14.1 and 14.2), or elastic end supports in the direction perpendicular to the length of the main member in the plane of initial imperfections (subscript e in Tables 14.1 and 14.2). The loading of all models was by uniform axial compression. Subscripts $L2$ and $L3$ indicate the additional analyses for models loaded by non-uniform linearly distributed axial compression.

The three main questions to be answered from the results of the presented analyses are following:

1. What is the minimum value of stiffness, the U-frame bracing must have, so that the resistance of the flange is sufficiently up on the shoulder of the curve, which characterises the relationship between $N_{(x)}/N_{pl}$ and $K_b L_u/N_{cr}$? $N_{(x)}$ is taken as the maximum allowed compression force in a flange which in bridge design cannot exceed the axial force at first yield in a cross-section, and is taken as this value; $N_{pl} = A_a f_y$; N_{cr} is the elastic critical Euler force; L_u is a distance between two bracings; K_b is the stiffness of an intermediate bracing.

2. What is the minimum ratio of K_1/K_b such that the conditions given in the previous question are satisfied? K_1 represents the stiffness of an elastic restraint

at an end support.

3. What is the minimum ratio of a lateral force at an internal support to an axial force in the main member, considering the main member to be present on each side of the support.

The summary in Section 13.6 suggests that the minimum value of stiffness of an elastic lateral restraint in the conditions given above is $K_b = 2N_{cr}/L_u$. However, the elastic buckling analyses introduces some doubts about this conclusion. Therefore it would be advisable to perform some more non–linear analyses to check on the validity of this conclusion. The additional analyses will be for slenderness of the main member, $\bar{\lambda} = 0.4$; 0.6; 0.8 and 1.0 and stiffness of the lateral restraint $K_b = 2N_{cr}/L_u$.

It has been shown that using a value of $K_1/K_b = 2$ was sufficient. The reduction in the axial force in the main member was less than 1 % in comparison with $K_1 = \infty$. In practice, a designer would never use lower ratios of K_1/K_b for ensuring the safety of the lateral restraint at a support.

The answer for the third question is $F_u = 0.01N_{pl}$, where F_u is a lateral force at an internal support and N_{pl} is an axial force in the main member. This conclusion is supported by the summary in Section 13.6 but the author feels that it is necessary to perform further investigations to verify this statement. The following discussion shows the reasons why additional analyses would be warranted.

When considering the overall length of $2L_u$, it was concluded that the antisymmetrical shape of the initial imperfections was more critical because the failure load of the main member was less for this type of initial imperfection. This type of initial imperfection was therefore used in the analyses. However, the models with the symmetrical initial imperfection were found to be more critical for the lateral force in the elastic intermediate restraint. It is therefore suggested to perform some more analyses for symmetrical shape A of the initial imperfection for the values of $\bar{\lambda}$ say 0.4; 0.8 and 1.0. It would show whether the design suggestion $F_u < 0.01N_{pl}$ for a whole range of slendernesses $0.4 < \bar{\lambda} < 1.0$ is always on the safe side.

Point 2 of the summary section 13.6 states that the axial force at first yield, N_y, in the main member is greater than the design force, N_R, taken from EC3 – curve c

for slendernesses $0.46 < \bar{\lambda} < 1.0$ when considering the antisymmetrical imperfections of the main member. This is not true for $\bar{\lambda} < 0.46$, but for this range buckling is hardly a problem. However, in the area of non–linear investigations it is suggested to perform some analyses with the slenderness of main member, $\bar{\lambda}$, to be 0.2 and 0.3. This would show the behaviour of the main member for lower values of slenderness than the chosen range.

Investigations of the models with overall length $3L_u$ were mostly done for shape D of the initial imperfection (see Fig. 12.3). As it was discussed in Section 13.3.1, this shape of initial imperfection is considered to be too adverse. It was shown that a lateral force in an elastic lateral restraint is approximately proportional to a value of the maximum initial imperfection. The suggestion was made to scale the initial imperfections of shape D down by a factor of 1.3 to create shape F. Investigations on shape D showed that the lateral force in the spring is always less than $0.012N_{pl}$. If this number is scaled down by a factor of 1.3 then the lateral force would be less than $0.01N_{pl}$. According to BS 5400: Part 6 the maximum imperfection of the main member is defined by the maximum ratio of the distance of any point along the main member to the line connecting any two points of the main member (and not necessarily the end points of the main member). From this point of view even shape F is too adverse. It is therefore suggested to reconsider the shapes of initial imperfections given by Fig. 12.3 and perform a few more investigations with new shapes. This would verify the statement $F_u < 0.01N_{pl}$.

All of the above recommendations imply that any further analyses would only support the conclusions given within this thesis. Moreover, they would only be regarded as *filling in the blanks* which it was not possible to spend much time on due to time constraints — the temporary licence for using the non–linear package of I–DEAS software was terminated at the time of writing up this thesis. The author believes that all the above mentioned analyses will be performed in near future and presented in the form of the paper at a later date.

References

[1] Aadnesen L.: *On behaviour of compression chords for through–bridges.* J. of Mechanics and Applied Mathematics, Vol. XIV, Pt. 1, Feb. 1961, p. 85–100.

[2] Allen H.G., Bulson P.S.: *Background to buckling*, McGraw–Hill, London, 1980.

[3] Bergfelt A., Leiva L.: *Shear buckling of trapezoidally corrugated girders webs.* Report Part 2, Publ.S84:2, Chalmers University of Technology, Sweden, 1984.

[4] Bryan E.R.: *Stressed skin design and construction: A state of the art report.* Struct. Engineer, Vol. 54, No. 9, Sept. 1976, p. 347–351.

[5] Bryan E.R., Jackson P.: *The shear behaviour of corrugated steel sheeting.* Thin Walled Steel Structures, Their Design and Use in Building. Symposium at University College of Swansea School of Engineering, 11–14 Sept 1967, edited by K.C. Rockey, H.V. Hill, Crosby Lockwood & Son Ltd., London, 1969, p. 258–274.

[6] Cheyrezy M., Combault J.: *Composite bridges with corrugated steel webs. – Achievements and prospects.* I.A.B.S.E., Zurich, Reports, *Proc. Conf., Mixed structures, including new materials, Brussels*, Vol. 60, 1990, p. 479–484.

[7] Combault J., Duviard M., Bonnet M., Thivans P., Thibonnet J.L.: *Viaduct du vallon de Maupre, a Charolles (Saone et Loire). (Viaduct of Maupre Valley at Charolles (Saone and Loire region)).* Travaux No. 636, Oct. 1988, p. 67–80. (in French)

[8] Crisfield M.A.: *Non–linear finite element analysis of solids and structures, Volume 1: Essentials.* John Wiley & Sons, New York, 1991.

[9] Dove C., Adams P.A.: *Experimental stress analysis and motion measurements.* Columbus, Ohio, C.E. Merrill Books, 1964.

[10] Easley J.T.: *Buckling formulae for corrugated metal shear diaphragms.* J. of Struc. Div. ASCE, Vol. 101, No. ST7, July 1975, p. 1403–1417.

[11] Easley J.T., McFarland D.E.: *Buckling of light-gage corrugated metal shear diaphragms.* J. of Struct. Div. ASCE, Vol. 95, No. ST7, July 1969, p. 1497–1516.

[12] Harrison J.D.: *Exploratory fatigue tests of two girders with corrugated webs.* British Welding Journal, Vol. 12, No. 3, March 1965, p. 121–125.

[13] Hlaváček V.: *Shear Instability of Orthotropic Panels.* Acta Technica ČSAV, Vol. 13, No. 1, 1968, p. 134–158.

[14] Hughes T.J.R., Cohen M.: *The 'Heterosis' finite element for plate bending.* Comput. Struct., Vol. 9, No. 5, Nov. 1978, p. 445–450.

[15] Hussain M.I., Libove C.: *Trapezoidally corrugated plates in shear.* J. of Struc. Div. ASCE, Vol. 102, No. ST5, May 1976, p. 1109–1131.

[16] Hussain M.I., Libove C.: *Stiffness tests of trapezoidally corrugated shear webs.* J. of Struc. Div. ASCE, Vol. 103, No. ST5, May 1977, p. 971–987.

[17] Jaeger L. G.: *Elementary theory of elastic plates.* Pergamon Press, The Macmillan company, New York, 1964.

[18] Jeffers E.: *U-frame restraint against instability of steel beams in bridges.* Structural Engineer, Vol. 68, No. 18, Sept. 1990, p. 359–366.

[19] Jeffers E.: *U-frame restraint against instability of steel beams in bridges. Correspondence.* Structural Engineer, Vol. 69, No. 23, Dec. 1991, p. 407–410.

[20] Johnson R.P.: *Distortional lateral buckling of composite beams.* Technical paper JB18, CEN/TC 250/SC4/WG2, University of Warwick, Dec. 1993.

[21] Johnson R.P.: *First draft clauses on lateral–torsional buckling for EC4: Part 2.* Technical paper JB37, TC 250/SC4/WG2, University of Warwick, Aug. 1994.

[22] Johnson R.P.: *Basis for design of lateral restraints to a non–composite flange in compression.* Technical paper JB38, CEN/TC 250/SC4/WG2, University of Warwick, Aug. 1994.

[23] Johnson R.P., Anderson D.: *Designers' handbook to Eurocode 4 Part 1.1: Design of composite steel and concrete structures.* Thomas Telford, London, 1993.

[24] Johnson R.P., Buckby R.J.: *Composite structures of steel and concrete, Volume 2: Bridges.* 2nd edition, Collins Professional & Technical Books, London, 1986.

[25] Johnson R.P., Chen S.: *Stability of continuous composite plate girders with U–frame action.* Proc. Instn Civ. Engrs, Structs & Bldgs, Vol. 99, No. 2, May 1993, p. 187 197.

[26] Johnson R.P., Chen S.: *Strength and stiffness of discrete U–frames in composite plate girders.* Proc. Instn Civ. Engrs, Structs & Bldgs, Vol. 99, No. 2, May 1993, p. 199–209.

[27] Johnson R.P., Fan C.K.R.: *Distortional lateral buckling of continuous composite beams.* Proc. Instn Civ. Engrs, Part 2: Research and Theory, March 1991, p. 131–161.

[28] Johnston B.G.: *Design criteria for metal compression members.* The Column Research Council of the Engineering Foundation, New York, 1966.

[29] Korashy M., Varga J.: *Comparative evaluation of fatigue strength of beams with web plate stiffened in the conventional way and by corrugation.* Acta Technica Academia Scientiarum Hungariche, Budapest, 1979.

[30] Leiva L.: *Skjuvbuckling hos Platbalkar med Trapetsprofilerat Liv.* Delrapport 1: Inledande försök, Publ.S83:3, Chalmers University of Technology, Sweden, 1983. (in Swedish)

[31] Leiva L.: *Trapezoidally Corrugated Panels, Buckling Behaviour under Axial Compression and Shear.* Publ.S87:1, Chalmers University of Technology, Sweden, 1987.

[32] Leiva L., Edlund B., Bergfelt A.: *Trapezoidally corrugated girder webs. Shear buckling. Patch loading.* Ing. Archit. Suisses, Vol. 111, No. 1–2, Jan. 1985, p. 22–27.

[33] Libove C.: *Survey of recent work on analysis of discretely attached corrugated shear webs.* Syracuse Univ., NY, American Institute of Aeronautics and Astronautics/ASME/SAE, 13th Structures, Structural Dynamics and Materials Conference, San Antonio, Tex., April 10–12 1972, Vol. 3, paper No. 72–351, p. 1 23.

[34] Libove C.: *Buckling of corrugated plates in shear.* Int. Colloq. on Stab. of Struct. under Static and Dyn. Loads, Proc., Washington D.C., May 17–19, 1977, Publ. by ASCE, New York, NY, 1977, p. 435–462.

[35] Libove C., Wu L.H.: *Curvilinearly corrugated plates in shear.* J. of Struc. Div., Vol. 101, No. ST11, Nov. 1975, p. 2205–2222.

[36] Lindner J.: *Lateral torsional buckling of beams with trapezoidally corrugated webs.* Intern. Colloquium on stability of steel structures, Budapest, Hungary, 1990, p. 79–86.

[37] Lindner J.: *Shear capacity of beams with trapezoidally corrugated webs and openings.* Fourth Intern. Colloquium on structural stability, Mediterranean session, Istanbul, Sept. 16–20, 1991, p. 103–112.

[38] Luo R., Edlund B.: *Buckling analysis of trapezoidally corrugated web panels using spline finite strip method.* Nordic Steel Colloquium on Research and Development within the field of construction, Danish Steel Works, Ltd, Rautaruukki Oy, Swedish Steel, Ltd., Odense, Denmark, Sept. 1991, p. 1–12.

[39] Luo R., Edlund B.: *Buckling analysis of trapezoidally corrugated web under patch loading using spline finite strip method.* Proc. of IUTAM Symposium,

Prague, Sept. 1990, Contact loading and local effects in thin–walled plated and shell structures, Academia, Publishing House of Czechoslovak Academy of Sciences, Prague 1992, p. 119–127.

[40] Martin D.M., Tubman J.: *Commentary on BS 5400: Part 3: 1982. Code of practice for design of steel bridges.* SCI Publication 085, The Steel Construction Institute, 1991.

[41] Mindlin R.D.: *Influence of rotatory inertia and shear on flexural motions of isotropic, elastic plates.* Am. Soc. Mech. Engrs, Trans (J. of Applied Mechanics), Vol. 18, No. 1, March 1951, p. 31–38.

[42] Peterson J.P., Card M.F.: *Investigation of the Buckling Strength of Corrugated Webs in Shear.* NASA Tech. Note D–424, Washington, June 1960, p. 1–29.

[43] Raoul J.: *Some remarks concerning the use of corrugated webs for bridges.* Private communication, Jan. 1993.

[44] Stanway G.S., Chapman J.C., Dowling P.J.: *A simply supported imperfect column with a transverse elastic restraint at any position. Part 1: behaviour.* Proc. Instn Civ. Engrs Structs & Bldgs, Vol. 94, May 1992, p. 205–216.

[45] Stanway G.S., Chapman J.C., Dowling P.J.: *A simply supported imperfect column with a transverse elastic restraint at any position. Part 2: design models.* Proc. Instn Civ. Engrs Structs & Bldgs, Vol. 94, May 1994, p. 217–228.

[46] Timoshenko S.P.: *Theory of elastic stability.* McGraw–Hill Book Company, New York, 2nd edition, 1961.

[47] Vendráková J., Johnson R.P.: *Fabrication of cambered or non–uniform plate girders with corrugated webs.* Research Report CE44, Department of Engineering, University of Warwick, Nov. 1993.

[48] Virčík J.: *Približný výpočet nosníkov s konštrukčne ortotrópnou stenou. (The approximate calculation of beams with geometrically orthotropic webs).* Zborník

vedeckých prác, Civil Engineering Faculty of Slovak Technical University, Bratislava, 1973. (in Slovak)

[49] Virčík J., Vajda J.: *Nosníky so zvlnenou stenou. (Girders with undulated web plate).* Staveb. časopis SAV, Vol. 22, No. 7, Bratislava, 1974, p. 403–420. (in Slovak)

[50] Wang Y.C., Nethercot D.A.: *Bracing effects on 3-dimensional column sub-assemblages.* Proc. Instn Civ. Engrs, London, Part 1: Design and Construction, Vol. 87, Aug. 1989, p. 357–376.

[51] Wang Y.C., Nethercot D.A.: *Bracing requirements for laterally unrestrained beams.* J. Construct. Steel Research, Vol. 17, No. 4, 1990, p. 305–315.

[52] Weston G., Nethercot D.A, Crisfield M.A.: *Lateral buckling in continuous composite bridge girders.* Structural Engineer, Vol. 69, No. 5, March 1991, p. 79–87.

[53] Winter G.: *Lateral bracing of columns and beams.* Trans. Amer. Soc. Civ. Engrs, 125, Part 1, 807–826, 1960.

[54] Yoda T., Ohura T., Sekii K.: *Analysis of composite PC box girders with corrugated steel webs.* Fourth international conference on short and medium span bridges, Halifax, Nova Scotia, Canada, Aug. 1994, p. 1107–1114.

[55] DD ENV 1993-1-1 *Design of steel structures. Part 1.1-General rules and rules for buildings.* British Standards Institution, 1993.

[56] BS 5400: Part 3: 1982. *Steel, concrete, and composite bridges. Code of practice for design of steel bridges.* British Standards Institution, London, 1982.

[57] BS 5400: Part 1: 1980. *Steel, concrete, and composite bridges. Part 6. Specification for materials and workmanship, steel.* British Standards Institution, London, 1982.

[58] BS 5950: Part 1: 1990. *Code of practice for design in simple and continuous construction: hot rolled sections.* British Standards Institution, London, 1990.

[59] BS EN 10 002–1: 1990 *Tensile testing of metallic materials, Part 1. Method of test at ambient temperature.* British Standards Institution, London, 1990.

[60] SDRC. *I–DEAS Finite Element Modelling, I–DEAS Model Solution.* Structural Dynamic Research Corporation, Software Products Marketing Division, Inc., Milford, OH, 45150, U.S.A., 1990.

[61] ČSN 73 6205 *Navrhování ocelových mostních kostrukcí (Design of steel bridge structures).* Vydavatelství úřadu pro normalizaci a měření, Praha, 1984, revised 1989 (in Czech).

[62] *Design rules for plate girders with corrugated webs.* Report BSAB GS. 222, Tibnor Bygg, Stockholm, Nov. 1974. (in Swedish)

Part III

Appendices

Appendix A

Comparison between corrugated webs and flat stiffened webs, for steel and composite bridges

A.1 Advantages of corrugated webs

1. Stiffer transverse U-frame action with less concentration of transverse moments applied to the shear connection with a concrete slab above (or below).

2. Much better resistance to web crippling, important where girders are launched.

3. Higher resistance to vertical shear, for the same weight of steel in the web, and to torsion.

4. Lower force required to prestress a flange longitudinally, because none of the prestress compresses the web.

5. In a box girder, higher and more uniform resistance to distortion of the cross section.

6. There is experience of their use, in:
   — the 3–span Pont de Cognac (31+43+31 m), completed 1986, with trapezoidal box with concrete flanges and corrugated steel webs; and in the viaduct

de Charolles (53.5 m max.).

7. Shrinkage of concrete slabs can occur almost freely, without stressing the shear connectors or the webs.

8. The more rapid heating or cooling of a steel web (cf. a concrete slab) in morning and evening causes much lower temperature stresses in it and in the deck slab.

9. Lower sensitivity to imperfections, because the effective thickness is much greater.

A.2 Disadvantages of corrugated webs

1. Difficulty of welding the web to the flanges. This is not significant for bridges, once investment has been made in profile—following welding equipment. These webs in French bridges are typically 8 mm thick.

2. The complex nature of web buckling in shear. Local buckling of flat panels is stable with good post-buckling behaviour; but global buckling may be unstable and must be avoided in design, or given higher safety margin.

3. Fabrication of a corrugated plate is more costly.

4. Deflections due to shear may not be negligible compared with those due to flexure (but this is true also of flat webs).

5. Behaviour of a box section with concrete flanges in non-uniform torsion is less good than that of a concrete box girder — but probably not worse than that of a steel box with conventional webs.

6. Connections between vertical edges of web plates are slightly more frequent than for flat plates — but most of those can be shop welds because the "handling and transport" limitations on girder size are the same as for conventional girders.

Appendix B

Cross–sectional properties

The first two parts of Table B.1 list the effective geometrical properties of a section represented only by flanges. They were calculated from eqs. 8.6 and 8.7 using measured values from Table 7.1. The values A_{eff}, $I_{1,\text{eff}}$ and $y_{1,\text{eff}}$ are based on the effective thicknesses listed in the first part of Table B.1. They were calculated from eqs. 8.9 and 8.10. The values in the third part of the table were calculated from eqs. 8.9 and 8.10 using only the measured values listed in Table 7.1.

			CW1	CW2	CW3	CW4	CW5
1	EFFECTIVE THICKNESSES						
	$t_{\text{fc,I}}$	mm	8.989	6.642	8.844	6.756	6.658
	$t_{\text{ft,I}}$	mm	8.849	8.641	8.811	8.502	8.378
	$t_{\text{fc,A}}$	mm	8.693	6.326	8.537	6.476	6.377
	$t_{\text{ft,A}}$	mm	8.553	8.325	8.504	8.224	8.097
	h_{eff}	mm	448.08	444.28	444.52	443.79	443.50
2	EFFECTIVE CROSS–SECTIONAL PROPERTIES						
	A_{eff}	mm^2	3476.52	2944.42	3419.27	2955.40	2901.59
	$I_{1,\text{eff}} \times 10^{-8}$	mm^4	1.81	1.49	1.75	1.49	1.46
	$y_{1,\text{eff}}$	mm	226.86	254.68	226.65	251.10	250.48
3	MEASURED CROSS–SECTIONAL PROPERTIES						
	A	mm^2	3354.36	2813.60	3244.50	2796.61	2750.44
	$I_1 \times 10^{-8}$	mm^4	1.688	1.364	1.608	1.359	1.335
	y_1	mm	226.73	257.40	226.66	253.66	252.96

Table B.1: Effective thicknesses and cross–sectional properties of the specimens.

Appendix C

Stiffness of corrugated plate

C.1 Uniform tension

Fig. C.1 shows the deformations of one–quarter of a corrugation. The sheeting has thickness t_w. The axial extension is neglected and only bending deformations are considered. The following analyses (in both the uniform tension and pure bending) are based on an assumed deflected shape of a separated strip of depth dy – thus the expression $(1 - \nu^2)$ in I_y is neglected.

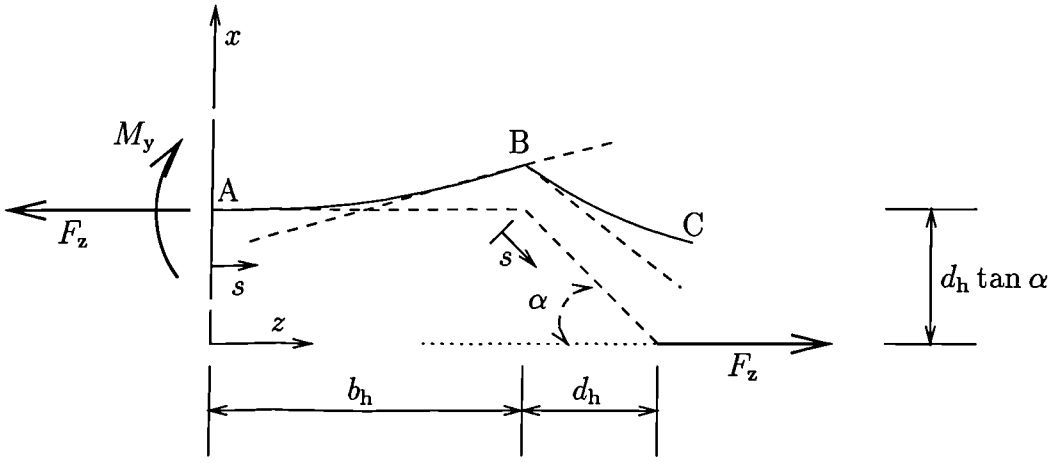

Figure C.1: One–quarter of a corrugated web in uniform tension.

For the strip AB the internal energy is

$$U_{\mathrm{AB}} = \frac{1}{2}\int_{\mathrm{AB}} \frac{M_{\mathrm{y}}^2}{EI_{\mathrm{y}}}\mathrm{d}s \tag{C.1}$$

where $M_{\mathrm{y}} = F_{\mathrm{z}} d_{\mathrm{h}} \tan\alpha$; $F_{\mathrm{z}} = \text{const.} = \sigma_{\max} t_{\mathrm{w}} \mathrm{d}y$; $I_{\mathrm{y}} = t_{\mathrm{w}}^3 \mathrm{d}y/12$.

$$U_{\mathrm{AB}} = \frac{1}{2}\int_0^{b_{\mathrm{h}}} \frac{\sigma_{\max}^2 t_{\mathrm{w}}^2 (\mathrm{d}y)^2 d_{\mathrm{h}}^2 (\tan\alpha)^2}{E t_{\mathrm{w}}^3 \mathrm{d}y/12}\mathrm{d}s$$

$$U_{\mathrm{AB}} = \frac{6\sigma_{\max}^2 b_{\mathrm{h}} d_{\mathrm{h}}^2 (\tan\alpha)^2}{E t_{\mathrm{w}}}\mathrm{d}y \tag{C.2}$$

For the strip BC the internal energy is

$$U_{\mathrm{BC}} = \frac{1}{2}\int_{\mathrm{AB}} \frac{M_{\mathrm{y}}^2}{3EI_{\mathrm{y}}}\mathrm{d}s \tag{C.3}$$

$$U_{\mathrm{BC}} = \frac{1}{2}\int_0^{d_{\mathrm{h}}\sec\alpha} \frac{\sigma_{\max}^2 t_{\mathrm{w}}^2 (\mathrm{d}y)^2 d_{\mathrm{h}}^2 (\tan\alpha)^2}{3E t_{\mathrm{w}}^3 \mathrm{d}y/12}\mathrm{d}s$$

$$U_{\mathrm{BC}} = \frac{2\sigma_{\max}^2 d_{\mathrm{h}}^3 (\tan\alpha)^2 \sec\alpha}{E t_{\mathrm{w}}}\mathrm{d}y \tag{C.4}$$

Thus the total internal energy of the strip AC with depth $\mathrm{d}y$ is the sum of eqs. C.2 and C.4

$$U_{\mathrm{i}} = \frac{2\sigma_{\max}^2 d_{\mathrm{h}}^2 (\tan\alpha)^2}{E t_{\mathrm{w}}} \left(3b_{\mathrm{h}} + d_{\mathrm{h}} \sec\alpha\right) \mathrm{d}y \tag{C.5}$$

The external energy of the strip AC with depth $\mathrm{d}y$ in uniform tension is

$$U_{\mathrm{e}} = \frac{1}{2}\int_0^{b_{\mathrm{h}}+d_{\mathrm{h}}} \frac{F_{\mathrm{z}}^2}{E_{\mathrm{e,t}} t_{\mathrm{w}} \mathrm{d}y}\mathrm{d}z \tag{C.6}$$

where $E_{\mathrm{e,t}}$ is an effective Young's modulus of a corrugated plate in uniform tension. Eq. C.6 can be further simplified to

$$U_{\mathrm{e}} = \left(\frac{b_{\mathrm{h}} + d_{\mathrm{h}}}{2}\right) \frac{\sigma_{\max}^2 t_{\mathrm{w}}^2 (\mathrm{d}y)^2}{E_{\mathrm{e,t}} t_{\mathrm{w}} \mathrm{d}y}$$

$$U_{\mathrm{e}} = \frac{\sigma_{\max} t_{\mathrm{w}}}{2E_{\mathrm{e,t}}} \left(b_{\mathrm{h}} + d_{\mathrm{h}}\right) \mathrm{d}y \tag{C.7}$$

From the equilibrium of the internal and external energies (eqs. C.5 and C.7)

$$\frac{2\sigma_{\max}^2 d_h^2(\tan\alpha)^2}{Et_w}(3b_h + d_h\sec\alpha)\,dy = \frac{\sigma_{\max}t_w}{2E_{e,t}}(b_h + d_h)\,dy$$

the effective Young's modulus of a corrugated plate in pure tension is

$$\frac{E_{e,t}}{E} = \frac{(b_h + d_h)\,t_w^2}{4d_h^2(\tan\alpha)^2(3b_h + d_h\sec\alpha)} \tag{C.8}$$

Assuming $b_h = \iota t_w$; $d_h = \kappa t_w$ eq. C.8 can be formed into:

$$\frac{E_{e,t}}{E} = \frac{\iota + \kappa}{4\kappa^2(\tan\alpha)^2(3\iota + \kappa\sec\alpha)} \tag{C.9}$$

C.2 Pure bending

In case of pure bending the stresses along the depth of a beam are not constant but they vary linearly as shown in Fig. C.2. To analyse the stiffness of a corrugated web in bending again the assumptions of constant thickness and neglected axial extension are made. Initially, an assumed deflected shape of one–quarter of a corrugated strip with a depth dy is analysed which means that the expression $(1 - \nu^2)$ in I_y is neglected.

From Fig. C.2 (a) the following formula is developed

$$F_z = \left(\frac{\sigma_{\max}y}{h_w/2}\right)t_w dy \tag{C.10}$$

The following method is based on the strain energy stored in a corrugated plate after its deformation. The strain energy of the rectangular plate $y \times z$ (for a coordinate system as shown in Figs. C.2 (a)) as given by Jaeger [17] is

$$U = \frac{D}{2}\int_{-y/2}^{y/2}\int_0^z \left\{\left(\frac{\partial^2 x}{\partial y^2} + \frac{\partial^2 x}{\partial z^2}\right)^2 - 2(1-\nu)\left[\frac{\partial^2 x}{\partial y^2}\frac{\partial^2 x}{\partial z^2} - \left(\frac{\partial^2 x}{\partial y \partial z}\right)^2\right]\right\} dz dy \tag{C.11}$$

where $D = Et_w^3/[12(1-\nu^2)]$ and ν is the Poisson's ratio. Using this expression another approximation was made. An assumed deflected shape for a whole plate

with depth h_w has straight lines along this depth – thus $\partial M_{yz}/\partial y = 0$. This is obviously not true at the top and bottom edges.

Fig. C.3 shows a separated strip AB with the applied bending moment only (force

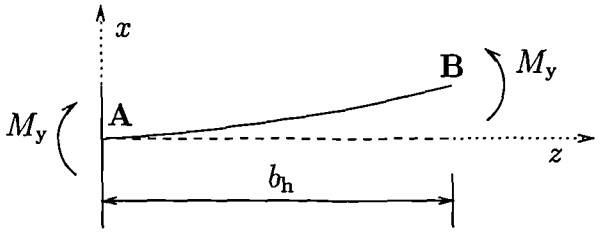

Figure C.3: Deformation of the strip AB with depth dy.

F_z as drawn in Fig. C.2 (b) has no influence on bending or twisting the strip AB). From this figure bending moment, M_y, is defined by

$$M_y = F_z d_h \tan\alpha = \frac{2\sigma_{max} d_h t_w \tan\alpha}{h_w} y \mathrm{d}y \tag{C.12}$$

Bending moment can be also expressed through the deformations as

$$M_y = -EI_y \frac{\partial^2 x}{\partial z^2} \tag{C.13}$$

where $I_y = t_w^3 \mathrm{d}y/12$. Substituting eq. C.13 into C.12 gives

$$\frac{\partial^2 x}{\partial z^2} = -\frac{24\sigma_{max} d_h \tan\alpha}{E t_w^2 h_w} y \tag{C.14}$$

From eq. C.14 it can be written

$$\frac{\partial x}{\partial z} = -\int \frac{24\sigma_{max} d_h \tan\alpha}{E t_w^2 h_w} y \mathrm{d}z$$

thus

$$\frac{\partial x}{\partial z} = -\frac{24\sigma_{max} d_h \tan\alpha}{E t_w^2 h_w} yz + C_1 \tag{C.15}$$

The boundary conditions in Fig. C.3 show that if $z = 0$ then $\partial x/\partial z = 0$ and so

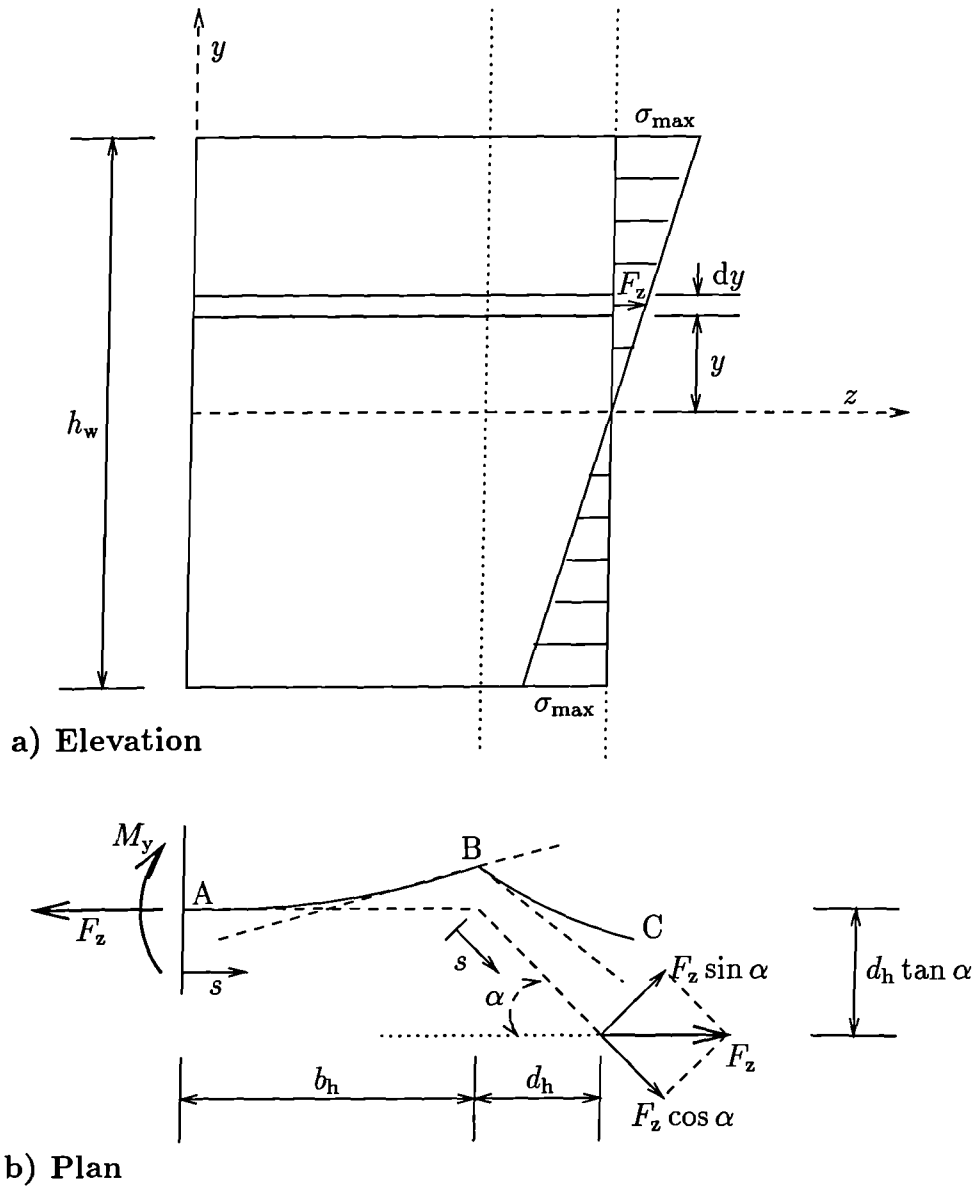

Figure C.2: One–quarter of a corrugated web in pure bending.

$C_1 = 0$. Therefore from eq. C.15

$$x = -\frac{12\sigma_{\max} d_h \tan\alpha}{E t_w^2 h_w} y z^2 + C_2$$

which after differentiating with respect to y twice gives

$$\frac{\partial^2 x}{\partial y^2} = 0 \tag{C.16}$$

Differentiating eq. C.15 with respect to y gives

$$\frac{\partial^2 x}{\partial y \partial z} = -\frac{24\sigma_{\max} d_h \tan\alpha}{E t_w^2 h_w} z \tag{C.17}$$

Substituting eqs. C.14, C.16 and C.17 into eq. C.11 for the boundary $y = h_w$ and $z = b_h$ gives

$$U_{AB} = \frac{D}{2} \int_{-h_w/2}^{h_w/2} \int_0^{b_h} \left[\frac{24^2 \sigma_{\max}^2 d_h^2 (\tan\alpha)^2}{E^2 t_w^4 h_w^2} y^2 + 2(1-\nu) \frac{24^2 \sigma_{\max}^2 d_h^2 (\tan\alpha)^2}{E^2 t_w^4 h_w^2} z^2 \right] dz dy$$

from which

$$U_{AB} = \frac{8\sigma_{\max}^2 b_h d_h^2 (\tan\alpha)^2}{E(1-\nu^2) t_w h_w} \left[\frac{h_w^2}{4} + 2(1-\nu) b_h^2 \right] \tag{C.18}$$

Strip BC is shown in Fig. C.4. The coordinate system is rotated by angle α.

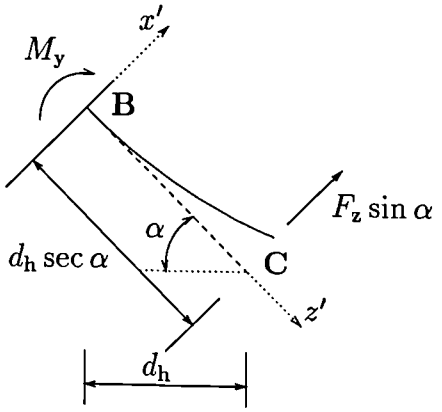

Figure C.4: Deformation of the strip BC with depth dy.

For the simplicity of the following calculations assume $x' = x$ and $z' = z$. Bending

moment, M_y, is not constant along the length of the strip.

$$M_y = F_z \sin\alpha \,(d_h \sec\alpha - z) \tag{C.19}$$

Substituting eqs. C.10 and C.13 into eq. C.19 gives

$$\frac{\partial^2 x}{\partial z^2} = -\frac{24\sigma_{max}\sin\alpha}{Et_w^2 h_w}(d_h \sec\alpha - z) \tag{C.20}$$

Differentiating and integrating eq. C.20 the same way as shown above for strip AB would give the following equations

$$\frac{\partial x}{\partial z} = -\frac{24\sigma_{max}\sin\alpha}{Et_w^2 h_w}\left(d_h yz\sec\alpha - \frac{yz^2}{2} + C_3\right) \tag{C.21}$$

where if $z = 0$ then $\partial x/\partial z = 0$ and so $C_3 = 0$.

$$x = -\frac{24\sigma_{max}\sin\alpha}{Et_w^2 h_w}\left(\frac{d_h yz^2}{2}\sec\alpha - \frac{yz^3}{6} + C_4\right)$$

from which

$$\frac{\partial^2 x}{\partial y^2} = 0 \tag{C.22}$$

From eq. C.21

$$\frac{\partial^2 x}{\partial y \partial z} = -\frac{24\sigma_{max}\sin\alpha}{Et_w^2 h_w}\left(d_h z\sec\alpha - \frac{z^2}{2}\right) \tag{C.23}$$

Substituting eqs. C.20, C.22 and C.23 into eq. C.11 for the boundary $y = h_w$ and $z = d_h \sec\alpha$ gives

$$U_{BC} = \frac{D}{2}\int_{-h_w/2}^{h_w/2}\int_0^{d_h\sec\alpha}\left[\frac{24^2\sigma_{max}^2(\sin\alpha)^2}{E^2 t_w^4 h_w^2}y^2(d_h\sec\alpha - z)^2\right.$$

$$\left.+2(1-\nu)\frac{24^2\sigma_{max}^2(\sin\alpha)^2}{E^2 t_w^4 h_w^2}\left(d_h z\sec\alpha - \frac{z^2}{2}\right)^2\right]dz\,dy$$

from which

$$U_{BC} = \frac{8\sigma_{max}^2 d_h^3 \sec\alpha\,(\tan\alpha)^2}{E t_w h_w (1-\nu^2)} \left[\frac{h_w^2}{12} + \frac{4(1-\nu)\,d_h^2\,(\sec\alpha)^2}{5}\right] \tag{C.24}$$

The strain energy of one–quarter of a corrugated web is then the sum of eqs. C.18 and C.24

$$U_i = \frac{8\sigma_{max}^2 h_w d_h^2 (\tan\alpha)^2}{E t_w (1-\nu^2)} \left[\frac{(3b_h + d_h \sec\alpha)}{12} + \frac{2(1-\nu)(5b_h^3 + 2d_h^3(\sec\alpha)^3)}{5h_w^2}\right] \tag{C.25}$$

The external energy of one–quarter of a corrugated plate bent by bending moment M_x is

$$U_e = \frac{1}{2}\int_0^{b_h+d_h} \frac{M_x^2}{E_{e,b} I_x} dz \tag{C.26}$$

where $M_x = \sigma_{max} t_w h_w^2/6$; $E_{e,b}$ is the effective Young's modulus for pure bending of a corrugated plate and $I_x = t_w h_w^3/12$. Then the external energy is

$$U_e = \frac{1}{2}\int_0^{b_h+d_h} \frac{\sigma_{max}^2 t_w^2 h_w^4/36}{E_{e,b} t_w h_w^3/12} dz$$

$$U_e = \frac{\sigma_{max}^2 t_w h_w}{6E_{e,b}} (b_h + d_h) \tag{C.27}$$

From the equilibrium of the internal and external energies $U_i = U_e$ the effective Young's modulus of a corrugated plate for pure bending is

$$\frac{E_{e,b}}{E} = \frac{(b_h + d_h)\,t_w\,(1-\nu^2)}{48 d_h^2 (\tan\alpha)^2} \left[\frac{3b_h + d_h \sec\alpha}{12} + \frac{(1-\nu)}{h_w^2}\left(2b_h^3 + \frac{4}{5}d_h^3(\sec\alpha)^3\right)\right]^{-1} \tag{C.28}$$

which assuming $b_h = \iota t_w$; $d_h = \kappa t_w$ leads to

$$\frac{E_{e,b}}{E} = \frac{(\iota+\kappa)(1-\nu^2)}{48\kappa^2(\tan\alpha)^2} \left[\frac{3\iota + \kappa\sec\alpha}{12} + \left(\frac{t_w}{h_w}\right)^2 (1-\nu)\left(2\iota^3 + \frac{4}{5}\kappa^3(\sec\alpha)^3\right)\right]^{-1} \tag{C.29}$$